Palaeo wind system reconstruction of the last glacial period over Europe, using high resolution proxy data and model-data-comparison

Dissertation
zur Erlangung des akademischen Grades
„Doktor der
Naturwissenschaften“

im Promotionsfach Geologie/Paläontologie

am Fachbereich Chemie, Pharmazie und Geowissenschaften
der Johannes Gutenberg-Universität Mainz

von

Stephan Dietrich

geb. in Wiesbaden

2011

JG|U
JOHANNES GUTENBERG
UNIVERSITÄT MAINZ

Dekan:

1. Gutachter:
2. Gutachter:
3. Gutachter:

Tag der mündlichen Prüfung: 19.07.2011

'Raw' data are noisy, shapeless, and uninterpretable. Models give them a definite form. Neither models nor [proxy] data alone can support a living understanding of physical phenomena.

Paul N. Edwards (2010) in
A Vast Machine: Computer Models, Climate Data, and the Politics of Global Warming

Contents

List of Figures

List of Tables

List of Publications

The present thesis is cumulatively written. Published or submitted articles, marked with an asterisk (*), are slightly modified presented in the chapters 4–6. Content of the other publications are used in the chapters 1 and 3, respectively.

Peer-reviewed Articles and Book Contributions

Dietrich, S.* and F. Sirocko: The potential for dust detection by means of µXRF scanning in Eifel maar lake sediments. E&G - Quarternary Science Journal, accepted.

Dietrich, S.* and K. Seelos: The reconstruction of easterly wind directions for the Eifel region (Central Europe) during the period 40.3 - 12.9 ka BP., Clim. Past, 6, 145-154, www.clim-past.net/6/145/2010/, 2010.

Lenaz, D., R. Marciano, D. Veres, S. Dietrich and F. Sirocko: Mineralogy of the Dehner and Jungferweiher maar tephras (Eifel, Germany). N.Jb.Geol.Palaont.Abh. Doi:10.1127/0077-7749/2010/0062., 2010.

Dietrich, S. und F. Sirocko: Korngrößenanalyse und Sedimentgeochemie von Seesedimenten als Grundlage der Klima- und Wetterrekonstruktion. In: Wetter, Klima, Menschheitsentwicklung, F. Sirocko (Ed.), Theiss-Verlag, Stuttgart, 2009.

Pfahl, S., F. Sirocko, K. Seelos, S. Dietrich, A. Walter and H. Wernli: A new windstorm proxy from lake sediments - a comparison of geological and meteorological data from western Germany for the period 1965-2001. J. Geophys. Res., 114, D18106, doi:10.1029/2008JD011643, 2009.

Seelos, K., F. Sirocko and S. Dietrich: A continuous high-resolution dust record for the reconstruction of wind systems in central Europe (Eifel, Western Germany) over the past 133 ka, Geophysical Research Letters, 36, L20712, doi:10.1029/2009GL039716,

2009.

Submitted

Dietrich, S.*, G. Lohmann, M. Werner, K. Seelos and F. Sirocko: More Variable Wind Directions and Stronger Winds in Central Europe during the Last Glacial Period, submitted to Climate Dynamics, 2011.

In preparation

Sirocko, F., K. Schaber, S. Dietrich, K. Seelos, P. M. Grootes, B. Kromer, B. Rein, M. Krbetschek, P. Appleby, U. Hambach, C. Rolf, D. Veres, M. Sudo, and S. Grim (in prep). Stratigraphy of 39 sediment cores from Pleistocene and Holocene maar lakes and dry maar lakes in the Eifel (Germany). Will be submitted to Quaternary Science Reviews.

Abstract

The atmosphere is a global influence on the movement of heat and humidity between the continents, and thus significantly affects climate variability. This applied under glacial conditions just as it does today. European wind systems are mainly affected by North Atlantic sea surface temperatures, the distribution and extent of sea ice and of the continental ice sheets, and by atmospheric heat transport.

Information from dust deposits in maar lakes and former, now silted-up maar lakes (dry maars) from the Eifel Volcanic Field (Germany) are used as proxy data for the reconstruction of past aeolian dynamics. Aeolian dust with a mean grain size of 30–40 µm is the dominating sediment fraction in the lake sediments during glacial periods. Maar lake sediments are typically finely laminated and not disturbed. Thus, the investigation of the aeolian dust fraction of those lake sediments is the key for the reconstruction of paleo atmospheric circulation.

In this thesis past atmospheric circulation patterns of the last glacial are studied. The results of the proxy data are compared with those of numerical climate model experiments. These models usually have a rather large spatial resolution of hundreds of kilometers. Thus, the question is whether the dust signal from the Eifel area corresponds to the supra-regional atmospheric circulation or records only a local weather phenomenon. In general, single dust storms are not supra-regional wide mass movements, but present time of high wind speed and local aeolian dust emission. However, the surprisingly good correlation of the dust content in continental dust records from Central Europe and in the Greenland ice cores leads to the suggestion that results from Eifel maar lakes correspond to a supra-regional atmospheric state by pointing to longer time intervals or major supra-regional storm events. In addition, the allocation of storm layers in the Eifel maar lake sediments to measured recent regional meteorological data of supra-regional storm gusts is statistically highly significant for at least the last decades.

The frequencies of glacial dust storm events and their paleo wind direction are detected by high resolution grain size and provenance analysis of the lake sediments. The characterization of different dust emission sources by means of provenance anal-

ysis is the key for reconstruction of paleo wind directions. For both the provenance analysis and the dust detection two different methods are applied: geochemical measurements of the sediment using µXRF-scanning and the particle analysis method RADIUS (rapid particle analysis of digital images by ultra-high-resolution scanning of thin sections). The energy dispersive µXRF is applied to continuously taken resin impregnated sediment samples, which are the basis for the production of petrographic thin sections. Thus, the measurement results can directly be compared with micro facies analysis and the results of the RADIUS methodology. Both methods measure the sediments with a high resolution of 1 mm or less and are thus in the range of annual sedimentation rates. Two sediment cores from the Eifel region are examined: the core SM3 from Lake Schalkenmehren and the core DE3 from the Dehner dry maar. Both cores contain the tephra of the Laacher See eruption, which is dated to 12,900 before present. Taken together the cores cover the last 60 000 years: SM3 the Holocene and DE3 the marine isotope stages MIS-3 and MIS-2, respectively. The age-depth models are based on various dating methods like radiocarbon dating, tephrochronology, and wiggle matching to the Greenland ice cores. The results of the investigations of the dust records are finally evaluated in relation a study of atmospheric general circulation models (ECHAM3 and ECHAM4) for a synoptic interpretation.

It is demonstrated that the µXRF scanning approach gives reliable evidence of the presence of dust. However, for the interpretation further knowledge is necessary about the lithology and the environmental background which control the geochemical composition of the lake sediment. A very important chemical element which appears in the dust content in both investigated cores is calcium, which reaches its highest values (>5 wt.-%) during glacial conditions and which has a major influence on the dust factor obtained by principal component analysis. In combination with grayscale values both the calcium content and the dust factor represent a record of aeolian dust in laminated lake sediments. However, calcium alone can not be used as a proxy for aeolian dust input since calcium is affected by a wide range of processes in the lake's water body itself. Furthermore, it was first realized by using the µXRF that the calcium content of single aeolian dust layers in the Dehner dry maar is variable.

It is shown that this variation is a signal of changing dust sources. The sediment layers with an enhanced calcium content show clearly aeolian transported carbonate particles with a diameter of around 50–60 µm. The limestone-bearing Eifel-North-South zone is the most likely source for the carbonate rich aeolian dust in the lake sediments of the Dehner dry maar. Once the location of a dust source is known, it is possible to deduce the wind direction. The Dehner dry maar is located on the

western side of the Eifel-North-South zone. Thus, carbonate rich aeolian sediment is most likely to be transported towards the Dehner dry maar within easterly winds. A methodology is developed which limits the detection to the aeolian transported carbonate particles in the sediment, the RADIUS-carbonate module. This method is based on particle analysis and measures the content of the aeolian transported carbonate particles.

The high resolution continuous reconstruction of dust event layers and east wind layers provide information about the variability of storm events and the variability of easterly wind directions for MIS-2 and MIS-3. The investigated time period from 40.3–12.9 ka can be subdivided into three units: the first unit covers the periods of the Greenland interstadial GI-9 and GI-8, including Heinrich event H4 (40.3–36 ka). With the exception of H4 the content of organics in our record is relatively high. With the end of GI-8 the content of organics decreases and the content of dust increases rapidly. This second time slice (36–24 ka) has an increasing content of dust accumulation and a high level of east wind layers (up to 19% of the dust storms per century came from the east). In comparison, the subsequent period 24–12.9 ka, which represents to a large extent the marine isotope stage MIS-2, is characterized by lower east wind sediments again. Increased frequencies of east wind occur during the time intervals corresponding with the Heinrich events H1 and H2. The late LGM (21–18 ka) is characterized by a slightly elevated east wind frequency again.

In summary, during the marine isotope stage MIS-3 the storm frequency and the east wind frequency are both increased in comparison to MIS-2. These results correspond to the dust accumulation in the NorthGRIP ice core and leads to the suggestion that atmospheric circulation was affected by more turbulent conditions during MIS-3 in comparison to the more stable atmospheric circulation during the full glacial conditions of MIS-2.

This significant change in the sedimentation patterns is most plausibly related to a shift in atmospheric circulation patterns. Numerical models of atmospheric circulation are therefore analyzed to give a synoptic interpretation of east wind activity over the glacial Europe. The extent to which change in general atmospheric circulation patterns has influenced the pathways of aeolian sediment transport in the Eifel area is tested. Here, AGCM experiments with different prescribed SST patterns are used to develop a synoptic interpretation of long-persisting east wind conditions and of east wind storm events, which are suggested to lead to an enhanced accumulation of sediment being transported by easterly winds to the proxy site of the Dehner dry maar.

The basic observations made on the proxy record are also illustrated in the 10 m-wind vectors in ECHAM3 and ECHAM4 model experiments under glacial conditions with different prescribed sea surface temperature patterns. However, all the glacial experiments show a lower frequency of east winds in comparison to the present-day control runs. In addition, all the glacial runs show a high variability of wind direction changes and stronger winds in comparison to the present-day control runs. Furthermore, the analysis of long-persisting east wind conditions (so-called LEWIC events) in the AGCM data shows a stronger seasonality under glacial conditions: all the different experiments are characterized by an increase of the relative importance of the LEWIC during spring and summer.

Synoptic analysis of the air flows with prevailing east wind over Central Europe are given for the spring, which is the most important season for dust emission. Under present-day conditions easterly wind directions are mainly generated by a strong high over the Baltic Sea region. The different glacial experiments consistently show a shift from a long-lasting high over the Baltic Sea towards the NW, directly above the Scandinavian Ice Sheet, together with contemporary enhanced westerly circulation over the North Atlantic.

This thesis is a comprehensive analysis of atmospheric circulation patterns during the last glacial period. It has been possible to reconstruct important elements of the glacial paleo climate in Central Europe. While the proxy data from sediment cores lead to a binary signal of the wind direction changes (east versus west wind), a synoptic interpretation using atmospheric circulation models was successful. This shows a possible distribution of high and low pressure areas and thus the direction and strength of wind fields which have the capacity to transport dust. In conclusion, the combination of numerical models, to enhance understanding of processes in the climate system, with proxy data from the environmental record is the key to a comprehensive approach to paleo climatic reconstruction.

Zusammenfassung

Die Atmosphäre ist eine globale Einflußgröße für den Wärme- und Feuchtigkeitstransport zu den Kontinenten und beeinflusst damit das dortige Klima stark. Dies gilt sowohl für das heutige warmzeitliche Klima als auch für Glaziale. Die europäischen Windsysteme werden vor allem von der Meeresoberflächentemperatur des Nordatlantiks, der Verteilung des Meereises sowie von der Lage und Größe der kontinentalen Eisschilde beeinflusst.

Informationen über den Zustand der atmosphärischen Zirkulation sind deswegen von großer Bedeutung für das Verständnis verschiedener klimatischer Zustände. Äolische Staubablagerungen können als Proxydaten für die Rekonstruktion der vergangenen glazialen äolischen Dynamik dienen. Die Zusammensetzung des abgelagerten Staubs wird dabei durch den atmosphärischen Transport beeinflusst und Änderungen der vorherrschenden Windrichtungen können so zum Beispiel zu unterschiedlichen Liefergebieten führen. Die in dieser Arbeit untersuchten Staubablagerungen wurden in Eifler Maarseen und ehemaligen, jetzt verlandeten Maaren, so genannten Trockenmaaren, beprobt. Die Seesedimente aus diesen Maarseen sind typischerweise feinlaminiert und nicht gestört. In diesen Seesedimenten ist äolischer Staub mit einer mittleren Korngröße von 30–40 µm die dominierende Sedimentfraktion während Kaltzeiten. Die Untersuchung der äolischen Staubkomponente ist somit der Schlüssel für die Rekonstruktion atmosphärischer Zirkulationsmuster der glazialen Vergangenheit.

In dieser Arbeit wird die Variabilität atmosphärischer Zirkulationsmuster während der letzten glazialen Periode untersucht. Dabei werden die Ergebnisse der Proxydaten mit denen von numerischen Klimamodellen verglichen. Diese Modellexperimente haben meist eine grobe räumliche Auflösung von Hunderten von Kilometern. Es stellt sich also die Frage, ob das gemessene Staubsignal aus der Eifel einer überregionalen atmosphärischen Zirkulation entspricht oder nur lokale Wetterereignisse repräsentiert. In der Regel stellen einzelne Staubstürme keine großen und überregionalen Massenbewegungen dar, sondern zeigen eher ein Ereignis lokaler Staubdeflation an. Allerdings führt die überraschend gute Korrelation europäischer Staub- und Lössvorkommen mit dem Staubgehalt in den grönländischen Eisbohrkernen zu der Vermutung, dass

die Ergebnisse aus den Eifelmaaren, zumindest bei der Betrachtung längerfristiger Trends, einem überregionalen atmosphärischen Zustand entsprechen. Darüber hinaus zeigen weitere Studien an den Sedimenten der Eifelmaare, dass die Zuteilung von einzelnen Sturmlagen, die in den Seesedimenten detektiert wurden, zu überregionalen und meteorologisch gemessenen Sturmböen zumindest für die letzten fünf Jahrzehnte statistisch hoch signifikant ist.

Die Häufigkeiten der glazialen Staubsturmereignisse einschließlich ihrer Paläowindrichtung werden mit Hilfe von hochauflösenden Korngrößen- und Provenanceanalysen der Seesedimente gemessen. Die Charakterisierung der verschiedenen Staubemissionsquellen durch die Provenanceanalyse ist dabei der Schlüssel zur Bestimmung der Paläowindrichtungen. Sowohl für die Provenanceanalyse als auch für die Staubdetektion werden zwei unterschiedliche Methoden angewandt: zum einen eine geochemische Analytik des Seesediments mittels einer µXRF (Röntgenfluoreszenzanalyse) und zum anderen eine Partikelanalyse durch die RADIUS-Methode (Partikelanalyse an digitalen Bildern durch ultra-hochauflösendes Scannen von Dünnschliffen). Die Messungen des energiedispersiven µXRF-Scanners werden an kontinuierlich genommenen und mit Kunstharz imprägnierten Sedimentproben durchgeführt. Diese sogenannten Tränklinge stellen auch die Grundlage für die Herstellung von petrographischen Dünnschliffen dar. So können die geochemischen Messergebnisse direkt mit Ergebnissen einer Mikrofaziesanalyse und der RADIUS-Routine verglichen werden. Die verwendeten Routinen messen dabei mit einer vergleichbar hohen Auflösung von 1 mm und weniger und bewegen sich somit im Bereich der jährlichen Sedimentationsraten von Maarseen.

In dieser Arbeit werden zwei Sedimentkerne aus der Eifel untersucht: der Kern SM3 aus dem Schalkenmehrener Maar und der Kern DE3 aus dem Dehner Trockenmaar. Beide Kerne enthalten die Tephra des Laacher See-Ausbruchs, der 12.900 Jahre vor heute datiert. So decken die Kerne zusammen die letzten 60 000 Jahre ab: der Kern SM3 das Holozän und DE3 die marinen Isotopenstadien MIS-3 und MIS-2. Die Altersmodelle basieren auf verschiedenen Datierungsmethoden wie der Radiokarbondatierung, der Tephrochronologie und dem Tuning zu den grönländischen Eisbohrkernen. Die an den Sedimentbohrkernen gewonnenen Daten werden schließlich durch eine Studie der atmosphärischen Zirkulation mittels Klimamodellexperimenten (ECHAM3 und ECHAM4) für eine zusammenfassende Interpretation ausgewertet.

Es wird gezeigt, dass der Ansatz äolisches Sediment mit einem µXRF-Scanner in den Bohrkernen zu detektieren, verlässliche Ergebnisse liefert. Notwendig ist dabei allerdings ein weitreichendes Vorwissen über beispielsweise die Lithologie und weitere Umweltparameter, die die geochemische Zusammensetzung der Seesedimente steuern.

Das auffälligste Element, welches mit einem hohen Staubgehalt im Sediment korreliert, ist in den beiden untersuchten Kernen Kalzium. So werden die höchsten gemessenen Kalziumwerte (> 5 Gew.-%) während glazialer Bedingungen erreicht. Kalzium hat somit einen wesentlichen Einfluss auf den Staubfaktor, der durch eine Hauptkomponentenanalyse errechnet wird. Vor allem in Kombination mit den während früherer Studien gemessenen Grauwerten stellt der Staubfaktor eine Detektionsmethode von äolischem Staub in laminierten Seesedimenten dar. Darüber hinaus wurde mit Hilfe der µXRF gezeigt, dass der Kalziumgehalt in den einzelnen Staublagen des Dehner Trockenmaares variiert.

Diese Varianz stellt sehr wahrscheinlich ein Signal unterschiedlicher Staubliefergebiete dar. Dabei zeigen die Staublagen mit einem erhöhten Kalziumgehalt einen hohen Anteil äolisch-transportierter Karbonatpartikel mit einem Durchmesser von etwa 50–60 µm. Die Eifel Nord-Süd-Zone mit ihren devonischen Kalkmulden ist die wahrscheinlichste Quelle des karbonathaltigen äolischen Staubs im Dehner Trockenmaar. Sobald die Lage einer Staubquelle bekannt ist, ist auch die Rekonstruktion der Windrichtung möglich. Das Dehner Trockenmaar befindet sich westlich der Eifel Nord-Süd-Zone. Demnach wurden die stark karbonathaltigen Staubsedimente höchstwahrscheinlich mit Winden aus östlicher Richtung zum Dehner Trockenmaar transportiert und dort abgelagert.

Es ist jedoch nicht ausreichend, den geochemisch gemessenen Kalziumgehalt als Proxy für Ostwind-Sedimentlagen zu verwenden. Kalzium ist von einer Großzahl unterschiedlicher Prozesse und biogeochemischen Reaktionen beeinflusst, die im Wasser des Sees stattfinden. Um die Ostwindlagen im Sediment zu detektieren, wurde deshalb eine spezielle Korngrößenanalyse entwickelt, die die Detektion von Karbonatpartikeln auf tatsächlich äolisch transportierte Karbonatpartikel eingrenzt.

Die so durchgeführten kontinuierlichen und hoch lösenden Messungen geben Auskunft über die Variabilität von Staub- und insbesondere von Ostwindlagen während der marinen Isotopenstadien MIS-3 und MIS-2. Der im Kern DE3 untersuchte Zeitraum von 40,3 bis 12,9 ka lässt sich in drei Einheiten unterteilen: Die erste Einheit umfasst die grönländischen Interstadiale GI-9 und GI-8 und beinhaltet so auch das Heinrich-Ereignis H4 (40,3 bis 36 ka). Mit Ausnahme von H4 ist der Gehalt an organischem Material in dieser Sedimentsequenz relativ hoch. Mit dem Ende des GI-8 beginnt der Gehalt an Organik zurückzugehen, gleichzeitig steigt der Staubgehalte rapide an. Dieser zweite Zeitabschnitt (36 bis 24 ka) zeigt neben dem ansteigenden Staubgehalt auch eine deutliche Zunahme an Ostwindlagen. In diesem Zeitintervall kamen bis zu 19% der Staubstürme pro Jahrhundert aus östlicher Richtung. Im Ver-

gleich dazu zeigt die nachfolgende Periode (24 bis 12,9 ka) eine durchweg niedrigere Häufigkeit von Ostwindereignissen. Vermehrtes Vorkommen von karbonatreichen Staublagen mit Herkunft aus der Eifler Nord-Süd-Zone zeigt sich allerdings während der Heinrich-Ereignisse H1 und H2. Das H3 zeigt dagegen keine höheren Ostwindhäufigkeiten an - im Gegensatz zu dem jeweils früheren und späteren Grönland-Stadial. Auch die späte Phase des letzten glazialen Maximums (21 bis 18 ka) ist von einer leichten Zunahme an Ostwindlagen gekennzeichnet.

Zusammenfassend ist während des marinen Isotopenstadium MIS-3 sowohl die Häufigkeit von Stürmen als auch von Ostwindlagen im Vergleich zum MIS-2 deutlich erhöht. Diese Ergebnisse stimmen mit den Staubakkumulationsdaten aus dem NorthGRIP-Eiskern überein. Diese signifikante Veränderung in den Staubsedimentationsmustern ist am sinnvollsten durch eine Veränderung der vorherrschenden atmosphärischen Zirkulation zu erklären. Es kann daher davon ausgegangen werden, dass die atmosphärische Zirkulation während des MIS-3 eine deutlich höhere Variabilität aufweist. Im Vergleich dazu scheint während der vollglazialen Bedingungen im MIS-2 eine stabilere atmosphärische Zirkulation vorgeherrscht zu haben. Es wird daher vorgeschlagen, dass der deutliche Rückgang der Variabilität in der atmosphärischen Zirkulation von dem marinen Isotopenstadium MIS-3 zum MIS-2 maßgeblich durch die Abnahme der abrupten Temperatur- und Klimaschwankungen der Dansgaard/Oeschger-Oszillation beeinflusst wird.

Aus diesem Grund werden in dieser Arbeit numerische Modellexperimente ausgewertet. Dabei werden atmosphärische Zirkulationsmuster über Europa mit verschiedenen glazialen Rahmenbedingungen analysiert, um zu einer synoptischen Interpretation der Staubtransportaktivität zu gelangen. Verwendet werden hierbei atmosphärische Zirkulationsmodelle mit verschiedenen vorgeschriebenen Verteilungsmustern der ozeanischen Wasseroberflächentemperaturen, um eine synoptische Interpretation von persistenten Ostwindbedingungen ableiten zu können. Zusammen mit Staubstürmen aus östlicher Richtung führen diese persistenten Ostwindbedingungen vermutlich zu der verstärkten Akkumulation von Ostwindlagen in den Seesedimenten des Dehner Trockenmaares.

Die generellen Beobachtungen aus der Windrichtungsstudie, die am Sedimentbohrkern DE3 durchgeführt wurde, sind auch in den 10 m-Windvektoren der ECHAM3 und ECHAM4 Modellversuche zu sehen. Generell weisen die glazialen Modellläufe eine geringere Häufigkeit der Ostwinde im Vergleich zu den Kontrollläufen mit heutigen klimatischen Bedingungen auf. Allerdings weisen alle glazialen Experimente auch eine höhere Variabilität der Windrichtungen und höhere Windgeschwindigkeiten auf

als die Kontrollläufe mit heutigem Klima. Darüber hinaus zeigt die Analyse der lang anhaltenden Ostwindbedingungen in den Modelldaten eine Verstärkung der Saisonalität während glazialer Bedingungen: In diesen Experimenten kommt es zu einem Anstieg der relativen Wichtigkeit dieser Wetterlagen im Frühjahr und Sommer.

Die Modellexperimente zeigen, dass heute lang anhaltende Ostwindbedingungen während des Frühjahrs meist durch ein Hoch über der Ostsee kontrolliert werden, was zu einem Luftstrom aus Ost bis Nordost über der Eifel führt. Die Rekonstruktion des glazialen Luftstroms mit vorherrschend östlicher Richtungen deutet auf eine Verschiebung eines lang anhaltenden Hochs von der Ostsee in Richtung NW, direkt über das skandinavische Eisschild, hin. Zeitgleich tritt eine verstärkte Westwindzirkulation im nördlichen Atlantik auf.

Ziel dieser Arbeit war eine umfassende Analyse der atmosphärischen Zirkulationsmuster während der letzten glazialen Periode. So konnten wichtige Elemente des glazialen Paläoklimas in Mitteleuropa rekonstruiert werden. Während die Daten aus den Bohrkernen ein binäres Signal über die Windrichtungswechsel (Ostwind gegen Westwind) geben, gelang mit Hilfe von atmosphärischen Zirkulationsmodellen eine synoptische Interpretation. Diese zeigt eine mögliche Verteilung von Hoch- und Tiefdruckgebieten und damit die Richtung und Stärke von Windfeldern an, die das Potenzial haben, Staub zu transportieren. Durch das Interagieren von numerischen Klimamodellen und Proxy-Daten ergibt sich so eine umfassende Möglichkeit, paläoklimatische Prozesse zu rekonstruieren.

Chapter 1

Introduction

1.1 Why study (Paleo) Wind Dynamics?

Within this thesis proxy data of aeolian dynamics for the last glacial cycle are analyzed. The atmosphere is and also was during glacials a global player for heat and humidity transport to the continents and strongly influences climate variability. European wind systems are mainly affected by N-Atlantic Sea Surface Temperatures (SST) in combination with the distribution and extend of sea ice (Denton et al., 2005; Sirocko et al., 2005) and atmospheric heat transport (Brauer et al., 2008). Proxy data for glacial atmospheric conditions are nowadays quite rare. In this thesis attention is therefore given to the reconstruction of former atmospheric circulation patterns by the detection of extreme storm events and the paleo wind direction, using high resolution grain size and provenance analysis for the last glacial. These events are subsequently evaluated by a study of atmospheric general circulation models (AGCM) to give a synoptic interpretation. These methods are applied to different sediment cores from maar lakes as well as dry maars from the West Eifel volcanic field (WEVF) in Germany.

During the present interglacial, the Holocene, dust storms only play a minor role on the European continent. But large parts of Europe are covered by aeolian sediments which were deposited during the last glacials (Fig. 1.1). An increase in wind velocities during the glacial, larger source areas for the dust deflation (eg. the English Channel was submerged during glacial times), and mostly important a lack of vegetation cover, led to a 2–5 times increase in dust deposition rates during glacial periods in comparison to present climate conditions (Maher et al., 2010; Kohfeld and Harrison, 2001). The major part of these aeolian sediments consists of loess, which is formed by the accumulation and subsequent diagenesis of wind-blown silt (2–63 μm) and lesser amounts of clay and sand. Outcrops of this pale yellow material form vertical

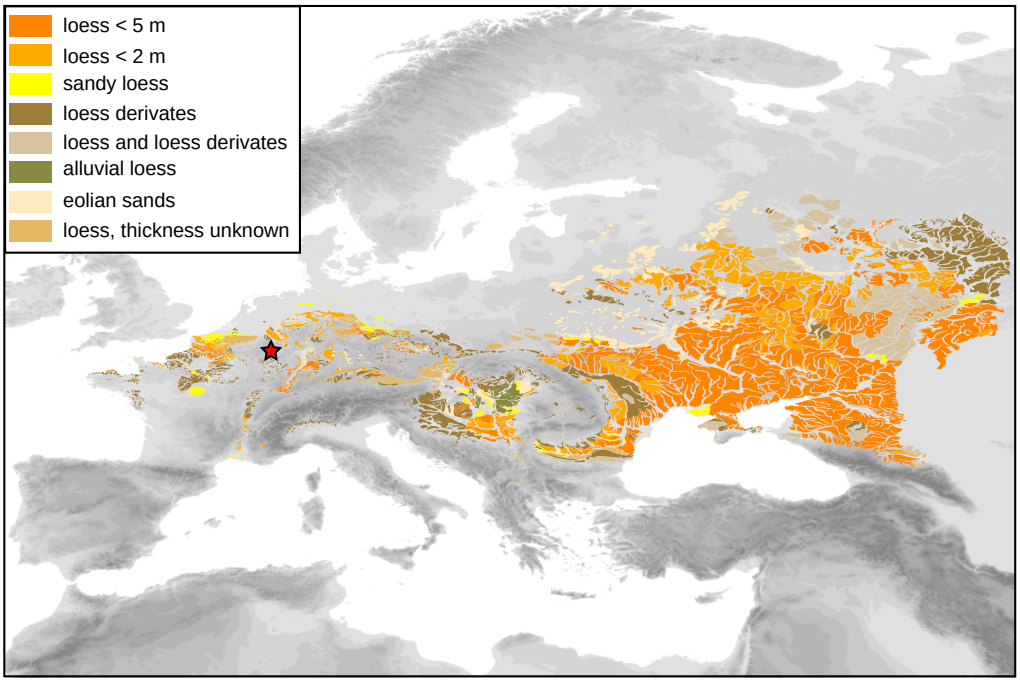

Figure 1.1: Sketch map of loess distribution in Eurasia after Haase et al. (2007). Red asterix marks the location of the Eifel Area, Germany.

cliffs and are usually homogeneous, highly porous, often calcerous, and typically non-stratified. Modern analogues for these strong, dust bearing storms can be found today in tundra environments which are strongly affected by glaciers, like Iceland or Alaska (Fig. 1.2a).

The maar lake sediments of the *Eifel Laminated Sediment Archive* (ELSA) of the University of Mainz offer a very good opportunity for identifying single events of the deposition of atmospheric dust (which is in this thesis defined as air-blown material with a grain size of 10's of μm) with a high temporal resolution. In contrast to loess deposits the aeolian material in the maar lake sediments is finely laminated and thus every single dust storm event can be analyzed. The reason for the excellent state of preservation lies in the morphology of maar lakes and silted-up maar lakes, which are called dry maars. Maar lakes are steep and have only a low ratio between water depth and diameter (Fig. 1.2b). The water column of Central European lakes are in general temperature stratified, from around 20° C during the summer season at the

top to around 5° C at the bottom of the lake. Only the water above the zone with the greatest change in temperature, the thermocline, is mixed by strong winds. In contrast the deep water is not affected by this mixing and becomes poor in oxygen by oxygen consumption. Under such anoxic conditions no organisms can bioturbate the sediments on the lake bottom and the original sedimentation structures, like layers of single dust events, are preserved (Fig. 1.2c).

The main aim of this study is to use these aeolian deposited maar lake sediments in the silt (or loess) grain size for the reconstruction of paleo wind events. From this the meteorological phenomena which led to dust deposition in a specific maar lake can be deduced.

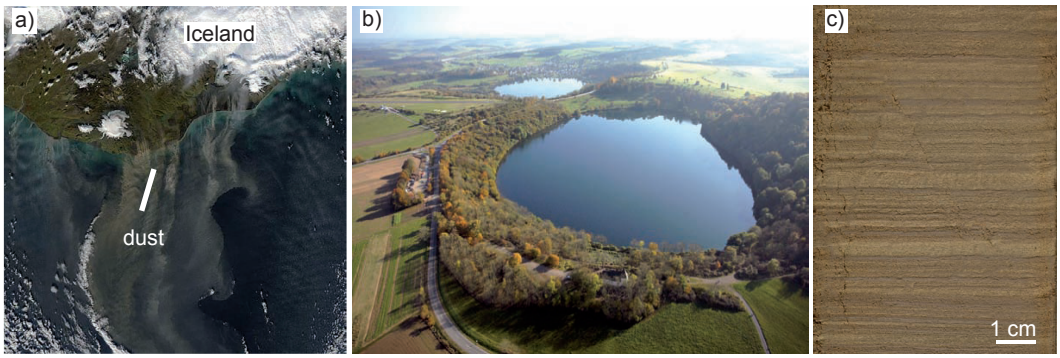

Figure 1.2: (a) A major dust storm coming off the dry highlands and sandur fields of Southern Iceland, 5th October 2004, as an analogue for dust plumes in NW-Europe during glacial periods. Image courtesy of MODIS Rapid Response Project at NASA/GSFC; http://rapidfire.sci.gsfc.nasa.gov/gallery/. (b) Aerial photograph of the Weinfelder maar lake without fluvial inflow (foreground) and Schalkenmehren maar lake (background). (c) Laminated dust sequence from the sediment core DE3 (Dehner dry maar, Eifel) showing the depth of single dust events, which are the basis of the thesis.

1.2 Glacial Dust Sedimentation in Central Europe

Aeolian sediments like glacial dust and loess spread all over Eurasia, but provenance of the grains, deflation areas, transport height of dust plumes, season of dust transport, mechanisms of dust removals are still under debate (Zöller, 2010; McGee et al., 2010; Smalley et al., 2009; Rousseau et al., 2007; Fischer et al., 2007). Thus, aeolian sediments are the key proxy for the reconstruction of past atmospheric dynamics.

1.2.1 Climatic Influence of Glacial Dust Sedimentation

The Pleistocene in Central Europe is dominated by processes of aeolian dust transport and accumulation. Thus, aeolian sediments are an important proxy for reconstruction of past atmospheric dynamics. Many records from the central European region show that the accumulation of aeolian sediments during the last glacial cycle corresponds to the climate of the Northern Atlantic and especially to dust in Greenland ice cores (e.g. Seelos and Sirocko, 2009; Rousseau et al., 2007; Ruth et al., 2007). Dust sedimentation in Central Europe reaches maximum values during Heinrich events and the last glacial maximum (LGM) and is in general higher during Greenland stadials than during Greenland interstadials (Antoine et al., 2009; Seelos and Sirocko, 2009; Rousseau et al., 2007). The most important factors of enhanced dust deflation are wind speed, precipitation, and the snow and vegetation cover which prevents dust emission in certain seasons (Laurent et al., 2006; Tegen et al., 2002). Threshold wind velocities for emission and transport of dust in the typical loess grain size range (20–100 µm) are larger than $5\,\mathrm{m\,s^{-1}}$, see chapter 2). Using dust in the loess grain size fraction means working with a record of wind extremes in general. Since the emission flux depends on wind speed cubed (Gillette, 1988), a small increase in wind velocity leads to a great enhancement in the dust flux.

The climatic situation in Central Europe during the Last Glacial Maximum (LGM) and the Late Pleniglacial is characterized by high wind activity and relatively low precipitation (Huijzer and Vandenberghe, 1998; Hatté et al., 1998). The general atmospheric patterns are characterized by a strong high over the Siberian ice sheet (SIS; e.g. COHMAP Members, 1988). The amount and the magnitude of storm events, which have the potential for dust emission, is still a matter of discussion. In comparison to the late Holocene conditions an enhanced baroclinic and temperature gradient in the North Atlantic is triggered by the southward shift of the winter sea ice edge during the LGM, which is itself forced by a reduction of the meridional overturning circulation (MOC) and which causes much colder winters from Greenland to Asia (Denton et al., 2005). The enhancement of the baroclinic and temperature gradient led to an E to SE shift of the storm tracks with strongest synoptic energy during winter. More or stronger storms over Europe during the LGM are observed in different general circulation models (Laîné et al., 2009; Kageyama et al., 2006; Justino and Peltier, 2005). And an enhanced gustiness during glacials is one of the supposed main drivers of increased aeolian dust transport (McGee et al., 2010). In

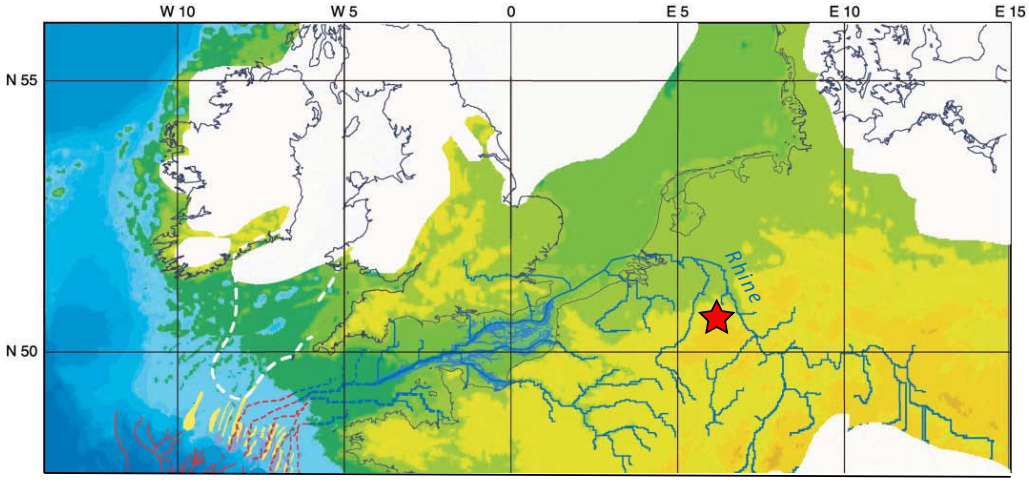

Figure 1.3: The modern line of the English Channel was previously a major river, draining the waterways of northern France, the southern counties of England, and also the rivers Scheldt, Rhine-Meuse and Thames, which today discharge into the North Sea. Location of the Eifel area is marked by the red asterix. Map modified after Bourillet et al. (2003).

contrast Li and Battisti (2008) have shown in a state-of-the-art fully coupled general circulation model (GCM) a strong, steady atmospheric jet and weak transient eddy activity. In other words, during the last full glaciation the climate was quite settled. In addition, a probable S to SE shift of the storm tracks led to a change in European precipitation patterns, resulting in less precipitation over Central and NW-Europe during the LGM. The precipitation dropped down to a nearly constant low level at around 280 mm/year which is observed (by inverse modeling using the isotopic signal of loess organic matter) for Central Germany between 28 kyr and 17 kyr BP during full glacial conditions (Hatté and Guiot, 2005). At that time, the sea-level droped around 120 m below present levels (Clark et al., 2009; Bourillet et al., 2003) and the English Channel was mostly dry land (Fig. 1.3). Such a geographical configuration is consistent with a great reduction of the inflow of wet oceanic air fluxes. These arid conditions with a prevailing lack of vegetation cover magnified the rate of dust emission.

In comparison to MIS-2, MIS-3 appears to be stormier (van Huissteden and Pollard, 2003). In data from dust proxies evidence is found that the frequency of dust storm events per time period is higher during MIS-3 than during MIS-2 and the LGM

(Seelos and Sirocko, 2009). In particular, the transitions from warm to cold periods during the last glacial cycle are characterized by turbulent climate conditions and an increase in weather extremes. This contrasts with aeolian records in general in which aeolian sediment accumulation dominates during MIS-2 (Tab. 1.1). The most reasonable explanation is a change of the source areas and the availability of deflation material rather than an effect of wind speed. The landscape and the alluvial plains were much more vegetated during MIS-3. Furthermore, the sea level decreased by around 60 m (Lambeck et al., 2002) and thus the source areas are much smaller then during MIS-2.

1.2.2 The ELSA Dust Stack

In comparison to the NW-European loess profiles (Tab. 1.1) the accumulation rates of aeolian sediments in lakes are much higher. A record from the Eifel area, the *ELSA dust stack*, covers the last glacial cycle (Seelos and Sirocko, 2009). The dust stack is a compilation of four different lake sediment cores from the West Eifel Volcanic Field to comprise the last 133 ka BP. All the core sections together measure 100 m and consists of finely laminated lake sediment. The four cores are denoted as SM3, DE3, OW1 and HL2 (Fig. 1.4). The first two cores together cover the last 60 000 years and are the working basis of this thesis. The temporal resolution is many times greater than in common loess profiles. Another difference is the good preservation of the MIS-3 interstades which is usually not present in loess sequences. The dust deposits which are preserved in these lake sediments provide detailed information about the climate variability during cold and dry periods (Fig. 1.4). In particular, the transitions from warm into cold periods are characterized by turbulent atmospheric conditions. The highest frequencies of dust storm events occur during the first cold events C24 and C23 after the last warm stage of MIS-5e. Major temperature oscillations were more common during MIS-3 as compared to MIS-2, which correlates with an higher frequency of dust events during MIS-3. The coldest periods of the last glacial cycle MIS-4 (70–60 ka BP) and MIS-2 (35–14 ka BP) are characterized by stable climate conditions that generate the accumulation of homogeneous dust sediments. This record indicates again that the frequency of dust storm events per time period is higher during MIS-3 than during MIS-2.

Table 1.1: Loess deposits and soils of MIS-3 and MIS-2 in loess sequences in Western and Central Europe. The aeolian sediment accumulation dominates during MIS-2. Table modified after van Huissteden and Pollard (2003).

Site name	Location	Thickness MIS-3 loess (m)	Thickness MIS-2 loess (m)	Soil types	Hiatuses, fluvial erosion/reworking
Kesselt[1]	50°50'N, 5°37'E	at least 3.5	up to 6.5	Tundra gley, luvisol	Reworked loess in channels; hiatus –38 000 yr
Harmignies[2]	50°14'N, 4°1'E	2.5	>5	Tundra gley, luvisol	
Remicourt[3]	50°11'N, 5°20'E	2.8	6.5	Tundra gley, luvisol	
Nussloch[4]	49°16'N, 8°24'E	3	10.2	Tundra gley, cambisol	44 000–34 000 yr
Achenheim[4]	49°30'N, 7°30'E	4.7	5.3	Cambisol	
Mainz-Weisenau[5]	49°57'N, 8°20'E	1.9	5.5	Weak brown soil	Reworked at base
Böckingen[6]	49°7'N, 9°12'E	2.6	2.5	Weak brown soils	Reworked at base
Bönningheim[6]	48°57'N, 9°10'E	2.4	1.9	Weak brown soils	Reworked at base
Dolní Veŝtonice[7]	49°0'N, 16°35'E	2.8	5.7	Weak brown soil	

*N*ote. References: 1, Huijzer (1993); Juvigne et al. (1996); Vandenberghe et al. (1998); 2, Frechen et al. (2001); 3, Haesaerts et al. (1999); 4, Antoine et al. (2001); 5, Sommé et al. (1986); Rousseau et al. (1998); 6, Frechen (1999); 7, Musson and Wintle (1994); Zöller et al. (1994); Frechen (1999)

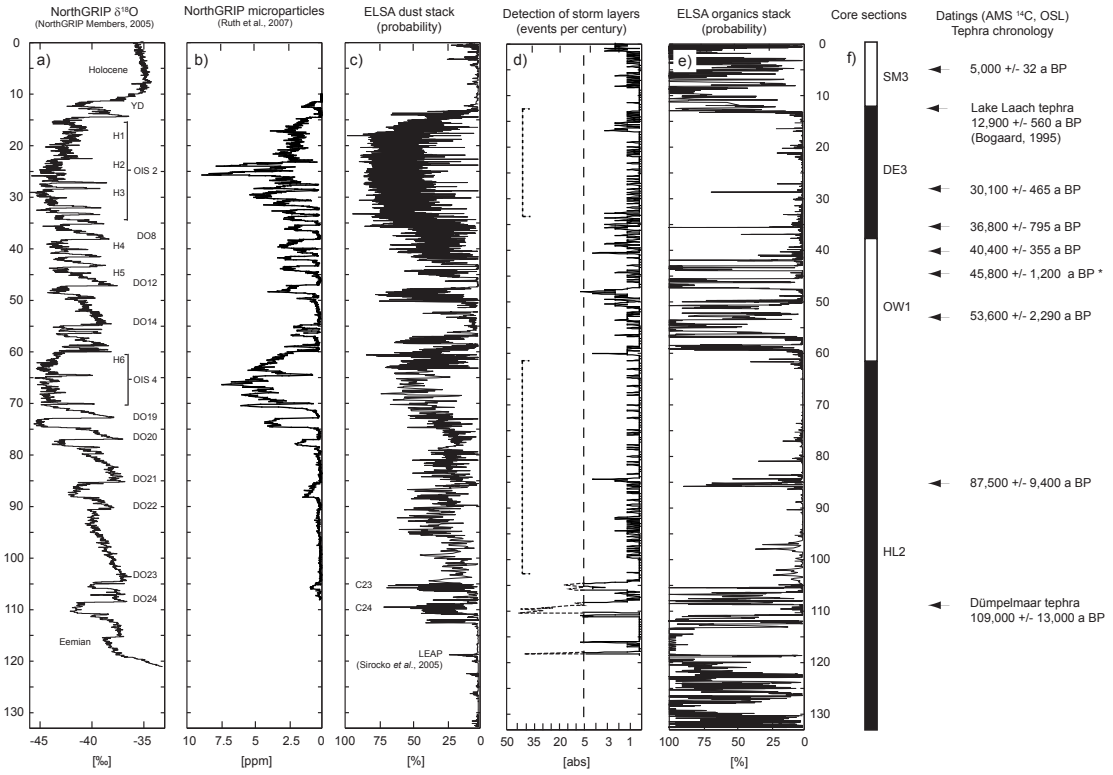

Figure 1.4: Comparison of climate proxy records for the period 132 – 0 ka BP. The correspondence in the signal between the ELSA dust stack and the signals from Greenland gives evidence for supra regional dust transporting systems: (a) NorthGRIP $\delta^{18}O$-record as a temperature proxy for the last glacial cycle in Greenland; (b) the NorthGRIP micro particles record, measured particle diameters $> 2\,\mu m$ (Ruth et al., 2007); (c) ELSA dust detection stack as a normalized probability record (see methods in chapter 3); (d) frequency of single dust storms in a 100-years-segmentation; (e) ELSA organic detection stack (see methods and Table 1); (f) the four core sequences of the stack, SM3 is a sediment core of a recent maar lake, DE3, OW1 and HL2 are cores from dry maars; (g) datings (AMS ^{14}C and OSL) and tephra chronology as age control for the stack, Lake Laach tephra dated by (van den Bogaard, 1995). The asterisk indicates a piece of wood (DE3 55.96 m, spruce) dated 2008, Leibnitz Institut, Kiel. From Seelos and Sirocko (2009).

1.3 Prevailing Wind Systems in the Eifel Region

The predominant wind directions on the Earth are associated with the global atmospheric circulation. The shape of this comprehensive circulations is based on the

major energy supplier to the earth's atmosphere, the irradiation of the sun, and the rotation of the Earth itself. The Eifel region is located in the middle latitudes between 35° and 65° of the Northern Hemisphere, where the general surface flow of the air is poleward. This air flow is deflected by the rotating earth (and thus by the influence of the Coriolis force) which results in westerly winds. These mid-latitude westerlies blow from west to east, in the Eifel region predominantly from SW. Thus, the westerlies are an important factor in transporting heat and humidity from the oceans towards the western coasts of continents. Furthermore, most atmospheric dust is transported within westerly air flows. Together with the extent and distribution of sea ice and SST patterns the westerlies have a major influence of the climate on the European continent. In the recent annual cycle the westerlies increase in strength during the winter and decrease during the summer (Gulev et al., 2001).

1.3.1 Is the wind signal recorded in the sediment archive only local, or supra-regional?

Even though westerly wind directions dominate on the European continent, changing wind directions determine the local weather conditions. Thus, the majority of dust storms are not supra-regional wide mass movements, but represent times of high wind speed and local deflation. The question is whether the sediment archives from the Eifel region record only local paleo weather phenomena or if they are also able to provide information about supra-regional atmospheric conditions. The first evidence for the latter is given by the surprisingly good correlation between continental records with the Greenland ice cores. Corresponding signals of aeolian activity were found in both the NorthGRIP ice core (Ruth et al., 2003, 2007) and sediment archives like the ELSA dust stack (Seelos and Sirocko, 2009) or the Nussloch loess profiles from the river Rhine (e.g. Antoine et al., 2009; Rousseau et al., 2002). Thus, atmospheric information on millenial time scales, which are times of meteorological homogeneity like interstadial, stadial, or Heinrich Events, is to be found in maar lake sediments. In addition, Pfahl et al. (2009) has found evidence that the allocation of storm layers in maar lake sediments to recent regional meteorological data of extreme supra-regional storm gusts (ERA-40 reanalysis data; Uppala et al. (2005)) is statistically highly significant for at least the last few decades (Fig. 1.5). Thus, it is suggested that results from Eifel maar lakes correspond to supra-regional atmospheric conditions on millennial time scales as well as to weather extremes.

Further hints of supra-regional climate and weather conditions concern not only the

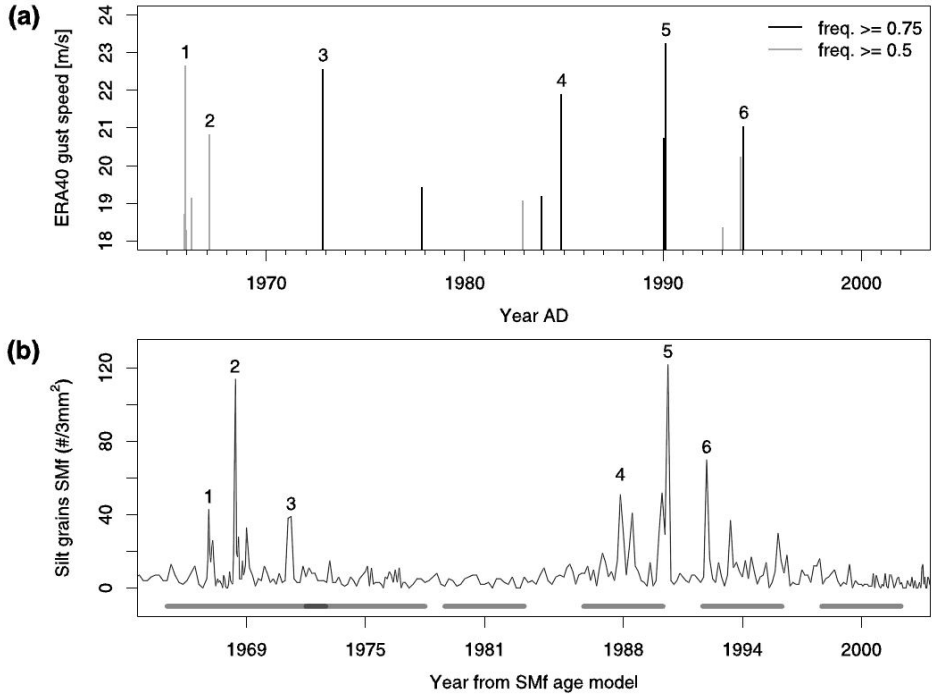

Figure 1.5: Statistically highly significant allocation of storm layers in a sediment core and meteorological data. (a) Storm index, combining gust peak wind speed from ERA40 data (vertical axis) and relative frequency of storm detection at weather stations (color) for strongest windstorm events. Note that the absolute values of ERA40 gust velocities are biased low compared to direct measurements of wind gusts. (b) Coarse silt fraction curve (number concentration of quartz grains between 20 and 63 µm) for the upper part of the core SMf from lake Schalkenmehren. Numbers indicate a mapping of the peaks on the storms shown in (a). Gray horizontal bars show the uncertainty of the age model, and darker gray indicates an overlap of the uncertainty bars. From Pfahl (2009).

atmospheric circulation itself but the distribution of precipitation patterns. Extreme precipitation events and the amplitudes of river runoffs correspond over wide parts of Germany, at least the German low mountain range (Pfahl, 2009). In a recent publication of Pausata et al. (2009) model intercomparison was used to test the relevance of proxy record locations for the study of atmospheric variability during the last glacial. It could be shown that precipitation data from Northern Germany and the Eifel region significantly correlate to the supra-regional variability of the NAO (North Atlantic Oscillation) during glacial winter.

1.4 Why is Geology important?

In the past several approaches were used to reconstruct paleo wind directions of North Western and Central Europe. Prevailing westerly wind directions are expected for the Holocene and the Pleistocene due to the location of the study area in the mid latitudes and evidence for that is found in different records.
The combination of meteorological simulations and proxy data shows that at least the Late Pleniglacial and the LGM were dominated by westerly wind directions (Renssen et al., 2007). Proxy data for paleo wind directions have been generated from studies of relict dune forms in Central Belgium (Vandenberghe, 1991) and Poland (Godzik, 1991), grain size trends of cover sand and loess in the Netherlands (Van Huissteden et al., 2001), provenance analyses by heavy mineral composition (Krook, 1993) and wind polished rock surfaces (Christiansen, 2004; Christiansen and Svensson, 1998; Vandenberghe et al., 1999). Indirect evaluation of changing wind direction was shown by Sweeney et al. (2004). The authors found evidence from aeolian deposits in North America that the strength of the glacial anticyclone (east wind near the ice border) was weakened by strong west wind conditions. But in general proxy archives older than the LGM are rare. This makes the ELSA dust stack a valuable record.

Geometrical approaches are not applicable to the reconstruction of paleo wind direction based on maar lake sediments. The most promising approach is thus the application of provenance analysis to reconstruct the sources of the dust. Geochemical and mineralogical finger prints of the source area are to be expected in the dust itself. And those fingerprints result from the geology of the catchment area.

1.4.1 The Geological Setting of the Eifel Region

The Eifel area is part of the Rhenish Massif in the west of the river Rhine. The Eifel is flanked by the Ardennes in the west, the river Moselle and the Hunsrück mountains in the South, and the niederrheinische Bucht, with its Cenozoic sediments in the North. The major part of the Rhenish Massif consists of metamorphic sediments, mostly of eponymous slates (Fig. 1.6). Metamorphosis and Deformation happened during the Variscian orogeny. Most of the sediments were deposited during the Devonian and Carboniferous in a back-arc basin called the Rhenohercynian basin. Near the coast sands were deposited, deeper in the basins silt and clay were the dominating fraction. The NE-SW alignment of structural units, which remains characteristic today, was already evident in the Devonian period.

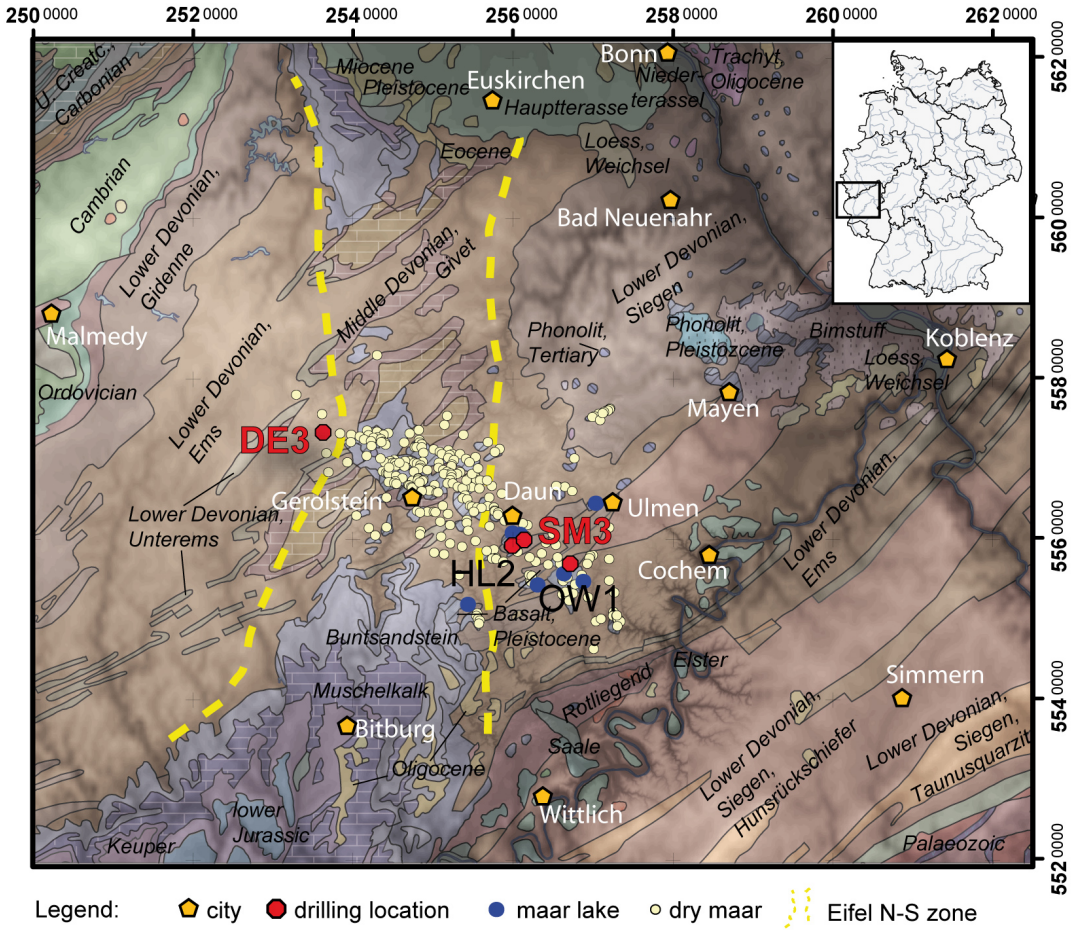

Figure 1.6: Geological sketch map of the Eifel region. Calcerous rock units are marked by brick wall symbol, the Eifel North-South-Zone is marked by yellow lines. Core positions of the four cores of the ELSA dust stack are shown, the cores which are studied in this thesis are highlighted in red. Note the location of the core DE3 on the western side of the Eifel N-S zone. Locations of the dry maars after Büchel (1994). Geological Map is based on the Geologische Übersichtskarte Deutschland 1:1 000 000 (BGR, 2002).

A structural feature of the Eifel is the so called *Eifel North-South-Zone*, a north south striking depression zone with some limestone basins reaching from the Trierer Bucht in the South to the Niederrheinischen Bucht in the North. The limestone consists of former riff complexes, which were deposited near the coast during the Givet. Triassic sediments, Buntsandstein and Muschelkalk, crop out in the tectonic basins north and south of this zone. To sum up, the Eifel is subdivided by a belt

of calcarous rocks, which are the only ones in a large surrounding area. Most of the maars lie within or on the eastern flank of this zone. Only some maars, including the Dehner dry maar, are located on its western side.

Another remarkable rock type are Tertiary and Quaternary igneous rocks. Uplift of the Rhenish Massive began around 45 million years before present, but was accelerated around 800 000 years BP, during the Pleistocene. Both uplift events were accompanied by extensive volcanic activity and three volcano fields can be distinguished in the Eifel region: (1) the High Eifel with its Tertiary volcanic rocks, (2) the East Eifel volcanic field with Quaternary rocks and prevailing eruption of well differentiated magmas and phonolites, and (3) the West Eifel volcanic field with primary and basaltic tephras direct from the mantle and with a large amount of maar eruptions which have formed above diatremes (Schmincke, 2010). The second phase of volcanic activity started during the Quaternary period not before 600 000 years BP.

The development of maars depends not only on the chemistry and the deep source of the mafic magma. A second prerequisite is necessary: A maar eruption begins when the ascending magma makes contact with the aquifers. The ground water in the pore space suddenly vaporizes and the resulting enormous pressure blows out the hanging wall rocks. New magma flows into the depression and mixes up with relapsing debris of the eruption, which seals the crater. Once the pressure has increased again a new succession of vaporization of ground water and eruption begins. The recurrence of this process deepens the maar more and more. This eruption type is called a phreatomagmatic eruption. Commonly the maar immediately fills with water to form a natural lake with a great depth relative to its small surface area. Thus, maar lakes have a unique chance to preserve laminated sediments which are the archives which enable us to reconstruct past climate.

1.4.2 First Indications of Dust Layers deflated from Changing Source Areas

One pilot study has found that carbonate content varies between single dust event layers (Fig. 1.7 and suggests that alternating calcium content may be used as a source signal (Dietrich and Sirocko, 2009). Grain sizes in different layers within the sample do not differ. It is therefore suggested that a change between local and more distant sources is a far less probable explanation. It appears that the higher calcium content is a result of an increase of detrital carbonate particles derived from the Eifel North-South zone. In this thesis it is tested whether the Eifel-North-South zone is a possible source of those dust layers with an strongly increased content of detrital carbonates.

This would result in a proxy record for changing wind directions during dust events in the past. Not every wind direction can be detected using this approach, but it is at least possible to distinguish between westerly and easterly wind directions.

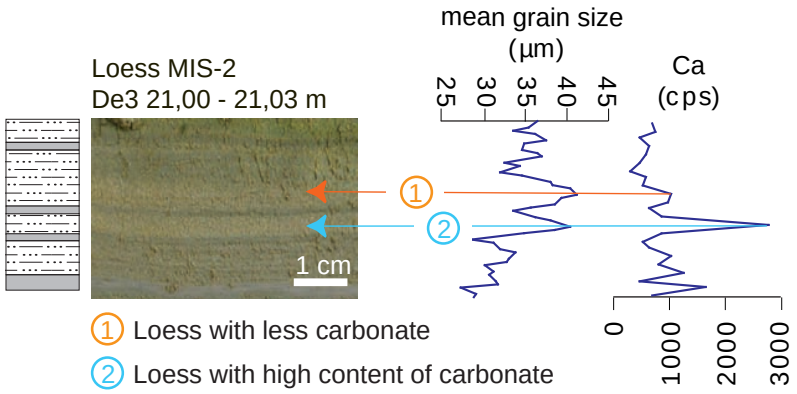

Figure 1.7: Alternating calcium content of two super-imposed dust event layers. The second one has a significantly increased content of calcium, which is suggested as an signal of changing dust source areas. Edited after Dietrich and Sirocko (2009).

1.5 Summary of Chapter 1 and resulting Scientific Questions

The aim of this research project is to explore the reconstruction of palaeo wind systems over Europe during the last glacial. Therefore aeolian dust deposits within maar lakes sediments were analyzed. Glacial aeolian sediments in the coarse silt fraction of typical loess are spread all over Europe and were much more common during glacial than during warm climate conditions like the Holocene. The investigation of aeolian sediments is thus a key to reconstruction of past climate variability, especially during glacial conditions.

The most important factors for dust deflation are wind speed, precipitation (surface humidity) and snow or vegetation cover which prevents dust emission during certain seasons or climate conditions. Vegetation cover especially has been found to be the limiting variable: dust deposition rates were 2–5 times higher during glacial periods in comparison to present climate conditions. In addition, many records from the central European region, like the ELSA dust stack, show that the accumulation of aeolian sediments during the last glacial cycle corresponds to the climate of the Northern Hemisphere and especially to the climate variability in the North Atlantic and the

dust content in Greenland ice cores. Dust sedimentation in Central Europe reaches maximum values during Heinrich Events and the LGM and is in general higher during Greenland stadials than during Greenland interstadials.

This covarying signal in both Eifel dust records and Greenland ice cores indicates that evidence from the Eifel Region corresponds to supra-regional atmospheric circulation patterns, at least on a millennial time scale. In addition, the correlation of major storm events from recent meteorological measuring data with storm layers within maar lake sediments is highly significant. This indicates that Eifel maar lake sediments indeed have the potential to record past atmospheric variability. It is thus suggested that results from Eifel maar lakes correspond to a supra-regional atmospheric state on millennial time scales as well as to extreme weather events.

Westerly to south-westerly wind directions predominate due to the location of the Eifel area in the mid latitudes. Thus the most important source area of dust in the Eifel region should be located somewhere in the West. Indeed, the English Channel had mostly dry land during the last glacial (sea-level around 120 m below present conditions) and most of the aeolian dust is suggested to come from this area. However, dust event layers with alternating contents of calcium were detected within the core DE3 (part of the ELSA dust stack) from the Dehner dry maar. It is suggested that the higher calcium content is a result of an increase of detrital carbonate particles derived from the Eifel-North-South zone. In this case dust layers with an enhanced carbonate or calcium content would represent a proxy of easterly wind directions. The variability of easterly wind layers thus have a high potential for reconstruction of past glacial atmospheric conditions.

To achieve the major aim, the reconstruction of paleo wind system of the last glacial over Europe, the following scientific problems are addressed.

- First, the Eifel North-South zone is theoretically evaluated for its suitability as a source of carbonate particle emission (chapter 2). Dust generation and possible transport widths are discussed in order to evaluate possible source areas.

In the second part of this thesis (chapter 4–6) different analytical approaches are applied to reconstruct the dust proxy data from the lake sediments. In addition, numerical climate model experiments are investigated. Each of this chapters has already been published or submitted to a scientific journal as an individual article.

- A new analytical approach of µXRF scanning is tested for its potential for aeolian dust detection in Eifel maar lake sediments.

S. Dietrich and F. Sirocko (acc.). The Potential for Dust Detection by means of μXRF Scanning in Eifel Maar Lake Sediments. E&G - Quaternary Science Journal.

- In addition, provenance analysis based on mineralogical evidence is applied to achieve information about changing source areas. A time series of the variability of easterly (and westerly) wind directions is created to reconstruct the variability of atmospheric circulation in the glacial past. Special attention is set on the frequency of changing palaeo wind directions during the marine isotope stages MIS-3 and MIS-2.
  S. Dietrich and K. Seelos (2010). The Reconstruction of Easterly Wind Directions for the Eifel Region (Central Europe) during the Period 40.3–12.9 ka BP. Climate of the Past.

- A synoptic interpretation of past atmospheric variability is based on a model-data comparison approach, using atmospheric general circulation models with different prescribed glacial climate conditions. The results of the model experiments are used to provide synoptic information which is able to explain the occurrence of east wind layers in the sediment record.
  S. Dietrich, G. Lohmann, M. Werner, K. Seelos, F.Sirocko (subm.). Reconstruction of European Atmospheric Circulation Patterns in the Spring Season during the Last Glacial. Climate Dynamics.

Chapter 2

Aeolian Sediments: Generation, Emission, Transport and Deposition - Estimation of the Transport Widths

The characterization of aeolian dust source areas for the application of provenance analysis makes an estimation of the dust's transport widths necessary. Dust sources are affected by the mechanisms of dust generation and dust emission. Transport mechanisms of aeolian dust in the lowest layer of the atmosphere, the planetary boundary layer, involve threes stages: (1) dust emission, (2) transport, and (3) settlement. All of these factors are controlled by the size of the particles, the nature of the ground surface and the properties of the airflow near the ground. For a detailed description of the different acting mechanisms refer to Bagnold (1941). Pye (1987) and Pye and Tsoar (2009) continued this work and notably extended it. Parameterizations of this physical basics of particle entrainment and transport are set for use in numerical models of dust emission or the dust cycle by, for example, Marticorena and Bergametti (1995) or Shao and Lu (2000). The estimation of particles' transport distances described in this chapter is fundamentally based on the works of these authors.

A major division is obligatory when speaking about aeolian dust, since a size distinction is observed in the nature (Stuut et al., 2009). *Large dust* with grain sizes larger then 16 µm is usually transported for relative short distances. *Fine dust* with smaller particle sizes travels very efficiently in suspensions over hugh distances. The research focus is only set on large dust particles in this thesis.

2.1 Generation of Large Aeolian Dust

Aeolian sediments which were deposited in the Eifel maar lakes are subject to a quite complex process of generation and transportation. However, the generation of the silt grain sized material is still a matter of discussion (Zöller, 2010; Iriondo and Kröhling, 2007; Smalley et al., 2009). Two main sources for the silt particles in aeolian dust and loess deposits are suggested by e.g. Smalley and Derbyshire (1990): ice-sheets and mountains. Continental ice-sheets produce ice-sheet loess. Glacial loess is generated by glacial grinding in the mountain regions. Both processes of silt generation have in common that the particle transport by rivers is a necessary event before subsequent aeolian deflation and loess deposition. This transportation event provides the distribution of loess material across the landscape (Smalley et al., 2009). Thus, in Central Europe the rivers, such as the Rhine river, are one major source of aeolian dust. However, prevailing westerly wind directions were forced by the west wind drift and, indeed, during glacial times in the West of the Eifel region was a huge deflation area. During glacial times the English Channel was mostly dry land. Such a geographical configuration is consistent with an increased flux of aeolian material from the English Channel towards NW-Europe (Antoine et al., 2009). However, the silt worm route (after Smalley et al., 2009) is not the only way to produce mineral dust of silt grain size. Cold weathering processes complement glacial grinding in mountain regions and could have contributed significantly to the world's major Pleistocene loess deposits (Pye, 1987). The production of quartz particles in silt fraction by physical weathering processes (basically by frost shattering) is already described by Pye (1995) and Cilek (2001). Lab experiments show the effects of frost shattering on carbonate rocks to produce carbonate granules (Lautridou and Ozouf, 1982). Secondary aeolian processes such as deflation, saltation and corrasion are able to produce fine grained material like silt. Thus, the abrasion of frozen soil, which is reported by Kasse (2002), when there is little or no vegetation cover during glacial winter and spring, is a likely scenario for enhanced dust production during the LGM.

2.2 Windstress on the Lower Earth Surface

The airborne transport of dust particles of the typical loess grain size fraction is usually limited to the planetary boundary layer. The planetary boundary layer is affected on a very short time scale (within hours and less) by the earth's surface. The major drivers are friction or heating on the surface which leads to turbulent flows in

the lowest atmosphere (e.g. Pye and Tsoar, 2009; Nickling and Neuman, 2009). The components of turbulent wind velocity are subdivided into a carthesian coordinate system with u (zonal component), v (meridonal component), and w (vertical component). The mean velocities $\bar{u}$, $\bar{v}$, and $\bar{w}$ can be defined by any interval of time. The eddy velocities u', v', and w' are defined by the difference between the instantaneous velocity and the mean velocity (Sutton, 1934):

$$\begin{aligned} u' &= u - \bar{u} \\ v' &= v - \bar{v} \\ w' &= v - \bar{w} \end{aligned} \tag{2.1}$$

The atmosphere is heated mainly by solar radiation which is absorbed by the earth's surface. One component of atmospheric flows, therefore, is convection which can vary locally due to different albedo patterns on the earth's surface. In contrast, surface friction has a big influence on the wind directions near the surface. Surface friction does not affect the troposphere, the free atmosphere, where the air flows straight with the isobars. This frictionless air flow is called geostrophic wind and results from a equilibrium of the pressure gradient force (air is moving perpendicular to the isobars direct from high pressure to low pressure centers) and of the Coriolis force. The magnitude of the Coriolis force is proportional to the wind speed and the angular velocity itself depends on the latitude, i.e. the distance to the axis of rotation. (e.g. Pye and Tsoar, 2009).

In the planetary boundary layer the orography begins to reduce the wind velocity. This braking effect is based on the roughness length z_0 as a measure of the wind friction velocity u_*. z_0 is a very thin layer just above the bed in which the velocity is zero. z_0 characterizes the loss of the wind momentum depending on the roughness characteristics of the bed. Typical values for the roughness length are given in Tab. 2.1. The thickness of this layer is about 1/30 of the diameter of the particles on a relatively smooth bed surface (Bagnold, 1941). The thickness can increase to a maximum of around 1/8 when the roughness elements are spread about two times their diameter (Greeley and Iversen, 1987). In the case of surfaces covered by tall vegetation or high densities of other roughness elements, the plane of zero velocity may be displaced upwards to some height determined by the height, density, flexibility and permeability of the roughness elements (Oke, 2009). Above the height of zero velocity the time-averaged forward velocity $u(z)$ of the wind in a neutral atmosphere

turbulent boundary layer increases approximately logarithmically with height z (Fig. 2.1a). The slope of the logarithmic wind profile of neutral atmospheric stability is defined by the Prandtl-von Kármán equation:

$$u(z) = \frac{u_*}{k} ln \left(\frac{z}{z_0} \right) \tag{2.2}$$

where k is the von Kármán constant which varies with temperature gradient but is usually taken to be 0.4 (Marticorena and Bergametti, 1995). $u(z)$ is the wind velocity measured at a height z above the ground. This air motion with decreasing wind velocities, u, from the top to the bottom is assumed to take place in a series of thin, parallel laminae with a thickness of dz (Fig. 2.1b). The force per area needed to slide one of the laminae over the other and overcomes the viscosity is called *laminar shear stress* (τ_l) and is equal to the rate of shearing (du/dz) and the dynamic viscosity η of the air (Pye and Tsoar, 2009):

$$\tau_l = \eta \frac{du}{dz} \tag{2.3}$$

The viscosity is the characteristic of a fluid which is indicative for its ability to resist the shear stress. Air and water are so called *Newtonian fluids*, which are fluids with a constant viscosity. Thus, all the processes described below are not only valid for the fluid air but also for other Newtonian fluids including water.

The surface friction also has another effect on the air flow: the wind direction is deflected. In an ideal model, the wind in the northern hemisphere turns clockwise as it rises above the earth's surface, developing into a spiral. These spirals are called *Ekman spirals*, after Vagn Walfrid Ekman who demonstrated for the first time these spirals in the ocean where currents rotate so depths increases. The friction velocity is highest at the surface. Accordingly the strongest deceleration and the largest deflection occur at the earth's surface, with deflection to the left and thus to the area with the lower air pressure. With increasing height the angle of deflection decreases. The wind direction turns following to the direction of the isobars, to the direction of the geostrophic wind.

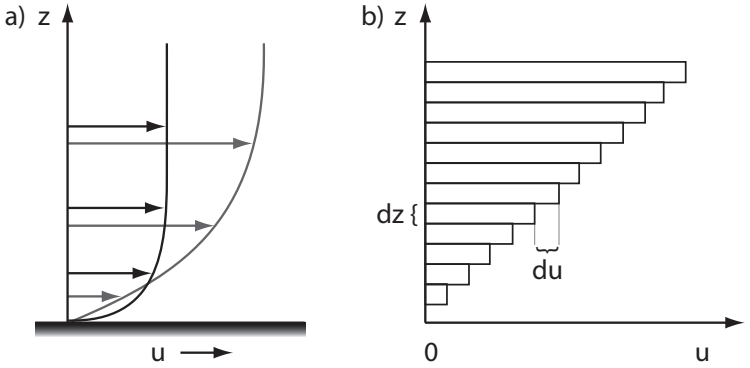

Figure 2.1: (a) Boundary layer velocity profiles for turbulent flow depending on increasing wind velocities for low turbulence (black line) and strong turbulence (grey line). The arrows are directly proportional to the velocity. (b) Deformation of laminar flow above the ground surface due to the viscosity and indicating the rate of shearing (du/dz). Modified after Pye and Tsoar (2009).

2.3 Particle Entrainment

The movement of particles that rest on a bed can be initiated by different mechanisms, which may act alone or in combination. The most important ones are drag exerted

Table 2.1: Typical roughness lengths (m) associated with terrain surface characteristics. The thickness of this layer is about 1/30 of the terrain surface characteristic. Modified after Troen and Petersen (1989).

Terrain surface characteristics	Roughness length (m)
Water	0.0001
Smooth sand	0.0003
Snow	0.001
Bare soil	0.005
Grass	0.008
Open Grass land	0.03
Farmland	0.05–0.1
Trees and Shrubs	0.2
Temperate forest	0.8
Groups of high buildings	1–10

by the wind and the impact of bouncing and rolling particles (e.g. other sediment grains or rain). Anthropogenic impact can be negated under glacial conditions but in recent times it also is an important factor.

Wind passing over a stable bed is characterized by turbulent eddies that create the drag. The forces that initiate particle motion are the wind shear stress on the surface, the particle's weight, and interparticle cohesion forces. The first depends on the roughness of the surface, which controls the transfer of wind energy to the erodible surface; the other forces are size dependent. The forming of drag involves the creation of locally higher pressure on the windward side of an object and a lateral pressure gradient. The *drag velocity*, or *friction velocity*, u_* of the wind is related to the shear stress (τ_l) exerted by the wind on the bed and to the density of air (ρ_a) by the equation

$$u_* = \frac{k \cdot u(z)}{ln\left(\frac{z}{z_0}\right)} = \sqrt{\frac{\tau_l}{\rho_a}} \tag{2.4}$$

by Arya (1975). Both u_* and τ_0 increase as the wind velocity (u) increases. At some critical point grains on the bed start to move. This point, referred to Bagnold (1941) as the *fluid threshold* or the *minimum threshold friction velocity*, can be expressed by

$$u_{*t} = A\sqrt{\frac{\rho_p}{\rho_a} g D_p} \tag{2.5}$$

u_{*t} is the fluid threshold velocity (which in this formula ignores the cohesion forces), ρ_p, is the relative density of the grains ($2.65\,\mathrm{g\,cm^{-3}}$ for quartz), ρ_a is the relative density of air ($1.275 \times 10^{-3}\,\mathrm{g\,cm^{-3}}$ at sea level and at 15 °C), g is the acceleration due to gravity ($981\,\mathrm{m\,s^{-2}}$), and D_p is the mean grain diameter (cm). A is the dimensionless threshold parameter and has been found to be constant between 0.1–0.2 (Shao and Lu, 2000) for particle friction Reynolds numbers (Re_p) greater than 3.5 with

$$Re_p = u_* D_p / \nu \tag{2.6}$$

Here, ν is the kinematic viscosity of the fluid, in this case the air and which is given by the dynamic viscosity, η, divided by the fluid density, ρ ($\nu = \eta/\rho$). Re_p provides a measure of how turbulent the flow is around a particle. Experimental data

by Bagnold (1941) show that the relationship between the fluid threshold velocity and mean grain diameter attains an increase of u_{*t} for the smallest particles and a minimum value when the mean grain size is approximately 60–100 µm. u_{*t} increases with larger particles due to the increasing dominance of the force of gravity. With finer average particle sizes, the surface becomes aerodynamically 'smooth' and the air drag, instead of being deflected by a few, more exposed, grains, is distributed more or less evenly across the whole surface. Iverson and White (1982) suggest that this behaviour is a result of interparticle cohesion forces. Consequently, the value of the coefficient A is substituted by a range of numerical expressions for A, each of them corresponding to a different range of the Reynolds number to isolate the particle Reynolds number from the interparticle cohesion (Iverson and White, 1982). This parametrization is used in recent dust emission models (Marticorena and Bergametti, 1995). Another recent expression for calculating u_{*t} by Shao and Lu (2000) is given with

$$u_{*t} = \sqrt{A_N \left(\frac{\rho_p}{\rho_a} g D_p + \frac{\gamma}{\rho_a D_p} \right)} \tag{2.7}$$

with A_N being around 0.0123 and γ being around $3 \times 10^{-4}\,\mathrm{kg\,s^{-2}}$, both empirically considered. A_N is here suggested to be a function of the particle Reynolds number $f(Re_{*t})$, only. Further on, the equation explicitly accounts for the effect of interparticle cohesion in the $\frac{\gamma}{\rho_a D_p}$ term. Van-der-Waals and electrostatic forces are the main contributors of the interparticle cohesion in γ. On average both are proportional to the particle's diameter (Shao and Lu, 2000). The equation (2.7) is of the form $u_{*t} = \sqrt{Y_1 D_p + Y_2 \frac{1}{D_p}}$. For large particles ($D_p$ >200 µm) the solutions are very similar to the equation (2.5) of Bagnold (1941). For small particles, the term Y_2/D_p dominates $Y_1 D_p$ and thus u_{*t} is in balance between the cohesive and the entrainment forces. The cohesive force is around 100 times larger than the force of gravity, for D_p <50 µm.

However, the different parameterizations give similar results in the particle size range (20–200 µm), on which this thesis is focused (Fig. 2.2). For D_p <20 µm the differences increase rapidly. Minimum friction velocities for particles occur in a range around 60–100 µm, for Shao and Lu (2000) $u_{*t} = 0.23\,\mathrm{m\,s^{-1}}$ at 107.5 µm, for Iverson and White (1982) with 0.03<Re<10 $u_{*t} = 0.20\,\mathrm{m\,s^{-1}}$ at 74.5 µm, and with Re>10 $u_{*t} = 0.16\,\mathrm{m\,s^{-1}}$ at 64.5 µm. All the expressions given are valid for spherical objects.

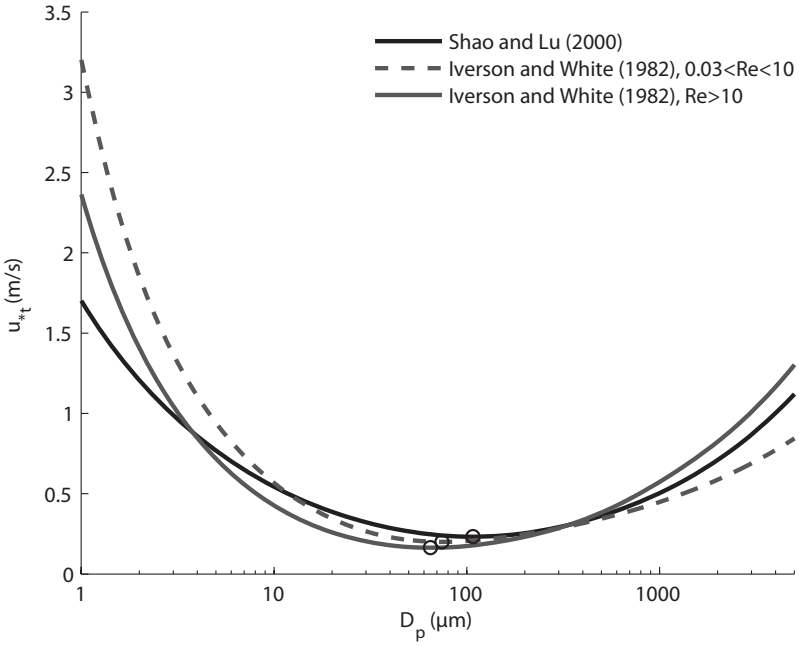

Figure 2.2: Threshold friction velocities according to different parametrizations indicate minimum friction velocities for particles in a range around 60–100 µm (black circles show the overall minimum values).

The required threshold shear velocity $u_{*}t$ to entrain dust particles is highly dependent on the grain-size distribution, sorting, cohesion and roughness of the source material.

In an example the threshold friction velocity $u_{*}t$ of a 63 µm large particle and a roughness length of 0.03 m, which is typical for open grass land, is calculated using equations (2.7).

$$\begin{aligned} u_{*t} &= \sqrt{A_N \left(\frac{\rho_p}{\rho_a} g D_p + \frac{\gamma}{\rho_a D_p} \right)} \\ &= \sqrt{0.0123 \left(\frac{\rho_p}{\rho_a} g \cdot 63\,\mu\mathrm{m} + \frac{0.3\,\mathrm{g\,s^{-2}}}{\rho_a \cdot 63\,\mu\mathrm{m}} \right)} \\ &\cong 0.25\,\mathrm{m\,s^{-1}} \end{aligned}$$

This theoretical value for the wind friction velocity is in the range of typical u_*t values as measured in the field or in wind channel experiments (e.g. Pye, 1987; Goossens, 2001, and references therein). These observations indicate that average u_* are required in the order of $0.2\,\mathrm{m\,s^{-1}}$ to $0.6\,\mathrm{m\,s^{-1}}$.

2.4 Estimation of the Transport Width

Once a particle is dislodged from the bed, its pathway depends on the ratio between the upward aerodynamic drag and the particle's weight acting in opposition. Bagnold (1941) has classified three major types of particle movement, depending on its grain size: a particle may move by creeping (sliding and rolling), bouncing (saltation) or in suspension (Fig. 2.3). The transport mode of the particle depends on its physical parameters, at least its density, grain size, and shape and on the characteristics of the wind, such as velocity or turbulence. A particle will remain in suspension if the vertical velocity of the transporting wind exceeds the settling velocity u_f. The settling velocities of quartz spheres can be approximately calculated according to Stokes's Law as a function of the square of the grain diameter:

$$u_f = K{D_p}^2 = \frac{1}{18}\frac{\rho_p - \rho_f}{\eta_f} g{D_p}^2 \tag{2.8}$$

with η_f for the dynamic viscosity and ρ_f for the density of the fluid. For air K is taken to be $8.1 \times 10^5\,\mathrm{cm^{-1}\,s^{-1}}$ at 15 °C, sea-level and for quartz spheres. Stoke's law is valid for slow sedimentation velocities u_f with a Reynolds number $Re < 1$ (when the inertia of the fluid is not significant) and u_f is proportional to the square of the particle's diameter (e.g. Hsü, 2004). This is generally true for particles with grain sizes up to medium sand (laminar approximation). The rapid settling of large particles is resisted predominantly by the turbulent drag of the wake behind each grain. For increasing u_f or larger particles (turbulent particle Reynolds numbers) u_f is calculated with the turbulent drag law (Dietrich, 1982). In a new approach both the Stoke's law and the drag law were combined into a single equation (Ferguson and Church, 2004).

$$u_f = \frac{R g {D_p}^2}{C_1 \nu + \sqrt{0.75 C_2 R g {D_p}^3}}, \quad \text{with} \quad R = \frac{(\rho_p - \rho_f)}{\rho_f} \tag{2.9}$$

The constants C_1 and C_2 are related to the shape and smoothness of the grains.

However, in the present thesis only grain sizes which are valid within Stoke's law are considered. The settling velocity can be calculated for both settling in the atmosphere or (after deposition on the water surface of a lake) settling through a water column, respectively.

It has been found that the ratio u_f/u_* is a suitable criterion to distinguish between different degrees of particle transport (e.g. Tsoar and Pye, 1987, and cited references therein). Indeed, there is no sharp boundary between saltation and transport in suspension but pure saltation occurs when turbulent flows have no significant effect on the particle trajectory. The maximum height of saltation is of the order of 1 m (Marticorena and Bergametti, 1995). The friction velocity u_* of turbulent flow in the boundary layer is given by

$$u_*^2 = (\nu + \epsilon)\frac{d\bar{u}}{dz}, \quad \text{with} \tag{2.10}$$

$$\epsilon = \sqrt{w'^2} \cdot l = \alpha\sqrt{w'^2} \cdot kz \tag{2.11}$$

with the product the kinematic velocity ν and the coefficient of turbulent exchange ϵ with the rate of shearing $\frac{d\bar{u}}{dz}$ (Owen, 1960). The coefficient of turbulent exchange (ϵ) can be expressed by the product of the mixing length l and the standard deviation of the vertical fluctuating velocity w' and represents the force opposing the tendency of small particles to settle (Tsoar and Pye, 1987). w' is derived from equation (2.1). The mixing length describes the length of a zone perpendicular to the main flow, with mixing air particles in the turbulent flow. Prandtl (1935) assumed the expression $l = \alpha kz$, with the von Kármán constant k, the height z, as well as $\alpha = 1$ for neutral atmospheres, $\alpha > 1$ for unstable atmospheres, and $\alpha < 1$ for stable atmospheres, respectively.

A quartz sphere is likely to remain in suspension when the friction velocity is larger than the settling velocity ($u_f/u_* < 1$). Pure suspension occurs when the friction velocity is much higher than the settling velocity, which depends strongly on the particle size. Between the two extremes of pure suspension and pure saltation both processes influence the particle's trajectory. This is called modified saltation. Gillette (1977) has estimated the effect on the particle trajectories for different ratios of $\frac{u_f}{u_*}$:

- $\frac{u_f}{u_*} \approx 0.7$: upper limit or pure saltation

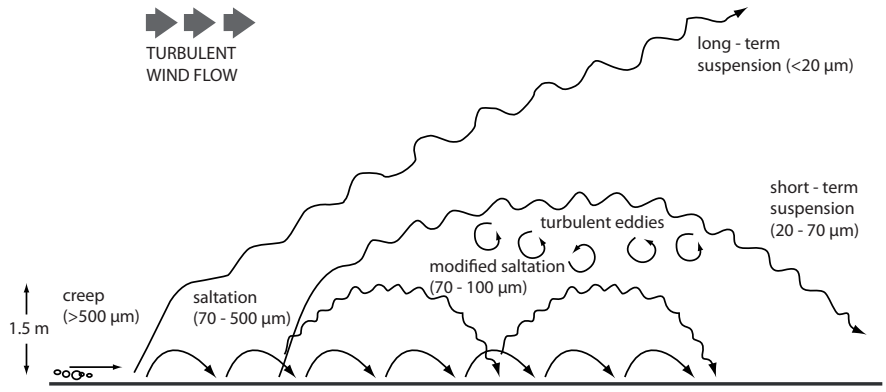

Figure 2.3: Modes of particle transport (quarz spheres) by wind after Pye (1987). The particle-size ranges indicated at the different transport modes are typically found during moderate windstorms.

- $\frac{u_f}{u_*} \approx 0.4$: ratio of upward to downward movement is 0.5
- $\frac{u_f}{u_*} \approx 0.4$: more non-settling grains than settling grains in the air

Thus, dust particles smaller than 20 µm are transported mainly in long-term suspension and can drift for thousands of kilometers. Dust in the typical medium to coarse silt fraction, which is the special subject of this thesis, is suggested to be transported mainly in 'inefficient' modified saltation or short-term suspension, when it is transported within typical storm conditions with friction velocities of $20\,\mathrm{cm\,s^{-1}}$ to $60\,\mathrm{cm\,s^{-1}}$ (Fig. 2.4).

The value of ϵ depends on the wind velocity but also on the mean atmospheric temperature gradient (atmospheric stability) and the nature of surface roughness. Equations to calculate the transport width, the transport height, and the concentration of particles at a particular height are based on the coefficient of turbulent exchange ϵ and are published by Tsoar and Pye (1987) and Pye (1987), respectively. The authors suggested a ratio of $u_f/\sqrt{w'^2} = 0.06$ with a high probability that a particle is transported well above the ground, since for long-term suspension u_f should be much smaller than $\sqrt{w'^2}$. Thus, using this relationship in equation (2.11), we can estimate the turbulent exchange coefficient which is needed to transport particles

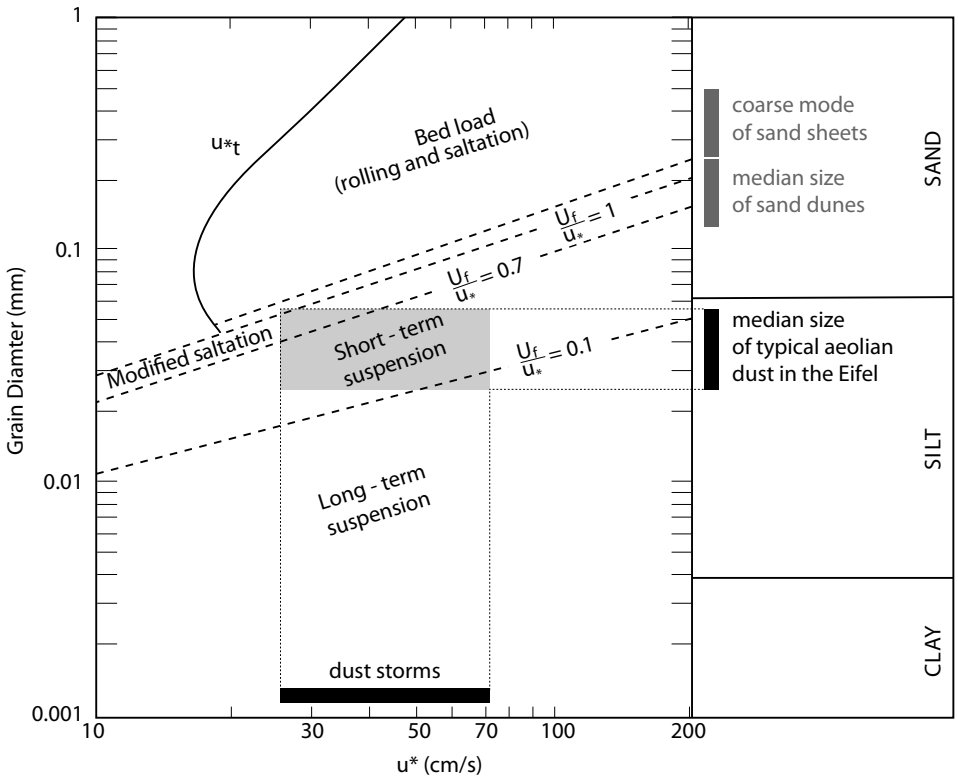

Figure 2.4: Modes of transport of quartz spheres at different wind shear velocities (u_*). Typical values for this thesis are marked with the black bars. Grey bars show typical values for other relevant wind blown sediments. The majority of the investigated aeolian dust particles are transported by short-term suspension. Modified after Tsoar and Pye (1987).

with a certain size to a particular elevation z (Tsoar and Pye, 1987):

$$\epsilon = \frac{\alpha u_f k z}{0.06} \tag{2.12}$$

Settling particles with grain sizes larger than 20 µm require at least values of $\epsilon > 10^5\,\mathrm{cm^2\,s^{-1}}$ to reach a height of 100 m such values are found only in intense cyclonic storms.

Tsoar and Pye (1987) have constructed a simplified model to estimate the maximum transport distance L that a particle can transported. Here, L depends on the duration

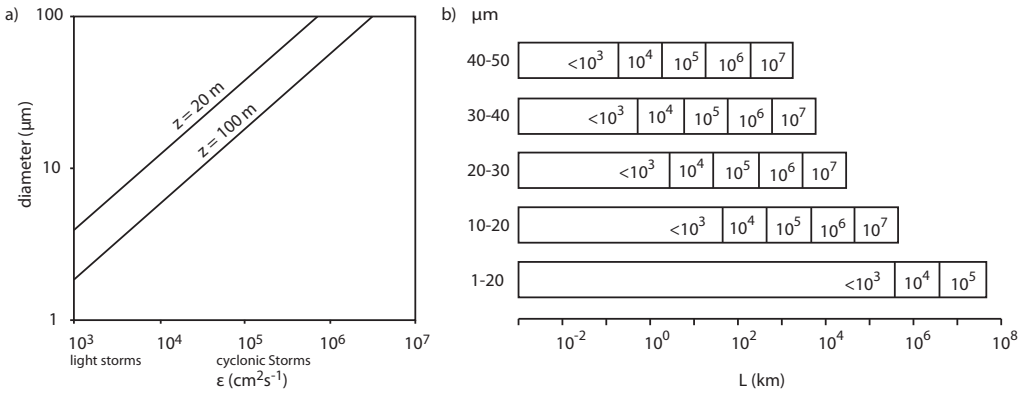

Figure 2.5: Transport height and width depending on the storm strength. (a) The approximate coefficient of turbulent exchange (ϵ) needed to transport quartz spheres to heights (z) of 20 m and 100 m under neutral atmospheric conditions. (b) The maximum distances (L) to be traveled by different grain size classes, considering $\bar{u}$ =15 m s^{-1} and $10^3 < \epsilon < 10^7$ cm^{2}s^{-1}. Modified after Tsoar and Pye (1987).

of the transport and the mean wind velocity ($L = \bar{u}t$). The duration t while a particle is in suspension depends on the settling velocity u_f and the coefficient of turbulent exchange (ϵ) which represents the force opposing the tendency of small particles to settle. t can be calculated by

$$t = \frac{2\epsilon}{{u_f}^2} \tag{2.13}$$

and using u_f in Stoke's law (2.8) the travel distance can be estimated depending on the grain size:

$$L = \bar{u}t = \bar{u}\frac{2\epsilon}{K^2 {D_P}^4} \tag{2.14}$$

The maximum transport distance L is inversely proportional to the fourth power of the particle diameter. Examples of transport height and width are given in Fig. 2.5. Particles larger than 20 µm are unlikely to travel more about 30 km from the source during a moderate storm, though this is not necessarily impossible. Strong, cyclonic storms are needed for transport distances greater than 100 km. Smaller

particles can easily be deflated over hundreds or thousands of kilometers. However, while the large majority of particles transported >100 km from source are <20 µm, single 'giant' particles (fine sand and larger) were also found to be transported over distances greater than 1000 km (Middleton et al., 2001).

This estimation of particle's transport duration and distance, given by Tsoar and Pye (1987), assumes steady winds and a uniform surface. In nature wind and sediment transport are affected by temporal fluctuations. A wide range of meteorological phenomena are able to generate the necessary wind fields required to uplift dust. These features ranges in scale from synoptic- and mesoscale systems which can result in intense dust emission to smaller scale processes (Maher et al., 2010, and references therein). For example, surface heat fluxes induces convective activity that can lead to dust uplift. At least in recent arid regions the generation of haboobs (a type of intense dust storms) is known to be a result of cold downdrafts from convective systems (Williams, 2008). In addition, surfacial factors also vary both spatially and temporally (Nickling and Neuman, 2009). Especially the soil moisture content can be vary on very small scales and has been found to be a major factor preventing for dust emission (Fécan et al., 1999).

Further parameterizations of vertical and horizontal particle fluxes, which can be used within dust emission models, are given by many authors, e.g. by Marticorena and Bergametti (1995). However, there is a need for further investigation of dust particle transport in the research area. A state-of-the-art estimation of particle transport distances could be applied by recent numerical dust emission models, like the Weather Research and Forecasting (WRF) Model (Darmenova et al., 2009; Michalakes et al., 2004), with glacial boundary conditions.

2.5 Particle Deposition and Dust Accumulation

In general, the deposition of dust and sand depends on the wind velocity and on the terrain topography, which influences both turbulence and particle trajectories. Turbulence is the main sedimentation force for aeolian dust, in contrast to sand, where gravity largely determines the deposition (Goossens, 1988). In the case of deposition in lake basins one can assume that the deposition rate is equal to the accumulation rate. This is an exception. In general material is resuspended after deposition, depending on the friction velocity u_* and consequently on the wind speed (Goossens, 2001). The deposition S is written as

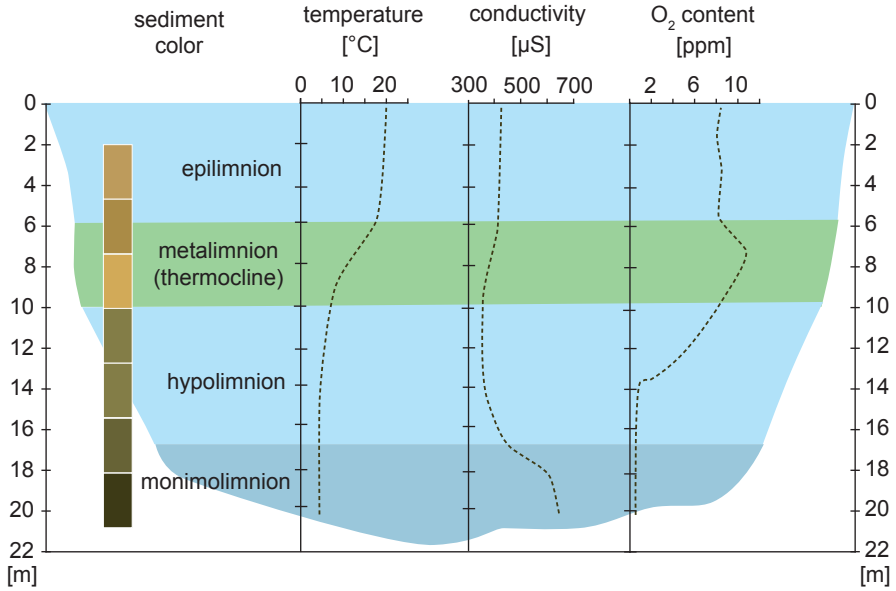

Figure 2.6: Sketch of the vertical stratification of the water column in a maar lake during summer, including temperature, conductivity, and oxygen content. Only the water above the thermocline is affected by wind induced currents. Modified after Seelos et al. (2009).

$$S = C \cdot u_d \tag{2.15}$$

where u_d is the velocity of deposition and C the airborne sediment concentration (Goossens, 1988) . u_d is a proportional to the wind speed, thus S increases with wind speed linearly until a deflation threshold velocity is reached, which is proportional to u_{*t} from equation (2.5). Deflation processes begin to act while the deposition is still increasing. As an result the accumulation rate begins to drop and accumulation will end once the deflation rate overshoots the deposition rate. Referring to Goossens (2001) this point is called accumulation limit. As soon as airborne sediment is deposited on the water surface of a lake it is protected from any deflation processes. Thus, deposition and accumulation rates in the Eifel maar lake sediments are analogues and lakes in general are perfect sediment traps due to their basin structure and the protective body of water.

2.5.1 Particle Deposition through the Water Column

The particle deposition through the water column is equivalent to the deposition through the atmosphere. Water, like air, is a Newtonian fluid and it is acceptable to use Stoke's law, equation (2.8), with adaptions for physical characteristics of the fluid such as viscosity or the density.

The wind is the main driver of currents in lakes, which may influence the settling of particles. However the effect of the wind only extends to a certain depth and varies over the annual cycle. In general, lakes of the temperate climate zone of the mid-latitudes show a distinct stratification of the water body, which also affects the settling. The insolation of the sun heats the surface water to about 20 °C during the summer season while the deep water still has temperatures of around 4–5 °C and therefore reaches the density maximum of water and as a result stays at the bottom (Fig. 2.6). The strongest change in the temperature profile is called the thermocline. Only the water above this layer is affected by wind induced currents and can consequently experience drifting of aeolian dust particles deposited on the lake surface. In addition, only the water of the epilimnion can incorporate new oxygen. During the summer season the water layer below the thermocline (hypolimnion) is not involved in the water circulation. In deep lakes, like maar lakes, the deep water close to the ground becomes depleted in oxygen and thus bioturbation is suppressed. If the bottom water remains undisturbed by circulation for several years it is referred to as the monimolimnion. Under these circumstances laminated sediments are preserved. Such laminates can consists of warves (annual layers) or of single event layers like dust events.

During autumn the temperatures of the air and thus of the surface water begin to decrease and the wind velocities increase. The strong temperature (and density) profile is weakened and surface water begins to descend. The full circulation of the lake starts when the temperature drops to 4 °C and the whole water body has the same density. Even here the wind is the main driver which induces the circulation. Additional cooling during winter leads to an overstratification of cold and less dense water or even to an ice cover which hinders direct dust deposition in the lake. During the spring season, as temperatures increase, the thermocline starts to develop again. The temperature stratification of the water body influences the settling of particles in two ways:

1. On the one hand, the temperature influences the viscosity and the density of the water. This has a strong influence on the settling velocity according to

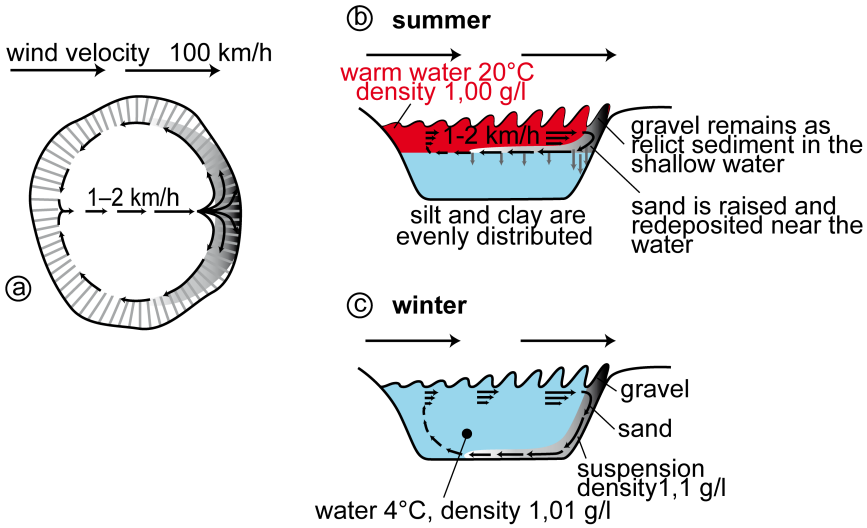

Figure 2.7: Sketch of storm forced currents in a maar lake and sediment redistribution. (a) Top view indicating the proportion of the wind velocity which forces the currents via friction. The flow velocity is typically 1–2% of the wind velocity. (b) During summer the current and induced return flow only influence the epi- and metalimnion. (c) During winter the whole water body is affected by the wind flow and the return flow takes place at the lake bottom. Secondary remobilization and depositon prozesses during storm events are shown in figures (b) and (c). Modified after Dietrich and Sirocko (2009).

Stoke's law. The settling velocity of a particle in the coarse silt fraction has a 52% higher settling velocity in 20 °C warm water than in 5 °C cold water (Tab. 2.2).

2. On the other hand, the flow regimes are different during summer and winter due to the water stratification (Fig. 2.7). A dust transporting storm also affects the circulation of the lake and particles drift within the flow. If the sorting of the particles is bad, the different settling trajectories are strongly biased.

The sorting of a particle sample is a statistical measure of the variance in the grain size distribution. Well sorted samples have a low variance of grain sizes. The sorting factor $\check{s}$ can be calculated by using a ratio of two percentiles in the grain size distribution:

$$\check{s} = \frac{per z_{25\%}}{per z_{75\%}} \tag{2.16}$$

Table 2.2: Example of settling velocities u_f and settling times t in a 10 m water column of quartz particles with different particle sizes and water temperatures, using Stoke's law, equation (2.8).

grain size	**20 μm**		**63 μm**		**100 μm**	
temperature	**20** °C	**5** °C	**20** °C	**5** °C	**20** °C	**5** °C
u_f [cm/s]	0.036	0.024	0.357	0.234	0.900	0.590
$t_{10\,\mathrm{meter}}$ [min]	462	702	46	71	18	28

The sorting process takes place in all modes of particle transport and is mainly based on the force of gravity dragging on particles with a certain density and diameter. Thus, aeolian transported dust is already extremely well sorted. In general, aeolian sediments show the best sorting of sediments in nature. Fractionation processes in the water column are therefore suggested to be insignificant.

2.6 Summary of Chapter 2

The major part of dust formation depends on changes in the source areas before the material is deflated. The main processes of dust generation are glacial grinding with subsequent fluvial transport to the source areas of dust emission. In addition, further processes like frost shattering or the abrasion of frozen soil generate particles of the coarse silt fraction and thus supply material for dust emission, even if these are only minor sources.

The whole path of particle transport consists of three major parts: (1) the particle's uplift, (2) its transport through a fluid, and (3) the deposition. All these steps are valid in every fluid and the given equations are valid for Newtonian fluids such as water and air.

Several criteria are important for dust emission. The most important factors are the grain size, the grain shape and the roughness length of the particle's bed. The roughness length depends on the terrain surface and exerts a frictional and therefore a braking effect on the wind velocity. Different parameterizations are given for the threshold friction velocity which is necessary to entrain a particle from the bed. This threshold friction velocity depends strongly on the grain size. The grain shape is also a strong influence on deflation. However, it is not further considered in this theoretical synopsis since the great majority of the particles of aeolian dust have a roughly spherical shape.

Once a particle is entrained from the bed, its pathway depends on the ratio of upward acting forces and its own weight acting in opposition. The weight depends on the grain size and the settling velocity of a grain is proportional to the square of its diameter following Stoke's law. The upward aerodynamic drag depends on the friction velocity of the turbulent flow in the lower most part of the atmosphere. The modes of dust transport are related to the ratio of the settling velocity and the friction velocity. Thus, particles with a diameter of 20–100 µm, which is the typical size of the investigated aeolian dust of this thesis, are transported within short-term suspension and modified saltation processes. Again, the grain size is the most relevant factor for estimating the transport height and distance (the distance is proportional to the fourth power of the diameter). For particles larger than 20 µm large cyclonic storms are required to lift those particles to a height of at least 100 m and transport distances longer than 100 km. The great majority of particles within a grain size range between 20–100 µm are thus transported over shorter distances. The distance from the Dehner dry maar to the Eifel North-south zone is in a range of 10–40 km.

The rate of dust deposition is proportional to the wind velocity. Deposition in lakes therefore has a big advantage: once a particle is deposited on the water surface it is protected from reentrainment. Thus, the deposition rate and the accumulation rate in this environment are equal. The subsequent settling of particles through the stratified water column of a lake might fractionate the different particle sizes. However, the sorting of the grain size distribution is excellent in aeolian dust samples. Thus, it is suggested that additional fractionation processes in the water column can be disregarded.

Chapter 3

Material and Methods

The major aim of the present research project is the reconstruction of palaeo atmospheric circulation patterns. This is achieved by a combination of several different approaches:

- The search for geochemical finger prints which lead to the source of aeolian dust by application of µXRF core scanning (proxy for wind direction changes).
- The detection and quantification of aeolian sediments by means of high-resolution grain size analysis (proxy for dust event frequency).
- Finally, the reconstruction of paleao circulation patterns using climate models to find a synoptic interpretation of the proxy data results.

The first two approaches were applied on maar lake sediments from the Dehner dry maar (sediment core DE3) which covers the late MIS-3 and MIS-2, respectively, and from lake Schalkenmehrener Maar (core SM3), which covers the last glacial termination and the whole Holocene. Both cores are part of the *Eifel Laminated Sediment Archive* ELSA. In a third step atmospheric general circulation models (AGCM) are used to systematically study the influence of different prescribed glacial SST patterns on past atmospheric circulation.

3.1 Lithology and Stratigraphy of Sediment Cores used in this Study

To achieve a proxy record for aeolian dynamics from maar lake sediments it is important that the deposition of aeolian dust is the dominant process of sedimentation in the lake itself. Other strong sedimentation processes like the deposition of suspension layers during flood events or secondary reworking processes like slumping and turbidits may disturb the primarily aeolian signal. Thus, it is necessary to choose a

lake like the Dehner dry Maar without any fluvial inflow to study aeolian dynamics (Fig. 3.1). By contrast, flash flood events are better detected in lakes with a riverine inflow.

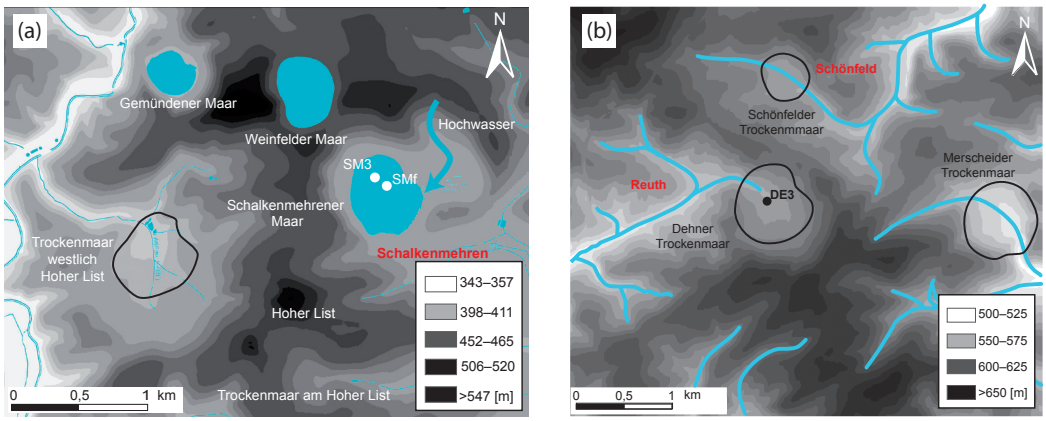

Figure 3.1: Digital elevation model showing important characteristics in the morphology of maar lakes. The Dehner dry maar is not influenced by any fluviatile inflow, which could disturb the signal of aeolian transported matter. The other two dry maars have riverine flow-throughs and are thus better suited to the detection of flood events. The position of the core DE3 from the center of the Dehner dry maar is marked. Modified after Sirocko (2009)

3.1.1 Schalkenmehrener Maar

The Schalkenmehrener Maar Lake(50°10′11.6″ N, 6°51′31.1″ E) was formed by a phreatomagmatic explosion some 20 000–25 000 years ago (Büchel and Lorenz, 1982). The modern maar lake is connected to a neighboring dry-maar structure, which has been filled with sediments from the late glacial up to Medieval times (Straka, 1975). The maar lake has a diameter of 575 m and is located 420 m above sea level. Six sediment cores were retrieved from Schalkenmehrener Maar in 2005–2009 by the ELSA Project, two with freeze core technology and four with a Niederreiter probe. The sediment cores SM2 and SM3 were correlated to each other by distinct lithological changes, which reveal that the depth of major transitions in these three neighbouring cores are almost identical (Tab. 3.1). Thus, the ^{14}C ages measured on the core SM2 (Tab. B.1 in the appendix) can be applied to the core SM3. SM3 is part of the the ELSA dust stack and and also part of the geochemistry study in chapter 4.

SM3 is one of most investigated sediment core from Lake Schalkenmehren. The sediments are finely laminated in the uppermost six meters with a large amount of organic gyttja (Fig. 3.2). Especially between 4.40–3.35 m depth the sediment has a high organic content and a dark brown color. From 6.5 m down the core, the sediment changes significantly to loess gyttja with a bright grey color, showing a strong influence of aeolian sediments during this period. A detailed plot of the SM3 lithology is given in appendix A.1. The Laacher See Tephra (LST) can be found in the core SM3 at a depth of 6.32 m. The eruption of the Laacher See occurred in the eastern Eifel Mountains, Germany, during the late Allerød and is dated to 12 880 varve years BP (Brauer et al., 1999), and to 12 900 years BP by $^{40}Ar/^{39}Ar$ dating (van den Bogaard, 1995), respectively.

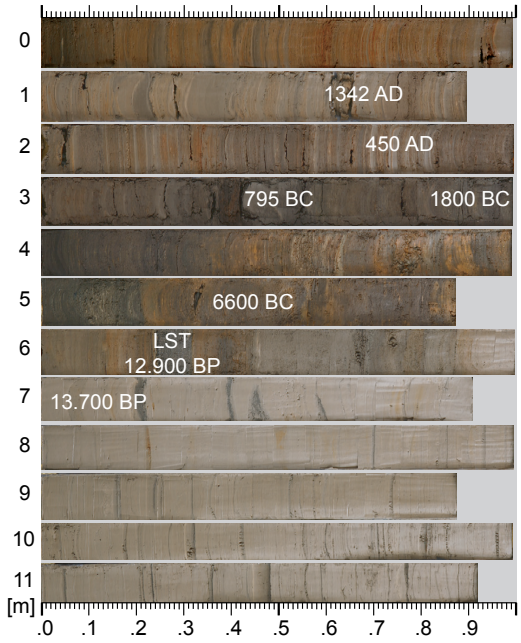

Figure 3.2: Core photography and time marks of the core SM3. The ash of the LST is clearly visible (6.3 m depth). The deeper core sequence is dominated by bright colored aeolian sediment of the late Weichselian.

Table 3.1: Correlation of distinct lithological changes between SM2 and SM3.

	SM2	SM3
Basis of the 1342 AD flashflood layer	1.62 m	1.80 m
Basis of the first gray flashflood layer	2.78 m	2.71 m
Basis of dark organic rich sediments	4.43 m	4.39 m
Basis of calcareous layers	5.13 m	5.15 m
Basis Laacher See Tephra (LST)	6.50 m	6.33 m

3.1.2 Dehner Dry Maar

Three sediment cores come from the Dehner dry maar (50°17′35.3″ N, 6°30′23.2″ E) which lies in the northwest of the western Eifel volcanic zone, south of the village of Schönfeld. Core DE3 from the center of the maar structure contains the LST at 3.4 m depth (Lenaz et al., 2010), followed by solifluction debris. Thus the lake silted up approximately 12 000 years ago. The maar is still very easily recognizable in the landscape. It has a diameter of 950 m and, with an elevation of 565m, it is at the crest of a hill. The maar basin is round and there is no recognizable evidence of any inflow in the past, though there is an outflow to the northwest (Fig. 3.1).

Core DE3 (Fig. 3.3) shows significant changes in environmental and climatic conditions in its sediments and oscillates between warm organic-rich and dust-rich glacial conditions. The core photograph (Fig. 3.3) shows these two dominant colors, thus defining the yellow, dust-rich, cold periods and the red to brown, clay-rich warm periods. A detailed plot of the DE3 lithology is given in appendix A.2.

Starting at the bottom sequence of the core, reddish to dark brown gyttja is dominant and implicates an interstadial character between 73 and 46 m (60 000–41 000 b2k, before 2000 AD). At 43 to 41 m depth are deposited from single but rather strong dust events and the sediment has a brighter color until 40.50–38.90 m (GI-8) where dark, organic-rich matter recurs. Beginning from 36 m depth the next ten meters are dominated by yellowish light brown loess gyttja with increasing dust influence. Sections with yellowish light brown sediments are always composed of silt-sized aeolian dust that was blown in from the wider surroundings. The content of aeolian sediment reaches its highest level at 26 m and remains stable until 10 m depth. In this sequence the content of organic matter drops to its lowest level and almost no pollen could be found. Exceptions are the core meters 30–27 (GI-4–GI-3) and 21–19.5 (GI-2) where the content of organic matter slightly increaeses. In the uppermost eight

meters dust decreases and the content of organic matter simultaneously increases (Seelos and Sirocko, 2009). At 8.50 m the first grass pollen appears again (Begin Meiendorf interstadial; Sirocko, 2009). Between 7 and 2.8 m the content of organic matter increases, whereas the uppermost core sequence is characterized by debris flow/solifluction debris.

The core DE3 is for the most part finely laminated and not disturbed. However, the deepest cores at 88–74 m depth are heavily disturbed and several thick layers of volcanic material, most probably from the maar's own eruption products, are intercalated with lake sediment. In the core meters 61, 57–54, and 36 m slides are recorded as decimeter large folds.

The black colored sediment defines singular, dm-thick volcanic ash layers in 3.49–3.40 m, 37.94–37.82 m, 42.93–42.78 m, and 50,09–50,87 m depth. The uppermost ash layer is a deposit of the LST since it shows the same mineralogical and geochemical composition (Lenaz et al., 2010) and Veres (in prep.). The latter ash layers might correspond to the eruption events of the Meerfelder Maar, the Pulvermaar and the Wartgesberg. All of these candidates are suggested to be large enough for deposition of dm-thick ash layers in the Dehner dry maar. The exact dates of their eruptions are still unknown. However, all of them are thought to have an eruption date of around 50 000 years. The Meerfelder maar eruption is radiocarbon dated to 47 557–43 110 cal BP (Schaber and Sirocko, 2005) using the IntCal09 calibration curve (Reimer et al., 2009). A similar date is given for the neighboring southern Mosenberg crater: A piece of schist from this lavaflow was dated to 42 ± 3 ka using thermoluminescence dating (Zöller, 1991).

The neighboring core DE2 and DE3 cores demonstrate a similar succession of sediments and can be correlated using major impacting depositions such as ash layers (Tab. 3.2). Most of the radiocarbon dates are measured on the core DE2.

Table 3.2: Correlation of two sediment cores from the Dehner dry maar.

	age (b2k)	DE2	DE3
Basis Laacher See Tephra (LST)	12.900 BP	3.20 m	3.49 m
Ash layer		27.66 m	28.33 m
Ash layer		37.37 m	37.94 m
Ash layer		42.20 m	42.93 m

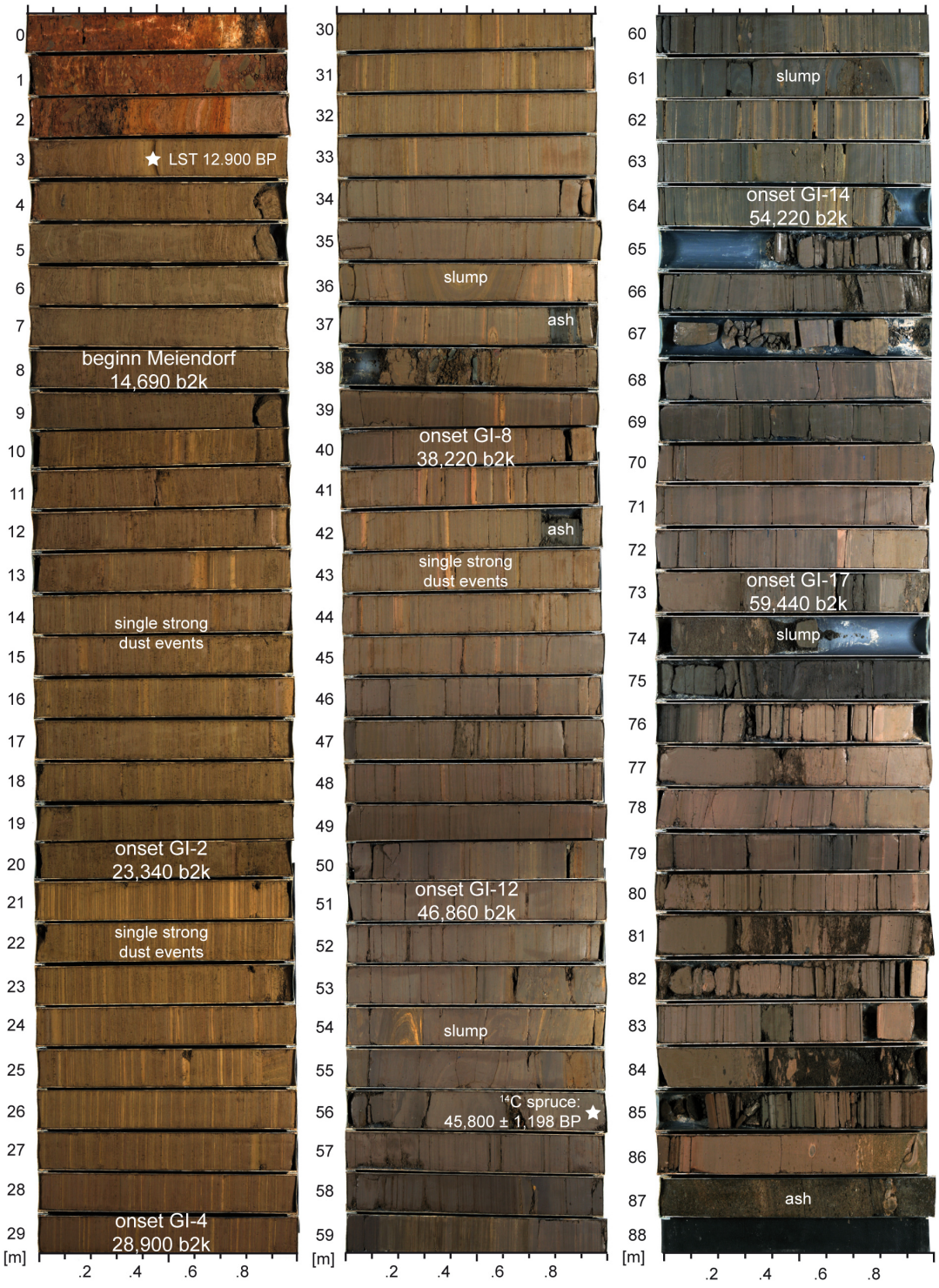

Figure 3.3: Core photography and time marks of core DE3, tuned to the Greenland ice core GICC05 stratigraphy (Svensson et al., 2008). The ash of the LST is clearly visible at 3.5 m depth. The core sections between 35 and 10 m are dominated by single strong dust events and represent the time of the late Weichselian.

3.1.3 Radiocarbon Dating of Lake Sediments

The most well-known and most commonly used method of dating lake sediments is the radiocarbon method. ^{14}C forms in the stratosphere through a reaction of the nitrogen in the air with cosmic radiation. The stable isotope ^{14}N exchanges a proton for a neutron creating the unstable ^{14}C. The ^{14}C isotope bonds with the oxygen forming atmospheric $^{14}CO_2$ thus entering the carbon cycle between the atmosphere, biosphere, geosphere, and the hydrosphere. One of the most important processes within the carbon cycle is the fixation of CO_2 in photosynthesizing plants (terrestrial trees and aquatic algae). Once the carbon dioxide is fixed, the radioactive decay of unstable ^{14}C begins with a half-life of 5 730 years. The majority of the biomass in a bulk sediment sample is composed of the organic matter of diatoms, which are algae that photosynthesize in the euphotic zone. If light reaches deep into the thermocline and upper hypolimnion the algae could incorporate carbon from the deep water where old CO_2 is present. This CO_2/HCO_3^- is derived from the remineralization of old organic carbon from the sediments. Depending on the amount of organic carbon consumed from the epilimnion (in equilibrium with the atmosphere) and hypolimnion (affected by the remineralization of old sedimentary carbon) the ^{14}C dates may be earlier than the true date of deposition of a sample. Evidence of additional alteration effects on the radiocarbon signal is given by outgasing mantle CO_2, which is known from a number of sites in the West Eifel Volcanic Field.

With today's mass spectrometer measuring technique, organic samples with an age of up to 55 000 years can be dated (Geyh, 2005). Dates in the range 0–50 000 years cal BP can be calibrated according to the recent IntCal09 radiocarbon age calibration curve (Reimer et al., 2009). In the framework of the ELSA project, 20 cores, which together encompass the last glacial cycle, were dated with more than 300 ^{14}C dates for the bulk sediment, organic remains and ostracods. The first of these dates were published by Schaber and Sirocko (2005). An update of maar sediment techniques and resulting age-depth model of all ELSA cores will be given in the article *Stratigraphy of 39 sediment cores from Pleistocene and Holocene maar lakes and dry maar lakes in the Eifel (Germany)* by Sirocko et al. (prep). The number of dates from the cores of Lake Schalkenmehren and Dehner dry maar is given in the appendix chapter B. 25 AMS ^{14}C dates for the cores of Lake Schalkenmehren and ten dates for the Dehner dry maar were applied for the age-depth modeling. Only AMS ^{14}C dates with a sufficient amount of carbon were used. The threshold values are given in the tables in the appendix.

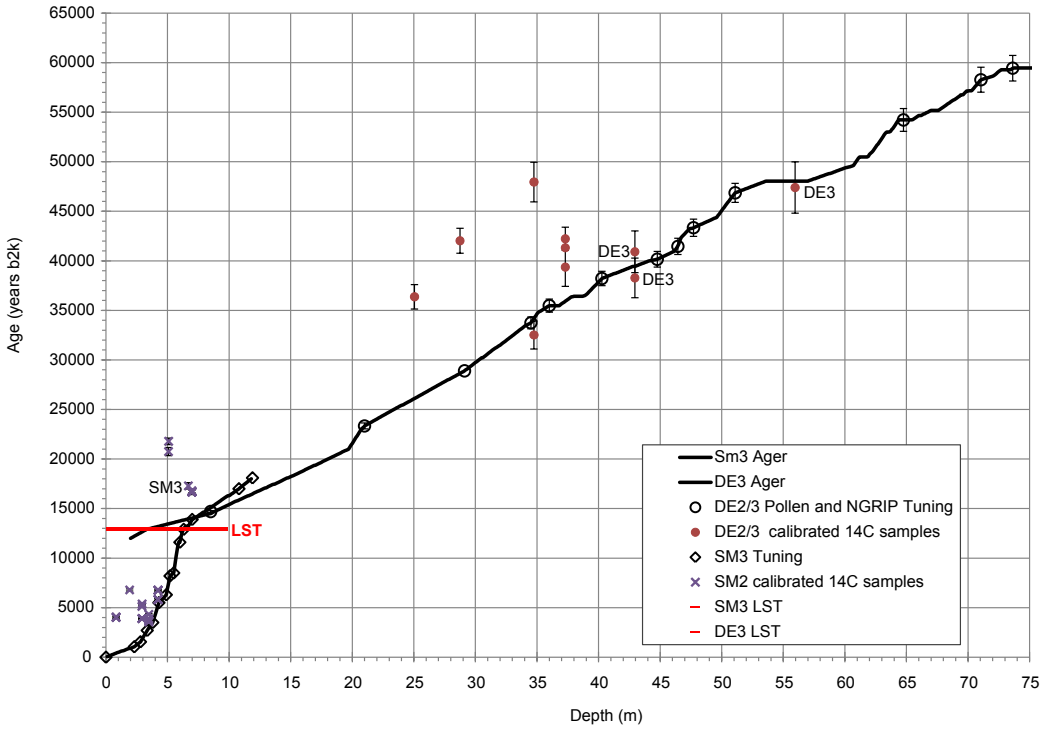

Figure 3.4: Age-depth models of the sediment cores SM3 and DE3, including calibrated radiocarbon ages and time marks of the tuning points (see text). The radiocarbon ages which come directly from the core SM3 or DE3 are marked. Unmarked ages come from the neighboring cores, respectively. Although the radiocarbon ages of the cores DE2 and DE3 do not match perfectly to the age depth model, yet they illustrate that the sediments of the Dehner dry maar were deposited during MIS-3.

The dates from the core DE3 and the neighboring core DE2 give uncalibrated ages between 31 000 and 46 000 BP, however, not in a strictly chronological order. Accordingly, these dates are surely MIS-3, but processes of erosion and resedimentation were also operating during MIS-3. Other ^{14}C dates are from ostracod samples. These uncalibrated ages fall between 32 000 and 37 000 years, and are apparently older than the bulk sediment data (Adams, 2010). Visible carbonate incrustations on the outer shells of the ostracods document diagenetic alteration of the shells. However, all samples clearly demonstrate that the Dehner Maar was an open lake during MIS-3. The deepest sample (DE3 55.96 m) was a large piece of *Picea* (spruce) wood, which proved an uncalibrated AMS ^{14}C age of 45 800 $\pm$1 198 BP and thus minimum 46 767 cal BP, using the IntCal09 calibration curve. The older boundary age could not be calculated since the age is older than the IntCal09 calibration curve (Reimer et al., 2009). Accordingly, this date is the final most reliable proof that all of DE3 is part of MIS-3, including the *Picea* zone which, according to the dating, most probably belongs to Greenland interstadial GI-14.

3.1.4 Tuning to the ice core chronology

The chronology of the ELSA core DE3 is tuned to the GICC05 chronology of the NorthGRIP ice core (Rasmussen et al., 2006; Svensson et al., 2008). Southon (2004) reported that within former ice core chronologies there are significant differences in the age models derived from different dating methods (e.g. 'ice flow models' and counting of annual layers). The recent Greenland ice core chronologies are based on the most probable age model (GICC05) and are applied to different ice cores by tephrochronological core correlations (Rasmussen et al., 2008). All dates are given using the *b2k notation* (years relative to AD 2000). The corresponding depth of the onset of interstadial climate conditions is based on sedimentological evidence like sediment color (grey scale values) and the content of organic matter (Sirocko et al., 2005; Schaber and Sirocko, 2005). The onsets of Greenland Interstadials are significant for matching up climate archives (Svensson et al., 2008), as they are the most clearly defined events (Tab. 3.3). The locations of the Greenland Interstadials (GI) in the core DE3 are shown in Fig. 3.3. The evidence of the LST and the scatter of ^{14}C samples corroborate the age-depth relation given by the NorthGRIP tuning (Fig. 3.4). A complete table of the age control and the core correlation is given in the appendix C.

It must be emphasized however that former ELSA sudies with respect to this

research, like Seelos and Sirocko (2009), and also the article Dietrich and Seelos (2010) in chapter 5 are tuned to the older ss09sea chronology of the Greenland ice cores (Johnsen et al., 2001). The reason for this is the comparison with the micro particle curve of Ruth et al. (2007) who also uses the older ss09sea chronology. There are plans to update the results of the ELSA studies. However, the maximum deviation between the two chronologies is about 500 years and thus over wide ranges smaller than the 1σ GICC05 counting uncertainty (Svensson et al., 2008).

Table 3.3: GICC05 ages (with reference to year AD 2000, "b2k") and matched ELSA DE3 depths for climatic events. The locations of the Glacial Interstadials (GI) are indicated in Fig. 3.3. References of the GICC05 ages: (1) Rasmussen et al. (2006), (2) Andersen et al. (2006), (3) Svensson et al. (2008).

Climate event	ELSA DE3 depth (m)	GICC05 Age (yr b2k)	Reference
Onset GI- 1/Beginn Meiendorf	8.50	14 692±93	(1)
Onset GI-2	21.00	23 340±298	(2)
Onset GI-4	29.90	28 900±449	(2)
Onset GI-8	40.25	38 220±725	(2)
Onset GI-10	51.09	41 460±817	(2)
Onset GI-12	64.80	46 860±956	(3)
Onset GI-14	73.20	54 220±1 150	(3)
Onset GI-17	73.20	59 440±1 150	(3)

3.2 The Detection of Aeolian Sediments within Lake Sediments

There is nowadays a wide range of procedures for reconstruction of climate variability from terrigenous sediments, especially lake sediments. During warm and humid climate conditions the sediments are dominated by the deposition of biogenic material. Temperature changes of the air or the water can be estimated via changing assemblages of vegetation indicators like pollen, macro remains of plants or planctonic organisms. During glacial climate conditions organic matter is minimized and the reconstruction of past climate is mainly based on the detection of different sedimentation events, like deposits from dust storms or flash floods (Fig. 3.5).

Both sediment cores were drilled in the center of the maar lake. The grain size of the sediment from these positions is thus to a large extent uniformly very fine (clay to

fine sand). In order to focus on aeolian dust the first objective is to identify the aeolian as distinct from the non-aeolian processes (like turbidites, volcanic ash layers, wave erosion layers, or suspension layers) and then to quantify them. A detailed compilation of different sedimentary patterns and their underlying sedimentation processes in lake sediments is given in Dietrich and Sirocko (2009).

The reconstruction of sedimentary processes is based on the analysis of their unique fingerprints. Each transport process sorts the sediment in different ways: (a) the geochemical composition or (b) the particle composition within the sediment.

The geochemical composition and the sedimentary patterns of the sediment cores are continuously measured on 10-cm long freeze dried samples impregnated with Araldite(R) resin impregnated samples. The resin impregnated blocks are a spin-off due to the production of thin sections (Dietrich and Sirocko, 2009). Thus, the geochemical results can be directly interpreted in context with micro facies analysis and the results of the grain size analysis method RADIUS (Rapid particle Analysis of Digital Images by Ultra-high-resolution Scanning of thin sections; Fig. 3.6).

3.2.1 Geochemistry, measured by µXRF core scanning

The core sections were scanned for selected elements at 1 mm resolution using the energy dispersive X-ray fluorescence scanner Eagle III (Röntgenanalytik Meßtechnik GmbH, Germany) of the University of Mainz (Germany). A detailed description of the µXRF measurement routines including operation parameters is given in chapter 4.2.2. The evaluation of the µXRF measured data is discussed in chapter 4 (Dietrich and Sirocko, 2010).

3.2.2 Grain size and Event analysis with the RADIUS method

The particle size distribution in a sample is an effect of fluid dynamics during particle transport (e.g. gravitative settling and turbulence) as mentioned in chapter 2. Thus, each different particle transport pathway and each different sedimentation process sort the particles in a sample according to their physical properties, which are mainly controlled by the the grain size and the density. The RADIUS approach has great potential to detect the different sedimentation processes which combine to produce the palaeoclimatic record (Seelos, 2004; Seelos and Sirocko, 2005).

The RADIUS approach has been successfully applied in several studies, e.g. Seelos and Sirocko (2005), Sirocko et al. (2005), Seelos and Sirocko (2007), and Seelos and Sirocko (2009). This particle-size measurement technique is based on the evaluation

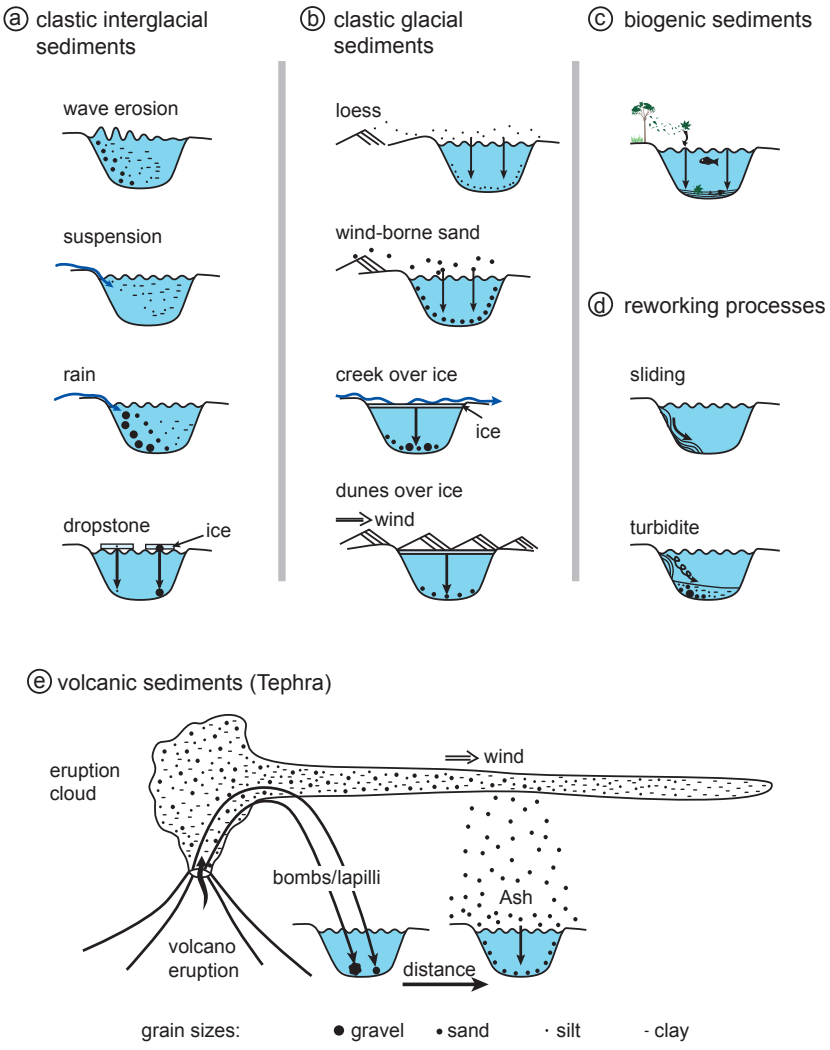

Figure 3.5: Major sedimentation processes within maar lakes: (a) detrital interglacial sediments are dominated by wind-driven wave erosion and inflow of fluvial material; (b) detrital glacial sediments are typically characterized by aeolian sediments; (c) biogenic sedimentation provides remains of organisms and plants as well as organic carbon; (d) reworked material like turbidites and slumps occur at events which destabilize the lake slope; (e) sediments due to volcanic activity. Modified after Dietrich and Sirocko (2009).

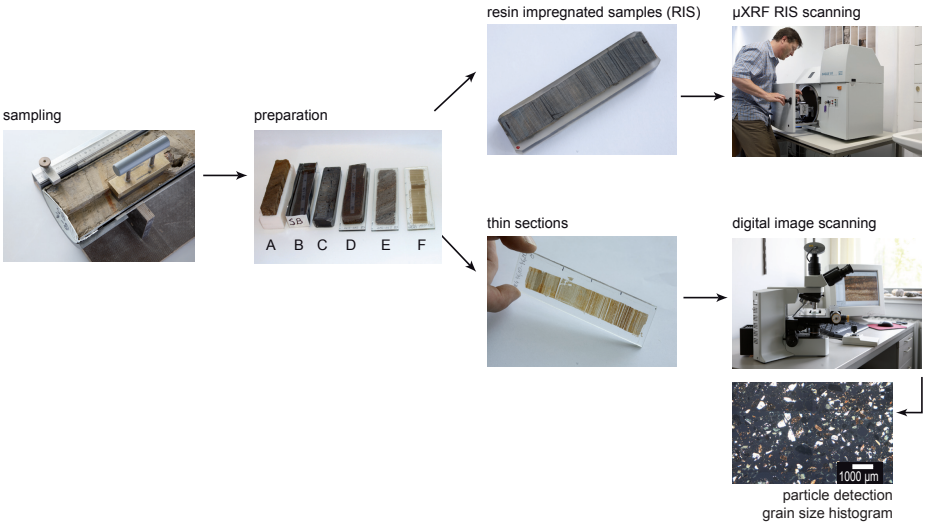

Figure 3.6: Sample preparation for µXRF core scanning and RADIUS analysis. Both measuring methods use the same samples and a similar resolution. Thus, the geochemical results can be directly interpreted in context with micro facies analysis of the RADIUS method. Modified after Dietrich and Sirocko (2009).

of digital images of thin sections, to achieve a sub-mm sample resolution and study sedimentation processes in the range from medium silt to coarse sand size. The particle-size analysis is separated into three different steps (Fig. 3.7): the first step, RADIUS-1, is automatic scanning of thin sections under a polarization microscope with 20x-magnification.

In RADIUS-2 the counting and measurement of different particle parameters (grain size, grain shape, separation of different particle phases) is undertaken by using the image processing software *AnalySIS* (Olympus Inc.). The continuous sample resolution of all parameters lies at 500 µm. Most of the parameters are measured with 100 µm resolution. The grain size is measured by applying an *equivalent circle diameter* with

$$ECD = 2\sqrt{\frac{a}{\pi}} \tag{3.1}$$

The ECD depends on the particle area measurement a. Neighboring particles with no space between their edges are separated by applying a so-called *watershed*

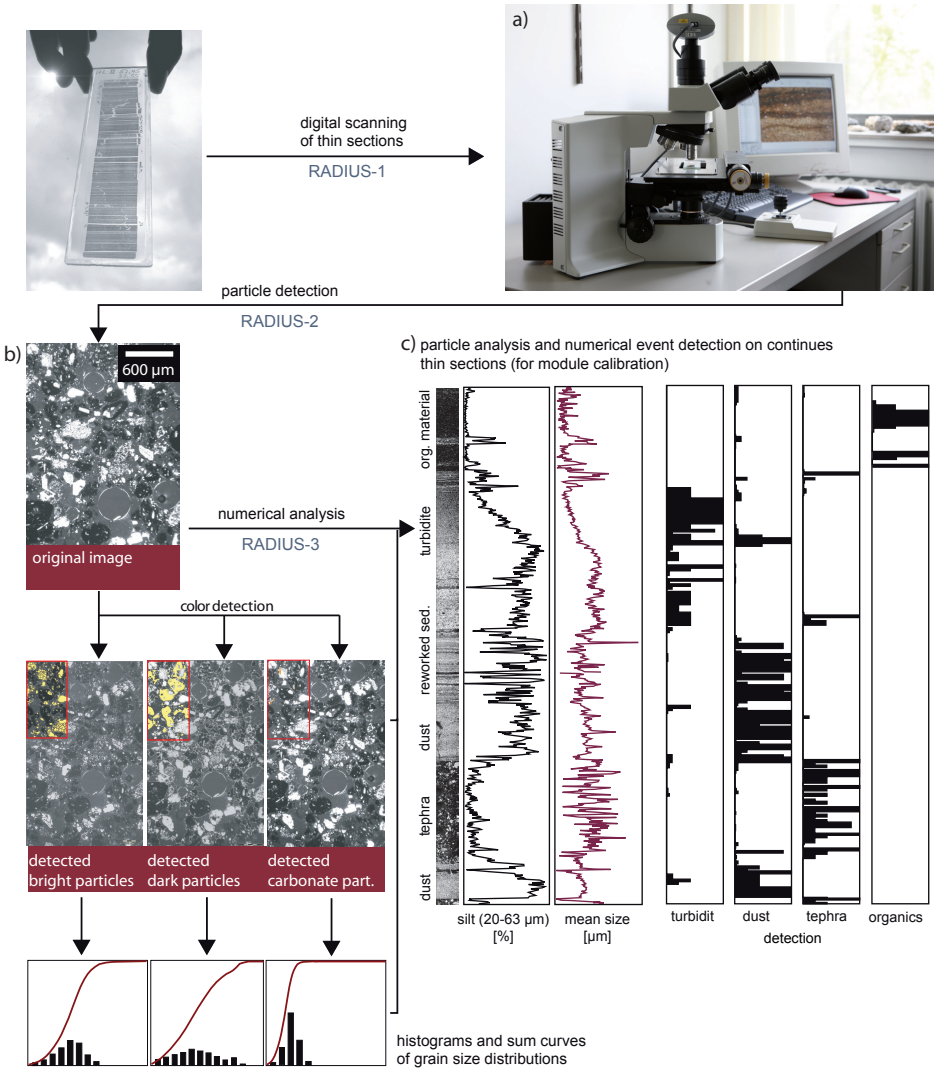

Figure 3.7: The RADIUS application after Seelos and Sirocko (2005). Notice the three steps beginning with digital scanning of thin section under polarized light (RADIUS-1), the detection and measurement of particles within the three phases bright, dark, and carbonate particles (RADIUS-2), and finally the numerical analysis and interpretation of the measured values (RADIUS-3). The last step determines the to probabilities of different sedimentation processes.

algorithm of the AnalySIS software. A major problem in quantitative thin-section analysis is the cutting effect of overlapping particles or particles which are cut in

an arbitrary plane during the thin section production. These particles are mostly attributed with false sizes caused by the limiting boundary layers of thin sections. Absolute parameters like particle size are adjusted by using an empiric correction matrix (Seelos and Sirocko, 2005). All particle measurements are applied for three different particle phases: bright particles (which form the majority of the typical lithic component in the sediment, like quartz and feldspar), dark particles (opaque matter, like organics or opaque minerals), and carbonate particles (which can be identified by their high interference color under polarized light).

The last module (RADIUS-3) is a numeric particle analysis application. It is coupled with an automatic pattern recognition system to identify several sedimentation processes in the sedimentary samples. The measurement of the pattern recognition is based on a probability approach, and combines several parameters like grain size distribution and sorting, maximum grain sizes, different shape factors, color factors, and the composition of the different particle phases to estimate the probability of a given sedimentation process (Tab. 3.4). The following sedimentary deposits could be detected in lake sediments: volcanic ash, organic matter, turbidites, and finally the deposition of aeolian dust. For further information refer to Seelos and Sirocko (2005) and Seelos and Sirocko (2009).

3.2.3 Combined geochemical/mineralogical RADIUS approach

The working hypothesis of this thesis is that the alternating amount of the calcium content in aeolian dust layers is based on changing source areas of dust deflation. A micrograph of a DE3 core section gives clear evidence for detritic and aeolian transported carbonate particles (Fig. 3.8). The Eifel North-South zone is the most probable source of carbonate particles in the coarse silt to fine sand grain size class (chapter 1.4.2; Fig. 1.7) which may lead to so-called *east wind layers* in the lake sediments. The measurement of the calcium content by the µXRF parallel to the RADIUS grain size analysis gives just a hint but not a proof of the existence of east wind layers. It is thus necessary to detect wind borne carbonate particles, since the carbonate can also originate from precipitation processes within the water body of any lake. The RADIUS method is enhanced in this study by a new *RADIUS of Carbonates* module which measures the content of aeolian transported carbonate grains. A detailed description of this approach is given in Dietrich and Seelos (2010) in chapter 5.2.2.

Table 3.4: Weighting factors of the RADIUS-3 module. Maximum 36 points comply with a probability of 100% for the detected sediment type. Grain sizes are described in the φ-scale with $\varphi = -log_2$(grain size in mm). Modified after Seelos and Sirocko (2009).

Detection	Dust	WF	Turbidite	WF	Tephra	WF	Organics	WF
Float. Gradient Analysis (depends on sampling steps, gradient)	no vertical particle-size gradient (± 0.05)	**1-3**	increasing particle sizes from top to bottom	**5-10**	no significance	**-**	no significance	**-**
Floating Correlation Analysis (depends on sampling steps, correlation factor)	high pos. correlation: 'mean size' vs 'max size' for bright particles	**1-5**	neg. correlation: 'silt of total' vs. 'silt of all classes' high positive correlation for the top area: 'silt of total' vs. 'mean particle size'	**1-5** **1-5**	high positive correlation: 'max size of bright particles' vs. 'max size of dark particles'	**1-8**	high negative correlation: 'max size of dark particles' vs. 'max size of bright partricles'	**1-10**
Mean particle sizes (500 µm sample segment)	35-50 µm 50-55 µm 55-60 µm > 60 µm < 30 µm	**5** **2** **0** **-3** **-2**	mean sizes (top): 20-35 µm mean sizes (bottom): 120-150 µm	**3** **3**	mean sizes (min. size bright particles: 80-130 µm): 150-300 µm (dark p.) 100-150 µm (dark p.) 70-100 µm (dark p.)	**3** **2** **1**	mean sizes for dark particles: > 350 µm 201-350 µm 150-200 µm	**12** **6** **2**
Modes	40 ± 5 µm bimodality:	**1** **-5**	top: 30 ± 5 µm bottom: 60 ± 5 µm	**1** **1**	100 ± 5 µm (dark & bright) bimodality:	**2** **5**	no significance	**-**
Skewness of distribution	0.0 ± 0.1 0.0 ± 0.15 0.0 ± 0.2	**5** **3** **1**	0.5 ± 0.1 0.3 ± 0.1 0.0 ± 0.1	**3** **1** **-2**	> 0.5 0.4 – 0.5 0.3 - 0.4	**3** **2** **1**	no significance	**-**
Distribution width (1/3φ - classification)	< 2φ (bright p.) < 2.33 φ < 2.66 φ	**5** **3** **1**	> 3.66 φ (bright p.) 3.33 φ - 3.66 φ 3.66 φ - 4φ	**3** **2** **1**	> 4φ (bright & dark) 3.33 φ – 4φ < 3.33 φ	**5** **3** **-2**	no significance	**-**
Silt content (20-63 µm)	> 60 % (bright p.) > 50 % > 40 % < 30 % > 5 % (dark p.)	**5** **3** **1** **-3** **-3**	no significance	**-**	5 – 8 % < 8 % (dark p.)	**3** **1**	< 5 % 5- 8 % (bright p.)	**6** **3**
Sorting	1.1-1.15 (bright p.) 1.15 – 1.25 1.25 – 1.35	**3** **2** **1**	no significance	**-**	> 1.9 (bright & dark) > 1.75 > 1.6	**3** **2** **1**	1.9 – 2.0 (dark p.) 1.8 – 1.9 1.7 – 1.8	**6** **3** **1**
Perzentile 95 – Perzentile 10	for bright p.: 40 – 50 µm 35 – 55 µm	**2** **1**	no significance	**-**	for dark & bright p.: 110 – 130 µm 90 – 110 µm	**2** **1**	no significance	**-**
Max. particle sizes	< 80 µm (bright p.)	**2**	80 – 110 µm (bright p.)	**2**	> 130 µm (dark p.)	**2**	> 200 µm (dark p.)	**2**
Max. sum		**36**		**36**		**36**		**36**

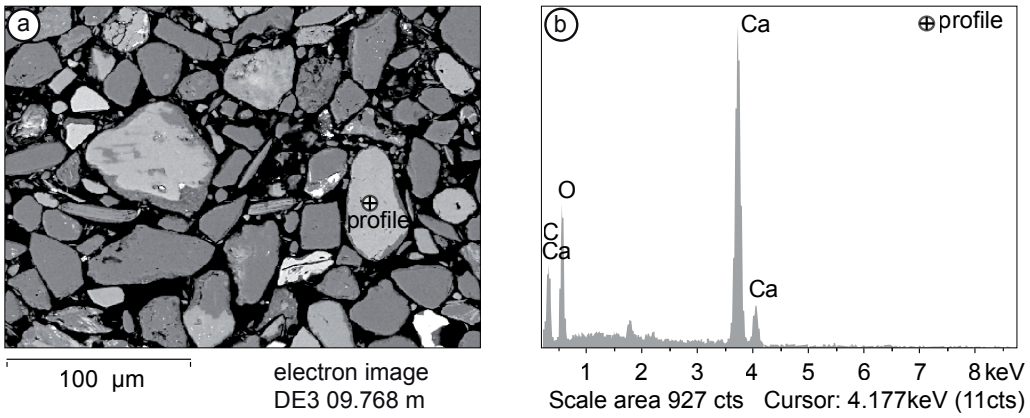

Figure 3.8: **(a)** The electron image of a sample sequence of core DE3 (depth: 9.768 m) shows the particle composition of an east wind layer. The sediment consists of well sorted quartz grains, carbonates and lithic components. The marked point in the center of a grain represents the geochemical profile shown in plot b. **(b)** The geochemical analysis (Zeiss DSM 962) of a large particle (a) shows a spectrum with pronounced carbonate bands. The ECD (equivalent circle diameter) of about 55 µm is equal to the main part of particles in the sample sequence and typical for loess-like eolian sediments.

3.3 Analysis of AGCM Experiments

Atmospheric general circulation model (AGCM) experiments are applied to reconstruct the large scale atmospheric patterns which have the highest potential for generating winds able to transport aeolian dust to the proxy site. This is the basis for developing a synoptic interpretation of long-persisting east wind conditions (LEWIC) or storm events with easterly wind directions. These are suggested to lead to an enhanced accumulation of sediment transported by easterly near-surface winds to the proxy site in the Eifel region. Thus, the 10 m-wind vectors of the AGCM experiments, $u10$ and $v10$, with daily resolution are analyzed. Here, ECHAM3/T42 (Roeckner and Coauthors, 1992) and ECHAM4/T31 models (Roeckner and Coauthors, 1996) are forced. T42 is a 128 by 64 regular longitude/latitude global horizontal grid with approximately 2.8°spatial resolution. T31 is a similar grid and has 96 by 48 horizontal grid cells (approximately 3.75°resolution).

The different AGCM experiments are forced with prescribed SST patterns to study systematically the influence of different glacial climate stages on atmospheric circula-

tion. The LEWIC and east storm events over Europe were analyzed for their timing, persistence, seasons, and location of occurrence. Thereby, a synoptic interpretation of east wind activity is addressed for different predefined glacial SST patterns as substitutes for different periods during MIS-3 and MIS-2. A detailed description of the model setups is given in chapter 6. The model experiments were evaluated by the comparison with the present day (PD) control runs with modern meteorological data from the ERA-40 reanalysis (Uppala et al., 2005).

For this reason a MATLAB based analysis method, GridMAT, was developed within this thesis.

3.3.1 GridMAT - The Grid Model Analysis Toolbox for MATLAB

GridMAT is able to analyze netCDF files and to calculate and plot the data, using the native MATLAB netcdf support since version R2008b as well as the Mapping Toolbox (TheMathworks). The GridMAT toolbox follows the basic commands of the software package `climate data operators` (cdo, www.mpimet.mpg.de/c̃do) and is enhanced by a set of functions for the analysis and visualization of u and v wind vectors. A complete list of the functions is given in appendix E.

For the investigation of easterly wind directions the 10 m-wind vectors are analyzed. The two vectors are mutually perpendicular. West wind (wind is blowing to the E) is expressed by $u10 > 0$, and in the meridional component the wind direction is defined with $v10 > 0$ for south wind (wind is blowing to the N). $u10$ and $v10$ were selected for an area which covers the Eifel region and subsequently the mean values of this field were calculated. In all experiments the field means of the wind vectors for 2x2 grid boxes are calculated. These field means are the basis for any further investigation.

The two-dimensional Cartesian coordinates of the wind vectors are transformed into polar coordinates with wind speed and wind direction. Easterly winds have defined wind directions between 0° and 180°. The monthly distribution of days with easterly wind direction is calculated using the function `grd_daydecomp.m`. Basic statistical information on wind speed and direction and their monthly distribution is computed with the function `grd_winddiranalyst.m`.

Temporal clusters of east wind, the long-persisting east wind conditions (LEWIC), are defined as time-related events with a length of at least three days and are separated from the rest of the data matrix (`grd_tclusterfinder.m`). These clusters are investigated for their length as well as for their time of occurrence (`grd_tclusteranalyzer.m`) and their relative frequencies in the annual cycle using the function `grd_tclustermonth.m`.

Maps of the overall seasonal means, seasonal composites of LEWIC, and the anomalies (results of glacial experiments minus the results of present day control runs) are plotted by the function `grd_mapplot.m` which uses the ncquiverref-function by Roberts (2010).

3.4 Summary of Chapter 3

In this thesis two maar lake sediment cores from the West Eifel Volcanic field are investigated for the reconstruction of past aeolian dynamics. SM3 covers the Holocene whereas the core DE3 covers the marine isotope stages MIS-3 and MIS-2. In both cores the Laacher See Tephra can be identified. Thus, the two cores together supply a continuous record for the last 60 000 years. The chronology of the cores is based on several dating methods like radiocarbon, tephrochronolgy and tuning to the Greenland ice core chronology.

To achieve the scientific aim of this thesis, the reconstruction of atmospheric variability, the content and the composition of aeolian dust in the sediment cores are analyzed using two different methods. In a first step the geochemical characteristic of dust is examined using a µXRF scanning approach which is applied on continuously taken resin impregnated samples. The scanning resolution is 1 mm. The resin impregnated samples are a spin-off from the production of petrographic thin sections. These thin sections are the basis for the second step, the quantification of the dust content by application of an automated micro facies analysis, the RADIUS approach (Seelos and Sirocko, 2005). The RADIUS method measures the grain size distribution as well as other physical properties of particles like shape factors with a resolution of 500 µm. Based on the analysis of these parameters the presence of aeolian dust within the lake sediment is measured. Thus, continuous geochemical measurements and micro facies analysis are applied to the same samples with a similar resolution which is in the range of typical annual sedimentation rates (around 1 mm a year).

In a third step the content of aeolian transported carbonate particles is measured with a newly developed RADIUS carbonate module. In the lake sediments of the Dehner dry maar ther are two different kinds of dust layers: either with a low content or with a much increased content of aeolian transported carbonate particles. Since the most reasonable sources of carbonate grains are located on the eastern side of the Dehner dry maar carbonate rich dust layers are defined as east wind layers.

The results of the dust proxies are subsequently investigated by the analysis of atmospheric general circulation models (AGCM). The surface wind vectors are inves-

tigated to reconstruct the large scale atmospheric patterns which have the highest potential for generating winds able to transport aeolian dust to the proxy site. The different AGCM experiments are forced with prescribed SST patterns to systematically study the influence of different glacial climate stages on atmospheric circulation. The model analysis is applied using a newly written MATLAB toolbox called GridMAT (Grid Model Analysis Toolbox). The focus of this thesis is the analysis of easterly wind directions to explain the east wind layers in the lake sediments of Dehner dry maar. The results of the model experiments are finally compared with those of the dust proxy data.

Chapter 4

The Potential for Dust Detection by means of µXRF Scanning in Eifel Maar Lake Sediments[1]

4.1 Introduction

The investigation of long continuous aeolian sediment records, such as loess profiles or dunes is widely used to reconstruct environmental and climate variability. Long records cover several glacial cycles and are primarily known from the large loess plains in Asia or from the Carpathian basin. Profiles with the potential to record deposition with annual resolution are less common. The West-Eifel Volcanic Field (WEVF), Germany, provides such records in maar lakes. Without a fluvial inlet, these lakes are perfect sediment traps for aeolian deposits (Dietrich and Sirocko, 2009; Pfahl, 2009). Furthermore, although the sediments do not show annual lamination, they are stratified by event layers due to anoxic conditions at the lake bottom (Zolitschka et al., 2000; Sirocko et al., 2005).

The detection of aeolian deposits in lake sediments is possible by using different approaches like micro facies analysis, measuring the minerogenous component of the bulk sediment (Zolitschka et al., 2000), magnetic susceptibility (Yancheva et al., 2007) or grain size analysis (Sun et al., 2002; Seelos and Sirocko, 2009). However, in this study a geochemical scanning approach is applied to measure aeolian deposits. High resolution geochemical analysis of lacustrine sediments offers a reliable method for investigation of environmental changes in the past (Engstrom and Wright Jr, 1984; Boyle, 2000, 2001; Melles et al., 2007). The potential of X-Ray fluorescence (XRF) core scanning is based on the rapid and non-destructive acquisition of high-resolution

[1] A slightly modified version of this chapter has been published as Dietrich and Sirocko (acc.) in the journal E&G - Quaternary Science Journal.

geochemical data from lacustrine sediment cores. This facilitates new approaches to many applications in paleolimnology, including pollution detection, varve counting, and estimation of past ecosystem productivity (Francus et al., 2009).

The µXRF scanner acquires bulk-sediment chemical data with sufficient accuracy of major elements (Boyle, 2000). Although elemental intensities are predominantly proportional to concentration, they are also influenced by the energy level of the X-ray source, the count time, and the physical properties of the sediment, such as the poorly constrained measurement geometry attributable to inhomogeneity of the specimens (e.g. variable water content and grain-size distribution), and irregularities of the sample surface (Rothwell, 2006; Weltje and Tjallingii, 2008). Nevertheless, the XRF methodology is a widely accepted, semi-quantitative core logging method that provides records of changing element intensities expressed in 'total counts', reflecting the geochemical composition of the sediments. Quantitative analysis is made more difficult by matrix effects especially for light elements such as Al and Si (Böning et al., 2007). Reasons are the pore volume of interstitial water or resin or the roughness of the sediment surface. However, recent approaches to calibration of XRF core scanners for quantitative geochemical logging are applied by Weltje and Tjallingii (2008) and Kido et al. (2006). As well as the direct measurement of the core surface via core loggers the analysis of resin impregnated samples (RIS) is to be seen in a growing number of studies. The single 10 cm long RIS are taken continuously down the core. The pore volume of the sediment is substituted by resin during the production of the RIS. These geochemical data can be directly assigned to micro-facies data because XRF scanning has been carried out on the same impregnated sediment blocks from which thin sections can be prepared. High resolution applications are shown by different studies, for example by Sorrel et al. (2007) or Brauer et al. (2008). The latter authors have applied a geochemical major element micro-X-ray fluorescence scanner at 50 µm resolution providing geochemical information for individual seasonal layers (5–8 data points/varve for the Allerod; 20–30 data points/varve for Younger Dryas) to investigate the structure and seasonal composition of varves. The first successful implementation of XRF techniques for the provenance analysis of dust is shown by Neff et al. (2008).

The objective of this study is separate the different lithofacies especially the aeolian input into the lake environment by means of µXRF geochemistry and to test whether µXRF data are not only a general paleoclimate signal but can be used to quantify the aeolian fraction directly to achieve dust records with annual resolution. In this study, we demonstrate how aeolian sediment within maar lake sediments might be

classified by certain elements and new factors, calculated by principal component analysis (PCA).

4.2 Material and Methods

4.2.1 Cores and drilling locations

The west Eifel volcanic field (Germany) is characterized by more than 70 maar lakes and dry maar lakes (Büchel, 1994). Two sediment cores, namely SM3 (N50°10'11.6", E6°51'31"), from lake Schalkenmehren and DE3 (N50°17'35.5", E6°30'22.7", 88 m depth) from the Dehner dry maar (Dehner Trockenmaar) were drilled in a maar lake and a dry maar, respectively (Fig. 1.6). On the Eastern side of lake Schalkenmehrener Maar an older dry maar is located which is connected to the lake by a marsh. Earlier fluvial input into the maar lake from this extended catchment could be proved until up to the Medieval Times (Straka, 1975). The rim of the Dehner dry maar exhibits a pronounced roundness and there is no recognizable evidence of any inflow in the past, though there is an outflow to the Northwest. Core SM3 from lake Schalkenmehrener Maar was drilled using a swimming platform and a piston corer (UWITEC, Austria). DE3 was drilled with the *Seilkernverfahren*. These two cores from the ELSA repository (Eifel Laminated Sediment Archive) cover between them the main periods with major climate changes of the last 60 kyrs, including the marine isotope stages MIS-3 and MIS-2 (DE3), and transition I as well as (anthropogenic) dust events during the Holocene (SM3). In total 82 meters of sediment cores with an average sedimentation rate of 1.5±0.5 mm/yr are analyzed. The sediments consist of detrital bearing sediment that documents weather extremes (flash floods and aeolian dust) or gyttja, containing a high amount of organic matter that documents past water conditions (temperature, nutrient content, pH), which are recorded in the remains of plants and animals that lived in the lake. Details of the chronology and lithology are presented in chapter 3.

4.2.2 Evaluation of chemical data

The two core sections were scanned for selected elements at 1 mm resolution using the energy dispersive X-ray fluorescence scanner Eagle III (Röntgenanalytik Meßtechnik GmbH, Germany) of the University of Mainz (Germany). The µXRF was used to measure major elements (e.g., Mg, Al, Si, P, S, K, Ca, Ti, Mn, and Fe) as well as trace elements (Sr, Zr, Cr, Ni, Cu, and Zn) on 10 cm long resin impregnated

samples. Na is too light for detection via the Eagle III and is therefore not included in this study. The Araldite(R) impregnated blocks are a spin-off from the production of thin sections (Dietrich and Sirocko, 2009). Thus, the geochemical results can be directly interpreted in context with micro facies analysis. The µXRF scanner acquires bulk-sediment chemical data from these samples. Scans of pure Araldite indicate zero counts of the investigated element and thus do not bias the results. Although elemental intensities are predominantly proportional to concentration, they are also influenced by the energy level of the X-ray source, the count time, and the physical properties of the sediment (Röhl and Abrams, 2000). The data were collected every 1 mm down-core with a 300 µm-spot size of the X-ray beam. The generator setting was of 30 kV and 500 mA with a sampling time of 16 seconds and a mean death time of 30 µs. The sample chamber is evacuated during measurement, thus light elements like Si and Al are also stimulated. The emitted fluorescence radiation is detected by an energy dispersive Si(Li)-detector with an area of 30 mm^2 and an energy resolution of 135 eV at maximum.

Discrete reference samples are taken from core DE3 and glass beads with a five times dilution are measured by a Philips MagiXPRO via WD-XRF method (Rh-anode, 3.2 kW). The quantification is based on international standards (Govindaraju, 1989). This study also examines whether the standard free fundamental parameter method is suitable for quantification of the Eagle µXRF. The alternative is using the intensities as relative results in combination with quantified but independent measurements by WD-XRF methodology.

4.2.3 Statistical processing of the data

Core sequences with reworked material were removed from the original data set. High amounts of resin (e.g. cracks caused by sample preparation) were detected by a locally low sum of measured intensities and are subsequently removed. Therefore a threshold of 500 cps was evaluated empirically.

A principal component analysis (PCA) was performed to identify different lithological facies, such as dust, by using inorganic geochemical data. The PCA was used to objectively describe the differences and similarities between the elements and to reduce the number of variables by showing the main variance of the data set by only a few factors. The factor loadings give the correlation between the newly found factor and the respective element. The higher the influence of an element for the factor, the higher is the factor loading. For all cores the following steps were per-

formed before applying the PCA: (a) Using every measured value at 1 mm resolution results in a total sample amount of several thousands. Hence, data are resampled after smoothing using a Gaussian kernel filter with a 20 point window size to give a sample amount less than 1000. (b) Most of the parameters exhibited a pronounced skewness. PCA and Pearson correlation give unbiased results only for Gaussian distribution, which would be especially crucial for small data sets. However, the data were log transformed and z-normalized to zero mean and unit standard derivation for each parameter separately in order to weight equally the different parameters in the multivariate analysis. (c) Subsequently, outliers were removed by deleting values greater/less than mean plus/minus three time standard derivation of each measured element (includes 99.7% of all normal distributed values). The amount of significant and nontrivial new variables is measured using the scree test. Sulfur is not considered in the PCA since it correlates less well to the reference values and did not change the major findings of the PCA. However, S is known to be precipitated as pyrite and is thus a proxy for anoxic conditions of the bottom water. The concentration of an element in the lake sediment depends on the amount of influx and the degree of preservation of this element (Engstrom and Wright Jr, 1984). Thus, the new calculated variables (principal component factors) are controlled by the same mechanisms of influx and preservation. For all numerical analysis MATLAB (TheMathworks, version 2009b) were used.

4.3 Results

4.3.1 Calibration of µXRF results

The results of the µXRF scanning are presented as intensities (counts per second, cps). Since core DE3 is one of the most important cores of ELSA, discrete (and destructive) sample analysis using the WD-XRF is obtained to evaluate the intensity values given by the ED-XRF scanner with certain element concentrations (Tab. D.1 and Tab. D.2 in the appendix D). For most elements (Al, Ti, Fe, Mn, Mg, Ca, Zr) good correlation ($R^2 > 0.75$) can be observed between the intensities counted by the Eagle III µXRF and the corresponding measured concentrations (Tab. 4.1). The correlation was also checked for the standard-free quantification (fundamental parameter method) for weight percentages and atomic percentages. While the main elements fit quite well, Zr is the only trace element which shows an acceptable correlation between the measurements by WD-XRF and the intensities but does not have a significant

correlation with the quantified results. However, Si matches better with the calculated weight percentages than with the intensity. The elements Cr, Ni, Cu, and Zn which show only weak correlation with the WD-XRF results are not further considered in this study. In the following the intensities are represented for the core SM3 and for DE3 weight% are shown because of good correlation between the ED- and WD-XRF results.

4.3.2 The elemental stratification

The comparison of the geochemical stratification (Fig. 4.1 and Fig. 4.2) with the lithology of each single core leads to the suggestion, that Ca, Si and K are the most prominent elements for the classification of aeolian sediments.

Core DE3 covers a time period from MIS-3–MIS-2, including the glacial inception of the late Weichselian ice sheets. However, single but severe dust events can be found between 43–41 m depth, which corresponds to the marine H4 event (Hemming, 2004), and beginning at 36 m the content of aeolian sediment increases, culminating in the last glacial maximum (LGM). Best correspondence with the lithological stratification can be found with the Si, Ca, and Zr. The stratification of the elements Si, Al, and Ti differ in the core DE3 (Fig. 4.1a, b). Si shows an overall increasing trend over the whole core section (from bottom to top), starting from around 60 wt.-% up to 70 wt.-%. The core section from 25–5 m has the highest content of Si with a slight increase between 25–15 m, while content in the core sections from 38–36 m and 60–58 m decreases in relation to the overall trend, corresponding to an increase of organic matter in the sediment. In the core DE3 Ca is obviously enriched (CaO content around 5 wt.-%) in the upper section, with a reduction between 20 and 10 m depth. Lower down the core the content is around 1 wt.-% and reaches only higher values at 39 m, between 41–45 m, and in places between 68–59 m. The strong shift at 33 m depth from low to high amounts of Ca and Zr coincides with the last glacial ice advance of the late Weichselian, when the climate became colder and dryer and thus deflation processes became more frequent. Al and Ti are anti-correlated relating to Si and Mg and K are anti-correlated to Ca, showing a strong decrease between 33 and 25 m. Thus, these elements do not reflect a signal of allogenic aeolian input. Higher amounts of Al (around 15 wt.-%) correspond with the increase of gyttja and thus with an increase of chemical weathering due to more precipitation.

In the Holocene core SM3, the elements Si, Ti, Al, K and Ca are the most prominent ones to characterize loess gyttja and dust bearing sediment. Si, Al and Ti show

	SiO_2 (Wt%) WD	Si - Int.	Si - Wt%	Si - At%
SiO2 (%) WD	1.00			
Si - Int.	*0.41*	1.00		
Si - Wt%	**0.69**	0.81	1.00	
Si - At%	0.53	0.74	0.97	1.00

	Na_2O (Wt %) WD	Na - Int.	Na - Wt%	Na - At%
Na2O (%) WD	1.00			
Na - Int.	***0.41***	1.00		
Na - Wt%	*0.20*	*0.11*	1.00	
Na - At%	*0.17*	*0.10*	1.00	1.00

	TiO_2 (Wt%) WD	Ti - Int.	Ti - Wt%	Ti - At%
TiO2 (%) WD	1.00			
Ti - Int.	**0.84**	1.00		
Ti - Wt%	0.70	0.86	1.00	
Ti - At%	0.71	0.82	0.98	1.00

	Cr (ppm) WD	Cr - Int.	Cr - Wt%	Cr - At%
Cr (ppm) WD	1.00			
Cr - Int.	***-0.32***	1.00		
Cr - Wt%	*-0.31*	*0.28*	1.00	
Cr - At%	***-0.32***	*0.33*	0.98	1.00

	Al_2O_3 (Wt%) WD	Al - Int.	Al - Wt%	Al - At%
Al2O3 (%) WD	1.00			
Al - Int.	0.66	1.00		
Al - Wt%	0.74	0.95	1.00	
Al - At%	**0.82**	0.91	0.98	1.00

	Ni (ppm) WD	Ni - Int.	Ni - Wt%	Ni - At%
Ni (ppm) WD	1.00			
Ni - Int.	***-0.21***	1.00		
Ni - Wt%	*-0.03*	*0.38*	1.00	
Ni - At%	*0.10*	*0.37*	0.94	1.00

	Fe_2O_3(t) (Wt%) WD	Fe - Int.	Fe - Wt%	Fe - At%
Fe2O3(t) (%) WD	1.00			
Fe - Int.	**0.95**	1.00		
Fe - Wt%	**0.95**	0.85	1.00	
Fe - At%	0.93	0.82	1.00	1.00

	Cu (ppm) WD	Cu - Int.	Cu - Wt%	Cu - At%
Cu (ppm) WD	1.00			
Cu - Int.	***-0.24***	1.00		
Cu - Wt%	*-0.18*	*0.05*	1.00	
Cu - At%	*-0.05*	*-0.15*	0.95	1.00

	MnO (Wt%) WD	Mn - Int.	Mn - Wt%	Mn - At%
MnO (%) WD	1.00			
Mn - Int.	**0.99**	1.00		
Mn - Wt%	0.98	0.98	1.00	
Mn - At%	0.98	0.97	1.00	1.00

	Zn (ppm) WD	Zn - Int.	Zn - Wt%	Zn - At%
Zn (ppm) WD	1.00			
Zn - Int.	***-0.35***	1.00		
Zn - Wt%	*-0.10*	0.60	1.00	
Zn - At%	*-0.01*	*0.46*	0.94	1.00

	MgO (Wt%) WD	Mg - Int.	Mg - Wt%	Mg - At%
MgO (%) WD	1.00			
Mg - Int.	**0.82**	1.00		
Mg - Wt%	0.72	0.77	1.00	
Mg - At%	0.79	0.81	0.99	1.00

	Sr (ppm) WD	Sr - Int.	Sr - Wt%	Sr - At%
Sr (ppm) WD	1.00			
Sr - Int.	*0.17*	1.00		
Sr - Wt%	*-0.34*	*0.28*	1.00	
Sr - At%	***-0.37***	*0.18*	0.98	1.00

	CaO (Wt%) WD	Ca - Int.	Ca - Wt%	Ca - At%
CaO (%) WD	1.00			
Ca - Int.	**0.98**	1.00		
Ca - Wt%	0.96	0.98	1.00	
Ca - At%	0.96	0.98	1.00	1.00

	Zr (ppm) WD	Zr - Int.	Zr - Wt%	Zr - At%
Zr (ppm) WD	1.00			
Zr - Int.	**0.78**	1.00		
Zr - Wt%	*0.39*	*0.02*	1.00	
Zr - At%	*0.24*	*-0.10*	0.96	1.00

Table 4.1: Correlation of the µXRF results (ED-XRF; Intensity, Wt.-%, At.-%) with WD-XRF (Wt-.%) results, both measured on the core DE3. In general, the main elements show the highest correlations, at least in comparison with the measured intensity values with the WD-XRF results. Italic printed values are not significant at the 0.05 level. Highest values of correlation are highlighted with bold letters.

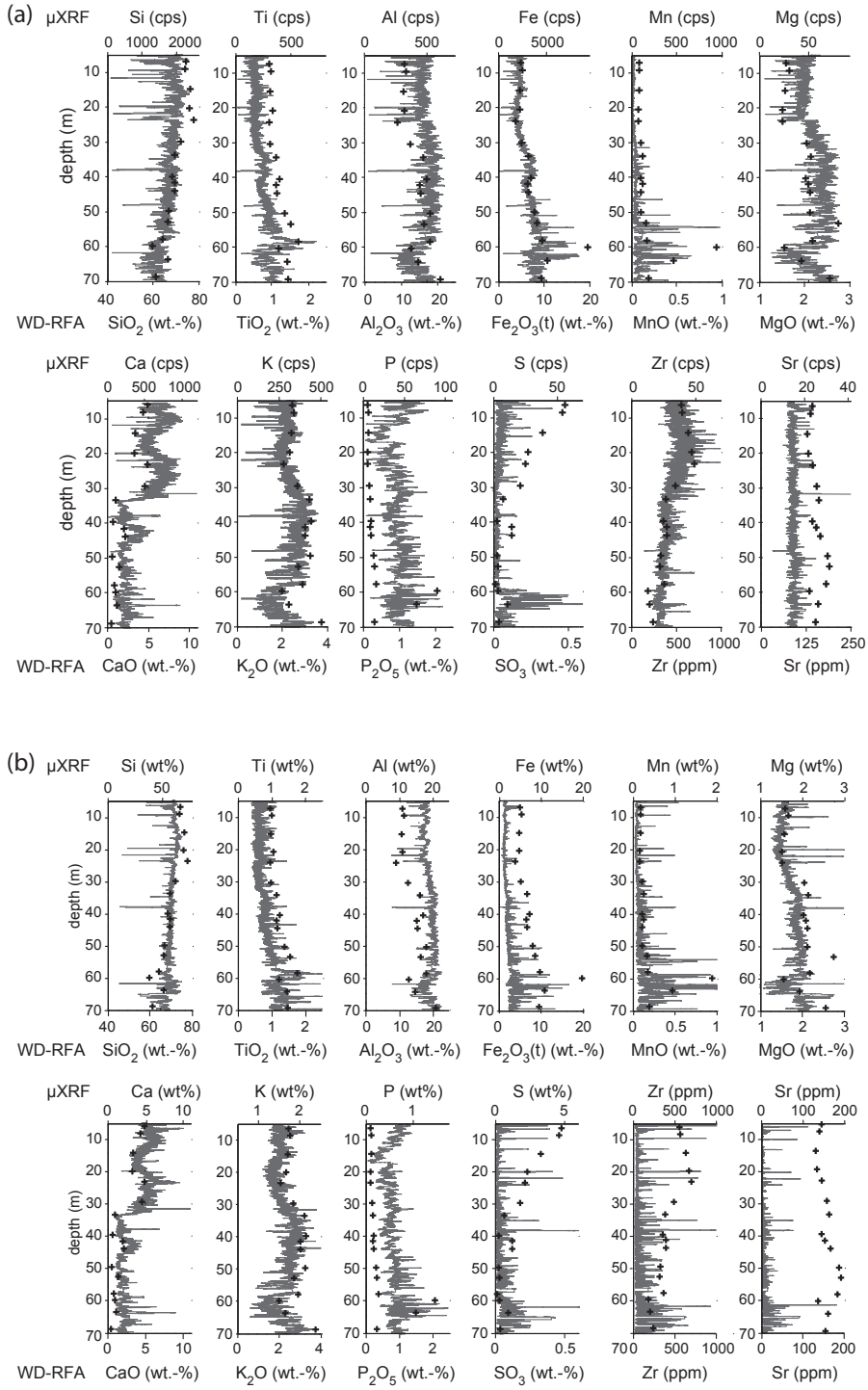

Figure 4.1: Continuous measured element concentrations of the core DE3 in (a) cps and (b) quantified (expressed as wt.-%) using fundamental parameter method (smoothed by a 50-point running mean filter) and measured with the Eagle III µXRF. Black crosses are corresponding results from WD-XRF, measured on discrete samples. Apart from Al all energy dispersive measured elements are underrepresented but show clearly covarying trends. High Ca and Zr values correspond to an increased dust content in the sediment. (Dietrich and Sirocko, 2009).

corresponding stratigraphic patterns over the whole core (Fig. 4.2). Highest intensities of these elements are significant for the uppermost core meter and the core section 6.3–12.0 m. The latter is characterized by quite stable intensities of these geogenic elements, corresponding with loess gyttja. SM3 is characterized by a highly correlated stratification of Mg and K, corresponding to the signal of Ti and Al. Ca shows significant peaks. In core SM3 certain amounts of Ca are in the layer 5.5–5 m and 7–6.3 m depth. The sections 2–1 m and 10–7.5 m are also enriched in Ca. Al, Ti and Mg reaches the highest level in the uppermost meters. Si, K and Ca are enriched in the deepest part of the core and coincide with the highest dust occurrence of the core. In core SM3 Zr shows a correlating trend to Si, Al and Ti, with maximum values around 2 m depth and from 6.5 m on down core. Sr peaks correspond to the major Ca peaks at 5 m and at 6.3 m. The latter peak represents the volcanic ash of the LST and also shows strongly elevated values of the major geogenic elements.

In both cores the elements Fe, Mn, S and P match to core sections with higher amounts of organic matter and reflect environmental conditions with changing oxygenation of the bottom water or changes of the redox potential at the lake bottom. Over wide parts Fe and P correspond to the Al signal. S is mostly anticorrelated to these elements. This accords with vivianite concretions which are found in the core DE3 between 40 and 70 m depth. The mineral vivianite, $(Fe)_3(PO_4)_2$*$8H_2O$, might be precipitated in the absence of sulphur, which would produce pyrite. In DE3 Fe, Mn and P have decreasing trends from the bottom to the top. Fe and Mn have corresponding trends. The Fe_2O_3(total) content increases from 10–5 wt.-%, with an extraordinarily high value of nearly 20 wt.-% at 60 m depth. The MnO content is low and also reaches a maximum of 1 wt.-% in 60 m. The highest values of S can be found at the same core sequence from 59 to 64 m depth. In this section the loss of ignition (LOI) is doubled from around 8 wt.-% to nearly 18 wt.-% (Tab. D.1). This section corresponds to the Greenland interstadial GIS-14, which is suggested to be the warmest interstadial of the last glacial cycle. The lowest levels of Fe and Mn are between 32 m depth and the top. A dip in their content is found between 40–46 m, the section where Ca and Zr are as well enriched as S. In SM3 the elements Fe, Mn, P and S stratify the core from bottom to top into four parts and S especially is anti-correlated to the geogenic elements: (1) the deepest section (up to 7 m depth) is quite stable and shows only low counts of these elements. (2) Strong increase of S with decreasing Fe values and stable counts of Mn and P follows from 6.5–5.2 m. (3) In the sequence from 5.2 to 2.2 m all these elements correlate with each other and S shows its maximum values. Indeed, this is the section with the highest amount of

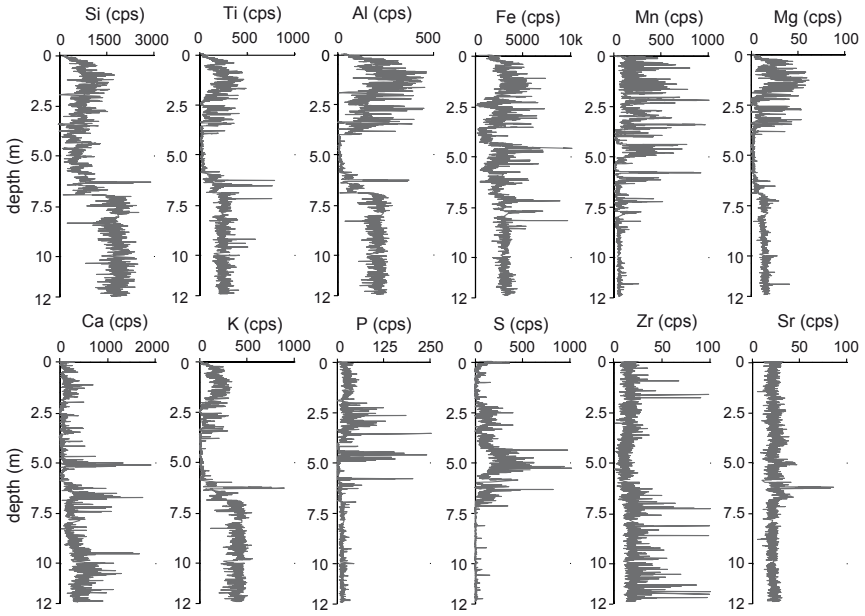

Figure 4.2: Continuous measured element concentrations of the core SM3 measured in cps (smoothed by a 5-point running mean filter). The distinctive split in a glacial (>7 m depth) and an interglacial part is clearly visible in the element concentrations of minerogenous elements. The LST at 6.3 m depth is characterized by distinct peaks of Si, Ti, Al, and K.

organics in the core SM3. (4) In the uppermost section Fe, Mn and P correlate, and S is nearly anticorrelated to the other elements.

4.3.3 From geochemical stratification towards a dust signal

PCA is applied to reduce the amount of variables and to achieve an integrated signal which corresponds better to the lithology of the sediment than the single element stratications. In both cores the first principle component factor (PC 1) illustrates the change from facies containing glacial and aeolian sediment to those which are characterized by organic gytta content (Fig. 4.3). The discrimination into these two lithological groups gives reliable results for SM3 and DE3, which is also indicated by the described variances of the PC 1. This dust factor accounts for 53.3% in DE3 and

for 56.9% in SM3, respectively (Tabs. 4.2–4.5). However, both cores show different factor loadings for the first variable. In core SM3 the main geogenic elements Si, Ti, and K represent those samples which are derived from minerogenic sediment, which is dominated by clear aeolian input in the lower core section. In SM3 Calcium is an additional element characteristic of loess gyttja, and is also the most prominent element in core DE3. The interpretation of the second PCA variable (PC 2) is more difficult, because of even larger differences between the single cores. In SM3 the PC 2 includes variables with high factor loadings on typical limnogenic and redox-sensitive elements like Mn, Fe, and P. High values of P are provided by oxic decay of organic matter. Fe and Mn can be used to indicate the redox conditions of the lake water (Engstrom and Wright Jr, 1984). When the lake is under anoxic conditions, Fe and Mn are present in soluble form and are easily released from the sediment. In DE3 the geogenic elements are the major contributors to PC 2. These elements are common constituents of primary minerals. Thus PC 2, with high factor loadings on geogenic elements reflects, the intensity of chemical weathering and leaching in the watershed and shows positive values from 35 m depth down the core in DE3.

Table 4.2: Correlation matrix of main elements (core De3 measured intensities by µXRF). Italic printed values are not significant at the 0.05 level.

	Mg	Al	Si	P	K	Ca	Ti	Mn	Fe
Mg	1	0.88	0.10	0.43	0.77	-0.48	0.56	0.29	0.58
Al	0.88	1	0.52	0.38	0.80	-0.24	0.28	0.05	0.29
Si	*0.10*	0.52	1	-0.15	0.40	0.40	-0.40	-0.45	-0.42
P	0.43	0.38	-0.15	1	0.11	-0.21	0.25	0.40	0.35
K	0.77	0.80	0.40	*0.11*	1	-0.27	0.20	0.00	0.28
Ca	-0.48	-0.24	0.40	-0.21	-0.27	1	-0.72	-0.54	-0.82
Ti	0.56	0.28	-0.40	0.25	0.20	-0.72	1	0.59	0.88
Mn	0.29	*0.05*	-0.45	0.40	*0.00*	-0.54	0.59	1	0.79
Fe	0.58	0.29	-0.42	0.35	0.28	-0.82	0.88	0.79	1

Summarizing these results one can identify that analysis of the first principal component separates glacial and aeolian dominated sediment from interglacial/interstadial organic-rich matter. However, in each core the elements with highest loadings differ in the respective factors. In SM3 the geogenic elements are those which characterize the first PC. In the core DE3 the geogenic elements describe the second PC,

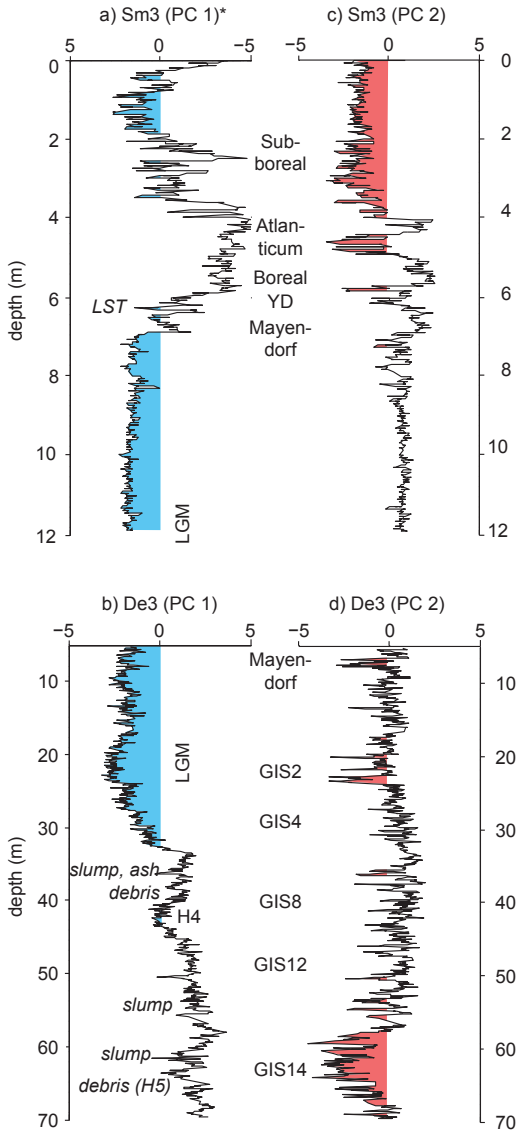

[ht]

Figure 4.3: The first two principal components PC 1 and PC 2 of each core are shown versus the depth (see tables 3b, 4b for associated factor loadings). (a, b) PC1 isolates a signal of minerogenic glacial/aeolian transported sediment (shaded in blue). Aeolian sediments have negative values in the core DE3 and positive ones in the core SM3, respectively (*For a better visualization the x-axis of (b) is inverted). (c ,d) PC 2 in both cores has in common that they have negative values during warm/humid climate conditions (red color). However, in core SM3 PC 2 is characterized by highly redox-sensitive elements (see text). PC 2 of core DE3 depends strongly on elements which indicate enhanced chemical weathering.

Table 4.3: Factor loadings after PCA calculation of main elements (core DE3 measured intensities by µXRF), including Eigenwert (Eigen.), the described variance (dVar.) and the cumulative sum of dVar (% Cumul). Bold printed values ($\geq |0.4|$) have a major influence on the single principle components.

	PC 1	PC 2	PC 3	PC 4	PC 5	PC 6	PC 7	PC 8	PC 9
Eigen	4.27	2.55	0.93	0.45	0.33	0.29	0.12	0.04	0.01
dVar.	53.3%	22.4%	9.2%	5.2%	4.6%	3.8%	1.0%	0.6%	0.1%
% Cumul.	53.3%	75.7%	84.9%	90.1%	94.7%	98.4%	99.4%	99.9%	100%
Mg	0.21	0.34	-0.10	0.11	-0.15	0.20	**-0.60**	-0.25	**0.59**
Al	0.10	0.39	-0.13	0.01	-0.09	-0.09	**-0.44**	-0.10	**-0.77**
Si	-0.22	**0.54**	0.00	**-0.48**	0.08	**-0.59**	0.14	0.01	0.22
P	0.17	0.06	**-0.81**	0.38	-0.13	-0.24	0.28	0.09	0.06
K	0.14	**0.63**	0.12	0.14	0.21	**0.53**	0.39	0.27	-0.02
Ca	**-0.48**	0.00	-0.38	**-0.44**	**-0.40**	**0.49**	0.10	-0.17	-0.05
Ti	**0.49**	-0.02	0.18	-0.26	**-0.70**	-0.06	0.08	**0.40**	0.01
Mn	0.36	-0.19	-0.35	**-0.53**	**0.50**	0.16	-0.22	0.32	0.01
Fe	**0.50**	-0.02	0.02	-0.21	0.05	0.02	0.36	**-0.75**	-0.07

whereas Ca and Si are the most important elements for classification of the glacial sediment in PC 1. On the other hand redox-sensitive elements like Mn and P have high loadings in PC 2 for core SM3 and are an indicator for the redox conditions at the lake bottom, with contemporaneous high amount of organic matter. The other factors do not influence aeolian sediment input into the maar lake and account only for a lower percentage of the total variation. In addition, the result of the scree test suggests using the first two factors, only. Consequently, they are of minor interpretative use for this study and not further considered.

4.4 Discussion

For the derivation of paleoclimate or economic conditions from geochemical data two assumptions must hold true (Boyle, 2001): (1) At any one time the sediment concentration must be proportional to the external element loading and (2) the element concentrations in the sediment must not change after burial. The latter is in discussion especially as regards the role of Mn and Fe reduction in potential remobilization

Table 4.4: Correlation matrix of main elements (core Sm3 measured intensities by µXRF). Italic printed values are not significant at the 0.05 level.

	Mg	Al	Si	P	K	Ca	Ti	Mn	Fe
Mg	1	0.88	0.59	0.47	0.75	0.42	0.85	0.08	0.54
Al	0.88	1	0.67	0.52	0.81	0.40	0.89	0.02	0.48
Si	0.59	0.67	1	0.07	0.85	0.66	0.74	-0.35	0.50
P	0.47	0.52	*0.07*	1	0.12	-0.16	0.30	0.60	0.38
K	0.75	0.81	0.85	*0.12*	1	0.69	0.94	-0.31	0.56
Ca	0.42	0.40	0.66	-0.16	0.69	1	0.61	-0.32	0.41
Ti	0.85	0.89	0.74	0.30	0.94	0.61	1	-0.14	0.57
Mn	*0.08*	*0.02*	-0.35	0.60	-0.31	-0.32	-0.14	1	0.25
Fe	0.54	0.48	0.50	0.38	0.56	0.41	0.57	0.25	1

of trace elements. Boyle (2001) has shown that post depositional alteration and migration is likely, but that this is only significant at extremely low sediment mass accumulation rates and is not likely for high glacial sediment yields. Thus we suggest that the elicitation of a dust signal within maar lake sediments is possible by application of inorganic geochemistry. However, wider knowledge about the lake's regional setting (location, morphology, presence of inflows, etc) is necessary. Thus, additional information from other proxies is required. This is shown in this study, since all cores show different inorganic geochemical reactions to environmental changes dependent on the regional setting. An example is the stratification of the geogenic elements in core SM3: All of these elements have a major influence on PC 1, but only the typical aeolian dust elements Si, Ca, and K have their highest values during glacial conditions.

The results show that there are three different groups of main elements which characterize the sediment.

1. Typical geogenic elements are magnesium (low differentiated volcanic products), potassium (low differentiated volcanic products), titanium and aluminum (lithics, feldspars). In oligotrophic lakes silica, aluminum as well as titanium and potassium represent the clastic input. This is clearly shown for all the cores. The alkali metal K and the alkaline earth metals Ca and Mg are major bedrock constituents. High amounts of these elements represent reduced soil stability and increased erosion. But Ca and Mg might have also significant con-

Table 4.5: Factor loadings after PCA calculation of main elements (core SM3 measured intensities by µXRF), including Eigenwert (Eigen.), the described variance (dVar.) and the cumulative sum of dVar (% Cumul). Bold printed values ($\geq |0.4|$) have a major influence on the single principle components.

	PC 1	PC 2	PC 3	PC 4	PC 5	PC 6	PC 7	PC 8	PC 9
Eigen	5.144	2.0437	0.7322	0.3646	0.2889	0.2024	0.1461	0.0553	0.0227
dVar.	56.9%	23.8%	7.5%	3.8%	3.2%	2.2%	1.7%	0.6%	0.3%
% Cumul.	56.9%	80.8%	88.2%	92.0%	95.2%	97.5%	99.1%	99.7%	100%
Mg	0.39	-0.18	-0.19	-0.31	-0.33	0.13	0.72	-0.20	0.08
Al	**0.42**	-0.16	-0.34	-0.10	0.01	-0.18	-0.15	0.78	0.05
Si	0.36	0.20	0.06	**0.45**	0.33	**-0.60**	0.30	-0.13	-0.21
P	0.16	**-0.60**	-0.15	0.18	**0.62**	0.36	-0.03	-0.19	0.06
K	**0.42**	0.15	-0.03	0.08	-0.13	-0.08	-0.39	-0.34	0.71
Ca	0.30	0.32	**0.56**	**-0.50**	**0.44**	0.19	0.05	0.13	0.02
Ti	**0.43**	0.01	-0.11	-0.14	-0.20	0.11	**-0.45**	-0.31	**-0.66**
Mn	-0.06	**-0.63**	**0.44**	-0.29	-0.12	**-0.53**	-0.12	-0.09	0.02
Fe	0.25	-0.16	**0.55**	**0.55**	-0.36	0.34	0.05	0.25	-0.03

centrations in authigenic carbonate and skeletal carbonates from invertebrates. The supply of conservative cations K (and also Na) increases with periods of rapid chemical erosion, similar to Ti. These elements are thus enriched during the Holocene and MIS-3 and only minor during MIS-2, when the climate was more arid.

2. Sulphur and phosphorous are limnogenic and redox-sensitive elements and thus the precipitation and release processes are complex. The deposition and conservation of the elements Fe, Mn, S, and P is strongly controlled by pH and redox conditions at the lake bottom (Engstrom and Wright Jr, 1984). Since maar lakes usually have anoxic bottom water reduced Fe(II) precipitates in combination with S, forming the mineral pyrite (FeS_2). Blue colored vivianite crystals, a ferrous phosphate, occur with increased burial of undecomposed organics(Gächter and Müller, 2003). High rates of organic matter deposition occur only during interstadials and interglacials. A second prerequisite for the formation of vivianite is the presence of orthophosphates which are provided by oxic decay. Thus,

the occurrence of vivianite in organic rich sediment sections is not a proxy for paleoproductivity (Fagel et al., 2005). It is an indicator of at least temporary deep circulation and high organic production (Voigt et al., 2008) and clearly precedes the formation of sulphides in the course of eutrophication (Gächter and Müller, 2003). From Lake Jues (Harz Mountains, Germany) Voigt et al. (2008) reported that the accumulation of massive vivianite may have prevented the cycling of phosphorus and hampered the establishment of a rich trophic system. We also suggest similar processes for the lakes of the Eifel area. The presence of pyrite shows on the other hand the level of aeration of the maar deep water and the occurrence of a monimolimnion, with anoxic water conditions for at least a period of several mixing cycles. Vivianite is found in the cores with a high content of Phosphorous in the DE3 47.7–50 m and at 70.7–72.7 m depth, in particular.

3. The third class is a mixed type: Silicon represents minerogenous SiO_2 in the clastic fraction as well as amorphous and autogenic SiO_2 production, mainly from the silicon shell of diatoms. Calcium is a major constituent of aeolian dust sediments (with provenance of the Devonian or Triassic limestone). Further reasons for high contents of Ca are the precipitation of $CaCO_3$ caused by a deficit of CO_2 in the lake water, and biogenic calcium precipitation e.g. in the lime shell of ostracods. Authigenic carbonates were not observed during glacial periods in the core DE3 (Dietrich and Seelos, 2010) and we suggest that this also applies to other glacial sequences. During times of dominant physical weathering $CaCO_3$ grains will be transported to the lake and most of them should quickly reach the lake bottom without significant in-lake chemical reaction (Koinig et al., 2003). Thus, we suggest that the content of calcium has not changed during settlement under glacial conditions and can be interpreted as a major contributor to the measured dust signal. However, a stack of the elemental stratification of different cores does not seem to be appropriate. The influence of the catchment and different biogeochemical processes in the lake water and bottom makes each maar lake unique, which is reflected in the distribution of the elements.

The focus of this study is on the detection of aeolian sediments by µXRF scanning and PCA. It is shown that the methodology gives reliable results within acceptable error margins but still needs additional information, at least from facies and microfacies analysis. However, in this study time slices including major climate changes

of the last glacial were used to evaluate this approach and are already discussed in early ELSA publications: e.g. the late Weichselian glacial inception and Heinrich events during MIS-3 and 2 (Dietrich and Seelos, 2010), transition I, the Younger Dryas and internal variability of the Holocene (Dietrich and Sirocko, 2009). A major finding of this study is that the previously used approach demonstrates weaknesses in comparison to high resolution grain size analysis, which was used in the cited publications by applying the RADIUS technique (Seelos and Sirocko, 2005). For example, the variability of MIS-2 dust sources could only be shown by a combination of mineralogical/geochemical analysis and grain size sorting parameters (Dietrich and Seelos, 2010). However, the transition into the glacial climate state is shown within an abrupt trend towards negative values of PC 1 in the core DE3. This signal is highly correlated to the dust detection for the same core published as the ELSA dust stack (Fig. 4.4). The timing of increased dust transport towards the Eifel maar lakes corresponds with the global decrease of sea-level 35 kyrs ago (Clark et al., 2009). An increased east wind frequency for Western Europe was suggested by Dietrich and Seelos (2010) for the time slice between 33 and 24 kyrs BP. These layers are enriched in aeolian transported carbonate grains in the same sediment core, DE3. Since Ca has a major influence on DE3's PC 1, these layers are also reflected in PC 1 (Fig. 4.4d, e). In addition a severe cold phase which corresponds to the strong Heinrich event H4 (Hemming, 2004) is detected by the PCA approach. Another major dust event correlates with H5 (Seelos and Sirocko, 2009) which is reworked by debris in the core DE3 at 65 m depth, and thus could not be shown by the applied approach.

The younger sediment sequence shows in core SM3 the major climate change from the last glacial to interglacial conditions of the Holocene. Fast environmental changes from the last glacial to the interglacial including the YD are also documented in this core. However, the tephra of the lake Laach eruption also shows negative factor scores and is wrongly classified by the PCA as glacial and aeolian sediment. PC 1 shows a high variability during the Holocene, which is also shown in the lithology and in the grayscale values of the core (Fig. 4.4). The strong shifts in the aeolian sediment proxy of the Holocene (especially the Atlanticum) might also be influenced by changing lake levels during the Holocene. Correlations between the North Atlantic IRD events defined by Bond et al. (1993) and lake level changes in mid-European lakes have been pointed out (Magny, 2004, 1999; Friedrich et al., 1999), supporting the hypothesis that changes in solar activity have been an important forcing factor in the Holocene climate (Renssen and Isarin, 2001). A pronounced Ca peak corresponds to the time of the strong cold spell during the 8.2-ka-event. This event is only minor correlated

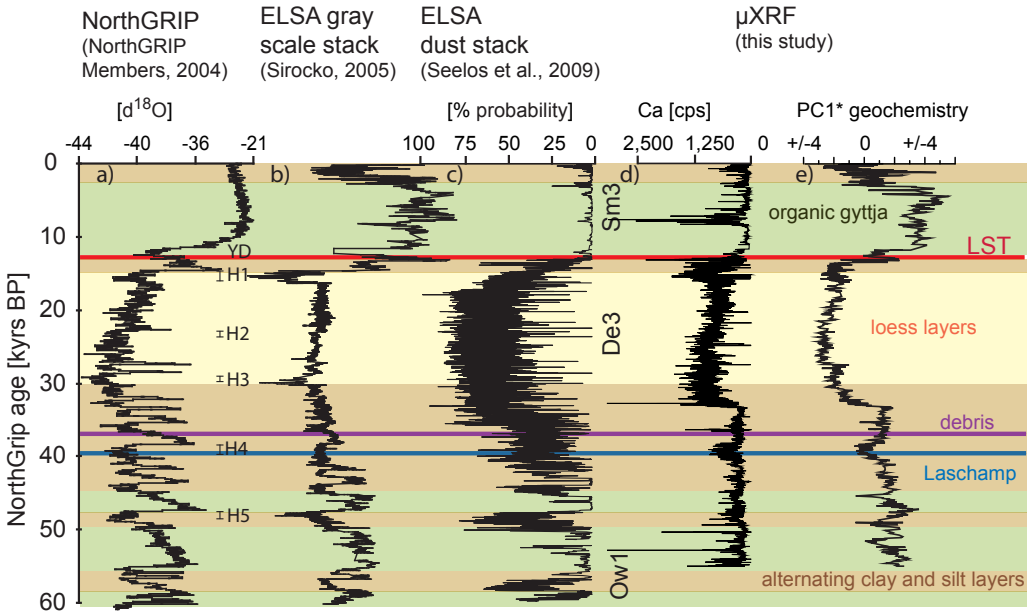

Figure 4.4: µXRF geochemistry stacks versus the time, (a) NorthGRIP d^{18}O record, (b) the ELSA grayscale stack, (c) the ELSA dust stack, and major litho zones of the last 60 kyrs. Ca (d) as well as the PCA stack (e) clearly shows the influence of aeolian sediment (* The SM3 part of the PC 1-stack is inverse; see Fig. 4.3). Heinrich events after Hemming (2004).

with an enhanced dust input in the Eifel area (Seelos and Sirocko, 2009). Here, we suggest that a strong ventilation of the bottom water has led to the precipitation of carbonate minerals. However, Prasad et al. (2009) suggested temperature to be the primary control on calcite formation. These authors focused on seasonal carbonate precipitates in the sublayers of single warves and found distinct minima of calcite during the 8.2-ka-event which were used as an proxy for cold summer temperatures. In deed, the calcium maximum in SM3 is not continuously on a high level when looking at high resolution µXRF scans, but also shows several phases with minimum values (not shown). The major impact of the 8.2-ka-event on the environment of Central Europe is also shown in many other records beside lake sediments, e.g. in reduced tree-ring widths from Central German oaks (Friedrich et al., 1999). In general, the deposition of aeolian dust plays only a minor role during the Holocene. The elements Al, K, Ti have the highest factor loadings in PC 1 of SM3 and reflect soil destabilization which

goes along with erosion and enhanced dust transport during the glacial stadium. Until the Boreal the environment is characterized by more open landscapes and high physical weathering. These conditions change within the Atlanticum when conditions changed to a warmer and more humid climate. As a result, the soils became more stabilized and the slopes were covered by dense forests. Human activities in the catchment are traced back to ca. 15.5 kyrs BP, long before late glacial warming ca. 14.7 kyrs BP (Street et al., 2006), but became most pronounced around 3,700 yrs BP (Sirocko, 2009). Deforestation, grazing, and agriculture caused an increase in erosion and physical weathering and thus enhanced deflation of dust. Since then the dust signal in the lake Schalkenmehrener Maar is mainly anthropogenically determined.

4.5 Conclusion

This study investigates whether the detection of aeolian sediment by µXRF scanning of resin impregnated sediment samples with a subsequent PCA approach give reliable results. Changes of aeolian supply over time are suggested in the inorganic geochemistry data, especially in Ca, Si, and the first new calculated PCA factor (PC 1) which is mainly influenced by Ca, Si, and Ti. It is demonstrated that this approach works well since, for the interpretation, further knowledge about the lithology and environmental background is available. The signal of geochemical aeolian proxies might be influenced by autochthonous and allochthounous accumulation changes and without further knowledge and necessary inter proxy comparison the results might be inconsistent or difficult to interpret. Thus, the detection of dust using high resolution grain size analysis is advantageous, because this approach recognizes different transport mechanisms of the sediment and is so far the only method which is able to quantify the content of aeolian dust in sediment. µXRF is a fast and inexpensive scanning method of the elemental stratification within sediment cores. In addition, the quantification of the main elements via a standardless fundamental parameter method gives significant results in comparison to the reference samples, which are measured by WD-XRF. Thus, a calibration of the µXRF results is reliable, if this evaluation is based on at least a reference sample for each litho zone.

Cores SM3 and DE3 show both fully glacial sediment and warm and wet climate conditions and the major dust deposition events and phases could be detected by µXRF geochemistry. These include the largest Heinrich event H4 during MIS-3, the onset of dust increase coupled to the growing of the Scandinavian Ice sheet, later on the whole MIS-2 including LGM, the YD as well as enhanced dust supply by human

activities since the Subboreal. In the applied PCA approach PC 1 discriminates in both lake sediment cores aeolian from non aeolian material. Volcanic ash and tephra is mostly classified as aeolian sediment because of the major influence of geogenic elements (Si, Al, Ti, K and mostly Ca) to PC 1. Ca has a major influence on the dust signal in both cores and a combination of Ca with the grayscale values gives the best signal of aeolian sediment. The occurrence of vivianite coincides with enriched amounts of P and Fe in organic rich gyttja and is thus suggested as a proxy for low sedimentation rates during interstadial climate conditions. In summary, µXRF scanning of bulk geochemistry has shown to be a sensitive indicator of both changes in the lake and in its (aeolian) catchment, if it is used together with other proxy data such as micro facies or grain size analysis.

4.6 Summary of chapter 4

Data for the annual variability of aeolian sediments is obtained from continuous and high resolution µXRF geochemistry within maar lake sediments from the last 60 kyrs. Two sediment cores from Eifel maar lakes and dry maars (Germany) were analyzed, covering the glacial inception of MIS-3, LGM and MIS-2 and transition I as well as the Holocene. The energy dispersive XRF scanning is obtained on resin impregnated blocks of the sediment, which are the basis for the production of petrographic thin sections. Thus, the measurement results can directly be compared with micro facies analysis.

Quantification of the Eagle III µXRF carried out on one sediment core, using the standard free fundamental parameter method, shows that this quantification method gives suitable results by comparison with WD-XRF analysis of discrete samples. Each maar differs in lithological composition, which is reflected in the geochemistry. The major processes of element deposition in lakes are therefore described, i.e. the different sedimentation and weathering processes as well as the circulation of the water body of the lake. Following on from this, it is shown that it is possible to derive an aeolian sediment signal by using principle component analysis of standardized variables. Because further knowledge about the lithology and environmental background is available (from the petrographic thin sections) it can be demonstrated that this principle component analysis approach gives reliable results for all the time slices investigated. The most prominent element for describing dust in both investigated cores is Ca, which reaches highest values (>5 wt.-%) during glacial conditions and which has a major influence on the dust factor obtained by principal component anal-

ysis. In combination with grayscale values both the Ca content and the dust factor, calculated by principal component analysis, serve to record aeolian dust in laminated lake sediments. In both cores periods with major dust events could be detected by µXRF geochemistry: during MIS-3 the largest Heinrich event H4 and the onset of dust increase coupled to the glacial inception of the Pleni-Weichselian, further on the whole MIS-2 including LGM and YD as well as enhanced dust supply generated by human activities since the Subboreal.

Chapter 5

The reconstruction of easterly wind directions for the Eifel region (Central Europe) during the period 40.3–12.9 ka BP [1]

5.1 Introduction

The climate situation in Central Europe during the Last Glacial Maximum (LGM) and the Late Pleniglacial is characterized by high wind activity and relatively low precipitation (Huijzer and Vandenberghe, 1998; Hatté et al., 1998). This conclusion is based on a comparison of proxy data and climate simulations. The sources of generating proxy data include relict dune forms in Central Belgium (Vandenberghe, 1991) and Poland (Godzik, 1991), grain size trends of cover sand and loess in the Netherlands (Van Huissteden et al., 2001), provenance analyses by heavy mineral composition (Krook, 1993) and wind polished rock surfaces (Christiansen, 2004; Christiansen and Svensson, 1998; Vandenberghe et al., 1999). The balancing of these data with climate model results allows wind direction reconstruction for Central Europe for the LGM and the Late Pleniglacial (Renssen et al., 2007). This combination of meteorological simulations and proxy data shows that the Late Pleniglacial and the LGM were dominated by westerly to north westerly wind directions due to the location of the study area in the mid latitudes. The same situation is postulated for the Younger Dryas, the so called Heinrich-0 event (Isarin et al., 1997). Brauer et al. (2008) have shown an abrupt increase in the strength of the westerlies during the Younger Dryas at the Meerfelder Maar in the Eifel region. Both models confirm the possibility of

[1] A slightly modified version of this chapter has been published as Dietrich and Seelos (2010) in the journal Climate of the Past (Clim. Past). Copyright 2010 European Geosciences Union.

a higher number of east winds during the modeled periods. Another simulation reconstructs the atmospheric circulation over the North Atlantic and Eurasia during the Heinrich event H2 (Hostetler et al., 1999). This model separates the H2 into three different phases of climate conditions. The variables are the thickness of the Laurentide ice sheet and the Sea Surface Temperature (SST) in the North Atlantic. According to Hostetler et al. (1999) the second phase, a combination of a lowered ice sheet thickness and an increased post-surge SST during the winter simulation, shows a high pressure cell over Europe, which implies a higher concentration of north-east winds. During the third phase, with an increasing Laurentide ice sheet thickness and decreasing SST, the high pressure cell over Europe becomes stronger again.

All presented proxy data mirror the paleo wind directions during Marine Isotope Stage (MIS) 2 very well. The question is whether they are qualified to be the basis for simulations at a very high temporal resolution. Regarding the data, the main disadvantage of using sand dune orientations for wind direction reconstructions is the fact that only the last phases of deposition are represented on top of the dune. In contrast, wind polished rocks represent the main wind direction over a long period, but hide the variations of wind direction in time. The analyses of grain size trends over a transect of dunes carry information about the paleo wind direction and sometimes also about the wind strength. But these techniques assume free transport paths over the surface without disturbance of topographic barriers (Schwan, 1988). Provenance analyses by heavy minerals or other index materials are very useful, if the potential sources of sediment are well known and the distance to the deposition areas is not too great. Mostly the river sediments that cross the northern part of Central Europe show typical fingerprints and can be used for wind direction reconstructions.

In addition to the availability of adequate proxy data, the question of the quality of climate models in respect of their resolution in space and time must be discussed. Small scale variances of topography and vegetation are not reproduced by low resolution atmospheric simulations. For example the ECHAM wind direction simulation for the Late Pleniglacial and the LGM (Renssen et al., 2007) has a horizontal resolution of 2.8°. This means that the complete area of Denmark is represented by only one seawater grid cell, but for the Netherlands and Poland the model allocates land cells. Because of the different physical parameters of land and sea cells, the model results for Denmark, the Netherlands and Poland are not comparable to each other. A slightly higher horizontal resolution of 2° is given by the GENESIS AGCM simulations of the atmospheric circulation during H2 (Hostetler et al., 1999). The most current modeling approach is carried out by Sima et al. (2009) with the LMDZ at-

mospheric circulation model (spatial resolution 60 km). Model results from this dust emission model show a proportional increase of east wind during Heinrich events in comparison to Greenland Stadial (GS) or Greenland Interstadial (GI) periods.

In this study we will show a continuous record of changing wind directions during the Late Weichselian. Because of the complexity of time transient atmospheric simulations, it would be helpful for climate modelers to get high resolution and continuous data of paleo east wind proxies in order to find interesting time slices for simulations. Such data could be used in future specific simulation runs.

5.2 Methods

The sediment core DE3 for this study comes from the Dehner dry maar, which lies in the northwest of the western Eifel volcanic field, north of the town of Reuth (Germany). DE3 is part of the ELSA (Eifel Laminated Sediment Archive) dust stack (Seelos and Sirocko, 2009). The dry maar is located on the west side of a large carbonate basin that crosses the region in a north-south alignment (Fig. 5.1). There are no nearby carbonate sources to the west of the Dehner dry maar. The nearest carbonate source to the west of the Dehner dry maar are cretaceous units near Liège or Aachen, which lie over 60 km to the NW. The nearest limestone units are Triassic outcrops in the Meuse valley (130 km to the west). All other maar lakes which are part of the ELSA are located within or at the east of the basin. Although it silted up approximately 12,000 years ago, the maar is still recognizable in the landscape. It has a diameter of 950 m and lies at an elevation of 565 m a.s.l. at the crest of a hill. The maar basin is round and does not display any recognizable past inflow, though there is an outflow to the south. Thus, the Dehner dry maar fulfills the morphological criteria to be suitable to conserve storm sediment layers (Pfahl, 2009).

Our east wind dataset depends on provenance analyses of wind transported carbonates. The continuous record is 39 m long, spans the time period 40.3–12.9 ka and has a sample interval of 500 µm. Using this high resolution the particle detection algorithm of RADIUS (Seelos and Sirocko, 2005) allows the measurement of single particle diameters.

5.2.1 Lithology and stratigraphy of core DE3

In all its fine-grained sections the DE3 core has a predominantly reddish tone, with sub-sections which are yellow and always composed of silt-sized dust particles that

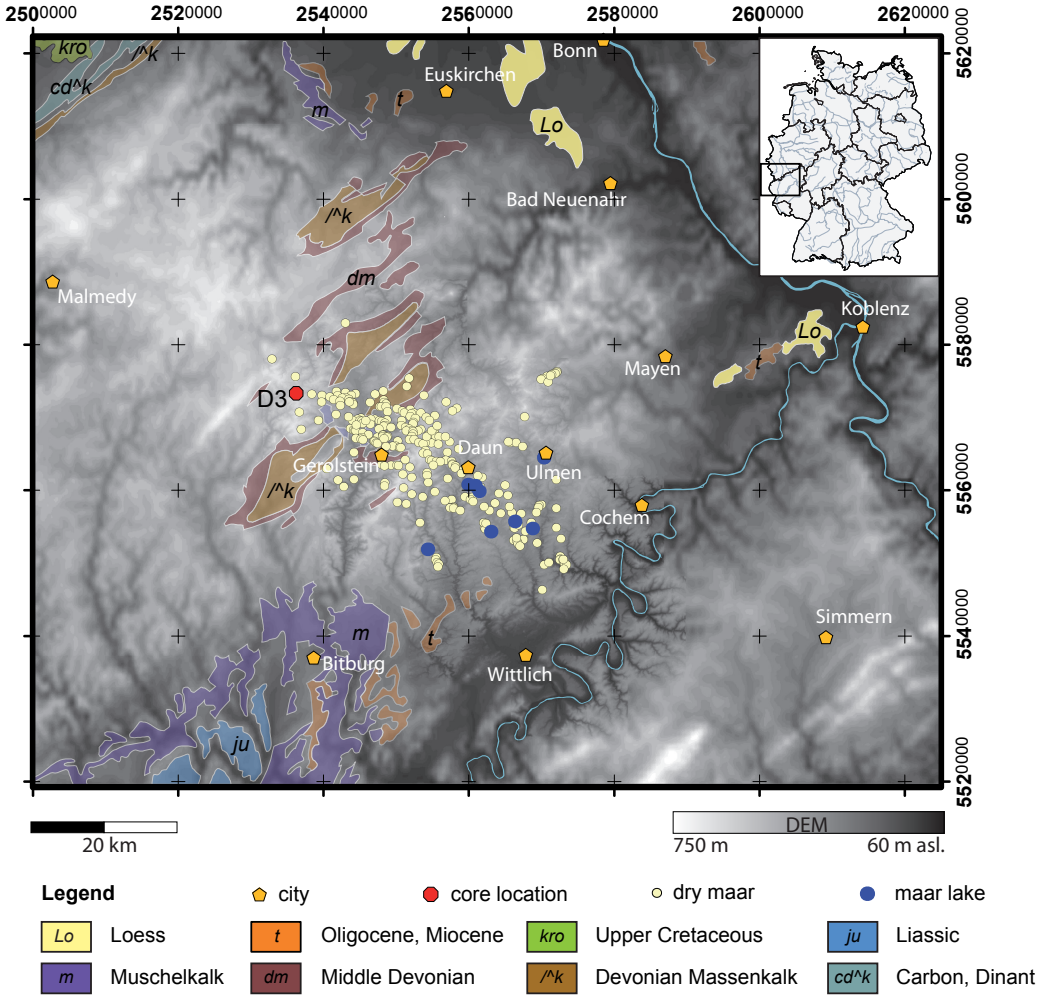

Figure 5.1: Geological sketch map and elevation model of the Eifel region, including the calcareous rocks, such as the limestone bearing "Kalkmulden" in the Eifel N-S-zone, loess deposits and the locations of Maar lakes and dry maars after Büchel (1994). The map is based on the Geological Map of Germany 1:1 000 000 (BGR 2002), GCS Deutsches Hauptdreiecksnetz, Gausszone 2, Bessel 1841. Location of the sediment core DE3 from the ELSA dust stack (see text) is marked with a red dot.

was blown in from the wider surroundings. The core photograph (Fig. 5.4) shows these two dominant colors, the yellow, loess-rich defining cold periods, the red tone-defining warm periods. The black colored sections are composed of singular,dm-thick volcanic ash layers. The uppermost three meters are composed of solifluction debris.

The age model for the core DE3 is based on ^{14}C-dating, tephrachronology and tuning to the ss09sea stratigraphy of the NGRIP ice core (NorthGRIP Members, 2004). The chronology is supported by radiocarbon dates (chapter 3.1.3) as well as geochemical evidence for the Laacher See Tephra at 3.49 m depth, which gives an age of 12.9 ka (van den Bogaard, 1995) and will be published by Sirocko et al. (prep).

The 39 m long core sequence (3–42 m depth) represents a period from 40.3 to 12.9 ka, and thus covers the late MIS-3, the transition into the MIS-2, the Late Pleniglacial, and Bølling/Allerød. The core sequence is event laminated and there is no evidence for a hiatus, with the exception of a slide between 37–36 m depth. The deepest section of the illustrated core is dominated by gyttja. Beginning at a depth of 38 m (36 ka), the content of homogeneous dust sediments increases rapidly and reaches the absolute maximum between 26–10 m depth, which represents the last glacial maximum. The organic content is very low during this period and increases once again with the Bølling transition 14 ka (Seelos and Sirocko, 2009).

5.2.2 The RADIUS east wind module

In the ELSA core DE3 the content of dust and carbonates (20–63 µm) carries information about the provenance of the windblown particles. Wind transported carbonates are detected in layers as single grains within the dust sections with the same grain size as the non-carbonate dust components. Authigenic carbonate particles are not detected by the algorithm used. The authigenic carbonate production in the maar lakes during the observed dry and cold period is very low. To reconstruct information about the dominant wind directions for the Eifel region, we analyzed the ELSA core sequence DE3 (Dehner dry maar, Fig. 5.1) for content of carbonates and loess.

The particle analysis method RADIUS (Rapid Particle Analysis of Digital Images by Ultra-high-resolution scanning of thin Sections, (Seelos and Sirocko, 2005)) was developed to analyze and identify the different sediment structures in sediment cores, especially for cores of the ELSA (Sirocko et al., 2005). The application allows the detection of climate controlled sedimentation processes like storm events under cool and dry conditions or finely laminated sequences during warm periods and spontaneous events like volcanic eruptions, slumps and turbidities (Seelos and Sirocko, 2009). The

procedure is based on digital image analysis of single particles at a 200 µm interval. Thus aggregates are separated into single components. The lower detection limit is around 10 µm . The thin sections were scanned with 20x magnification under cross polarized light.

To analyze the paleo east wind layers, we developed a new software module, which uses the ELSA dust stack results and combines them with a carbonate detection algorithm. The carbonate tool is a self-contained software module of RADIUS, based on an adapted color detection algorithm to measure the content of carbonates.

It is not possible by means of digital image analysis to measure a percentage by weight but an area ratio. A calibration study is applied on twelve artificial samples with known content of carbonate particles (Fig. 5.2). The carbonate particles used consist of ground Devonian limestone from the Eifel-N-S-zone. The loess material is taken from the core DE2, a neighbor core of DE3. The carbonate content of the loess is removed by boiling with hydrochloride acid. Different thin sections with a carbonate content of 0–80 wt.-%, with finer increments in the low carbonate content range, are analyzed by application of the RADIUS method, using the same setting as for scanning the original samples. Different parts of the samples were scanned five times for an error estimation. The measured results of the area content of the carbonate particles is plotted versus the weight percentage. The calculated correlation coefficient R^2 of 0.94 indicates the reliable classification of bright and carbonate particles.

The algorithm of the RADIUS east wind is applied using the same parameters for the whole core section and works in the following way (Fig. 5.3). In the first step the sediment is analyzed to identify, whether a dust sequence exists, which is defined as such if the probability of a dust event is higher than 70%. If the content of carbonates in the grain size class of 20–63 µm within such a detected dust sequence is higher than 2% we assume east winds. The wind crossed the carbonate basin and limestone particles were caught up and subsequently deposited in the Dehner dry maar. This fixed combination of dust and carbonate detection results prevents misinterpretations arising from authigenic carbonate productivity in the lake. If the climate situation changes to warm and wet conditions, the content of dust decreases at the same time and the wind detection algorithm is set to zero. The east wind frequency is calculated for fixed 100 years intervals by measuring the relationship between the thickness of carbonate containing layers (east wind layers) and layers below the threshold (west wind layers) in percent. The frequency analysis (100 year bins) depends on the continuous age depth model and all single 500 µm segments that show east wind sediments are summed after the time correlation procedure.

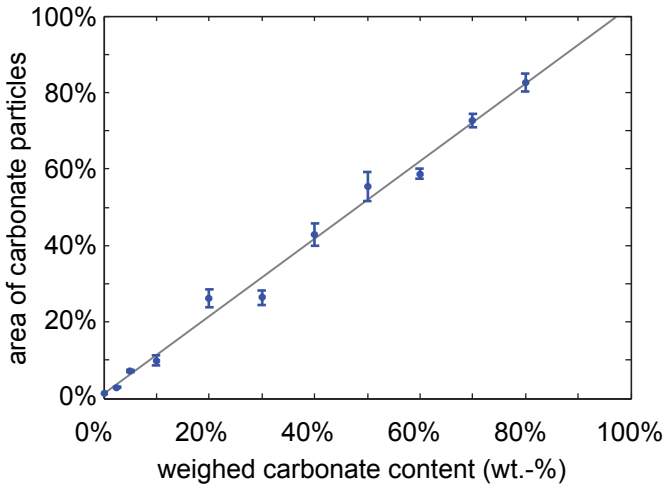

Figure 5.2: Scatter plot of the weighted carbonate-quartz test samples versus the area percentage of detected carbonate particles. A calculated correlation coefficient (R^2) of 0.94 shows the reliable detection and classification of carbonates by the RADIUS particle analysis system.

The RADIUS detection results are presented as 20 point arithmetic mean records.

5.3 Results

For the ELSA dust stack the Dehner dry maar core sequence provides a high resolution reconstruction of east wind directions for Central Europe by provenance analyses. The measured ground noise signal for the content of authigenic carbonates over all core sequences is about 0.2%. Two main modes according to wind speed and strength can influence deflating areas: (i) transport of fine grained silty material (<20 µm) at high altitude over very long distances, (ii) transport of coarser material over short distances. Our results correspond to the second model of dust transport (Pye, 1987) as coarse silt material has been blown from the nearby river valleys as well as from the Devonian carbonate basins. We suggest that the relatively low content of carbonates in the silt fraction (max. 19.4 % per sample) is produced by physical weathering in the carbonate belt. The measured grain sizes and shape parameters (elongation and form factor) of the aeolian transported carbonate particles correspond to those of the

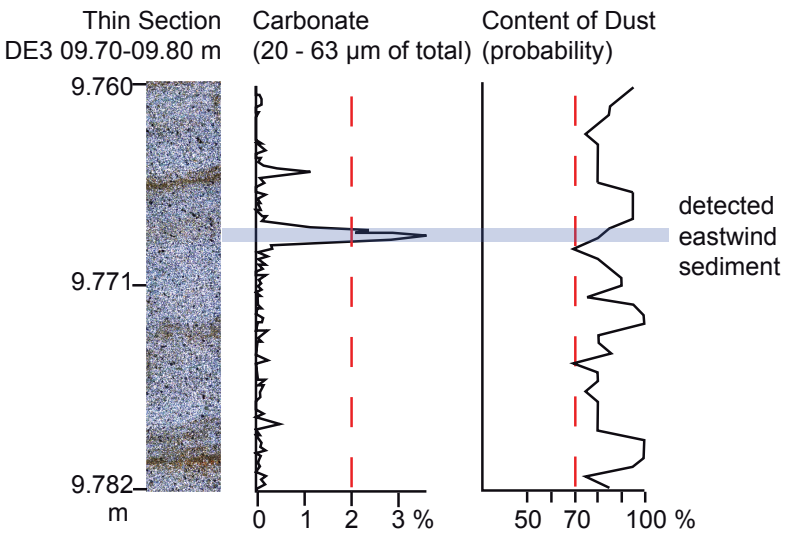

Figure 5.3: Example of a dust sequence of core DE3 showing a detected east wind layer (silt sized carbonate content greater than 2% and probability of dust scores greater than 70%) during the LGM. The aeolian transported carbonate particles of such layers are of the same mean size as the corresponding quartz grains.

quartz fraction.

The production of quartz particles in the silt fraction by physical weathering processes (basically by frost shattering) are already described by Cilek (2001). Lab experiments show the effects of frost shattering on carbonate rocks produce carbonate granules (Lautridou and Ozouf, 1982). Secondary aeolian processes such as deflation, saltation and corrasion are able to produce fine grained material like silt. This is in agreement with the generally low content of carbonate in our sequence. Motivated by questions about the sources and the transport distance of the carbonate particles we used electron microscopy to analyse one thick east wind layer (core DE3, 9.773 m depth). A micrograph (Fig. 3.8) from a scanning electron microscope (Zeiss DSM 962) demonstrates the distribution of large carbonate particles in an east wind layer. Fig. 3.8a shows a carbonate particle with a diameter of about 55 µm surrounded by quartz and feldspar minerals of the same size. The qualitative geochemistry analysis in Fig. 3.8b, measured in the center of the observed grain, shows the typical calcite pattern.

Taking the record as a whole (Fig. 5.4), west winds dominate the period 40.3–12.9 ka. The lowest content of east wind layers is about 0.2%, representing the highest west wind activity during the period 24–22.5 ka. The maximum content of east wind formed sediments in a hundred years interval is 19.4% (32 ka). The overall time period studied an be subdivided into three units:

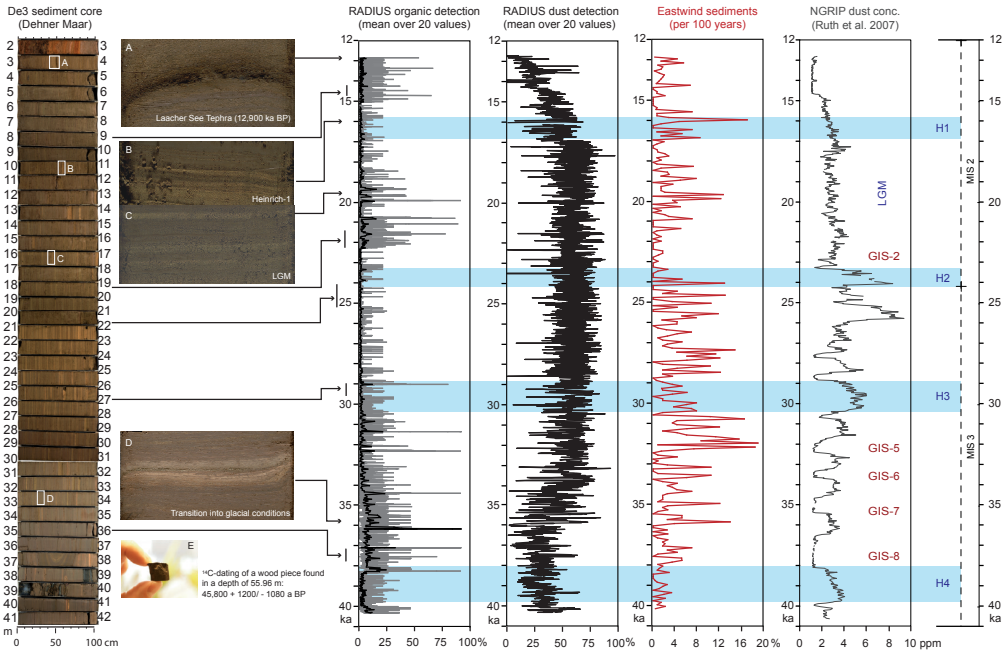

Figure 5.4: Core sequence DE3 40.3–12.8 ka (Dehner dry maar): left: core images over the whole sequence (2–42 m); center-left: detailed sediment images: **(A)** Laacher See Tephra (LST, 12,900 years BP), **(B)** H1 equivalent layer, **(C)** example of a LGM layer, **(D)** transition into MIS-2, **(E)** ^{14}C-dating of a piece of wood (spruce) found at a depth of 55.96 m (45.8+1.2/-1.08 ka BP); center-right: Radius detection records for the content of organics, Radius detection of dust (both with an original sampling resolution of 500 µm Seelos and Sirocko, 2009). Frequency of carbonate rich east wind sediments per 100 years (red). The comparison with the micro particle record (gray) from Greenland (Ruth et al., 2007) shows a common process of aeolian dynamics linking North Atlantic and European regions. Blue bars marking Heinrich events (Hemming, 2004).

1. The first time period during MIS-3 (40.3–36 ka) is dominated by relatively organic rich gyttja. Although H4 (39.4–37.2 ka) is the largest Heinrich event during the last glacial period (Hemming, 2004), in the Dehner dry maar the loess input does not increase. However, the organic content in this period is very low. Thus, the analysis of carbonate bearing east wind layers is not possible for this time slice. The strong increase in dust accumulation starts quiet after the GI8.

2. When the global sea level began to fall even more (36 ka) the climate passed into a colder and dryer state in middle Europe, which climaxed finally in the LGM (Clark et al., 2009). At this point, our data show that the content of east wind sediments increases. During this declining phase of MIS-3 (36–32 ka) thick east wind layers are accumulated (Fig. 5.4 D), but the frequency of east wind events is moderate. During the following period (32–24 ka) the content of dust sediments is always high (around 75%), whereas the content of organics decreases to a very low level. The east wind frequency is relatively stable at a high level, about 9% of east wind events per 100 years until the end of H2 equivalent. Maximum values occur during the period 32.5–30.5 ka (shortly before the H3 event), during 28.5–27 ka (corresponding with the time slice of GI4 and 3), and during 25–24.5 (H2 event).

3. The period between H2 and the LGM is characterized by a major change in the climate system over Europe. The content of east wind transported sediments drops to a level of about 2%. The number of east wind events per century decreases rapidly. During the late LGM (21–18 ka) and the subsequent H1 event (16.6 ka) the content of east wind sediments is once again noticeably high (mean value is around 6% per century).

The domination of west winds, mainly influenced by westerlies, is also approved by our data. The continuous high resolution dust records of the ELSA dust detection allow very detailed analyses of east wind frequencies for the complete time period 40.3–12.9 ka. One result of this study is a correlation of increased east wind frequency with extreme cold phases like Heinrich events or the maximum advance of the glacial ice sheets during the LGM.

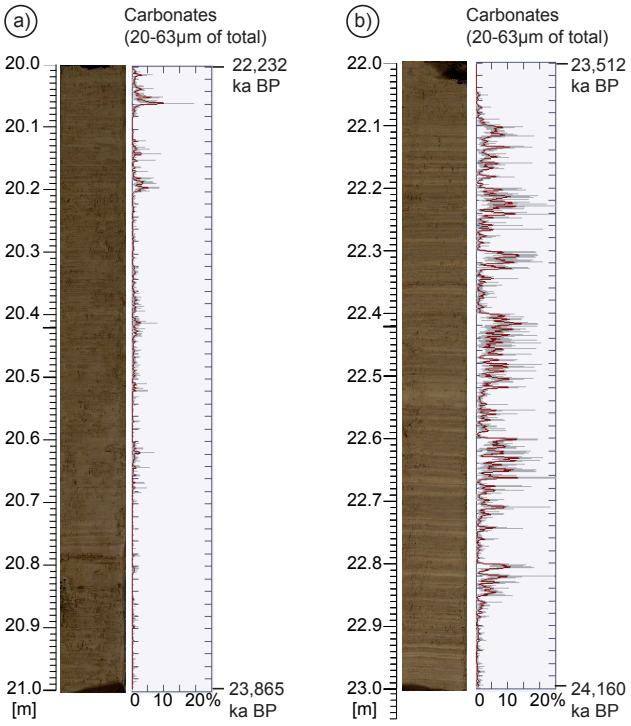

Figure 5.5: The comparison of two sediment core sequences. DE3 21–20 m (22,865–22,232 years BP) and DE3 23–22 m (24,160–23,512 years BP) show the variation of sediment structures for the periods of **(a)** the interstadial GI2 and **(b)** the previous H2. It is obvious that the core sequence 23–22 m is characterized by coarse lamination because of variable sediment composition. This alternation of carbonate rich and carbonate poor sections is caused by frequently changing wind directions.

5.4 Discussion

We suggest that the easterly wind proxy in the Dehner dry maar corresponds to Heinrich events or extreme cold climate phases like the late LGM, when the 21 June–20 July insolation at 65°N rises again (Laskar et al., 2004; Berger and Loutre, 2002). During this time sea surface temperature (SST) records also show minimum values (Lea et al., 2003).

Both the Greenland Stadials (GS) before and after GS4, which correspond to H3 in marine cores, are characterized by the highest number of east winds during MIS-2,

the former up to 160 identified east wind layers per century. However, the period representing the H3 itself has only a small amount of east wind sediments. It seems that the climate situation during H3 is in contrast with other Heinrich events (Gwiazda et al., 1996) and is coupled to relatively stable high-pressure systems over the eastern part of Europe.

In contrast to H3, H2 (24.8–23.2 ka) is dominated by strong east winds, but the number of detected events per century drops to a value around 20. A comparison of two core sequences shows significant differences between the interstadial GI2 and the previous H2 (Fig. 5.5).

H1 (16.6–15.2 ka), which is not recorded in the NGRIP micro particles, shows like H2 a high amplitude in the record of east wind frequency. A higher east wind frequency is also modeled by Renssen et al. (2007) for the time slice of the late pleniglacial (18–15 ka).

H4 (39.4–37.2 ka) is known as the strongest Heinrich event. However, the analysis of the core DE3 does not showing a similar dust signal to other European records like Nussloch (Antoine et al., 2009; Rousseau et al., 2007) but a distinctive minimum of organic matter.

During MIS-2, the atmospheric conditions over middle Europe seem to be more stable and west winds dominate during the whole period (indicated by low content of wind transported carbonate particles). However, at about 24 ka after the beginning of the H2 event we recognize a major change in the climate system over Europe. The period of 21–18 ka (late LGM) is characterized by a lower east wind frequency than the Heinrich events H2 and H1. However, the time slice 20.5–19.5 ka shows numerous east wind events (about 12% per century). In addition our results show a slightly increased east wind frequency during the LGM within the period between 24 and 17 kyr BP. This is the time when SST and insolation in the northern hemisphere reach minimum values. Climate simulations (Renssen et al., 2007) show a low east wind activity and increasing west winds for the LGM. These results may be supported by the data from DE3, relating to the period from 24–21 ka when east wind layers are less present.

The high resolution east wind frequencies of the Dehner dry maar allow for a recognition of stadial-interstadial cyclicity. The correspondence between this record and other European sediment archives (Antoine et al., 2009) implies the existence of a link between the variations in the aeolian dynamics over Western Europe and the atmospheric circulation over the North Atlantic area (Rousseau et al., 2007). The study of Antoine et al. (2009) compares possible centers of loess origin in the Upper

Rhine Area (Germany) and interpret these results with the migration of the North Atlantic low. In general our east wind layers coincide with coarser sediment (high grain size index) in the Nussloch P4 loess profile. A higher grain size index in the Rhine area is suggested as an enforced proximal aeolian transport. We suggest the same mechanism for the Eifel region: Coarse carbonate grains are transported from sources in the direct neighborhood to the Dehner dry maar sediment trap. Thus, the carbonate outcrops of the Eifel-North-South-Zone are the most likely source.

The most probable seasonality for dust entrainment is shown in the latest dust emission model for Europe by Sima et al. (2009). The authors suggest maximum dust emission from April to June. During HE the maximum activity is shifted by 1–2 months towards summer in comparison to GS and GI conditions. During HE their model results show an increase of eastern wind directions, corresponding to the DE3 data.

Since there is general lack of precision in the age-depth-model used, it is not possible to decide whether high easterly wind activity corresponds to the 'beginning' or to the 'end' of Heinrich events. Thus, we think that H1, H2 and LGM show a direct coupling to easterly wind systems. Renssen et al. (2007) and Isarin et al. (1998) demonstrated the important impact of slight N-S shifts in the belt of strong westerlies. Probably such shifts occurred concurrently with the numerous climatic oscillations that are recorded within the studied period 40-12 ka BP, which may have resulted in changing wind directions at the Eifel region.

The continuous data, shown in this chapter, illustrate a high variability in changing wind directions. Climate simulation might help to answer the question of possible causes of east winds during extremely cold climate conditions. Earlier results give some hints of atmospheric conditions.

Simulations of the LGM suggest that the glacial ice sheets had major effects on atmospheric circulation patterns. A glacial anticyclone, produced during summer months by high atmospheric pressure over the ice sheet, generated an easterly surface wind anomaly directly to the south of the ice sheet (Bartlein et al., 1998; COHMAP Members, 1988; Kutzbach and Wright, 1985). Some models show a permanent easterly flow south of the ice sheet (COHMAP Members, 1988; Kutzbach and Wright, 1985), but recent simulations show that easterly flows are less pronounced and more seasonal with a westerly flow returning in winter months (Whitlock et al., 2001; Bartlein et al., 1998). Evidence from aeolian deposits in North America verify that the glacial anticyclone altered surface wind patterns and affected aeolian systems during the LGM (Sweeney et al., 2004). Similar atmospheric processes are suggested

for the European region. Katabatic and zonal winds controlled by the Weichselian Ice Sheet may be irrelevant: dominant easterly wind directions only existed in areas being deglaciated or located immediately in front of the ice sheet during its maximum extension (Christiansen and Svensson, 1998; Renssen et al., 2007).

Atmospheric blocking as mentioned by Rimbu et al. (2007, 2008) is a large-scale, mid-latitude atmospheric phenomenon often associated with persistent quasi-stationary, synoptic-scale, high-pressure systems. The formation, maintenance and collapse of atmospheric blocking cause large-scale circulation anomalies and strongly impact on weather patterns. Such a situation can block the large-scale westerly flow over the northeast Atlantic and influence the wind direction over Europe.

The shutdown or reduction in strength of the North Atlantic meridional overturning allows the spread of winter sea ice across the North Atlantic, thus causing much colder winter from Greenland to Asia (Denton et al., 2005). Widespread sea ice cover might lead to a southward relocation of the polar front and the Icelandic Low as well as the westerlies. Subsequently, the strength of western winds in the Eifel region is reduced and an east wind anomaly, probably by the result of a glacial anticyclone, represents this weakening. This is what Sweeney et al. (2004) also suggested for the N-American continent. However, these explanations, especially the amplitude and seasonality have to be checked against climate models. According to Antoine et al. (2009) an ENE replacement of North Atlantic low pressure centers leads to a high grain size index in the loess sediments at Nussloch. However, this does not explain the increase in east wind sediments detected in our data. Renssen et al. (2007) show in climate models that during the late pleniglacial northwestern winds are dominant in direct response to an easterly relocation of the Icelandic low.

5.5 Conclusions

The high-resolution analysis of aeolian transported sediments into the Dehner dry maar lead to the following conclusions:

1. The Dehner Dry maar is suitable for regarding paleo east wind layers due to its location west of Devonian carbonate basins. Thus, aeolian sediments with high carbonate content from the Dehner dry maar (Eifel, Germany) can be interpreted as an east wind signal.

2. There remains a problem in proposing a regional atmospheric situation from a single sample location. However, Pfahl (2009) has shown that the allocation of

storm layers in maar lake sediments to recent regional meteorological data is statistically highly significant for at least the last few decades. In addition, our results correspond to other European dust proxies. Thus, we suggest that our results from the Dehner dry maar correspond to a regional atmospheric state.

3. The time period studied, from 40.3–12.9 ka can be subdivided into three units: the first time period during MIS-3 (40.3–36 ka) is characterized by relatively organic rich sediments of MIS-3. Thus, there is little accumulation of dust in the Dehner dry maar and H4 (39.4–37.2 ka) is not recorded in the archive by a dust proxy. This period is dominated by an extreme low content of organic matter. The second time slice (36–24 ka) has an increased content of dust accumulation as well as of carbonate particles. These results correspond with growth of the global ice sheets (Clark et al., 2009). The third unit (24–12.9 ka) is characterized by lower east winds sediment deposition.

4. Increased east wind frequencies occur during the time intervals corresponding to the Heinrich events H1 and H2, whereas the unusual H3 shows no increased east wind frequency. The former and subsequent Greenland stadial intervals do so. In addition to the east winds the dust sedimentation in Central Europe also reaches maximum values during Heinrich events, which is suggested by Antoine et al. (2009) and Rousseau et al. (2007) for the Nussloch section (Germany).

5. This division into two different atmospheric circulation modes is also indicated by the frequency of storm events (Seelos and Sirocko, 2009). Here, it is shown that the storm activity is higher during MIS-3 in comparison to MIS-2. In addition, the micro particle record of the NorthGRIP ice core shows increased dust accumulation in Greenland during the Greenland stadials (Ruth et al., 2007). The MIS-3 is dominated by Dansgard/Oeschger cycles, whereas the subsequent MIS-2 shows a relatively stable, low amount of dust concentrations. According to this study, the significant change in atmospheric patterns might have also resulted in a change of wind directions near to the surface in middle Europe.

5.6 Summary of chapter 5

A high resolution continuous reconstruction of wind directions during the last glacial is based on provenance analysis of aeolian sediments in a sediment core from the

Dehner dry Maar in the Eifel region (Germany). This maar is suitable for recording easterly wind directions due to its location west of the Devonian carbonate basins of the Eifel North-South Zone. Thus, aeolian sediments with high clastic carbonate content can be interpreted as an east wind signal. The detection of such east wind sediments is applied by a new module of the RADIUS grain size analysis technique.

The high resolution continuous reconstruction of dust event layers and east wind layers provides information about the variability of storm events and the variability of easterly wind directions for MIS-2 and MIS-3. The investigated time period from 40.3–12.9 ka can be subdivided into three units. The first unit covers the periods of the Greenland interstadial GI-9 and GI-8, including Heinrich event H4 (40.3–36 ka). With the exception of H4 the content of organics in our record is relatively high. With the end of GI-8 the content of organics decreases and the content of dust increases rapidly. This second time slice (36–24 ka) has an increasing content of dust accumulation and a large amount of east wind layers (up to 19% of the dust storms per century came from the east). In comparison, the subsequent period 24–12.9 ka, which represents to a large extent the marine isotope stage MIS-2, is characterized by lower east wind sediments again. Increased frequencies of east wind occur during the time intervals corresponding with the Heinrich events H1 and H2. The late LGM (21–18 ka) is characterized by a slightly raised east wind frequency again.

In summary, during the marine isotope stage MIS-3 the storm frequency and the east wind frequency are both increased in comparison to MIS-2. These results correspond to the dust accumulation in the NorthGRIP ice core and lead to the suggestion that atmospheric circulation was affected by more turbulent conditions during MIS-3 in comparison to the more stable atmospheric circulation during the full glacial conditions of MIS-2.

Chapter 6

More Variable Wind Directions and Stronger Winds in Central Europe during the Last Glacial Period[1]

6.1 Introduction

Changing atmospheric patterns are one of the most effective mechanisms to influence the climate and on a synoptic scale the weather on the European continent. The mean circulation in the middle latitudes is dominated by the westerlies. During recent climate conditions this circulation is characterized by a strong zonal flow. Under glacial conditions during the marine isotope stages MIS-2 and MIS-3 the atmospheric circulation is strongly influenced by sea surface temperature (SST) patterns and the orography of the continental ice sheets, respectively. Atmospheric blocking highs over the ice sheets lead to a stable wave-like distribution of sea level pressure centers. Highs over the ice sheets alternate with lows over the oceans (Justino and Peltier, 2005; Romanova et al., 2006). In consequence, the Icelandic Low is deepened and shifted to the south or southeast. Thus, the meridional pressure gradient is strengthened and dislocated from the present-day configuration. Storm trajectories in general follow the strongest meridional temperature gradient. The increased pressure gradient over the North-East Atlantic during glacial conditions leads to an increase in cyclonic activity and thus of the wind speed in Europe (Renssen et al., 1996; Romanova et al., 2006), which is also reflected in a higher flux of aeolian dust during glacial conditions. Over the North-Western European continent wind directions from west to southwest prevail. Only regions which are directly influenced by katabatic winds at the edge of the inland ice sheets show dominant easterly wind directions (Christiansen, 2004;

[1] A slightly modified version of this chapter has been submitted as Dietrich et al. (subm) in the journal Climate Dynamics (Clim. Dyn).

Renssen et al., 2007).

According to on geological evidence, the inland ice sheets were reduced to small islands during MIS-3 (Arnold et al., 2002; Wohlfarth, 2010). The sea level was around 50 m below present conditions, in contrast to the last glacial maximum (LGM) when the sea level declined about 120 m (Clark et al., 2009). The MIS-3 ice volume changes are most likely primarily controlled by Northern Hemisphere climate not only on orbital, but also on millennial timescales (Arz et al., 2007). The major implication is that a varying orography leads to changing atmospheric circulation patterns during MIS-3. In a series of sensitivity studies with an atmospheric circulation model coupled to an ocean mixed layer, Romanova et al. (2006) found evidence in AGCM experiments that the large-scale glacial atmospheric circulation depends primarily on the orography affecting SST, while changes in the meridional oceanic circulation are of secondary importance. The mean climate state of MIS-3 is suggested to be similar to LGM conditions (e.g., Barron and Pollard (2002); Romanova et al. (2006)). However, Barron and Pollard (2002) report that MIS-3 numerical experiments captured a number of systematic changes in sea-level pressure and precipitation over Europe. In winter, MIS-3 simulations are characterized by strong high pressure over all of southern Europe and a strong westerly flow. Southern Europe has substantial decreases in precipitation, while the northwestern part of the domain has slight increases.

High resolution proxy data for changing wind strength and especially for wind directions are the key data for reconstruction of the variability of atmospheric circulation of the past. Several results from wind direction proxies for the last glacial in Central and Western Europe were published in the last years. The methods of generating proxy data of wind directions include relict dune forms (Vandenberghe, 1991; Godzik, 1991), grain size trends of cover sand and loess (Van Huissteden et al., 2001), orientation of wind-polished rock surfaces (Christiansen, 2004; Christiansen and Svensson, 1998), provenance analyses by heavy mineral composition (Krook, 1993), derivation from anisotropy of magnetic susceptibility (Nawrocki et al., 2006), and provenance analysis of aeolian-transported dust into lake basins (Dietrich and Seelos, 2010). As far as we know, only the latter study covers a long enough time interval (40.3–12.9 kyrs BP) with sufficient time resolution (100 years) to enable us to compare the millennial variability of changing atmospheric patterns between the marine isotope stages MIS-3 and MIS-2. This dust proxy data for easterly wind directions in the Eifel region, central Germany, is based on the position of a maar which is suitable for recording easterly wind directions due to its location west of the Devonian carbonate basins of the Eifel-North-South-zone (Fig. 6.1). The results of this

study show that more east winds and a higher variability of changing wind directions in general occur during MIS-3 and more stable atmospheric conditions, with a strong depletion of easterly winds, during MIS-2. During all time intervals wind from westerly directions dominates in Central and Western Europe, with a background level of 4% of dust transporting east wind levels and peaks of 19% occurring during MIS-3. At the same time, the overall frequency of dust events is significantly decreased during MIS-2 in comparison to MIS-3 with its large and rapid temperature shifts (Ruth et al., 2007; Seelos and Sirocko, 2009). The nature of this significant change in the variability of atmospheric circulation is the focus of this study.

One major question relates to the seasonality of dust emission during different glacial climate stages like MIS-2 and MIS-3. This is difficult to answer from the proxy data point of view due to dating uncertainties and lack of proxies for describing the season itself. In general, winter and spring are the most likely seasons for dust deflation (Werner et al., 2002; Denton et al., 2005; Sima et al., 2009). In the seasonal cycle the highest wind velocities occur in Central Europe during winter, which is suggested to be true for both glacial conditions and recent climate (Sima et al., 2009). However, for MIS-3 recent model results which focus on dust emission during stadials, interstadials, and Heinrich events indicate that spring to early summer, with maximum activity in April–May, are the seasons with the most dust deflation (Werner et al., 2002; Sima et al., 2009). In addition, the dusty season is shifted towards summer in a colder climate. This dust emission model takes the local restrictions related to the soil conditions (snow cover, soil moisture, vegetation) into account.

Here, we use AGCM runs with different prescribed climate means to develop a synoptic interpretation of long-persisting east wind conditions (LEWIC) as well as stormy days with easterly wind directions. These are suggested to lead to an enhanced accumulation of sediment which was transported by easterly winds to the proxy site in the Eifel region. The different AGCM experiments are forced with prescribed SST patterns to study systematically the influence of different glacial climate stages on atmospheric circulation. The LEWIC over Europe were analyzed for their timing, persistence, seasons, and location of occurrence. We thereby address one major objective, which is to give a synoptic interpretation of east wind activity for different glacial conditions with a special focus on seasonal changes.

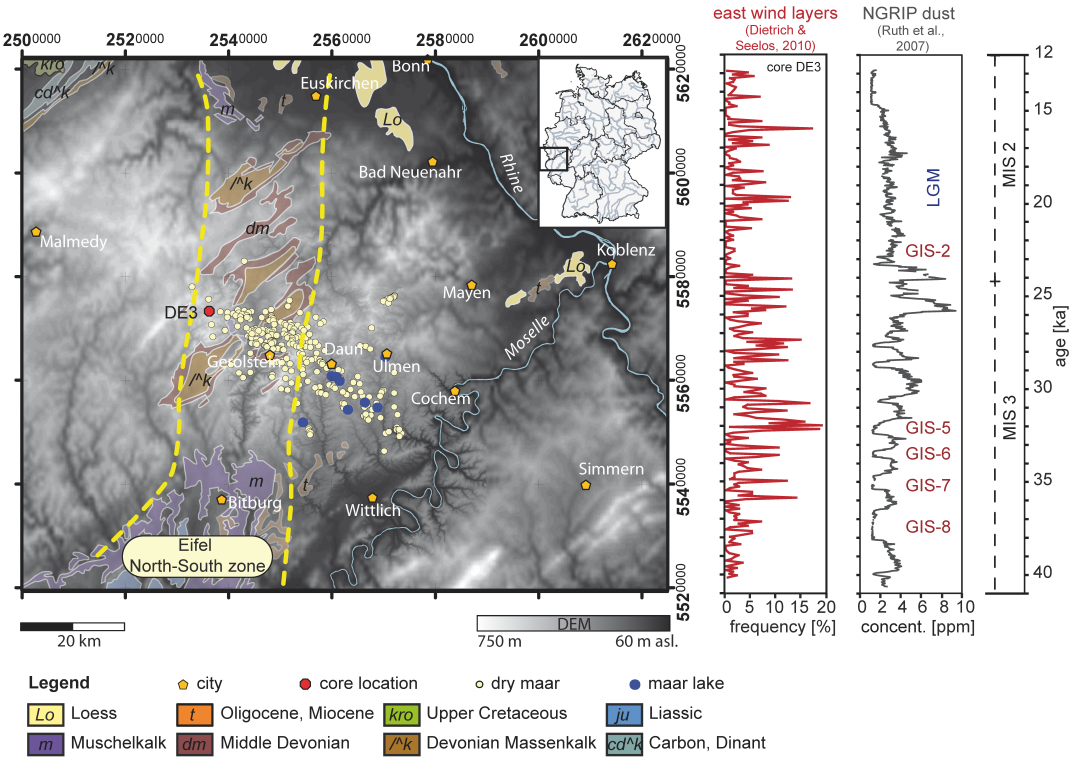

Figure 6.1: Geological sketch map and elevation model of the Eifel region, including the calcareous rocks, such as the limestone bearing "Kalkmulden" in the Eifel N-S-zone, loess deposits and the locations of Maar lakes and dry maars after Büchel (1994). The map is based on the Geological Map of Germany 1:1 000 000 (BGR, 2002), GCS Deutsches Hauptdreiecksnetz, Gausszone 2, Bessel 1841. Only wind with easterly directions can transport carbonate bearing dust to the location of the sediment record (red dot) of the western side of the Eifel N-S-zone. Red curve: Frequency of sediment layers in the core DE3 which were transported by easterly wind. Grey curve: content of dust in the NorthGRIP ice core (Ruth et al., 2007). Both records show higher amplitudes and a higher variability during MIS-3 in comparison to MIS-2. Figure modified after Dietrich and Seelos (2010).

6.2 Numerical Models and Analysis Methods

Instead of state-of-the-art fully coupled models, we use different ECHAM AGCMs with prescribed SST patterns in order to analyze systematically different glacial circulation patterns of surface air flow. This simplified approach provides another perspective to understand the glacial climates. (1) We force the ECHAM4/T31 model (Roeckner and Coauthors, 1996) with the CLIMAP project members (1981) reconstruction. In addition, we employ two different SST reconstructions for the Last Glacial Maximum to force the ECHAM3/T42 (Roeckner and Coauthors, 1992): (2) with the new GLAMAP 2000 Atlantic reconstruction (Pflaumann et al., 2003; Sarnthein et al., 2003) and (3) the CLIMAP project members (1981) reconstruction with an additional cooling of 3 °C in the tropics (Lohmann and Lorenz, 2000). Both versions of ECHAM have a vertical resolution of 19 layers (Tab. 6.1). As compared to CLIMAP, the North Atlantic sea ice cover is substantially reduced in the newer reconstructions. The GLAMAP winter sea ice margin is similar to CLIMAP's summer sea ice boundary, and the Nordic Seas are ice-free during summer (Schäfer-Neth and Paul, 2003). GLAMAP provides higher SSTs in the northern North Atlantic than CLIMAP and its winter conditions are similar to those of the CLIMAP summer. These experiments with varying predefined SST reconstructions are applied as a substitution-study with colder (LGMN) and warmer (LGMG) climate conditions during the last glacial including MIS-2 and MIS-3, respectively.

Table 6.1: Model description of the ECHAM AGCM simulations used. Each model year is 360 days long. All other boundary conditions (greenhouse gas forcing, orbital parameters, etc.) have been set to present-day and LGM values, accordingly.

model run	model years	spatial resolution	SSTs
ECHAM4 PD	10	T31, L19	modern
ECHAM4 LGMC	10	T31, L19	CLIMAP
ECHAM3 PD	15	T42, L19	modern
ECHAM3 LGMG	15	T42, L19	GLAMAP2000
ECHAM3 LGMN	15	T42, L19	CLIMAP with additional cooling of 3° C in the Tropics

The three glacial experiments are denoted as experiments LGMG (GLAMAP), LGMN (CLIMAP with additional cooling in the tropics) and LGMC (ECHAM4 with CLIMAP). Orbital forcing, reduced concentration of carbon dioxide (200 ppm),

and topographic changes are taken into account (Lohmann and Lorenz, 2000). Two control experiments are carried out with present-day forcing for both ECHAM3 and ECHAM4 and are denoted as PD3 and PD4. For a detailed description of the simulated glacial climates, including analysis of the hydrologic cycle, we refer to Lohmann and Lorenz (2000) and (Romanova et al., 2004). Each ECHAM3 run is 15 years long; the ECHAM4 runs span 10 years. The AGCM results are evaluated by comparison with the ERA-40 reanalysis data from the European Centre for Medium-Range Weather Forecast (ECMWF). The ERA-40 data set (Uppala et al., 2005) contains 10 m-wind vectors for 6-hourly time periods during the years 1969 to 2001. ERA-40 data with 6-hourly time steps for the years 1969–2001 have a spatial resolution of T159 and linear interpolation has been applied to obtain ERA-40 values at the location of the Eifel region (Pfahl et al., 2009).

In this study we focused on the 10 m-wind vectors of the ECHAM experiments and calculated the day and field mean for the grid boxes which cover the area of interest, in this case the Eifel area. Since using a 3 x 3-matrix or a smaller 2 x 2-matrix gives no significantly different results (not shown) we decided to use the smaller matrix for calculating the field mean. Boundary coordinates for the T31 grid fields are 4°– 12° W and 46°–52° N and for the T42 fields 4°–10° W and 48° –52° N, which cover NW-Europe with the Eifel Volcanic Field (EVF, Germany) in the center. The ERA-40 data cover a square with an edge length of 80 km and its center at 6.9° E and 50.1° N. These data are adopted from a previous study (Pfahl et al., 2009). The proxy site of the Dehner dry maar is located at 6.505° W and 50.295° N. For the field mean values the daily, monthly, and seasonal wind directions and velocities are calculated, focusing on the easterly wind directions. LEWIC are defined as temporal clusters with continuous easterly wind directions with a minimum persistence of three days, in accordance to Croci-Maspoli et al. (2007), who suggested this length as the minimum life time of atmospheric blocking events. Subsequently, these temporal clusters of easterly winds over the Eifel are analyzed for their frequency, for their persistence, and for when those atmospheric patterns occur in the seasonal cycle with a critical wind speed ($\geq 5\,\mathrm{m\,s^{-1}}$). Composite maps of the circulation patterns of the 10 m-wind vectors for LEWIC states indicate quasi-stationary troughs and highs, which induced easterly wind conditions over the Eifel area.

Table 6.2: Descriptive statistics of the AGCM runs and the ERA-40 dataset in relation to the frequency of east wind events in general, storm events with easterly directions and wind velocities larger than 5 ms^{-1}, long-persisting east wind conditions (LEWIC), and storm events in general.

model run	relative freq. of E-wind	E-wind ($\geq$5 ms^{-1})	LEWIC freq. $\geq$3 days	storm freq. ($\geq$5 ms^{-1})
ECHAM4 PD	21.4%	1.4%	2.9%	13.1%
ECHAM4 LGMC	17.5%	1.0%	1.6%	18.8%
ECHAM3 PD	26.6%	2.4%	3.3%	21.5%
ECHAM3 LGMG	16.2%	1.9%	1.7%	40.4%
ECHAM3 LGMN	19.7%	2.6%	1.8%	32.3%
ERA-40	34.8%	0.6%	4.5%	11.6%

6.3 Results of the model study

For the Eifel region, in both models and in all investigated time slices, westerly wind of the 10 m-wind vectors dominates, with a modal value of SW directions. In comparison to the control runs the glacial wind conditions have a stronger meridional component, which is most obvious for LGMC (Fig. 6.2). The colder ECHAM3 LGMN run shows a slight increase of the meridional component in comparison to the LGMG run. Easterly wind directions of the 10 m-wind lay in a range between 16 and 27% of all computed wind directions (Tab. 6.2). These values are lower when compared with recent wind data from the ERA40 reanalysis data set which was computed for the Eifel area. The modeled wind speeds have a median value of around 4 m/s with increased wind velocities during winter and higher velocities for the glacial runs in general (Fig. 6.3). Both the glacial and the present-day wind velocities are increased in the ECHAM3 experiments compared to ECHAM4. ERA-40 data also show lower velocities (Fig. 6.4).

The persistence of LEWIC events, also called temporal cluster size, reaches from three days, by definition, up to more than three weeks. However, the majority of these events are less than ten days long (Fig. 6.5). The annual cycle of LEWIC events is characterized by a strong seasonality (Fig. 6.6). All glacial model simulations show an enhanced occurrence of LEWIC situations during the warm period in summer and early autumn. This is a striking difference from the seasonal cycles of the control runs which do not show such a distinct seasonal high, but more a bimodal frequency

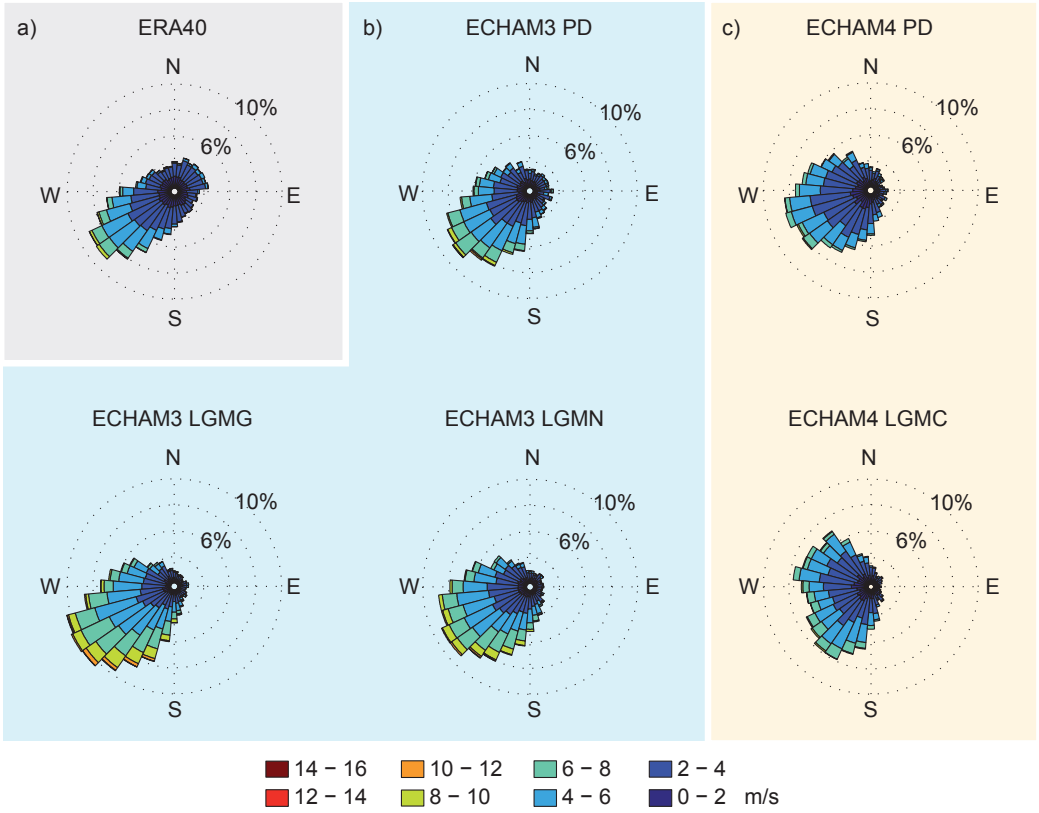

Figure 6.2: Wind roses for the analyzed time slices of wind direction and velocity in m/s, covering mean values over the Eifel region. a) ERA-40 reanalysis data representing the wind direction and velocities for 1969-2001, b) ECHAM3, and c) ECHAM4 data for both present-day control runs (PD) and glacial runs (LGM). Wind velocities and the fluctuation of the wind directions are enhanced in the glacial experiments.

distribution of LEWIC for autumn and spring.

Corresponding seasonal cycles are also observed for the timing when the longest-persisting LEWIC happen (not shown). In all experiments the longest LEWIC occur during those seasons with the highest frequency of LEWIC in general. Thus, changes in the seasonal cycle between present-day and glacial conditions are also found in the extreme values of long-lasting east wind clusters. The general probability for LEWIC events in northwestern to Central Europe is quite low. Only less than 4% of all modeled daily data are part of such a temporal cluster of east wind conditions and they appear twice as often in the present-day control runs as in the glacial runs

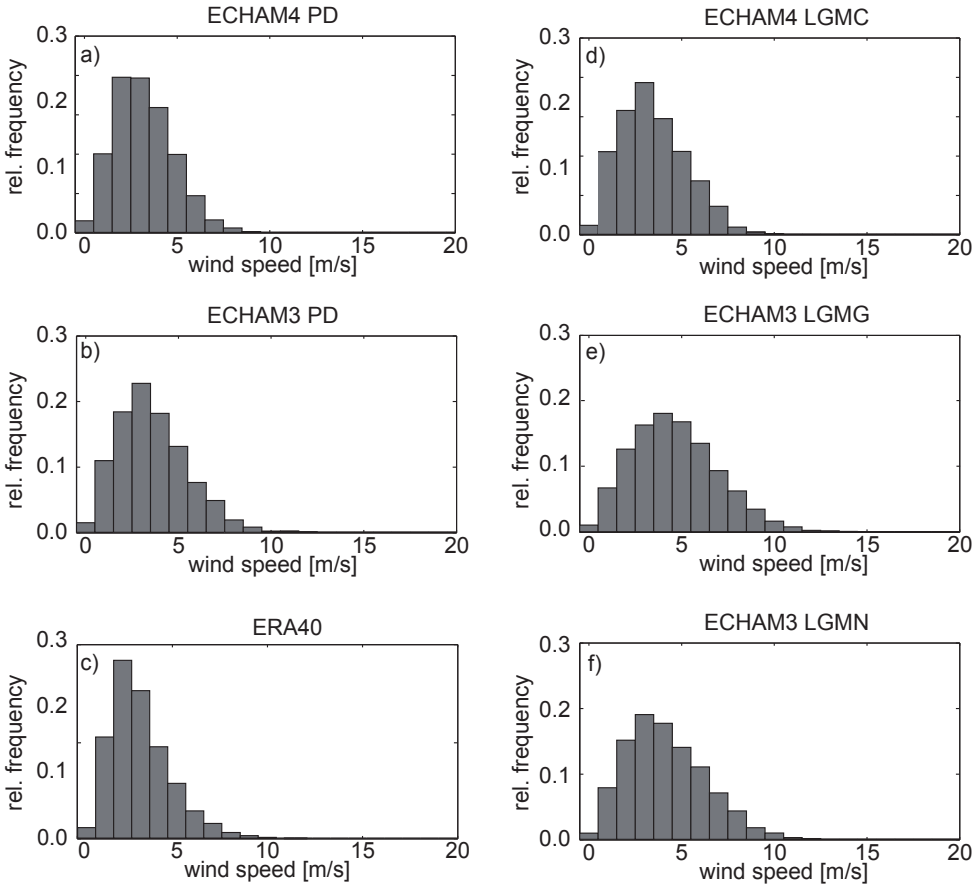

Figure 6.3: Wind velocities of the 10 m-wind for a, d) ECHAM4, b, e–f) ECHAM3, and c) ERA-40 data (LGM runs on the left side). Data are plotted as relative frequencies. Faster wind velocities are found in the glacial simulations.

(Tab. 6.2). Here, both models show similar results.

The annual distribution of storms ($\geq$5 m/s) with easterly wind directions indicates the boreal winter (October to April) as the stormiest season for east wind also (Fig. 6.6). While the ERA-40 east wind data show that wind storms begin in October and last until May, the control runs indicate a shorter stormy east wind season lasting until March. In the glacial runs this season is shifted towards summer, and lasts longest (until May) in the ECHAM3 LGMN.

We want to detect the atmospheric patterns which lead to prevailing and long-

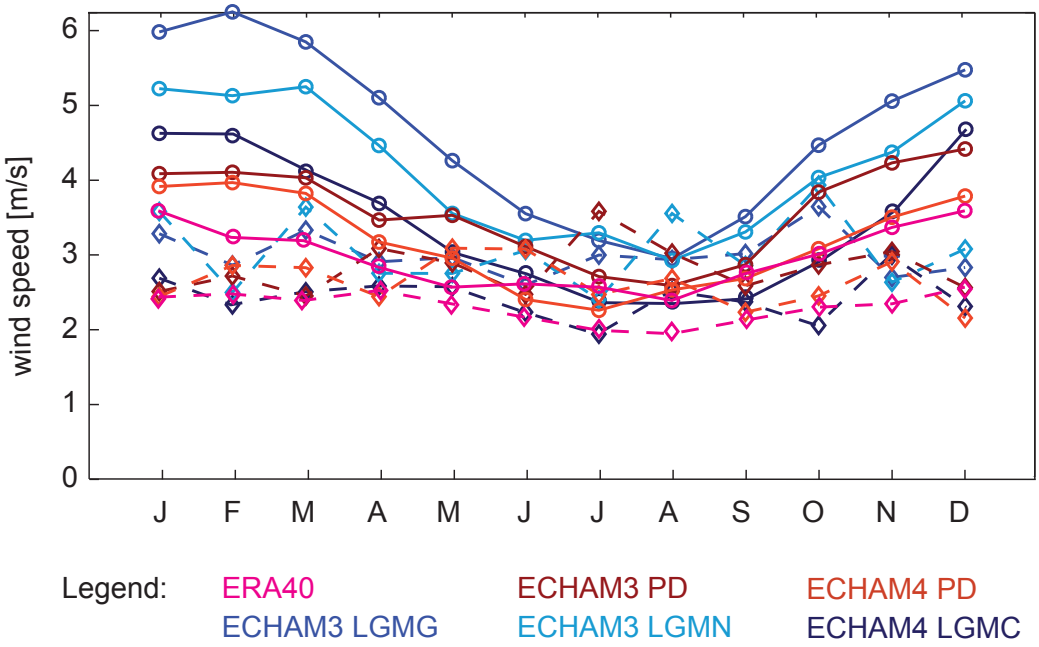

Figure 6.4: Annual cycle of the wind speed, computed using the field mean of 12-hourly data from the four selected grid boxes in the Eifel area. Solid lines: all data; dashed lines: easterly wind directions only. The computed standard deviation of approximately 1.5 m/s in the summer and 2 m/s in winter is not shown. During the glacial the wind velocities are enhanced during the boreal winter (October–April). Easterly wind velocities do not show a large variability in the annual cycle.

persisting easterly winds in Central Europe. In general, the analyzed results of all model runs are comparable for winter (DJF, not shown) and spring (MAM). The latter is shown because it is supposed to be the main season of dust emission. Under present-day conditions easterly wind directions over Central to North-Western Europe are mainly driven by a strong high over the Baltic Sea realm, leading to predominant wind directions direct from the E during LEWIC states. In addition, an anticyclonic circulation between Iceland and Spitsbergen can be seen for present-day conditions (Fig. 6.7). Furthermore, the pattern shows a clear Azores High. The composite maps were constructed by plotting the surface wind vectors for the seasonal mean and for the mean of LEWIC during MAM, respectively.

The atmospheric patterns in the different glacial simulations show good agreement. The Baltic High (see above) is replaced by the high over the Scandinavian Ice Sheet. In the seasonal mean of the LGMG experiment the wind flow from the west is similar

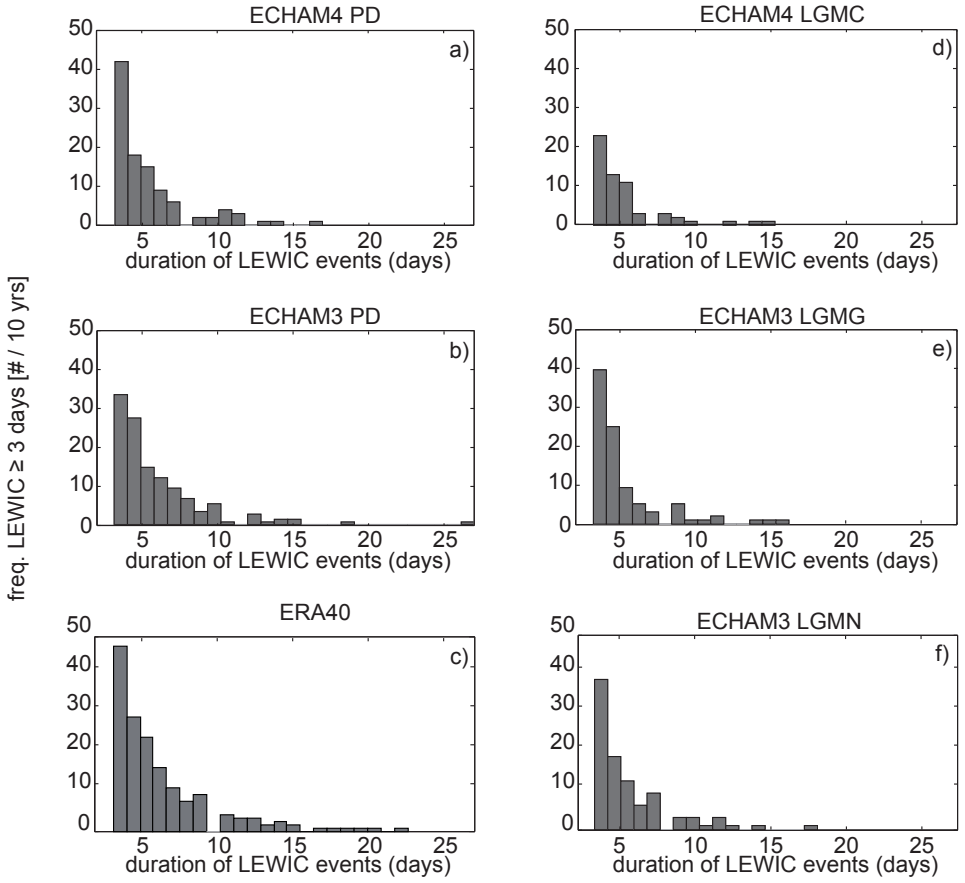

Figure 6.5: Same as Fig. 6.3, showing frequency distribution of the persistence of LEWIC events indicating the amount of east wind conditions with certain duration. Values are plotted as standardized frequencies (number of LEWIC per ten years). The simulations with present-day (PD) conditions as well as the ERA-40 data show more and longer persisting LEWIC.

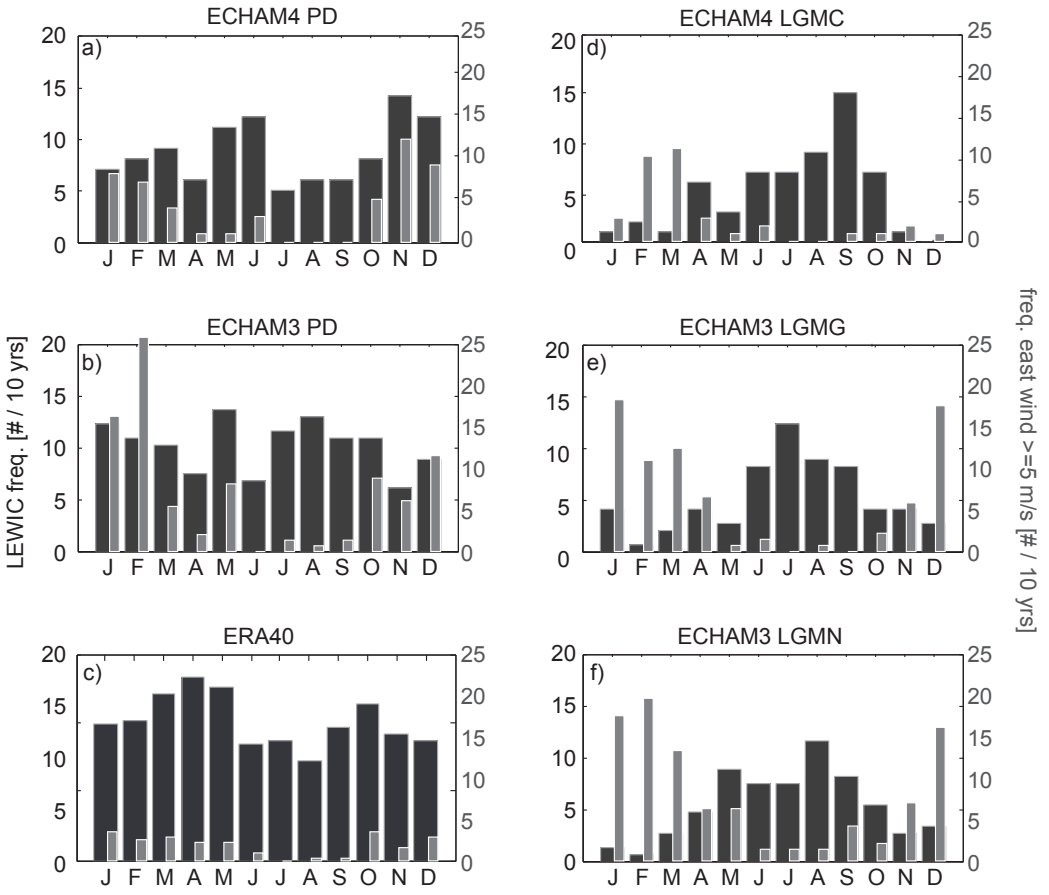

Figure 6.6: Same as Fig. 6.5, showing the seasonal cycle of long-persisting east wind conditions (LEWIC, dark bars) and of stormy days with easterly wind directions and wind velocities $\geq$5 m/s (bright bars). Values are plotted as standardized frequencies. All glacial experiments show a stronger glacial seasonality. The glacial runs are characterized by maximum LEWIC values during summer season and a higher frequency of east-wind storm days in the boreal winter, which is shifted towards late spring in the cold LGMN experiment. Both, LEWIC and stormy days are shifted towards the summer in the LGMN simulation in comparison to LGMG.

to the simulation with present-day conditions. The experiments LGMN and LGMC show air flow from southwesterly directions. The NW shift of the glacial anticyclone leads to LEWIC wind directions which come more from ESE and from SE in the LGMN experiment (Fig. 6.8). The air flow in the latter scenario is clearly influenced by the shift of the North Atlantic storm tracks to the S or SE, in this case towards the Celtic Sea south of England. This mechanism is thought to be triggered by a southward replacement of the North Atlantic sea ice edge for the cool LGMN boundary conditions. Similarly, within the LGMC experiment the Icelandic Low is moved to the south by a few degrees in comparison with the LGMG run. LEWIC are characterized by stronger westerly circulations over the North-Atlantic and the Barents Sea in comparison to the seasonal means. Generally, eastern wind speeds during LEWIC are stronger in all LGM runs in comparison to present-day circulation (Fig. 6.9), which might be strengthened by the pronounced glacial anticyclone over the Scandinavian Ice Sheet. Furthermore, the anomaly maps show more winds from south-westerly directions during the glacial spring. The results of the different glacial simulations are summarized in Tab. 6.3.

6.4 Discussion and model-data comparison

In the proxy records from the Eifel area both the east wind frequency (Dietrich and Seelos, 2010) and the overall frequency of strong storm events (Seelos and Sirocko, 2009) significantly decreased during MIS-2 in comparison to MIS-3 (Fig. 6.1). This accords with changes in dust deposition in Greenland (Ruth et al., 2007). The significant change in the sedimentation patterns is most plausibly related to a shift in the atmospheric circulation patterns. One major objective in this study therefore is the synoptic interpretation of east wind activity over glacial Europe and the question to which extent a change in the general atmospheric circulation patterns has influenced the pathways of aeolian sediment transport.

A comparison of proxy data with climate models is in general no small undertaking, since the grid cells of the models usually span several tens to hundreds of square kilometers. However, many records from the Central European region show that the accumulation of aeolian sediments corresponds to that in Greenland ice cores during the last glacial cycle (Seelos and Sirocko, 2009; Antoine et al., 2009; Ruth et al., 2007; Rousseau et al., 2007). In addition, Pfahl et al. (2009) have shown that the allocation of sedimentary layers of major and supra-regional storm events in maar lake sediments to recent regional meteorological data is statistically highly significant

Table 6.3: Summary of the results from the different glacial model simulations.

	LGMC (ECHAM4)	LGMN (ECHAM3)	LGMG (ECHAM3)
SST reconstruction	CLIMAP	CLIMAP + cooling	GLAMAP 2000
Analog for	LGM	Stadial	Interstadial
Sea ice	Summer boundaries similar to winter boundaries in GLAMAP	Further extended sea ice	Summer ice free
Wind speed	Lowest simulated glacial wind speed	In between	Highest simulated wind speed
Wind direction	Enormous variance in comparison to control run	Higher variance then in LGMG	Low variance only
Stormy days	Least stormy east wind days; Stormy days in February and March only	Most stormy east wind days; stormy days during boreal winter; additionally, storminess moved towards boreal spring (Nov—May)	Stormy days during boreal winter (Nov—Apr)
LEWIC	During boreal summer/autumn (Jun—Oct)	During boreal summer (May—Oct)	During boreal summer, earlier the year (Jun—Sep)
Mean circulation in the Eifel (seasonal composites MAM)	Air flow from SW	Air flow from SW	Air flow from W, similar to PD conditions
Mean circulation during LEWIC (MAM)	Air flow from ESE	Air flow from ESE	Air flow from E—ESE
Indicators for turbulences	Highest variance in changing wind directions, but less easterly wind events (LEWIC, stormy days)	Longest seasons and highest frequency of stormy east wind days and LEWIC; maximum amplitudes shifted towards summer	Long seasons of east wind events and highest simulated wind velocities

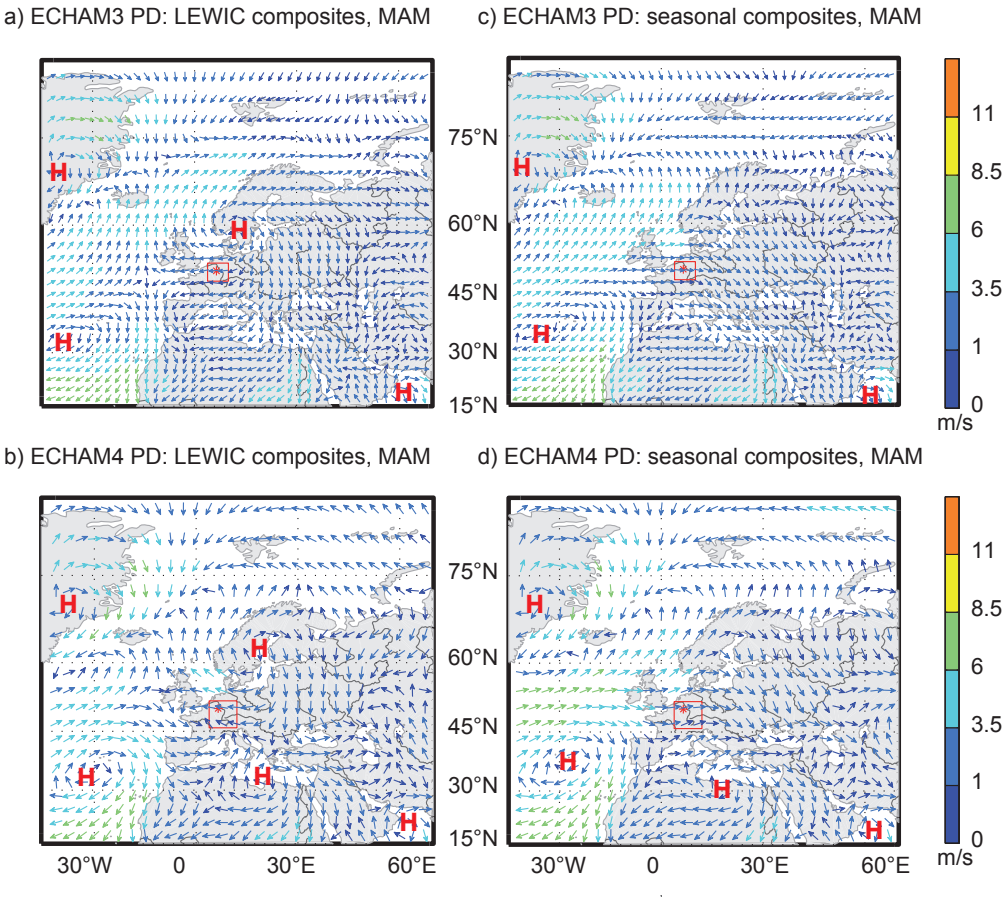

Figure 6.7: MAM 10 m-wind vectors, composite maps of the PD control runs. Panels a) and b) show the mean air flow for the LEWIC states, using daily data. Panels c) and d) show the seasonal composites. Wind vectors are colored according to the wind velocity. Grid cells used for the analysis are marked as the red rectangle, the location of the reference proxy site of the Eifel maar lake sediment core DE3 after Dietrich and Seelos (2010) is marked with the asterisk. Under present-day conditions (PD) easterly wind directions over Central Europe are mainly generated by a strong high over the Baltic region.

for at least the last few decades. We suggest that results from continental archives with sufficient temporal resolution like the Eifel maar lakes (Germany) corresponds to regional atmospheric circulation and are therefore comparable to related atmospheric simulation results of different past climates.

It is found that a low spatial resolution of model experiments biases the climate of the model experiments. The higher diversity of wind directions in the ECHAM4 relative to ECHAM3 runs is possibly due to the larger grid cells (T31 in comparison to T42), with an enhanced influence from the coastal areas with dominating wind directions from W to NW. East wind frequencies are underestimated in comparison to recent wind data from the ERA40 reanalysis data set which was computed for the Eifel area but correspond closely to the wind direction proxy data for glacial conditions (Dietrich and Seelos, 2010).

Atmospheric circulation is strongly influenced by the orography of the continental ice sheets and of the distribution of the SST patterns (Barron and Pollard, 2002; Romanova et al., 2006) and thus different modes of atmospheric circulation for MIS-2 and MIS-3 are expected. In comparison to the late Holocene conditions an enhanced baroclinic and temperature gradient in the North Atlantic is triggered by the southward shift of the winter sea ice edge during the last glacial maximum, which is accompanied by a reduction of the meridional overturning circulation (Prange et al., 2002; Knorr and Lohmann, 2007) and which causes much colder winters from Greenland to Asia (Denton et al., 2005). The enhancement of the latitudinal temperature gradient leads to an E to SE shift of the storm tracks with strongest synoptic energy during winter and more or stronger storms over Europe during the LGM, as detected in different GCMs (Laîné et al., 2009; Kageyama et al., 2006; Justino and Peltier, 2005). Model results from this study show that the meridional component becomes significantly stronger for colder climates in general. The strong influence of the topography of the Scandinavian Ice Sheet as mentioned by Justino and Peltier (2005) and Romanova et al. (2006) might have influenced the surface wind fields in the Eifel area in two ways:

1. The southward relocation of the westerlies might reduce the strength of western winds in the Eifel region, and easterly wind, probably supported by a glacial anticyclone, represents this weakening (Sweeney et al., 2004). However, our models indicate more days with easterly air flow for present-day conditions. Furthermore, our model experiments indicate a strengthening of the glacial westerly circulation over Europe. Thus, an anticyclonic air flow is thought to

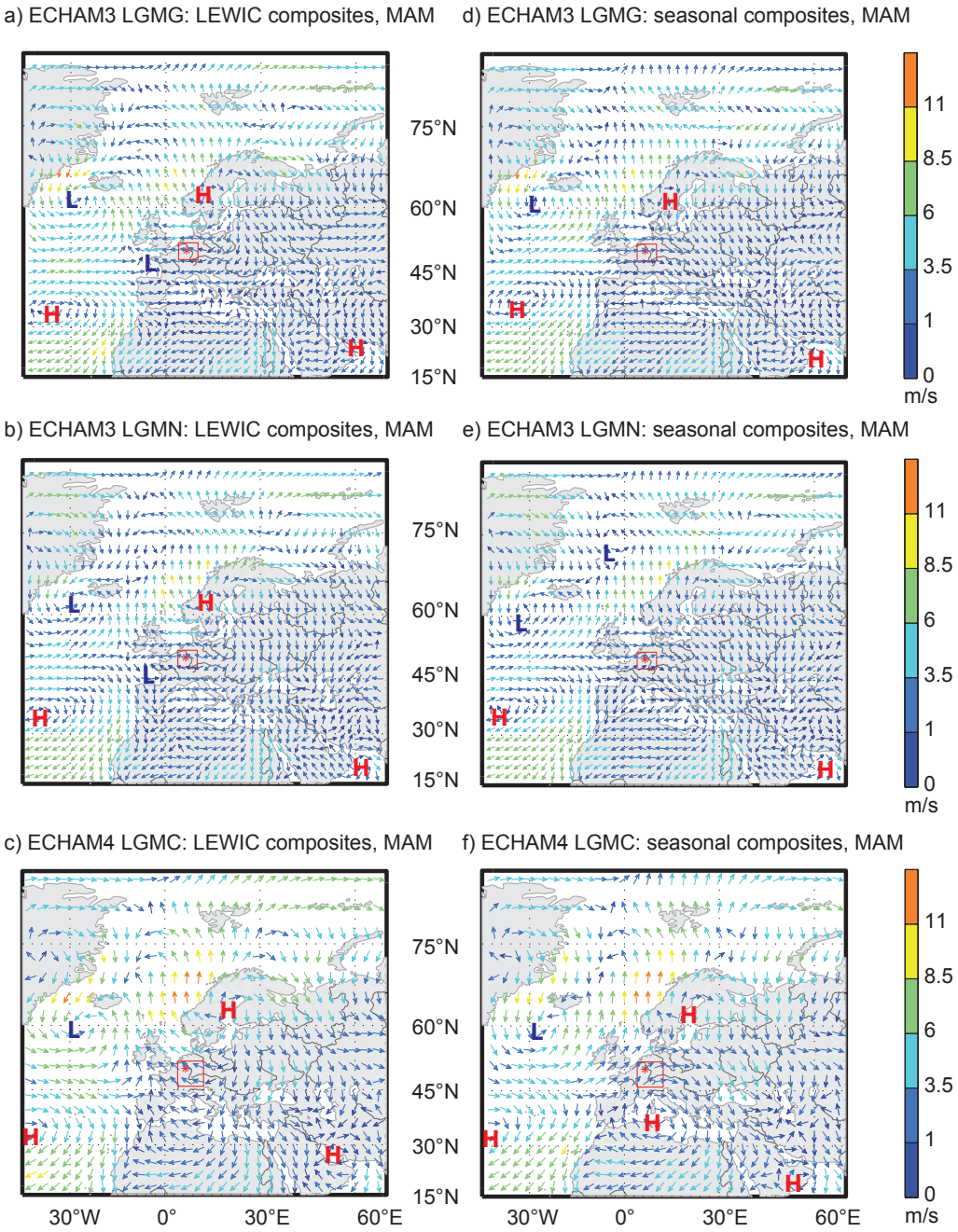

Figure 6.8: Same as Fig. 6.7, showing MAM 10 m-wind vectors, composite maps of daily LEWIC states (left panels) and the seasonal composites (right panels) of the LGM runs. The wind patterns in the LGMG experiment are similar to the PD simulations. In the glacial experiments the anticyclone over the Baltic region (Fig. 6.7) is shifted towards NW. Easterly winds come thus from more south-easterly directions.

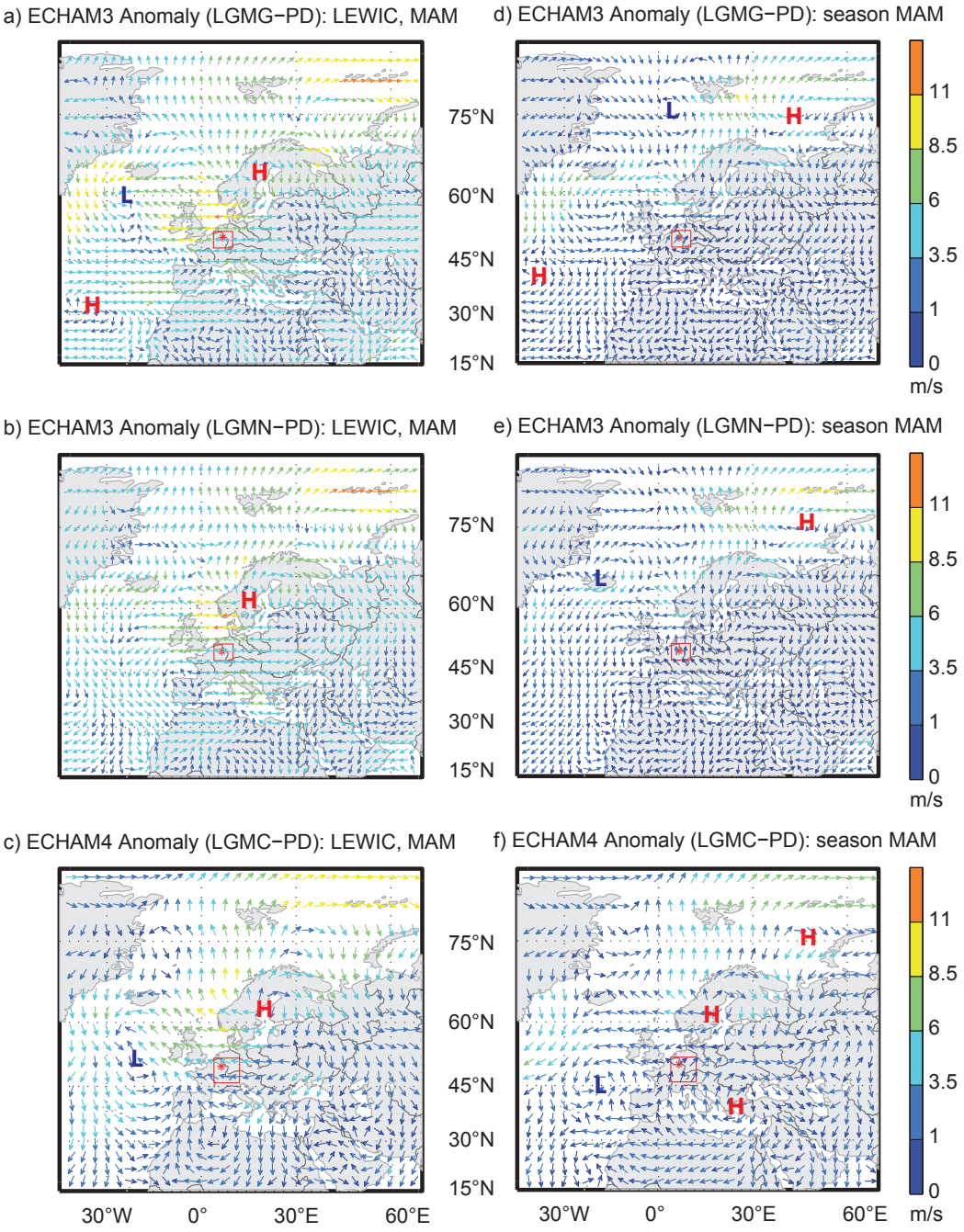

Figure 6.9: Same as Fig. 6.8, showing the 10 m-wind anomalies (LGM runs - PD runs) of daily LEWIC states for all three model runs. The anomaly maps show that easterly winds are stronger and that the mean seasonal flow comes more from southerly directions in the glacial experiments.

play only a minor role for the wind regime in Northwest Europe which is too distant from the ice sheet.

2. The increase of sedimentation patterns from the Eifel sediment core are associated with enhanced turbulence during MIS-3 in comparison with MIS-2. The ECHAM3 experiments with varying prescribed SSTS reconstructions can be interpreted as a substitution-study for stadial (LGMN) and interstadial (LGMG) climate conditions. The CLIMAP summer sea ice margin is similar to GLAMAP's winter sea ice and in the latter reconstruction the Nordic Seas are ice-free during summer (Schäfer-Neth and Paul, 2003). Our numerical experiment with warmer SST patterns at the glacial North Atlantic shows a more turbulent atmosphere with accelerated westerlies over the North Atlantic during LEWIC and the highest amount of modeled wind velocities $\geq 5\,\mathrm{m\,s^{-1}}$ in all experiments. Furthermore, the significant increase in turbulence during MIS-3 is suggested to be strengthened by the abrupt temperature/climate shifts and the impact of the varying size of the continental ice sheets over millennial timescales (e.g. Arz et al., 2007). The annual occurrence of glacial LEWIC shows an increased seasonality in comparison to the present-day simulations with a maximum during the glacial summer. Thus, during glacial periods not only are the winter and spring affected by an increased seasonality (Denton et al., 2005) but so is the atmospheric circulation during the summer. Gustiness is thought to be one of the main drivers of aeolian dust emission (McGee et al., 2010). Stormy days occur in general during the boreal winter and spring. Additionally, in the cold LGMN run the occurrence of stormy days is moved to the late glacial spring. During MIS-2, a stable wave-like distribution of sea level pressure centers leads to a more steady atmospheric circulation (Justino and Peltier, 2005; Romanova et al., 2006), relative to MIS-3 where switches in cold and warm states are detected. This is also indicated by the LGMC experiment with original CLIMAP boundary conditions when stormy east wind days only occur in February and March.

Our reconstruction of the air flow with prevailing easterly wind directions during LEWIC states over Northwestern and Central Europe and the results of Dietrich and Seelos (2010) indicate a shift from a long-lasting high over the Baltic Sea towards the NW, directly above the Scandinavian Ice Sheet. In addition, prevailing east to south-east winds over the study area occur simultanously with enhanced westerly circulation at the North Atlantic. Cyclonic weather conditions between the Iberian

Peninsula and the British Isles are associated with east wind conditions in LGMN (Fig. 6.8).

The here used glacial experiments can be interpreted as substitutes for different periods during MIS-3 and MIS-2 since they show slight differences among each other. But it remains unclear how far this differences are related to the changes which can be observed in the proxy record. Dust emission is a far more complicated feature than air flow and further investigation on the dust emission would be necessary to link the model results to the proxy data. However, many observations of our model experiments are robust and can be found in all glacial runs. Those experiments are characterized by a strongly increased variability of changing wind directions as well as of higher wind velocities. In addition, the relative importance of long-persisting east wind conditions during summer is shown in all glacial experiments as a robust feature.

6.5 Conclusion

The surface wind vectors of different AGCM experiments for glacial and interglacial boundary conditions are analyzed for long-persisting east wind conditions over Europe (LEWIC). By using this LEWIC data a synoptic interpretation of changing wind directions is derived which were obtained from a proxy record from an Eifel Maar lake (Dietrich and Seelos, 2010). This record indicates a high variability of changing wind directions and a higher frequency of easterly wind directions during MIS-3 in general. In contrast, MIS-2 is characterized by a marked drop in easterly wind directions and thus a lower variability of wind direction changes. Later on, the overall frequency of dust storm events is also lower during MIS-2 (Seelos and Sirocko, 2009). This corresponds to a decreasing content of micro particles in the NorthGRIP ice core in comparison to stadials during MIS-3 (Ruth et al., 2007).

A major result from the study is that for all glacial experiments a lower east wind frequency is observed for the European region in comparison to the present-day control runs. It is thus suggested that the glacial anticyclone (associated with east wind) only plays a minor role for the regime of wind directions in Northwest Europe and that the increase of east wind layers cannot be explained by this model. All AGCM runs show dominant southwesterly directions of the surface wind, with an increase of the meridional component during glacial climate states, and a simultaneous enhancement of the wind velocity by 1–3.5 $\mathrm{m\,s^{-1}}$.

The occurrence of long-persisting east wind conditions over Central Europe is

shifted towards late spring in all glacial runs. In addition, winter and spring are shown to be the major seasons of single but strong storm events with easterly directions. The spring is thus favorable for dust transport within easterly winds to the Eifel maar in relation to both single but strong storm events and aeolian dust transport during long-persisting east wind conditions.

Our synoptic reconstruction of the glacial air flow with prevailing easterly wind directions during long-persisting east wind conditions indicates (a) a shift from a long-lasting high over the Baltic Sea towards NW, directly above the Scandinavian Ice Sheet, together with (b) the contemporary occurrence of enhanced westerly circulation over the North Atlantic.

A logical next step could be the systematic analysis of atmospheric blocking patterns as revealed in proxy data. Rimbu and Lohmann (2010) found a clear relation between decadal variability in a central Greenland high-resolution record and their relationship to daily atmospheric circulation patterns from the North Atlantic region. Clusters of circulation from the North Atlantic region (Philipp et al., 2007) are associated with large-scale circulation patterns, wave trains and SST. A subsequent study will explore in more detail the dependence of these structures and of our data on the mean climate.

6.6 Summary of chapter 6

Changes of atmospheric circulation patterns are an essential feature of rapid climate changes which accounts for hemispheric wide teleconnections. Here we present the synoptic interpretation of prevailing paleo wind systems for Central Europe during glacial times and compare the results with a proxy record of changes from easterly to westerly wind directions from maar lake sediments in Germany. This record indicates a high level of east wind and a high variability on a millennial time scale of wind direction changes for the last glacial period.

The basic observations, made on the proxy record, are also demonstrable in the 10 m-wind vectors in ECHAM3 and ECHAM4 model experiments under glacial conditions with different prescribed sea surface temperature patterns. All the glacial experiments show a lower frequency of east wind in comparison to the present-day control runs. However, all the glacial runs also show a high variability of wind direction changes and stronger winds in comparison to the present-day control runs. Furthermore, the analysis of long-persisting east wind conditions (so-called LEWIC events) in the AGCM data shows a stronger seasonality during glacial conditions: all

the different experiments are characterized by an increase of the relative importance during spring and summer.

Synoptic analysis of the air flows with prevailing east wind over Central Europe is given for the spring, which is the most important season for dust emission. Under present-day conditions easterly wind directions are mainly generated by a strong high over the Baltic Sea realm. The different glacial experiments consistently show a shift from a long-lasting high over the Baltic Sea towards the NW, directly above the Scandinavian Ice Sheet, together with the contemporary occurrence of enhanced westerly circulation over the North Atlantic.

Chapter 7

Conclusion and Outlook

The aim of this thesis is the comprehensive reconstruction of atmospheric circulation patterns during the last glacial period (marine isotope stages MIS-3 and MIS-2). It was possible to reconstruct important elements of the glacial paleo climate in Central Europe. While the proxy data from sediment cores lead to a binary signal of the wind direction changes (east versus west wind), a synoptic interpretation using atmospheric circulation models was successful. This shows a possible distribution of high and low pressure areas and thus the direction and strength of wind fields which have the capacity to transport dust.

The proxy data for aeolian dynamics are recorded in maar lake sediments from the West Eifel Volcanic Field (Germany). Two different methods, µXRF scanning and high resolution grain size analysis, are used to measure the dust fraction in two sediment cores. From these data information is derived about atmospheric variability during the last glacial period: (a) the variability in frequency of storm events and (b) the variability of easterly wind directions for MIS-2 and MIS-3.

The detection of easterly wind directions is based on a study which shows the potential of µXRF geochemistry scanning of sediment cores for the quantification of the dust content within sediment cores. The transport distances are estimated for particles in the typical range of the aeolian dust which is found in the maar lake sediments (diameter 20–100 µm). It is shown that the limestone-bearing Eifel North-South zone is the most likely source for carbonate rich aeolian dust in the lake sediments.

Once the source is known, the reconstruction of the wind direction (westerly or easterly) is possible. In general, westerly wind directions dominate in the sediment record, since the wind fields in the Eifel area are strongly influenced by the mid-latitude westerlies. However, the results indicate an increased variability of the overall frequency of dust events and of wind direction changes during MIS-3 in contrast to the

full glacial conditions of MIS-2 where the dust record shows a more stable atmospheric circulation.

This seems to contrast with aeolian records in general in which aeolian sediment accumulation dominates during MIS-2. The most plausible explanation is a change in the source areas and the availability of deflation material rather than an effect of wind speed. Thus, further investigation of available dust source areas for different climate stages would be necessary in future work. An improved estimation of the dust deflation area within the reach of the Eifel maar lakes could be based on a refinement of the provenance analyses as well as on further parameters which control the source areas:

1. Precipitation, for example, is a major factor of in preventing dust emission. It is planned to investigate stable isotope analysis on ostracods found in the glacial section of the sediment cores from the Dehner dry maar as a precipitation proxy. This approach has been allready successfully demonstrated in a diploma thesis (Adams, 2010). In addition, these precipitation data could help to improve numerical climate model results for the analysis of soil moisture and vegetation. Using this model-data comparison approach the path of aeolian sediment transport and thus the atmospheric circulation patterns could be elaborated.

2. The source areas should be identified in more detail by means of trace element analysis of aeolian transported carbonates and heavy minerals. The measurement of strontium isotopes could indicate whether an aeolian transported carbonate particle might have its origin in the Devonian lime stone units just within the Eifel North-South zone or whether it comes from the Triassic limestone of the *Trierer Bucht* in the south or from another and yet unknown source. However, this approach could add a third possible wind direction to the data set of paleo wind direction changes.

3. A state-of-the-art estimation of particle transport distances could be applied by recent numerical dust emission models, like the Weather Research and Forecasting (WRF) Model (Darmenova et al., 2009), with glacial boundary conditions. Using this approach the dust fluxes from different source areas (like the English Channel, the Eifel North-South Zone or the Rhine valley) towards the Dehner dry maar could be more intensively investigated.

In a further study within this thesis the air flow of the 10 m-wind vectors is analyzed, using atmospheric general circulation models. Spring is thought to be the most

important season for dust emission. To explore this, a synoptic analysis is made of spring air flows with prevailing east winds over Central Europe. Under present-day conditions easterly wind directions are mainly generated by a strong high over the Baltic Sea region. The different glacial experiments consistently show a shift from a long-lasting high over the Baltic Sea towards the NW, directly above the Scandinavian Ice Sheet, with contemporary enhanced westerly circulation over the North Atlantic. In addition, all the glacial experiment runs show a high variability in wind direction changes and stronger winds in comparison to the present-day control runs. Furthermore, the analysis of long-persisting east wind conditions (so-called LEWIC events) in the AGCM data shows a stronger seasonality during glacial conditions: all the different experiments are characterized by an increase of the relative importance of LEWIC occurence during spring and summer.

The glacial experiments carried out here can be interpreted as substitutes for different periods during MIS-3 and MIS-2 since they show slight differences between each other. It remains unclear how far these differences are related to the changes which can be observed in the proxy record. Dust emission is a far more complicated process than air flow and further investigation of the dust emission would be necessary to link the model results to the proxy data. However, it may be supposed that the significant decrease in the atmospheric circulation variability from MIS-3 to MIS-2 which is shown in the dust proxy records is influenced by less abrupt temperature/climate shifts within millennial timescales.

Atmospheric turbulence during MIS-3 and MIS-2 might have different causes. However, the continental ice sheets seem to play a major role by influencing the atmospheric circulation. During MIS-3 turbulence might be strengthened by the varying size of the continental ice sheets over millennial timescales (e.g. Arz et al., 2007). During MIS-2 a stable wave-like distribution of sea level pressure centers leads to more stable atmospheric circulation relative to MIS-3 where cold and warm states switches are detected (e.g. Justino and Peltier, 2005; Romanova et al., 2006). But in addition, during the full glacial MIS-2 it is assumed that with an increasing temperature gradient the mid-latitude jets are strengthened, which it is suggested to be accompanied by enhanced synoptic eddy wind variance (e.g. McGee et al., 2010). Numerical climate models with a coupled ice model should be applied to the different climatic conditions of MIS-2 and MIS-3 to investigate what drives atmospheric turbulence. Unfortunately, fully coupled atmosphere-ocean-ice models are so far not available. The improvement, mentioned above, of the wind direction proxy to include more wind directions could give further hints as to past atmospheric circulation patterns.

The present thesis, by focusing on the reconstruction of glacial atmospheric circulation patterns, serves as a starting point for future studies on glacial climate research. Once again, the combination of numerical models, to enhance understanding of processes in the climate system, with proxy data from the environmental record is the key to a comprehensive approach to paleo climatic reconstruction.

Bibliography

Adams, C. (2010). Häufigkeit und Isotopensignal von Ostrakoden in Sedimenten aus dem Dehner Trockenmaar (Eifel) für die Zeit 13.000–40.000 J.v.h. Diplomarbeit, Johannes Gutenberg-Universität, Mainz.

Andersen, K. K., A. Svensson, S. J. Johnsen, S. O. Rasmussen, M. Bigler, R. Röthlisberger, U. Ruth, M.-L. Siggaard-Andersen, J. Peder Steffensen, D. Dahl-Jensen, B. M. Vinther, and H. B. Clausen (2006). The Greenland Ice Core Chronology 2005, 15-42 ka. Part 1: constructing the time scale: Critical Quaternary Stratigraphy. *Quaternary Science Reviews 25*(23-24), 3246–3257.

Antoine, P., D.-D. Rousseau, O. Moine, S. Kunesch, C. Hatté, A. Lang, H. Tissoux, and L. Zöller (2009). Rapid and cyclic aeolian deposition during the Last Glacial in European loess: a high-resolution record from Nussloch, Germany. *Quaternary Science Reviews 28*(25–26), 2955–2973.

Antoine, P., D.-D. Rousseau, L. Zöller, A. Lang, A.-V. Munaut, C. Hatté, and M. Fontugne (2001). High-resolution record of the last Interglacial-glacial cycle in the Nussloch loess-palaeosol sequences, Upper Rhine Area, Germany. *Quaternary International 76-77*, 211–229.

Arnold, N. S., T. H. van Andel, and V. Valen (2002). Extent and Dynamics of the Scandinavian Ice Sheet during Oxygen Isotope Stage 3 (65,000-25,000 yr B.P.). *Quaternary Research 57*(1), 38–48.

Arya, S. P. S. (1975). A Drag Partition Theory for Determining the Large-Scale Roughness Parameter and Wind Stress on the Arctic Pack Ice. *J. Geophys. Res. 80*(24), 3447–3454.

Arz, H. W., F. Lamy, A. Ganopolski, N. Nowaczyk, and J. Pätzold (2007). Dominant Northern Hemisphere climate control over millennial-scale glacial sea-level variability. *Quaternary Science Reviews 26*(3-4), 312–321.

Bagnold, R. A. (1941). *The physics of blown sand and desert dunes* (Dover ed., 1. publ. in 2005, is an unabridged republ. of the ed. publ. by Methuen and Co., Ltd., London, in 1954 ed.). London: Methuen.

Barron, E. and D. Pollard (2002). High-Resolution Climate Simulations of Oxygen Isotope Stage 3 in Europe. *Quaternary Research 58*(3), 296–309.

Bartlein, P. J., K. H. Anderson, P. M. Anderson, M. E. Edwards, C. J. Mock, R. S. Thompson, R. S. Webb, T. Webb III, and C. Whitlock (1998). Paleoclimate simulations for North America over the past 21,000 years: features of the simulated climate and comparisons with paleoenvironmental data. *Quaternary Science Reviews 17*(6), 549–586.

Berger, A. and M. F. Loutre (2002). An exceptionally long interglacial ahead. *Science 297*, 1287–1288.

BGR (2002). Geologische Karte der Bundesrepublik Deutschland 1:1000000: GÜK1000.

Bond, G., W. Broecker, S. Johnsen, J. McManus, L. Labeyrie, J. Jouzel, and G. Bonani (1993). Correlations between climate records from North Atlantic sediments and Greenland ice. *Nature 365*, 143–147.

Böning, P., E. Bard, and J. Rose (2007). Toward direct, micron-scale XRF elemental maps and quantitative profiles of wet marine sediments. *Geochemistry Geophysics Geosystems 8*(5), Q05004.

Bourillet, J.-F., J.-Y. Reynaud, A. Baltzer, and S. Zaragosi (2003). The 'Fleuve Manche': the submarine sedimentary features from the outer shelf to the deep-sea fans. *Journal of Quaternary Science 18*(3-4), 261–282.

Boyle, J. F. (2000). Rapid elemental analysis of sediment samples by isotope source XRF. *Journal of Paleolimnology 23*(2), 213–221.

Boyle, J. F. (2001). Inorganic geochemical methods in palaeolimnology. In W. M. Last, J. P. Smol, and H. J. B. Birks (Eds.), *Tracking Environmental Change Using Lake Sediments: Physical and Geochemical Methods*, Volume 2, pp. 83–141. Springer.

Brauer, A., C. Endres, C. Günter, T. Litt, M. Stebich, and J. F. W. Negendank (1999). High resolution sediment and vegetation responses to Younger Dryas climate change in varved lake sediments from Meerfelder Maar, Germany. *Quaternary Science Reviews 18*(3), 321–329.

Brauer, A., G. H. Haug, P. Dulski, D. M. Sigman, and J. F. W. Negendank (2008). An abrupt wind shift in western Europe at the onset of the Younger Dryas cold period. *Nature Geoscience 1*(8), 520–523.

Büchel, G. (1994). Vulkanologische Karte West-und Hocheifel. *Landesvermessungsamt Rheinland-Pfalz*.

Büchel, G. and V. Lorenz (1982). Zum Alter des Maarvulkanismus der Westeifel. *Neues Jahrbuch für Geologie und Paläontologie 163*, 1–22.

Christiansen, H. H. (2004). Windpolished boulders and bedrock in the Scottish Highlands: evidence and implications of Late Devensian wind activity. *Boreas 33*(1), 82–94.

Christiansen, H. H. and H. Svensson (1998). Windpolished boulders as indicators of a Late Weichselian wind regime in Denmark in relation to neighbouring areas. *Permafrost and Periglacial Processes 9*(1), 1–21.

Cilek, V. (2001). The loess deposits of the Bohemian Massif: silt provenance, palaeometeorology and loessification processes. *Quaternary International 76–77*, 123–128.

Clark, P. U., A. S. Dyke, J. D. Shakun, A. E. Carlson, J. Clark, B. Wohlfarth, J. X. Mitrovica, S. W. Hostetler, and A. M. McCabe (2009). The Last Glacial Maximum. *Science 325*(5941), 710–714.

CLIMAP project members (1981). Seasonal reconstruction of the earth's surface at the last glacial maximum. *Geological Society of America Map and Chart Series 36*.

COHMAP Members (1988). Climatic changes of the last 18,000 years: observations and model simulations. *Science 241*, 1043–1052.

Croci-Maspoli, M., C. Schwierz, and H. Davies (2007). Atmospheric blocking: space-time links to the NAO and PNA. *Climate Dynamics 29*(7), 713–725.

Darmenova, K., I. N. Sokolik, Y. Shao, B. Marticorena, and G. Bergametti (2009). Development of a physically based dust emission module within the Weather Research and Forecasting (WRF) model: Assessment of dust emission parameterizations and input parameters for source regions in Central and East Asia. *J. Geophys. Res. 114*(D14), D14201.

Denton, G. H., R. B. Alley, G. C. Comer, and W. S. Broecker (2005). The role of seasonality in abrupt climate change. *Quaternary Science Reviews 24*(10-11), 1159–1182.

Dietrich, S., G. Lohmann, M. Werner, K. Seelos, and F. Sirocko (subm.). Reconstruction of European Atmospheric Circulation Patterns in the Spring Season during the Last Glacial. *Climate Dynamics*.

Dietrich, S. and K. Seelos (2010). The reconstruction of easterly wind directions for the Eifel region (Central Europe) during the period 40.3–12.9 ka BP. *Climate of the Past 6*, 145–154.

Dietrich, S. and F. Sirocko (2009). Korngrößenanalyse und Sedimentgeochemie als Grundlage der Klima- und Wetterrekonstruktion. In F. Sirocko (Ed.), *Wetter, Klima, Menschheitsentwicklung*, pp. 26–32. Darmstadt: Wiss. Buchges.

Dietrich, S. and F. Sirocko (2010). The Potential of Dust Detection by means of µXRF Scanning in Eifel Maar Lake Sediments. *E&G - Quaternary Science Journal*, acc.

Dietrich, W. E. (1982). Settling velocity of natural particles. *Water Resour. Res. 18*(6), 1615–1626.

Engstrom and H. E. Wright Jr (1984). Chemical stratigraphy of lake sediments as a record of environmental change. In E. Y. Haworth and J. W. G. Lund (Eds.), *Lake sediments and environmental history*. Leicester Univ. Pr.

Fagel, N., L. Y. Alleman, L. Granina, F. Hatert, E. Thamo-Bozso, R. Cloots, and L. Andre (2005). Vivianite formation and distribution in Lake Baikal sediments: Progress towards reconstructing past climate in Central Eurasia, with special emphasis on Lake Baikal. *Global and Planetary Change 46*(1-4), 315–336.

Fécan, F., B. Marticorena, and G. Bergametti (1999). Parametrization of the increase of the aeolian erosion threshold wind friction velocity due to soil moisture for arid and semi-arid areas. *Annales Geophysicae 17*(1), 149–157.

Ferguson, R. I. and M. Church (2004). A Simple Universal Equation for Grain Settling Velocity. *Journal of Sedimentary Research 74*(6), 933–937.

Fischer, H., F. Fundel, U. Ruth, B. Twarloh, A. Wegner, R. Udisti, S. Becagli, E. Castellano, A. Morganti, M. Severi, E. Wolff, G. Littot, R. Röthlisberger, R. Mulvaney, M. A. Hutterli, P. Kaufmann, U. Federer, F. Lambert, M. Bigler, M. Hansson, U. Jonsell, M. de Angelis, C. Boutron, M.-L. Siggaard-Andersen, J. P. Steffensen, C. Barbante, V. Gaspari, P. Gabrielli, and D. Wagenbach (2007). Reconstruction of millennial changes in dust emission, transport and regional sea ice coverage using the deep EPICA ice cores from the Atlantic and Indian Ocean sector of Antarctica. *Earth and Planetary Science Letters 260*(1-2), 340–354.

Francus, P., H. Lamb, T. Nakakawa, M. Marshall, E. T. Brown, and Suigetsu 2006 Project Members (2009). The potential of high-resolution X-ray fluorescence core scanning: Applications in paleolimnology: A new generation of XRF core scanners allows rapid, non-destructive acquisition of high-resolution geochemical and X-radiographic data from lacustrine sediment cores, facilitating new approaches to many applications in paleolimnology, including pollution detection, varve counting, and estimation of past ecosystem productivity. *PAGES News 17*(3), 93–95.

Frechen, M. (1999). Upper Pleistocene loess stratigraphy in Southern Germany. *Quaternary Science Reviews 18*(2), 243–269.

Frechen, M., B. van Vliet-Lanoë, and P. van den Haute (2001). The Upper Pleistocene loess record at Harmignies/Belgium – high resolution terrestrial archive of climate forcing. *Palaeogeography, Palaeoclimatology, Palaeoecology 173*(3-4), 175–195.

Friedrich, M., B. Kromer, M. Spurk, J. Hofmann, and K. Felix Kaiser (1999). Paleo-environment and radiocarbon calibration as derived from Lateglacial/Early Holocene tree-ring chronologies. *Quaternary International 61*(1), 27–39.

Gächter, R. and B. Müller (2003). Why the Phosphorus Retention of Lakes Does Not Necessarily Depend on the Oxygen Supply to Their Sediment Surface. *Limnology and Oceanography 48*(2), 929–933.

Geyh, M. A. (2005). *Handbuch der physikalischen und chemischen Altersbestimmung.* Darmstadt: Wiss. Buchges.

Gillette, D. A. (1977). Fine Particulate Emissions Due to Wind Erosion. *Transactions of the American Society of Agricultural Engineers 20*(5), 890–897.

Gillette, D. A. (1988). Threshold Friction Velocities for Dust Production for Agricultural Soils. *Journal of Geophysical Research 93*(D10), 12645–12662.

Godzik, J. (1991). Sedimentological record of aeolian processes from the Upper Plenivistulian and the turn of Pleni- and Late Vistulian in Central Poland. *Zeitschrift für Geomorphologie, Supplement-Band 90*, 51.60.

Goossens, D. (1988). The effect of surface curvature on the deposition of loess: A physical model. *Catena 15*(2), 179–194.

Goossens, D. (2001). The aeolian dust accumulation curve. *Earth Surf. Process. Landforms 26*(11), 1213–1219.

Govindaraju, K. (1989). 1989 compilation of working values and sample description for 272 geostandards. *Geostandards and Geoanalytical Research 13*, 1–113.

Greeley, R. and J. D. Iversen (1987). *Wind as a Geological Process: On Earth, Mars, Venus and Titan*. Cambridge: Cambridge University Press.

Gulev, S. K., O. Zolina, and S. Grigoriev (2001). Extratropical cyclone variability in the Northern Hemisphere winter from the NCEP/NCAR reanalysis data. *Climate Dynamics 17*(10), 795–809.

Gwiazda, R. H., S. R. Hemming, and W. S. Broecker (1996). Provenance of icebergs during Heinrich event 3 and the contrast to their sources during other Heinrich episodes. *Paleoceanography 11*(4).

Haase, D., J. Fink, G. Haase, R. Ruske, M. Pécsi, H. Richter, M. Altermann, and K.-D. Jäger (2007). Loess in Europe – its spatial distribution based on a European Loess Map, scale 1:2,500,000. *Quaternary Science Reviews 26*(9-10), 1301–1312.

Haesaerts, P., H. Mestdagh, and D. Bosquet (1999). The sequence of Remicourt (Hesbaye, Belgium): new insights on the pedoand chronostratigraphy of the Rocourt soil. *Geologica Belgica (Belgium)*.

Hatté, C., M. Fontugne, D.-D. Rousseau, P. Antoine, L. Zöller, N. T. Laborde, and I. Bentaleb (1998). d13C variations of loess organic matter as a record of the vegetation response to climatic changes during the Weichselian. *Geology 26*(7), 583–586.

Hatté, C. and J. Guiot (2005). Palaeoprecipitation reconstruction by inverse modelling using the isotopic signal of loess organic matter: application to the Nußloch loess sequence (Rhine Valley, Germany). *Climate Dynamics 25*(2), 315–327.

Hemming, S. R. (2004). Heinrich events: Massive late Pleistocene detritus layers of the North Atlantic and their global climate imprint. *Reviews on Geophysics 42*, –.

Hostetler, S. W., P. U. Clark, P. J. Bartlein, A. C. Mix, and N. J. Pisias (1999). Atmospheric transmission of north Atlantic Heinrich events. *Journal of Geophysical Research 104*(D4).

Hsü, K. J. (2004). *Physics of sedimentology: Textbook and reference*. Berlin: Springer.

Huijzer, A. S. (1993). *Cryogenic macrofabrics and macrostructures: interrelations, processes, and environmental significance*. Ph. D. thesis, Vrije Universiteit, Amsterdam.

Huijzer, B. and J. Vandenberghe (1998). Climatic reconstruction of the Weichselian Pleniglacial in north western and central Europe. *Journal of Quaternary Science 13*(5), 391–417.

Iriondo, M. H. and D. M. Kröhling (2007). Non-classical types of loess. *Sedimentary Geology 202*(3), 352–368.

Isarin, R. F., H. Renssen, and E. A. Koster (1997). Surface wind climate during the Younger Dryas in Europe as inferred from aeolian records and model simulations. *Palaeogeography, Palaeoclimatology, Palaeoecology 134*(1), 127–148.

Isarin, R. F. B., H. Renssen, and J. Vandenberghe (1998). The impact of the North Atlantic Ocean on the Younger Dryas climate in northwestern and central Europe. *Journal of Quaternary Science 13*(5), 447–453.

Iverson, J. D. and B. R. White (1982). Saltation threshold on Earth, Mars and Venus. *Sedimentology 29*(1), 111–119.

Johnsen, S. J., D. Dahl-Jensen, N. Gundestrup, J. P. Steffensen, H. B. Clausen, H. Miller, V. Masson-Delmotte, A. E. Sveinbjörnsdottir, and J. White (2001). Oxygen isotope and palaeotemperature records from six Greenland ice-core stations: Camp Century, Dye-3, GRIP, GISP2, Renland and NorthGRIP. *J. Quaternary Sci. 16*(4), 299–307.

Justino, F. and W. R. Peltier (2005). The glacial North Atlantic Oscillation. *Geophysical Research Letters 32*(L21803).

Juvigne, E., P. Haesaerts, H. Mestdagh, A. Pissart, and S. Balescu (1996). Révision du stratotype loessique de Kesselt (Limbourg, Belgique)= Revision of the loess stratotype of Kesselt (Limbourg, Belgium). *Comptes rendus de l'Académie des sciences. Série 2. Sciences de la terre et des planètes 323*(9), 801–807.

Kageyama, M., A. Laîné, A. Abe-Ouchi, P. Braconnot, E. Cortijo, M. Crucifix, A. de Vernal, J. Guiot, C. D. Hewitt, A. Kitoh, M. Kucera, O. Marti, R. Ohgaito, B. Otto-Bliesner, W. R. Peltier, A. Rosell-Melé, G. Vettoretti, S. L. Weber, and Y. Yu (2006). Last Glacial Maximum temperatures over the North Atlantic, Europe and western Siberia: a comparison between PMIP models, MARGO sea-surface temperatures and pollen-based reconstructions. *Quaternary Science Reviews 25*(17-18), 2082–2102.

Kasse, C. (2002). Sandy aeolian deposits and environments and their relation to climate during the Last Glacial Maximum and Lateglacial in northwest and central Europe. *Progress in Physical Geography 26*(4), 507–532.

Kido, Y., T. Koshikawa, and R. Tada (2006). Rapid and quantitative major element analysis method for wet fine-grained sediments using an XRF microscanner. *Marine Geology 229*(3-4), 209–225.

Knorr, G. and G. Lohmann (2007). Rapid transitions in the Atlantic thermohaline circulation triggered by global warming and meltwater during the last deglaciation. *Geochem. Geophys. Geosyst. 8*(12), Q12006.

Kohfeld, K. E. and S. P. Harrison (2001). DIRTMAP: the geological record of dust. *Earth-Science Reviews 54*(1-3), 81–114.

Koinig, K. A., W. Shotyk, A. F. Lotter, C. Ohlendorf, and M. Sturm (2003). 9000 years of geochemical evolution of lithogenic major and trace elements in the sediment of an alpine lake – the role of climate, vegetation, and land-use history. *Journal of Paleolimnology 30*(3), 307–320.

Krook, L. (1993). Heavy minerals in the Belvédère deposits. *Mededelingen Rijks Geologische Dienst 47*, 25–30.

Kutzbach, J. E. and H. E. Wright (1985). Simulation of the climate of 18000 years BP: results for the North American, North Atlantic, European sector and comparison with the geological records of North America. *Quaternary Science Reviews 4*, 147–187.

Laîné, A., M. Kageyama, D. Salas-Mélia, A. Voldoire, G. Rivière, G. Ramstein, S. Planton, S. Tyteca, and J. Peterschmitt (2009). Northern hemisphere storm tracks during the last glacial maximum in the PMIP2 ocean-atmosphere coupled models: energetic study, seasonal cycle, precipitation. *Climate Dynamics 32*(5), 593–614.

Lambeck, K., T. M. Esat, and E.-K. Potter (2002). Links between climate and sea levels for the past three million years. *Nature 419*(6903), 199–206.

Laskar, J., P. Robutel, F. Joutel, M. Gastineau, A. C. Correia, and B. Levrard (2004). A long-term numerical solution for the insolation quantities of the Earth. *A&A 428*(1), 261–285.

Laurent, B., B. Marticorena, G. Bergametti, and F. Mei (2006). Modeling mineral dust emissions from Chinese and Mongolian deserts: Monitoring and Modelling of Asian Dust Storms. *Global and Planetary Change 52*(1-4), 121–141.

Lautridou, J. P. and J. C. Ozouf (1982). Experimental frost shattering: 15 years of research at the Centre de Géomorphologie du CNRS. *Progress in Physical Geography 6*, 215–232.

Lea, D. W., D. K. Pak, L. C. Peterson, and K. A. Hughen (2003). Synchroneity of Tropical and High-Latitude Atlantic Temperatures over the Last Glacial Termination. *Science 131*(5), 1361–1364.

Lenaz, D., R. Marciano, D. Veres, S. Dietrich, and F. Sirocko (2010). Mineralogy of the Dehner and Jungferweiher maar tephras (Eifel, Germany). *Neues Jahrbuch für Geologie und Paläontologie - Abhandlungen 257*(1), 55–67.

Li, C. and D. S. Battisti (2008). Reduced Atlantic Storminess during Last Glacial Maximum: Evidence from a Coupled Climate Model. *Journal of Climate 21*(14), 3561–3579.

Lohmann, G. and S. Lorenz (2000). On the hydrological cycle under paleoclimatic conditions as derived from AGCM simulations. *Journal of Geophysical Research 105*(D13), 417—436.

Magny, M. (1999). Lake-level fluctuations in the Jura and french subalpine ranges associated with ice-rafting events in the north atlantic and variations in the polar atmospheric circulation. *Quaternaire 10*(1), 61–64.

Magny, M. (2004). Holocene climate variability as reflected by mid-European lake-level fluctuations and its probable impact on prehistoric human settlements: The record of Human /Climate interaction in Lake Sediments. *Quaternary International 113*(1), 65–79.

Maher, B. A., J. M. Prospero, D. Mackie, D. Gaiero, P. P. Hesse, and Y. Balkanski (2010). Global connections between aeolian dust, climate and ocean biogeochemistry at the present day and at the last glacial maximum. *Earth-Science Reviews 99*(1-2), 61–97.

Marticorena, B. and G. Bergametti (1995). Modeling the atmospheric dust cycle: 1. Design of a soil-derived dust emission scheme. *Journal of Geophysical Research 100*(D8), 16415–16430.

McGee, D., W. S. Broecker, and G. Winckler (2010). Gustiness: The driver of glacial dustiness? *Quaternary Science Reviews 29*(17-18), 2340–2350.

Melles, M., J. Brigham-Grette, O. Glushkova, P. Minyuk, N. Nowaczyk, and H.-W. Hubberten (2007). Sedimentary geochemistry of core PG1351 from Lake El'gygytgyn—a sensitive record of climate variability in the East Siberian Arctic during the past three glacial–interglacial cycles. *Journal of Paleolimnology 37*(1), 89–104.

Michalakes, J., J. Dudhia, D. Gill, T. Henderson, J. Klemp, W. Skamarock, and W. Wang (2004). The Weather Research and Forecast Model: Software Architecture and Performance.

Middleton, N. J., P. R. Betzer, and P. A. Bull (2001). Long-range transport of [']giant' aeolian quartz grains: linkage with discrete sedimentary sources and implications for protective particle transfer. *Marine Geology 177*(3-4), 411–417.

Musson, F. M. and A. G. Wintle (1994). Luminescence dating of the loess profile at Dolní Vestonice, Czech Republic. *Quaternary Science Reviews 13*(5-7), 411–416.

Nawrocki, J., O. Polechonska, A. Boguckij, and M. Lanczont (2006). Palaeowind directions recorded in the youngest loess in Poland and western Ukraine as derived from anisotropy of magnetic susceptibility measurements. *Boreas 35*, 266–271.

Neff, J., A. Ballantyne, G. Farmer, N. Mahowald, J. Conroy, C. Landry, J. Overpeck, T. Painter, C. Lawrence, and R. Reynolds (2008). Increasing eolian dust deposition in the western United States linked to human activity. *Nature Geoscience 1*(3), 189–195.

Nickling, W. G. and C. M. Neuman (2009). Aeolian Sediment Transport. In A. J. Parsons and A. D. Abrahams (Eds.), *Geomorphology of Desert Environments*, pp. 517–555. Springer Netherlands.

NorthGRIP Members (2004). High-resolution record of Northern Hemisphere climate extending into the last interglacial period. *Nature 431*(7005), 147–151.

Oke, T. R. (2009). *Boundary layer climates* (2. ed., reprinted. ed.). London: Routledge.

Owen, P. R. (1960). Dust deposition from a turbulent airstream. *Internation Journal of Air Pollution 3*(1–3), 8–25.

Pausata, F. S. R., C. Li, J. J. Wettstein, K. H. Nisancioglu, and D. S. Battisti (2009). Changes in atmospheric variability in a glacial climate and the impacts on proxy data: a model intercomparison. *Climate of the Past 5*(3), 489–502.

Pfahl, S. (2009). *Exploring physical processes related to past climate proxies: lake sediments and stable water isotopes*. Ph. D. thesis, Johannes Gutenberg-Universität, Mainz.

Pfahl, S., F. Sirocko, K. Seelos, S. Dietrich, A. Walter, and H. Wernli (2009). A new windstorm proxy from lake sediments - a comparison of geological and meteorological data from western Germany for the period 1965-2001. *Journal of Geophysical Research 114*, D18106.

Pflaumann, U., M. Sarnthein, M. Chapman, L. d'Abreu, B. Funnell, M. Huels, T. Kiefer, M. Maslin, H. Schulz, J. Swallow, S. van Kreveld, M. Vautravers, E. Vo-

gelsang, and M. Weinelt (2003). Glacial North Atlantic: Sea-surface conditions reconstructed by GLAMAP 2000. *Paleoceanography 18*(3), 1065.

Philipp, A., P. M. Della-Marta, J. Jacobeit, D. R. Fereday, P. D. Jones, A. Moberg, and H. Wanner (2007). Long-Term Variability of Daily North Atlanticic European Pressure Patterns since 1850 Classified by Simulated Annealing Clustering. *Journal of Climate 20*(16), 4065–4095.

Prandtl, L. (1935). The mechanics of viscous fluids. In F. Durand (Ed.), *Aerodynamic Theory*, Volume 111, pp. 57–109. Berlin: Julius Springer.

Prange, M., V. Romanova, and G. Lohmann (2002). The glacial thermohaline circulation: Stable or unstable? *Geophysical Research Letters 29*(21), 2028.

Prasad, S., A. Witt, U. Kienel, P. Dulski, E. Bauer, and G. Yancheva (2009). The 8.2 ka event: Evidence for seasonal differences and the rate of climate change in western Europe. *Global and Planetary Change 67*(3-4), 218–226.

Pye, K. (1987). *Aeolian dust and dust deposits*. Academic Press London.

Pye, K. (1995). The nature, origin and accumulation of loess. *Quaternary Science Reviews 14*(7-8), 653–667.

Pye, K. and H. Tsoar (2009). *Aeolian sand and sand dunes*. Berlin: Springer.

Rasmussen, S. O., K. K. Andersen, A. M. Svensson, J. P. Steffensen, B. M. Vinther, H. B. Clausen, M. L. Siggaard-Andersen, S. J. Johnsen, L. B. Larsen, D. Dahl-Jensen, M. Bigler, R. Röthlisberger, H. Fischer, K. Goto-Azuma, M. E. Hansson, and U. Ruth (2006). A new Greenland ice core chronology for the last glacial termination. *Journal of Geophysical Research 111*(D6), D06102.

Rasmussen, S. O., I. K. Seierstad, K. K. Andersen, M. Bigler, D. Dahl-Jensen, and S. J. Johnsen (2008). Synchronization of the NGRIP, GRIP, and GISP2 ice cores across MIS 2 and palaeoclimatic implications: INTegration of Ice-core, Marine and Terrestrial records (INTIMATE): Refining the record of the Last Glacial-Interglacial Transition. *Quaternary Science Reviews 27*(1-2), 18–28.

Reimer, P. J., M. G. L. Baillie, E. Bard, A. Bayliss, J. W. Beck, P. G. Blackwell, C. B. Ramsey, C. E. Buck, G. S. Burr, R. L. Edwards, M. Friedrich, P. M. Grootes, T. P. Guilderson, I. Hajdas, T. J. Heaton, A. G. Hogg, K. A. Hughen, K. F. Kaiser,

B. Kromer, F. G. McCormac, S. W. Manning, R. W. Reimer, D. A. Richards, J. R. Southon, S. Talamo, C. S. M. Turney, J. van der Plicht, and C. E. Weyhenmeyer (2009). IntCal09 and Marine09 radiocarbon age calibration curves, 0-50,000yeats cal BP.

Renssen, H. and R. F. B. Isarin (2001). The two major warming phases of the last deglaciation at 14.7 and 11.5 ka cal BP in Europe: climate reconstructions and AGCM experiments. *Global and Planetary Change 30*(1-2), 117–153.

Renssen, H., C. Kasse, J. Vandenberghe, and S. J. Lorenz (2007). Weichselian Late Pleniglacial surface winds over northwest and central Europe: a model-data comparison. *Journal of Quaternary Science 22*(3), 281–293.

Renssen, H., M. Lautenschlager, and C. J. E. Schuurmans (1996). The atmospheric winter circulation during the Younger Dryas stadial in the Atlantic/European sector. *Climate Dynamics 12*(12), 813–824.

Rimbu, N. and G. Lohmann (2010). Decadal Variability in a Central Greenland High-Resolution Deuterium Isotope Record and Its Relationship to the Frequency of Daily Atmospheric Circulation Patterns from the North Atlantic Region. *Journal of Climate 23*(17), 4608–4618.

Rimbu, N., G. Lohmann, and K. Grosfeld (2007). Northern Hemisphere atmospheric blocking in ice core accumulation records from northern Greenland. *Geophysical Research Letters 34*(9), 9704.

Rimbu, N., G. Lohmann, and K. Grosfeld (2008). Northern hemisphere atmospheric blocking in ice core accumulation records from northern Greenland. *PAGES News 16*(2).

Roberts, A. (2010). ncquiverref: MATLAB toolbox.

Roeckner, E. and Coauthors (1992). Simulation of the present-day climate with the ECHAM model: Impact of model physics and resolution. *Max-Planck-Institut für Meteorologie Rep 93*, 171.

Roeckner, E. and Coauthors (1996). The atmospheric general circulation model ECHAM-4: Model description and simulation of present-day climate. *Max-Planck-Institut für Meteorologie Rep* (218), 171.

Röhl, U. and L. J. Abrams (2000). High-resolution, downhole and non-destructive core measurements from sites 999 and 1001 in the Caribbean Sea: application to the late Paleocene thermal maximum. In R. M. Leckie, H. Sigurdsson, G. D. Acton, and G. Draper (Eds.), *Proc. ODP Sci. Results*, Volume 165 of *(Ocean Drilling Program)*, pp. 191–203. College Station, TX.

Romanova, V., G. Lohmann, K. Grosfeld, and M. Butzin (2006). The relative role of oceanic heat transport and orography on glacial climate. *Quaternary Science Reviews 25*(7-8), 832–845.

Romanova, V., M. Prange, and G. Lohmann (2004). Stability of the glacial thermohaline circulation and its dependence on the background hydrological cycle. *Climate Dynamics 22*(5), 527–538.

Rothwell, R. G. (Ed.) (2006). *New Techniques in Sediments Core Analysis*, Volume 267 of *Special Publication*. London: Geological Society.

Rousseau, D. D., P. Antoine, C. Hatté, A. Lang, L. Zöller, M. Fontugne, D. Ben Othman, J. M. Luck, O. Moine, M. Labonne, I. Bentaleb, and D. Jolly (2002). Abrupt millennial climatic changes from Nussloch (Germany) Upper Weichselian eolian records during the Last Glaciation. *Quaternary Science Reviews 21*(14-15), 1577–1582.

Rousseau, D.-D., P. Antoine, S. Kunesch, C. Hatté, J. Rossignol, S. Packman, A. Lang, and C. Gauthier (2007). Evidence of cyclic dust deposition in the US Great plains during the last deglaciation from the high-resolution analysis of the Peoria Loess in the Eustis sequence (Nebraska, USA). *Earth and Planetary Science Letters 262*(1-2), 159–174.

Rousseau, D.-D., A. Sima, P. Antoine, C. Hatté, A. Lang, and L. Zöller (2007). Link between European and North Atlantic abrupt climate changes over the last glaciation. *Geophysical Research Letters 34*.

Rousseau, D.-D., L. Zöller, and J.-P. Valet (1998). Late Pleistocene Climatic Variations at Achenheim, France, Based on a Magnetic Susceptibility and TL Chronology of Loess. *Quaternary Research 49*(3), 255–263.

Ruth, U., M. Bigler, R. Röthlisberger, M. L. Siggaard-Andersen, S. Kipfstuhl, K. Goto-Azuma, M. E. Hansson, S. J. Johnsen, H. Lu, and J. P. Steffensen (2007).

Ice core evidence for a very tight link between North Atlantic and east Asian glacial climate. *Geophysical Research Letters 34*(3), L03706.

Ruth, U., D. Wagenbach, J. P. Steffensen, and M. Bigler (2003). Continuous record of microparticle concentration and size distribution in the central greenland NGRIP ice core during the last glacial period. *Journal of Geophysical Research 108*(D3), 4098.

Sarnthein, M., R. Gersonde, S. Niebler, U. Pflaumann, R. Spielhagen, J. Thiede, G. Wefer, and M. Weinelt (2003). Overview of Glacial Atlantic Ocean Mapping (GLAMAP 2000). *Paleoceanography 18*(2), 1030.

Schaber, K. and F. Sirocko (2005). Lithologie und Stratigraphie der spätpleistozänen Trockenmaare der Eifel. *Mainzer geowissenschaftliche Mitteilungen 33*, 295–340.

Schäfer-Neth, C. and A. Paul (2003). The Atlantic Ocean at the last glacial maximum: 1. Objective mapping of the GLAMAP sea-surface conditions. *The South Atlantic in the Late Quaternary: material budget and current systems. Springer, Berlin*, 531–548.

Schmincke, H.-U. (2010). *Vulkanismus* (3., überarb. Aufl. ed.). Darmstadt: Primus-Verl. WBG.

Schwan, J. (1988). The structure and genesis of Weichselian to Early Holocene aeolian sand sheets in western Europe. *Sedimentary Geology 55*(3-4), 197–232.

Seelos, K. (2004). *Entwicklung einer numerischen Partikelanalyse auf Basis digitaler Dünnschliffaufnahmen und Anwendung der Methode auf die ELSA-HL2-Kernsequenz 66-41 m.* Ph. D. thesis, Johannes Gutenberg-Universität, Mainz.

Seelos, K. and F. Sirocko (2005). RADIUS-rapid particle analysis of digital images by ultra-high-resolution scanning of thin sections. *Sedimentology 52*(3), 669–681.

Seelos, K. and F. Sirocko (2007). Abrupt cooling events at the very end of the last interglazial. In F. Sirocko, M. Claussen, M. Sánchez Goñi, and T. Litt (Eds.), *The climate of past interglacials*, Volume 7 of *Developments in quaternary science*, pp. 207–230. Amsterdam: Elsevier.

Seelos, K. and F. Sirocko (2009). Limnologie der Maarseen und typische Sedimente. In F. Sirocko (Ed.), *Wetter, Klima, Menschheitsentwicklung*. Darmstadt: Wiss. Buchges.

Seelos, K., F. Sirocko, and S. Dietrich (2009). A continuous high resolution dust record for the reconstruction of wind systems in Central Europe (Eifel, Western Germany) over the last 133 ka. *Geophysical Research Letters 36*(L20712), 1–6.

Shao, Y. and H. Lu (2000). A simple expression for wind erosion threshold friction velocity. *Journal of Geophysical Research 105*(D17), 22437–22443.

Sima, A., D.-D. Rousseau, M. Kageyama, G. Ramstein, M. Schulz, Y. Balkanski, P. Antoine, F. Dulac, and Christine Hatté (2009). Imprint of North-Atlantic abrupt climate changes on western European loess deposits as viewed in a dust emission model. *Quaternary Science Reviews 28*(25–26), 2851–2866.

Sirocko, F. (Ed.) (2009). *Wetter, Klima, Menschheitsentwicklung: Von der Eiszeit bis ins 21. Jahrhundert*. Darmstadt: Wiss. Buchges.

Sirocko, F., K. Schaber, S. Dietrich, K. Seelos, P. Grootes, B. Kromer, M. Krebetschek, P. Appleby, U. Hambach, C. Rolf, D. Veres, M. Sudo, and S. Grim (in prep.). Stratigraphy of 39 sediment cores from Pleistocene and Holocene maar lakes and dry maar lakes in the Eifel (Germany). *To be subm. to Quaternary Science Reviews*.

Sirocko, F., K. Seelos, K. Schaber, B. Rein, F. Dreher, M. Diehl, R. Lehne, K. Jäger, M. Krbetschek, and D. Degering (2005). A late Eemian aridity pulse in central Europe during the last glacial inception. *Nature 436*(7052), 833–836.

Smalley, I., K. O'Hara-Dhand, J. Wint, B. Machalett, Z. Jary, and I. Jefferson (2009). Rivers and loess: The significance of long river transportation in the complex event-sequence approach to loess deposit formation: Loess in the Danube Region and Surrounding Loess Provinces: The Marsigli Memorial Volume. *Quaternary International 198*(1-2), 7–18.

Smalley, I. J. and E. Derbyshire (1990). The definition of ice sheet and mountain loess. *Area 22*, 300–301.

Sommé, J., J. P. Lautridou, J. Heim, J. Maucorps, J. J. Puisségur, D. D. Rousseau, A. Thévenin, and B. van Vliet-Lanoë (1986). Le cycle climatique du Pléistocène supérieur dans les loess d'Alsace à Achenheim. *Bulletin de l'Association française pour l'étude du quaternaire 23*(1), 97–104.

Sorrel, P., H. Oberhansli, N. Boroffka, D. Nourgaliev, P. Dulski, and U. Rohl (2007). Control of wind strength and frequency in the Aral Sea basin during the late Holocene: Reconstructing past environments from remnants of human occupation and sedimentary archives in western Eurasia. *Quaternary Research 67*(3), 371–382.

Southon, J. (2004). A radiocarbon perspective on Greenland ice-core chronologies: Can we use ice cores for 14C calibration? *Radiocarbon 46*(3), 1239–1259.

Straka, H. (1975). Die spätquartäre Vegetationsgeschichte der Vulkaneifel. *Beiträge zur Landespflege in Rheinlandand-Pfalz 3*, 1–163.

Street, M., F. Gelnhausen, S. Grimm, F. Moseler, L. Niven, E. Turner, S. Wenzel, and O. Jöris (2006). L'occupation du basin de Neuwied (Rhénanie centrale, Allemagne) par les Magdaléniens et les groupes à Federmesser (aziliens). *Bulletin de la Société préhistorique française 103*, 753–780.

Stuut, J.-B., I. Smalley, and K. O'Hara-Dhand (2009). Aeolian dust in Europe: African sources and European deposits: Loess in the Danube Region and Surrounding Loess Provinces: The Marsigli Memorial Volume. *Quaternary International 198*(1-2), 234–245.

Sun, D., J. Bloemendal, D. K. Rea, J. Vandenberghe, F. Jiang, Z. An, and R. Su (2002). Grain-size distribution function of polymodal sediments in hydraulic and aeolian environments, and numerical partitioning of the sedimentary components. *Sedimentary Geology 152*(3-4), 263–277.

Sutton, O. G. (1934). Wind Structure and Evaporation in a Turbulent Atmosphere. *Proceedings of the Royal Society of London. Series A, Containing Papers of a Mathematical and Physical Character 146*(858), 701–722.

Svensson, A., K. K. Andersen, M. Bigler, H. B. Clausen, D. Dahl-Jensen, S. M. Davies, S. J. Johnsen, R. Muscheler, F. Parrenin, S. O. Rasmussen, et al. (2008). A 60 000 year Greenland stratigraphic ice core chronology. *Climate of the Past 4*, 47–57.

Sweeney, M. R., A. J. Busacca, C. A. Richardson, M. Blinnikov, and E. V. McDonald (2004). Glacial anticyclone recorded in Palouse loess of northwestern United States. *Geology 32*(8), 705–708.

Tegen, I., S. P. Harrison, K. Kohfeld, I. C. Prentice, M. Coe, and M. Heimann (2002). Impact of vegetation and preferential source areas on global dust aerosol: Results from a model study. *Journal of Geophysical Research 107*(26).

Troen, I. and E. L. Petersen (1989). *European Wind Atlas*. Roskilde, Denmark: Risø National Laboratory.

Tsoar, H. and K. Pye (1987). Dust transport and the question of desert loess formation. *Sedimentology 34*, 139–153.

Uppala, S. M., P. W. KÅllberg, A. J. Simmons, U. Andrae, V. D. C. Bechtold, M. Fiorino, J. K. Gibson, J. Haseler, A. Hernandez, G. A. Kelly, X. Li, K. Onogi, S. Saarinen, N. Sokka, R. P. Allan, E. Andersson, K. Arpe, M. A. Balmaseda, A. C. M. Beljaars, L. V. D. Berg, J. Bidlot, N. Bormann, S. Caires, F. Chevallier, A. Dethof, M. Dragosavac, M. Fisher, M. Fuentes, S. Hagemann, E. Hólm, B. J. Hoskins, L. Isaksen, P. A. E. M. Janssen, R. Jenne, A. P. Mcnally, J. F. Mahfouf, J. J. Morcrette, N. A. Rayner, R. W. Saunders, P. Simon, A. Sterl, K. E. Trenberth, A. Untch, D. Vasiljevic, P. Viterbo, and J. Woollen (2005). The ERA-40 re-analysis. *Q.J.R. Meteorol. Soc. 131*(612), 2961–3012.

van den Bogaard, P. (1995). 40Ar/39Ar ages of sanidine phenocrysts from Laacher See Tephra (12,900 yr BP): Chronostratigraphic and petrological significance. *Earth and Planetary Science Letters 133*(1-2), 163–174.

van Huissteden, K. and D. Pollard (2003). Oxygen isotope stage 3 fluvial and eolian successions in Europe compared with climate model results. *Quaternary Research 59*(2), 223–233.

Van Huissteden, K., J. C. Schwan, and M. D. Bateman (2001). Environmental conditions and paleowind directions at the end of the Weichselian Late Pleniglacial recorded in aeolian sediments and geomorphology (Twente, Eastern Netherlands). *Geologie en Mijnbouw/Netherlands Journal of Geosciences 80*(2), 1–18.

Vandenberghe, J. (1991). Changing conditions of aeolian sand deposition during the last deglaciation period. *Zeitschrift für Geomorphologie, Neue Folge, Supplement 90*, 193–207.

Vandenberghe, J., B. S. Huijzer, H. Mücher, and W. Laan (1998). Short climatic oscillations in a western European loess sequence (Kesselt, Belgium). *Journal of Quaternary Science 13*(5), 471–485.

Vandenberghe, J., R. F. B. Isarin, and H. Renssen (1999). Comments on windpolished boulders as indicators of a Late Weichselian wind regime in Denmark in relation to neighbouring areas by Christiansen and Svensson [9(1): 1-21, 1998]. *Permafrost and Periglacial Processes 10*(2), 199–201.

Voigt, R., E. Grüger, J. Baier, and D. Meischner (2008). Seasonal variability of Holocene climate: a palaeolimnological study on varved sediments in Lake Jues (Harz Mountains, Germany). *Journal of Paleolimnology 40*(4), 1021–1052.

Weltje, G. J. and R. Tjallingii (2008). Calibration of XRF core scanners for quantitative geochemical logging of sediment cores: Theory and application. *Earth and Planetary Science Letters 274*(3-4), 423–438.

Werner, M., I. Tegen, S. P. Harrison, K. E. Kohfeld, I. C. Prentice, Y. Balkanski, H. Rodhe, and C. Roelandt (2002). Seasonal and interannual variability of the mineral dust cycle under present and glacial climate conditions. *Journal of Geophysical Research 107*, 4744.

Whitlock, C., P. J. Bartlein, V. Markgraf, and A. C. Ashworth (2001). The midlatitudes of North and South America during the Last Glacial Maximum and early Holocene: Similar paleoclimatic sequences despite differing large-scale controls. *Interhemispheric Climate Linkages: Present and Past Interhemispheric Climate Linkages in the Americas and their Societal Effects. Academic Press, New York, NY*, 391–416.

Williams, E. R. (2008). Comment on "Atmospheric controls on the annual cycle of North African dust" by S. Engelstaedter and R. Washington. *J. Geophys. Res. 113*(D23), D23109.

Wohlfarth, B. (2010). Ice-free conditions in Sweden during Marine Oxygen Isotope Stage 3? *Boreas 39*(2), 377–398.

Yancheva, G., N. R. Nowaczyk, J. Mingram, P. Dulski, G. Schettler, J. F. Negendank, J. Liu, D. M. Sigman, L. C. Peterson, and G. H. Haug (2007). Influence of the intertropical convergence zone on the East Asian monsoon. *Nature 445*(7123), 74–77.

Zolitschka, B., A. Brauer, J. F. W. Negendank, H. Stockhausen, and A. Lang (2000). Annually dated late Weichselian continental paleoclimate record from the Eifel, Germany. *Geology 28*(9), 783–786.

Zöller, L. (1991). Thermoluminescence dating of upper Pleistocene volcanoes. In J. F. W. Negendank and B. Zolitschka (Eds.), *Symposium on Paleolimnology of Maar Lakes*, pp. 62. Bitburg.

Zöller, L. (2010). New approaches to European loess: a stratigraphic and methodical review of the past decade. *Central European Journal of Geosciences 2*(1), 19–31.

Zöller, L., E. A. Oches, and W. D. McCoy (1994). Towards a revised chronostratigraphy of loess in Austria with respect to key sections in the Czech Republic and in Hungary. *Quaternary Science Reviews 13*(5-7), 465–472.

A High Resolution Lithology of Sediment cores

Figure A.1: High-resolution lithoplot of the sediment core Sm3

Kern: Sm3

Datum : 13.3.2009
Bearbeiter: Dietrich

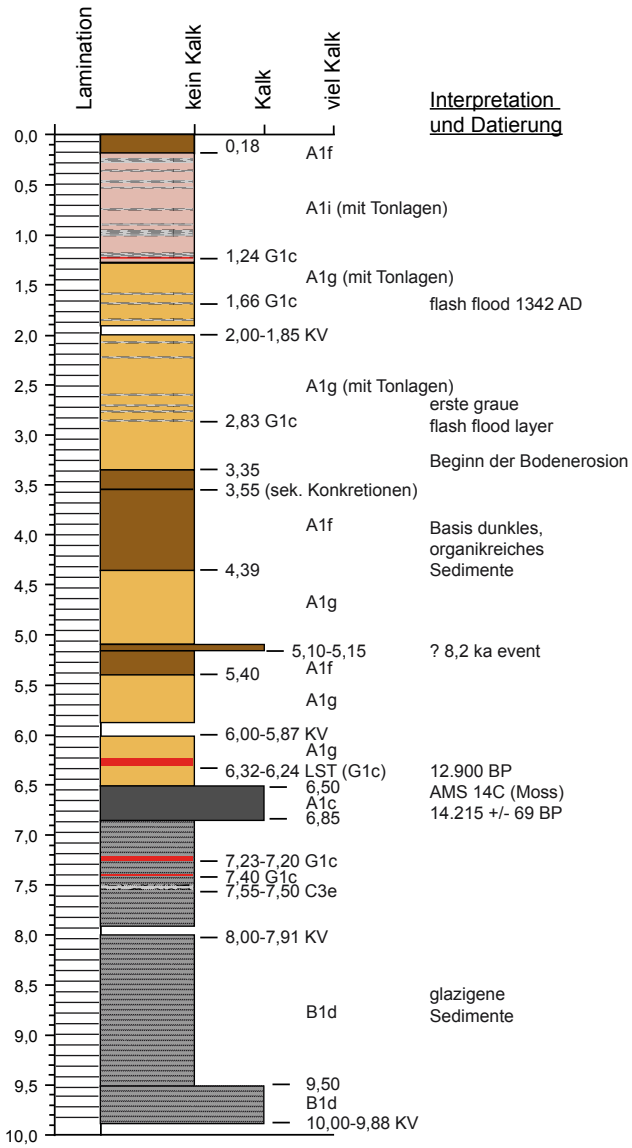

Proben:

Pollen •
Diatomeen ○

Farben

a	Weisslich	d	Mittelgrau	g	Braun/gelb	j	Oliv
b	Weiss	e	Hellgrau	h	Gelb		
c	Dunkelgrau	f	Braun	i	Rötlich		

A) Interglazial/Interstadial
1 Gyttja
2 Sapropel
3 Diatomeengyttja

B) Glazial
1 Silt-Lamination
2 Silt-Ton Lamination

C) Schutt
1 gerundet
2 eckig
3 matrixgestützt

D) Umlagerung
1 Sandlagen
2 dunkle Sandlagen
3 Tonlagen
4 Turbidit
5 Schrägschichtung
6 Bodenhorizont

E) Rutschung
1 gefaltet
2 verwürgt, fleckig

F) Diagenese
1 Kalkkonkretion
2 Verfestigung (spröde)
3 Vivianit

G) Tephra
1 Asche
2 Lapilli
3 Tuff

H) Makroreste
1 Holz
2 Muscheln
3 Pflanzenreste

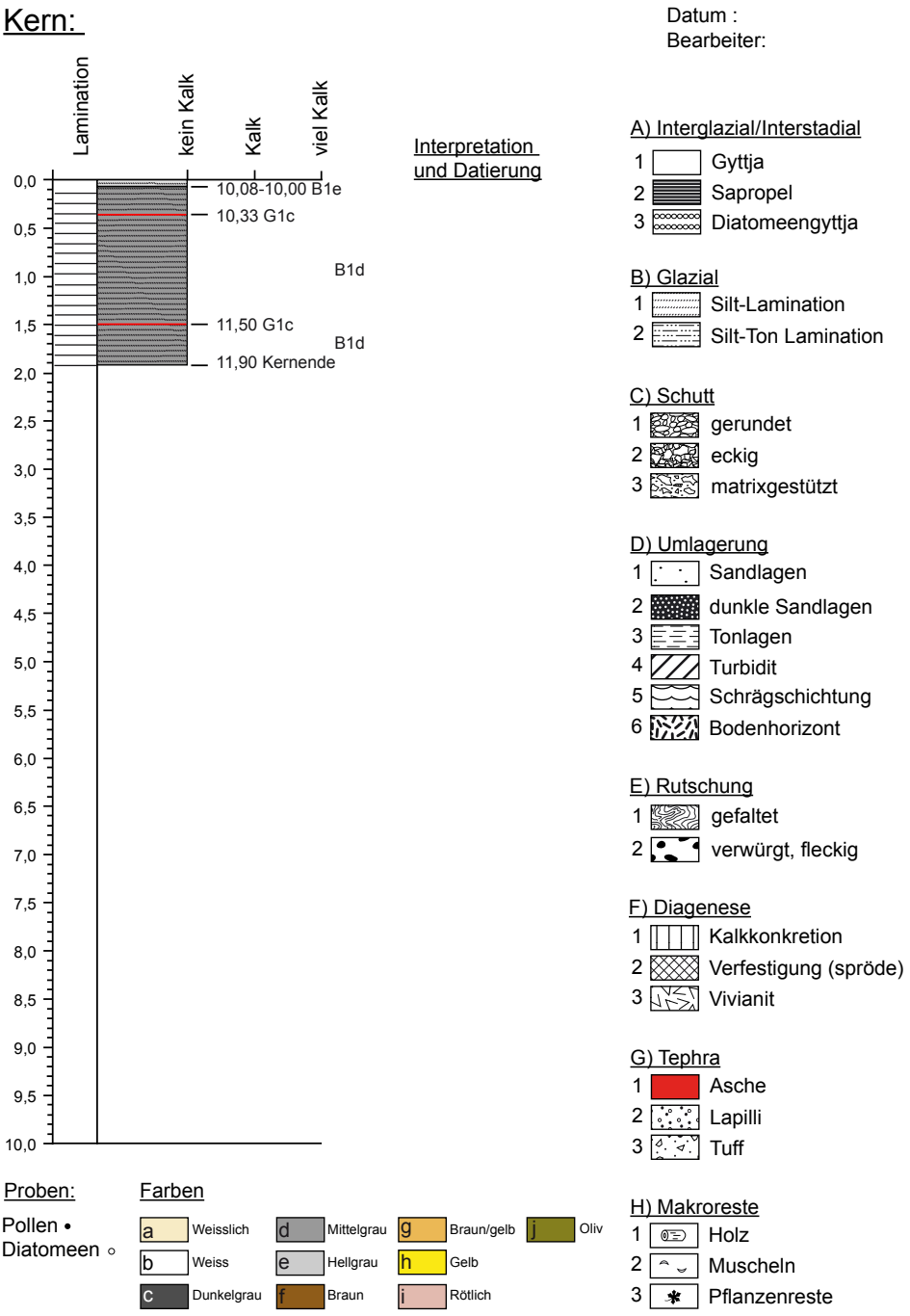
Kern:
Datum :
Bearbeiter:
Lamination
kein Kalk
Kalk
viel Kalk
Interpretation und Datierung
0,0
0,5
1,0
1,5
2,0
2,5
3,0
3,5
4,0
4,5
5,0
5,5
6,0
6,5
7,0
7,5
8,0
8,5
9,0
9,5
10,0
10,08-10,00 B1e
10,33 G1c
B1d
11,50 G1c
B1d
11,90 Kernende
A) Interglazial/Interstadial
1 Gyttja
2 Sapropel
3 Diatomeengyttja
B) Glazial
1 Silt-Lamination
2 Silt-Ton Lamination
C) Schutt
1 gerundet
2 eckig
3 matrixgestützt
D) Umlagerung
1 Sandlagen
2 dunkle Sandlagen
3 Tonlagen
4 Turbidit
5 Schrägschichtung
6 Bodenhorizont
E) Rutschung
1 gefaltet
2 verwürgt, fleckig
F) Diagenese
1 Kalkkonkretion
2 Verfestigung (spröde)
3 Vivianit
G) Tephra
1 Asche
2 Lapilli
3 Tuff
H) Makroreste
1 Holz
2 Muscheln
3 Pflanzenreste
Proben:
Pollen •
Diatomeen ○
Farben
a Weisslich
b Weiss
c Dunkelgrau
d Mittelgrau
e Hellgrau
f Braun
g Braun/gelb
h Gelb
i Rötlich
j Oliv

Figure A.2: High-resolution lithoplot of the sediment core De3

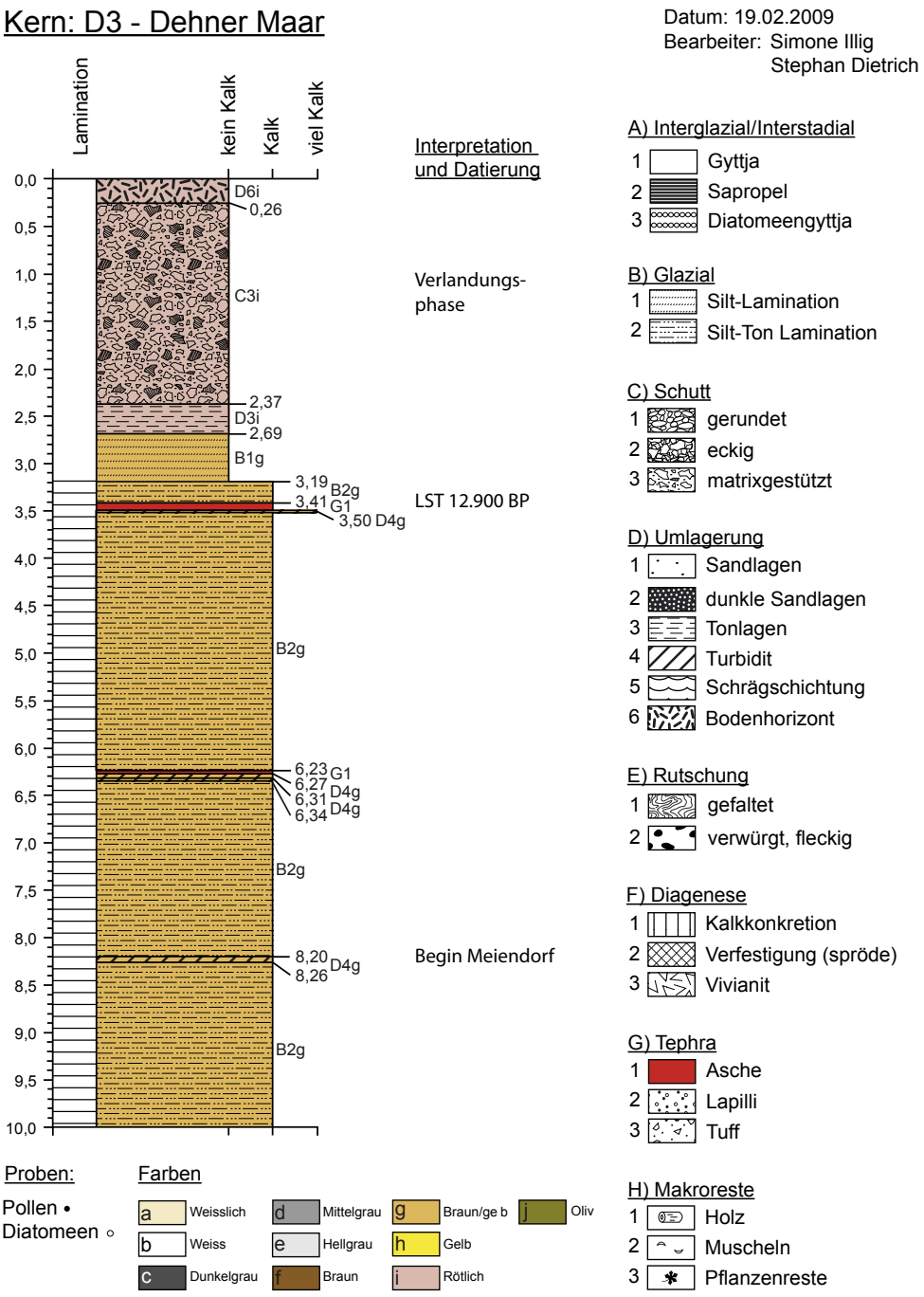
Kern: D3 - Dehner Maar
Datum: 19.02.2009
Bearbeiter: Simone Illig
Stephan Dietrich
Lamination
kein Kalk
Kalk
viel Kalk
Interpretation und Datierung
D6i
0,26
C3i
Verlandungs-phase
2,37
D3i
2,69
B1g
3,19 B2g
3,41 G1
3,50 D4g
LST 12.900 BP
B2g
6,23 G1
6,27 D4g
6,31 D4g
6,34
B2g
8,20 D4g
8,26
Begin Meiendorf
B2g
0,0
0,5
1,0
1,5
2,0
2,5
3,0
3,5
4,0
4,5
5,0
5,5
6,0
6,5
7,0
7,5
8,0
8,5
9,0
9,5
10,0
A) Interglazial/Interstadial
1 Gyttja
2 Sapropel
3 Diatomeengyttja
B) Glazial
1 Silt-Lamination
2 Silt-Ton Lamination
C) Schutt
1 gerundet
2 eckig
3 matrixgestützt
D) Umlagerung
1 Sandlagen
2 dunkle Sandlagen
3 Tonlagen
4 Turbidit
5 Schrägschichtung
6 Bodenhorizont
E) Rutschung
1 gefaltet
2 verwürgt, fleckig
F) Diagenese
1 Kalkkonkretion
2 Verfestigung (spröde)
3 Vivianit
G) Tephra
1 Asche
2 Lapilli
3 Tuff
H) Makroreste
1 Holz
2 Muscheln
3 Pflanzenreste
Proben:
Pollen •
Diatomeen ○
Farben
a Weisslich
b Weiss
c Dunkelgrau
d Mittelgrau
e Hellgrau
f Braun
g Braun/ge b
h Gelb
i Rötlich
j Oliv

Kern: D3 - Dehner Maar

Datum: 19.02.2009
Bearbeiter: Simone Illig
Stephan Dietrich

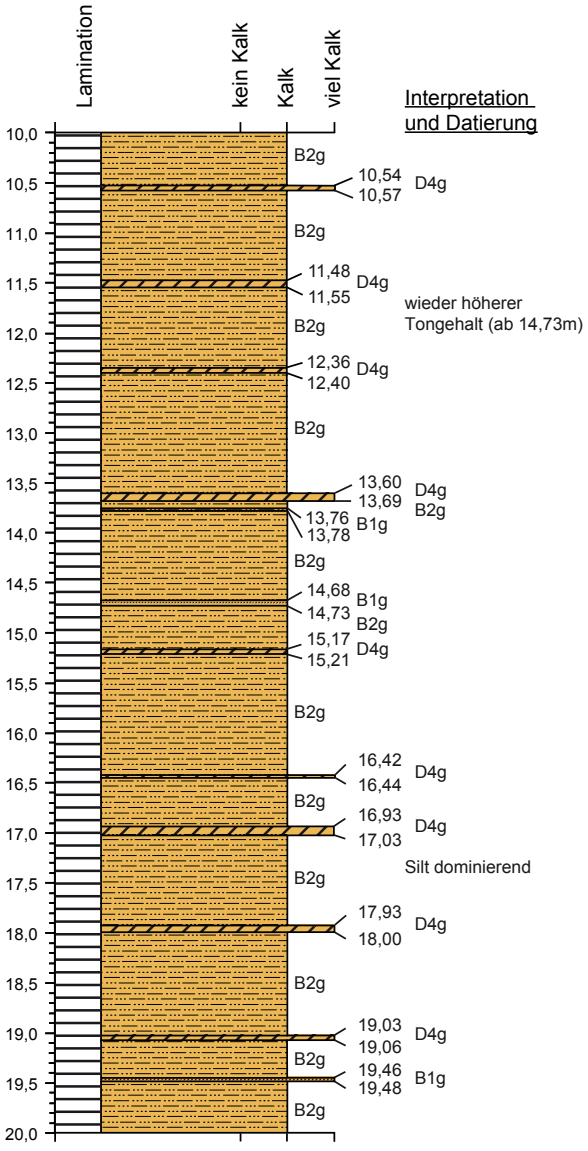

A) Interglazial/Interstadial
1 Gyttja
2 Sapropel
3 Diatomeengyttja

B) Glazial
1 Silt-Lamination
2 Silt-Ton Lamination

C) Schutt
1 gerundet
2 eckig
3 matrixgestützt

D) Umlagerung
1 Sandlagen
2 dunkle Sandlagen
3 Tonlagen
4 Turbidit
5 Schrägschichtung
6 Bodenhorizont

E) Rutschung
1 gefaltet
2 verwürgt, fleckig

F) Diagenese
1 Kalkkonkretion
2 Verfestigung (spröde)
3 Vivianit

G) Tephra
1 Asche
2 Lapilli
3 Tuff

H) Makroreste
1 Holz
2 Muscheln
3 Pflanzenreste

Proben:
Pollen •
Diatomeen ○

Farben
a Weisslich
b Weiss
c Dunkelgrau
d Mittelgrau
e Hellgrau
f Braun
g Braun/gelb
h Gelb
i Rötlich
j Oliv

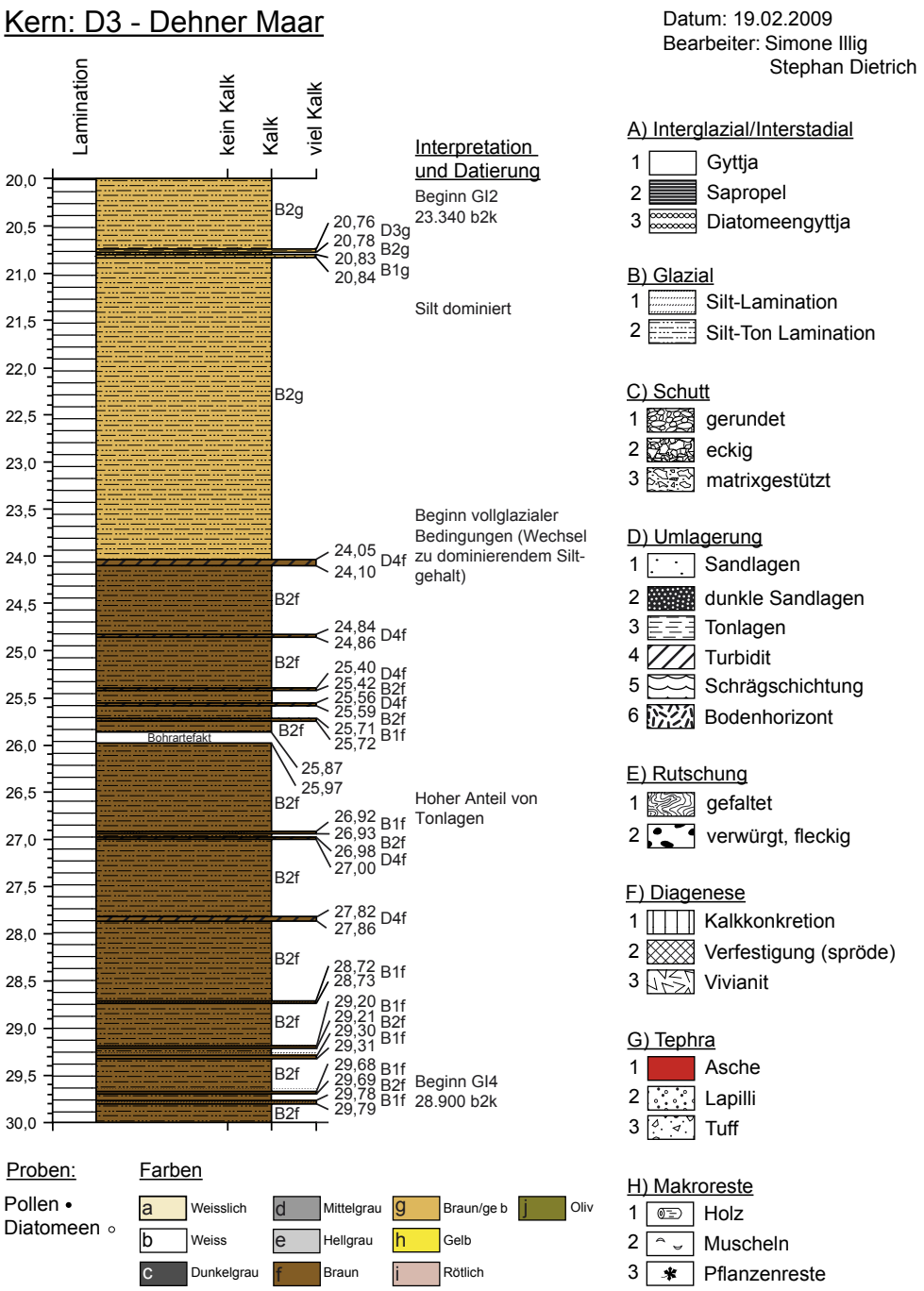
Kern: D3 - Dehner Maar
Datum: 19.02.2009
Bearbeiter: Simone Illig
Stephan Dietrich
Lamination
kein Kalk
Kalk
viel Kalk
Interpretation und Datierung
Beginn GI2
23.340 b2k
Silt dominiert
Beginn vollglazialer Bedingungen (Wechsel zu dominierendem Siltgehalt)
Hoher Anteil von Tonlagen
Beginn GI4
28.900 b2k
Bohrartefakt
20,0
20,5
21,0
21,5
22,0
22,5
23,0
23,5
24,0
24,5
25,0
25,5
26,0
26,5
27,0
27,5
28,0
28,5
29,0
29,5
30,0
B2g
20,76 D3g
20,78 B2g
20,83 B1g
20,84
B2g
24,05 D4f
24,10
B2f
24,84 D4f
24,86
B2f
25,40 D4f
25,42 B2f
25,56 D4f
25,59 B2f
25,71 B1f
25,72
25,87
25,97
B2f
26,92 B1f
26,93 B2f
26,98 D4f
27,00
B2f
27,82 D4f
27,86
B2f
28,72 B1f
28,73
29,20 B1f
29,21 B2f
29,30 B1f
29,31
B2f
29,68 B1f
29,69 B2f
29,78 B1f
29,79
B2f
A) Interglazial/Interstadial
1 Gyttja
2 Sapropel
3 Diatomeengyttja
B) Glazial
1 Silt-Lamination
2 Silt-Ton Lamination
C) Schutt
1 gerundet
2 eckig
3 matrixgestützt
D) Umlagerung
1 Sandlagen
2 dunkle Sandlagen
3 Tonlagen
4 Turbidit
5 Schrägschichtung
6 Bodenhorizont
E) Rutschung
1 gefaltet
2 verwürgt, fleckig
F) Diagenese
1 Kalkkonkretion
2 Verfestigung (spröde)
3 Vivianit
G) Tephra
1 Asche
2 Lapilli
3 Tuff
H) Makroreste
1 Holz
2 Muscheln
3 Pflanzenreste
Proben:
Pollen •
Diatomeen ○
Farben
a Weisslich
b Weiss
c Dunkelgrau
d Mittelgrau
e Hellgrau
f Braun
g Braun/ge b
h Gelb
i Rötlich
j Oliv

Kern: D3 - Dehner Maar

Datum: 19.02.2009
Bearbeiter: Simone Illig
Stephan Dietrich

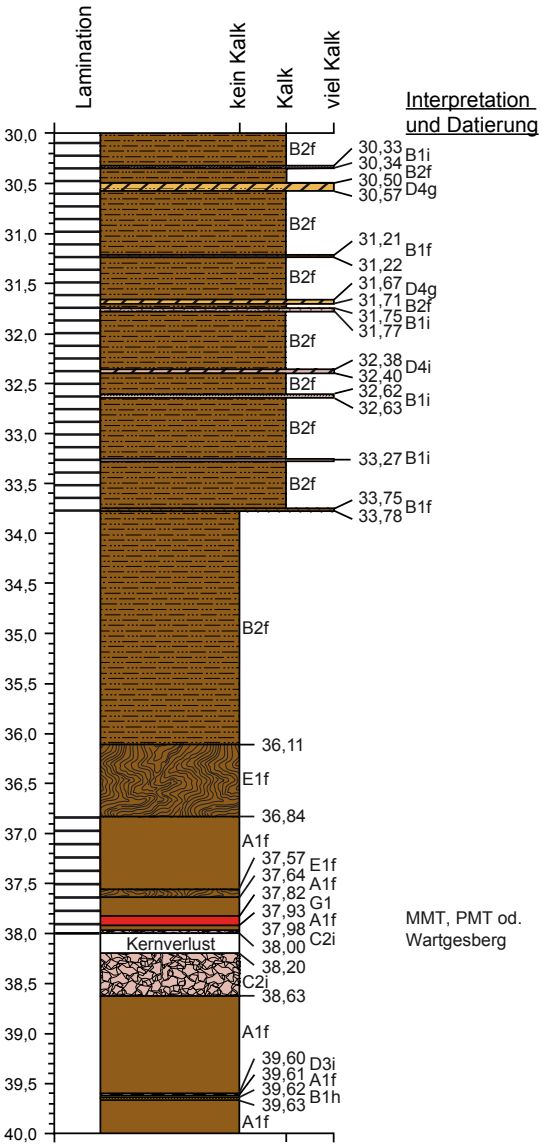

A) Interglazial/Interstadial
1 Gyttja
2 Sapropel
3 Diatomeengyttja

B) Glazial
1 Silt-Lamination
2 Silt-Ton Lamination

C) Schutt
1 gerundet
2 eckig
3 matrixgestützt

D) Umlagerung
1 Sandlagen
2 dunkle Sandlagen
3 Tonlagen
4 Turbidit
5 Schrägschichtung
6 Bodenhorizont

E) Rutschung
1 gefaltet
2 verwürgt, fleckig

F) Diagenese
1 Kalkkonkretion
2 Verfestigung (spröde)
3 Vivianit

G) Tephra
1 Asche
2 Lapilli
3 Tuff

H) Makroreste
1 Holz
2 Muscheln
3 Pflanzenreste

Proben:
Pollen •
Diatomeen ○

Farben
a Weisslich
b Weiss
c Dunkelgrau
d Mittelgrau
e Hellgrau
f Braun
g Braun/gelb
h Gelb
i Rötlich
j Oliv

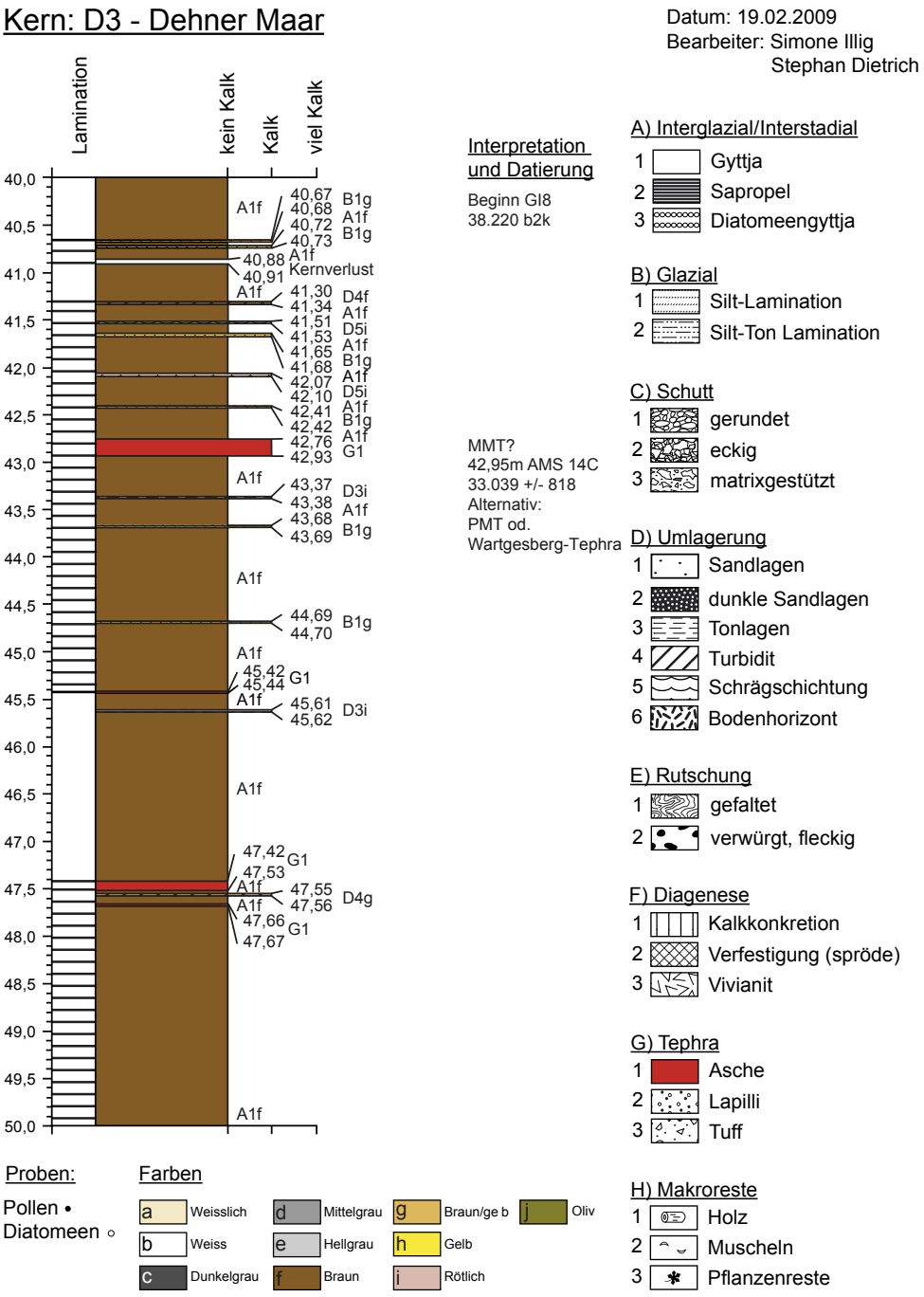
Kern: D3 - Dehner Maar
Datum: 19.02.2009
Bearbeiter: Simone Illig
Stephan Dietrich
Lamination
kein Kalk
Kalk
viel Kalk
Interpretation und Datierung
Beginn GI8
38.220 b2k
MMT?
42,95m AMS 14C
33.039 +/- 818
Alternativ:
PMT od.
Wartgesberg-Tephra
A) Interglazial/Interstadial
1 Gyttja
2 Sapropel
3 Diatomeengyttja
B) Glazial
1 Silt-Lamination
2 Silt-Ton Lamination
C) Schutt
1 gerundet
2 eckig
3 matrixgestützt
D) Umlagerung
1 Sandlagen
2 dunkle Sandlagen
3 Tonlagen
4 Turbidit
5 Schrägschichtung
6 Bodenhorizont
E) Rutschung
1 gefaltet
2 verwürgt, fleckig
F) Diagenese
1 Kalkkonkretion
2 Verfestigung (spröde)
3 Vivianit
G) Tephra
1 Asche
2 Lapilli
3 Tuff
H) Makroreste
1 Holz
2 Muscheln
3 Pflanzenreste
Proben:
Pollen •
Diatomeen ◦
Farben
a Weisslich
b Weiss
c Dunkelgrau
d Mittelgrau
e Hellgrau
f Braun
g Braun/ge b
h Gelb
i Rötlich
j Oliv

Kern: D3 - Dehner Maar

Datum: 19.02.2009
Bearbeiter: Simone Illig
Stephan Dietrich

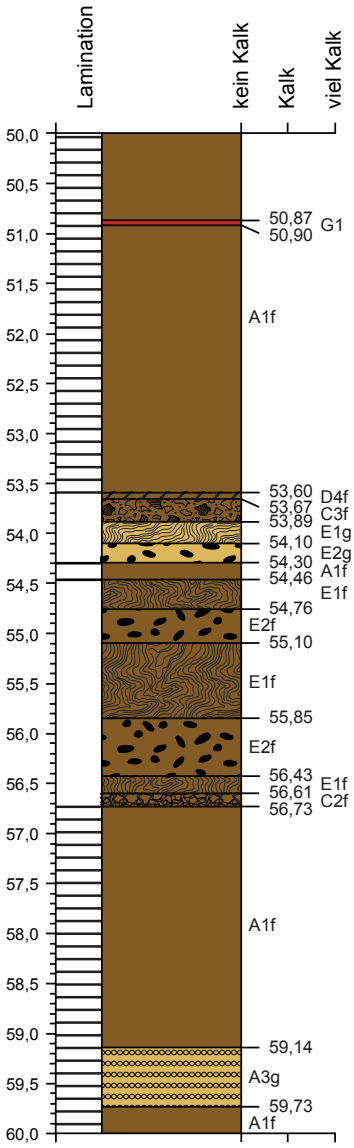

Interpretation und Datierung

Beginn GI12
46.880 b2k
MMT, PMT od.
Wartgesberg

Fichtenholz
AMS 14C
45.804 +/- 1.198

A) Interglazial/Interstadial
1 Gyttja
2 Sapropel
3 Diatomeengyttja

B) Glazial
1 Silt-Lamination
2 Silt-Ton Lamination

C) Schutt
1 gerundet
2 eckig
3 matrixgestützt

D) Umlagerung
1 Sandlagen
2 dunkle Sandlagen
3 Tonlagen
4 Turbidit
5 Schrägschichtung
6 Bodenhorizont

E) Rutschung
1 gefaltet
2 verwürgt, fleckig

F) Diagenese
1 Kalkkonkretion
2 Verfestigung (spröde)
3 Vivianit

G) Tephra
1 Asche
2 Lapilli
3 Tuff

H) Makroreste
1 Holz
2 Muscheln
3 Pflanzenreste

Proben:
Pollen •
Diatomeen ○

Farben
a Weisslich
b Weiss
c Dunkelgrau
d Mittelgrau
e Hellgrau
f Braun
g Braun/ge b
h Gelb
i Rötlich
j Oliv

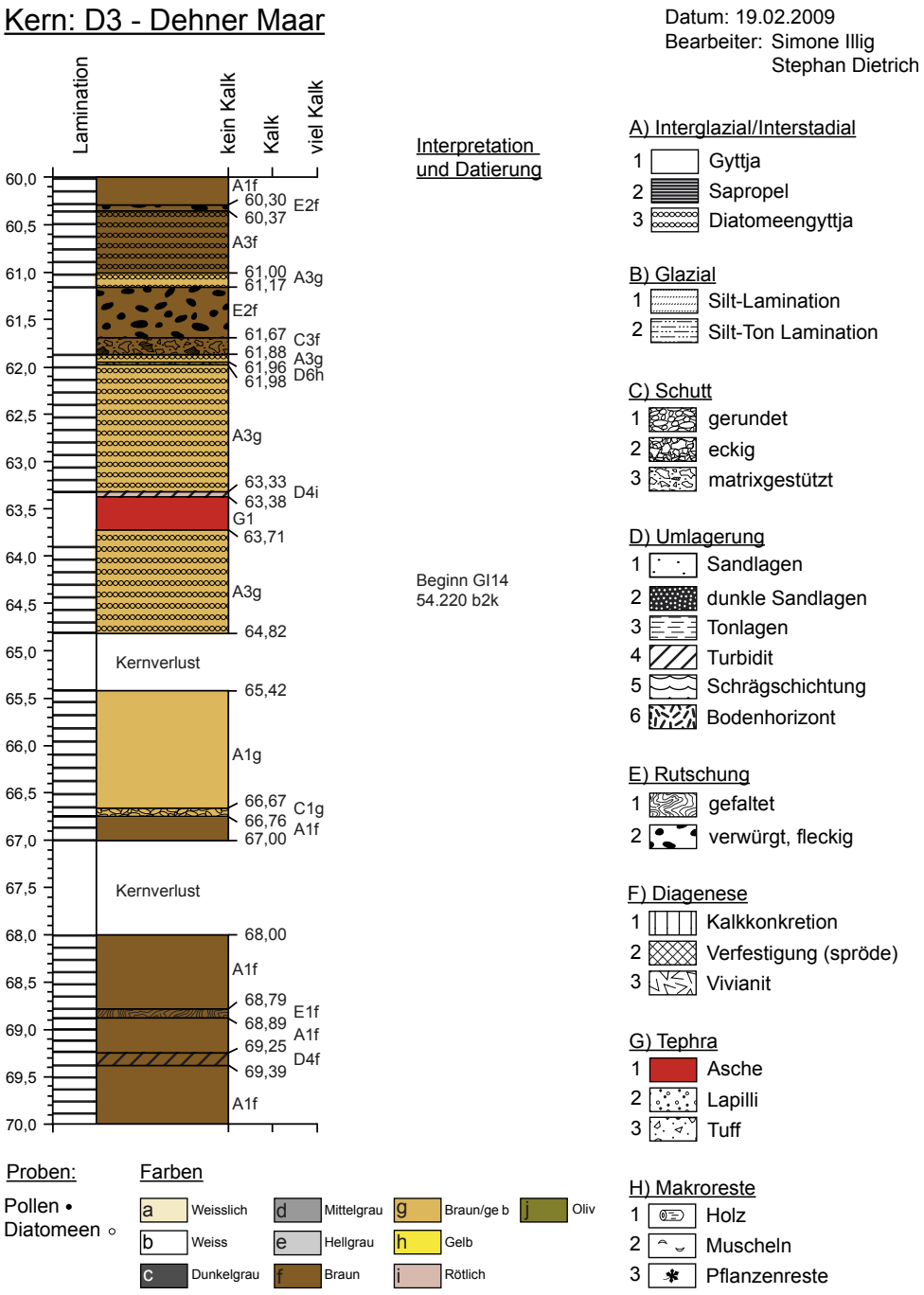
Kern: D3 - Dehner Maar
Datum: 19.02.2009
Bearbeiter: Simone Illig
Stephan Dietrich
Lamination
kein Kalk
Kalk
viel Kalk
Interpretation und Datierung
60,0
60,5
61,0
61,5
62,0
62,5
63,0
63,5
64,0
64,5
65,0
65,5
66,0
66,5
67,0
67,5
68,0
68,5
69,0
69,5
70,0
A1f
60,30
E2f
60,37
A3f
61,00
A3g
61,17
E2f
61,67
C3f
61,88
A3g
61,96
D6h
61,98
A3g
63,33
D4i
63,38
G1
63,71
Beginn GI14
54.220 b2k
A3g
64,82
Kernverlust
65,42
A1g
66,67
C1g
66,76
A1f
67,00
Kernverlust
68,00
A1f
68,79
E1f
68,89
A1f
69,25
D4f
69,39
A1f
A) Interglazial/Interstadial
1 Gyttja
2 Sapropel
3 Diatomeengyttja
B) Glazial
1 Silt-Lamination
2 Silt-Ton Lamination
C) Schutt
1 gerundet
2 eckig
3 matrixgestützt
D) Umlagerung
1 Sandlagen
2 dunkle Sandlagen
3 Tonlagen
4 Turbidit
5 Schrägschichtung
6 Bodenhorizont
E) Rutschung
1 gefaltet
2 verwürgt, fleckig
F) Diagenese
1 Kalkkonkretion
2 Verfestigung (spröde)
3 Vivianit
G) Tephra
1 Asche
2 Lapilli
3 Tuff
H) Makroreste
1 Holz
2 Muscheln
3 Pflanzenreste
Proben:
Pollen •
Diatomeen ○
Farben
a Weisslich
b Weiss
c Dunkelgrau
d Mittelgrau
e Hellgrau
f Braun
g Braun/ge b
h Gelb
i Rötlich
j Oliv

Kern: Dehner Maar

Datum: 19.02.2009
Bearbeiter: Simone Illig
Stephan Dietrich

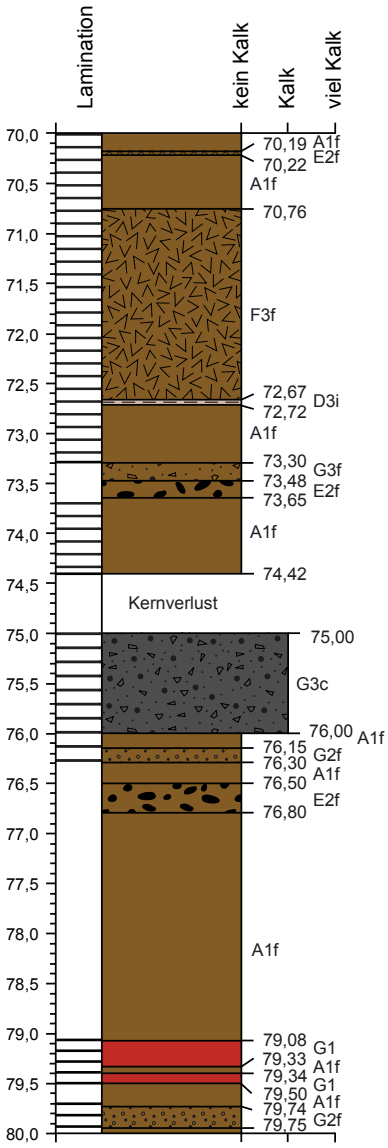

Interpretation und Datierung

Beginn GI17
59.440 b2k

A) Interglazial/Interstadial
1 Gyttja
2 Sapropel
3 Diatomeengyttja

B) Glazial
1 Silt-Lamination
2 Silt-Ton Lamination

C) Schutt
1 gerundet
2 eckig
3 matrixgestützt

D) Umlagerung
1 Sandlagen
2 dunkle Sandlagen
3 Tonlagen
4 Turbidit
5 Schrägschichtung
6 Bodenhorizont

E) Rutschung
1 gefaltet
2 verwürgt, fleckig

F) Diagenese
1 Kalkkonkretion
2 Verfestigung (spröde)
3 Vivianit

G) Tephra
1 Asche
2 Lapilli
3 Tuff

H) Makroreste
1 Holz
2 Muscheln
3 Pflanzenreste

Proben:
Pollen •
Diatomeen ○

Farben

a	Weisslich	d	Mittelgrau	g	Braun/ge b	j	Oliv
b	Weiss	e	Hellgrau	h	Gelb		
c	Dunkelgrau	f	Braun	i	Rötlich		

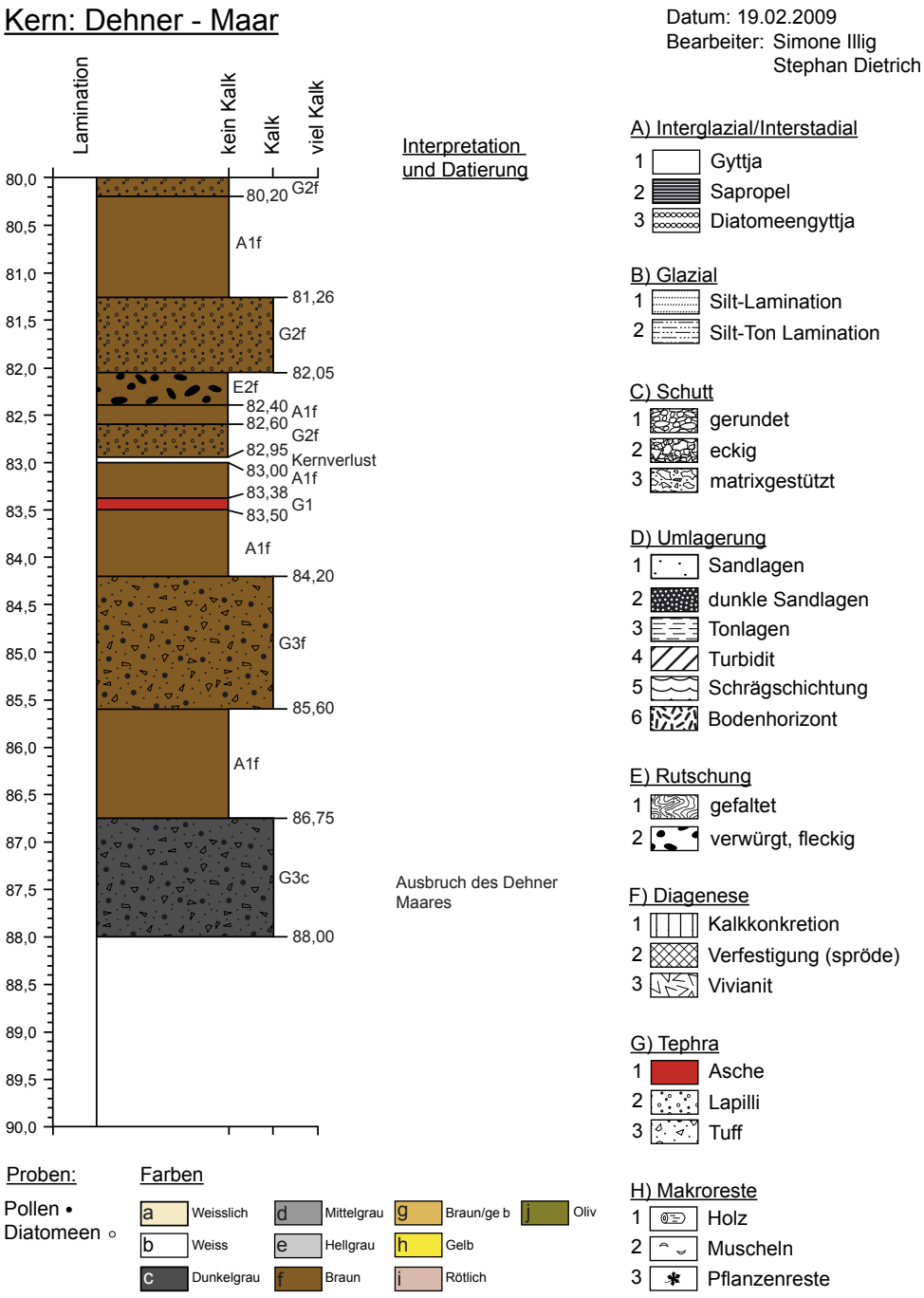
Kern: Dehner - Maar
Datum: 19.02.2009
Bearbeiter: Simone Illig
Stephan Dietrich
Lamination
kein Kalk
Kalk
viel Kalk
Interpretation und Datierung
80,0
80,5
81,0
81,5
82,0
82,5
83,0
83,5
84,0
84,5
85,0
85,5
86,0
86,5
87,0
87,5
88,0
88,5
89,0
89,5
90,0
80,20 G2f
A1f
81,26
G2f
82,05
E2f
82,40 A1f
82,60 G2f
82,95 Kernverlust
83,00 A1f
83,38 G1
83,50
A1f
84,20
G3f
85,60
A1f
86,75
G3c
88,00
Ausbruch des Dehner Maares
A) Interglazial/Interstadial
1 Gyttja
2 Sapropel
3 Diatomeengyttja
B) Glazial
1 Silt-Lamination
2 Silt-Ton Lamination
C) Schutt
1 gerundet
2 eckig
3 matrixgestützt
D) Umlagerung
1 Sandlagen
2 dunkle Sandlagen
3 Tonlagen
4 Turbidit
5 Schrägschichtung
6 Bodenhorizont
E) Rutschung
1 gefaltet
2 verwürgt, fleckig
F) Diagenese
1 Kalkkonkretion
2 Verfestigung (spröde)
3 Vivianit
G) Tephra
1 Asche
2 Lapilli
3 Tuff
H) Makroreste
1 Holz
2 Muscheln
3 Pflanzenreste
Proben:
Pollen •
Diatomeen ○
Farben
a Weisslich
b Weiss
c Dunkelgrau
d Mittelgrau
e Hellgrau
f Braun
g Braun/ge b
h Gelb
i Rötlich
j Oliv

B Radiocarbon Dates

Table B.1: Radiocarbon ages of the sediment cores from the Schalkenmehrener Maar. Including AMS ^{14}C ages and calibrated ages using INTCAL09 calibration curve (Reimer et al., 2009) and the OxCal software, version 4.1 (http://c14.arch.ox.ac.uk). Carbon contents are shown. Only ages with higher values than the threshold values (red) are used for age-depth models.

Sample ID	Coring Method	Core Number	Depth (m)	Material	Extraction Fraction	14C Age > x	14C Age	14C Age error +	14C Age error -	2 sigma min [AD/BC]	2 sigma max [AD/BC]	delta-13	mg C reduced	%C in fraction	Sample C content in this fraction (%)	Current (% of "normal")
		SM2				**AMS 14C BP**				**cal yrs**				**> 10%**	**> 0,40 %**	**> 80%**
KIA-26170	Rammkern	SM2	0,82	bulk	humic acid		3668	28	28	2137	1962	-31,1	4,0	45,3%	0,2%	99
KIA-26645	Rammkern	SM2	0,82	bulk	humic acid		3906	31	31	2472	2297	-29,8	3,7	45,2%	0,3%	100
KIA-26645	Rammkern	SM2	0,82	bulk	base residue		3171	38	38	2207	2016	-27,7	6,2	4,6%	0,3%	100
KIA-26646	Rammkern	SM2	2,92	bulk	humic acid		4551	28	28	3239	3105	-30,5	3,5	43,1%	0,9%	98
KIA-26646	Rammkern	SM2	2,92	bulk	base residue		3579	24	24	1983	1881	-28,4	5,4	10,6%	0,7%	103
KIA-26171	Rammkern	SM2	2,93	bulk	humic acid		4702	30	30	3471	3372	-30,4	3,8	32,8%	0,6%	98
KIA-26171	Rammkern	SM2	2,93	bulk	base residue		3615	25	25	2034	1898	-29,6	14,9	12,2%	0,7%	100
KIA-26172	Rammkern	SM2	3,48	bulk	humic acid		3870	26	26	2464	2283	-29,4	3,0	28,1%	0,6%	104
KIA-26172	Rammkern	SM2	3,48	bulk	base residue		3553	25	25	1973	1870	-28,9	19,4	3,9%	0,8%	100
KIA-26647	Rammkern	SM2	3,48	bulk	base residue		3443	30	30	1831	1685	-27,7	1,1	2,2%	0,8%	99
KIA-26647	Rammkern	SM2	3,48	bulk	humic acid		3336	26	26	1689	1530	-27,1	3,5	43,6%	0,8%	103
KIA-26173	Rammkern	SM2	4,23	bulk	humic acid		5917	29	29	4849	4716	-31,6	6,9	59,2%	1,1%	104
KIA-26173	Rammkern	SM2	4,23	bulk	base residue		5042	32	32	3953	3764	-29,7	6,8	42,1%	1,2%	103
KIA-26648	Rammkern	SM2	4,23	bulk	humic acid		5950	41	41	4935	4726	-31,7	4,7	59,6%	1,3%	101
KIA-26648	Rammkern	SM2	4,23	bulk	base residue		5075	31	31	3958	3797	-29,0	4,3	42,5%	1,3%	91
KIA-26649	Rammkern	SM2	5,08	bulk	humic acid		17383	70	70	19212	18390	-27,6	4,7	59,0%	0,6%	103
KIA-26174	Rammkern	SM2	5,09	bulk	humic acid		18223	70	70	20164	19501	-31,5	6,2	52,9%	0,5%	96
KIA-26175	Rammkern	SM2	6,98	bulk	base residue		13528	62	62	14955	14472	-26,3	22,9	6,0%	0,9%	102
KIA-26175	Rammkern	SM2	6,98	bulk	humic acid		13506	48	48	14938	14470	-27,6	5,2	49,8%	0,4%	106
KIA-26650	Rammkern	SM2	6,98	bulk	humic acid		13643	53	53	15026	14655	-27,3	3,9	49,0%	0,5%	105
KIA-26650	Rammkern	SM2	6,98	bulk	base residue		13564	49	49	14971	14543	-26,0	5,7	5,6%	0,8%	108
KIA-26176	Rammkern	SM2	9,98	bulk	base residue		28402	161	161	31331	30077	-26,4	6,9	0,4%	0,2%	101
KIA-26176	Rammkern	SM2	9,98	bulk	humic acid		20930	423	423	24209	22004	-25,8	0,4	4,7%	0,0%	57
KIA-26651	Rammkern	SM2	9,99	bulk	base residue		27804	485	485	31346	29287	-26,5	0,9	0,1%	0,0%	87
		SM3														
KIA-29193	Rammkern	SM3	6,69	moss	base residue		14215	69	69	15666	15021	-33,9	3,9	48,2%	32,1%	102
		SM4														
KIA-29194	Rammkern	SM4	10,01	bulk	base residue		11785	56	56	11840	11497	-28,7	1,9	1,3%	0,9%	98
KIA-29194	Rammkern	SM4	10,01	bulk	humic acid		11692	49	49	11767	11442	-28,9	2,8	35,6%	0,8%	103
		SMf														
KIA-30679	freeze core	SMf	1,92	moss	base residue		5961	41	41	4944	4727	-33,7	2,2	47,2%	12,6%	100

Alter genutzt; sichere Messparameter

Alter genutzt; tw. sichere Messparameter

Alter genutzt; Ostrakoden

Alter nicht genutzt

Table B.2: Radiocarbon ages of the sediment cores from the Dehner dry maar. Including AMS ^{14}C ages and calibrated ages using INTCAL09 calibration curve (Reimer et al., 2009) and the OxCal software, version 4.1 (http://c14.arch.ox.ac.uk). Carbon contents are shown. Only ages with higher values than the threshold values (red) are used for age-depth models.

Sample ID	Coring Method	Core Number	Depth (m)	Material	Extraction Fraction	14C Age > x	14C Age	14C Age error +	14C Age error -	2 sigma min [AD/BC]	2 sigma max [AD/BC]	delta-13	mg C reduced	%C in fraction	Sample C content in this fraction (%)	Current (% of "normal")
		DE2				AMS 14C BP				cal yrs				> 10%	> 0,40 %	> 80%
Hd-26719	Seilkern	DE2	12,15	ostracod	ostracod extraction, kont.		30170	270	270	33310	32504	-17,4				
KIA-12413	Seilkern	DE2	20,7	bulk	humic acid	> 47585	47585	--	--	45637	45636	-24,4	1,2	14,9%	1,4%	
KIA-12414	Seilkern	DE2	20,7	bulk	base residue		25672	336	336	29103	27748	-24,4	1,0	0,1%	0,0%	
KIA-12414	Seilkern	DE2	20,7	bulk	base residue		19009	267	267	21512	20171	-27,0	0,5	0,1%	0,0%	
KIA-39902	Seilkern	DE2	23,5	ostracod	ostracod extraction, kont.		32613	493	493	36695	34454	-7,0	0,6	11,7%	0,0%	63
KIA-39903	Seilkern	DE2	25,05	ostracod	ostracod extraction		31917	452	452	35653	33186	-6,2	0,6	10,6%	0,0%	89
KIA-12415	Seilkern	DE2	26,9	bulk	base residue		27165	480	480	30834	28982	-26,8	0,8	0,1%	0,0%	
KIA-39904	Seilkern	DE2	28,75	ostracod	ostracod extraction		37108	805	805	41335	38818	-10,7	0,4	11,7%	0,0%	93
KIA-10947	Seilkern	DE2	34,75	plantdebris	base residue		46107	1376	1376	48000	44000	-25,3	3,4	46,8%	23,5%	
KIA-10947	Seilkern	DE2	34,75	plantdebris	humic acid		27759	651	651	31983	29153	-30,5	0,6	38,5%	3,8%	
KIA-13110	Seilkern	DE2	37	bulk	humic acid	> 40421	40421	--	--	42719	42107	-31,6	0,5	5,8%	0,1%	
KIA-13110	Seilkern	DE2	37	bulk	base residue		31836	557	557	35938	33076	-27,1	1,3	0,1%	0,1%	
KIA-12416	Seilkern	DE2	37,3	bulk	humic acid	> 36134	36134	--	--	39667	39072	-31,5	0,3	3,4%	0,1%	
KIA-12416	Seilkern	DE2	37,3	bulk	base residue		37369	779	779	41446	39106	-26,4	2,0	0,2%	0,1%	
KIA-12416	Seilkern	DE2	37,3	bulk	base residue		34396	813	813	39376	35472	-24,6	1,3	0,1%	0,3%	
KIA-12416	Seilkern	DE2	37,3	bulk	humic acid	> 38014	38014	--	--	40901	40236	-33,3	0,3	4,3%	0,1%	
KIA-12416	Seilkern	DE2	37,3	bulk	base residue		26210	309	309	29296	28443	-26,7	1,3	0,1%	0,1%	
		DE3														
KIA-30686	Seilkern	DE3	42,95	bulk	humic acid		36030	1146	1146	41069	36861	-28,2	1,2	11,7%	0,1%	93
KIA-30686	Seilkern	DE3	42,95	bulk	base residue		33039	818	818	38326	34327	-27,6	1,1	0,1%	0,1%	90
KIA-34607	Seilkern	DE3	55,96	wood	base residue		45804	1198	1198	44817	max (50000)	-19,9	4,3	53,3%	31,9%	104

Alter genutzt; sichere Messparameter

Alter genutzt; Ostrakoden

Alter genutzt; tw. sichere Messparameter

Alter nicht genutzt

C Synoptical Table of Stratigraphic Marker Layers

Table C.1: Synoptical Table of Stratigraphic Marker Layers. Landscape evolution zone (LEZ) after (?).

Zeitmarken	Typische Umweltänderungen	Referenz (für Alter)	AD	Alter BC	b2k	SMf m	SM2 m	SM3 m	SM4	DE2 m	DE3 m
	137Cs Maximum, Reaktorunfall Tschernobyl (1986)		-1986		14	0,09					
Nachkriegszeit	137Cs, Maximum der Atombombentests (1963)		-1963		37	0,18					
	Doppelhochwasser Jan./Mar. 1784	Sirocko et al. (in prep)	-1784		216	0,48					
Kleine Eiszeit	Hochwasserlage mit viel Organik, Kgr Max 1595	Sirocko et al. (in prep)	-1595		405	0,72					
1342 AD	Hochwasserlage mit viel Organik, Julihochwasser 1342, Top	Sirocko et al. (in prep)	-1342		658	1,42	1,56	1,74	1,60		
Mittelalter	Hochwasserlage mit viel Organik, Julihochwasser 1342, Basis	Sirocko et al. (in prep)	-1342		658	1,46	1,62	1,80	1,63		
	Hochwasserlage mit viel Organik, Julihochwasser 1270	Sirocko et al. (in prep)	-1270		730	1,62					
1000 AD	Farbwechsel, Anstieg der Getreidepollen, Ende Hainbuchen (ca 900-1100)	Sirocko et al. (in prep)	-1000		1000		2,30		2,20		
450 AD	Basis Birkenpeak, Pioniervegetation auf aufgelassenen Feldern	Sirocko et al. (in prep)	-470		1530		2,75				
Römerzeit	Letzte Hochwasserlage, Ende Römerzeit	Sirocko et al. (in prep)	-450		1550		2,78	2,71	2,79		
Eisenzeit	Beginn Bodenerosion nach Einführung des Pflugs, Anstieg Gras und Getreide	Sirocko et al. (in prep)		700	2700		3,35	3,35			
795 BC	Extremes Hochwasser 795BC, Basis	Sirocko et al. (in prep)		795	2795			3,46			
Subboreal (Bronzezeit)	Ausbreitung Buchen	Sirocko et al. (in prep)		1800	3800		3,80	3,80			
Subboreal (Neolithikum)	erstes Erlenmax.; Einsetzen dunkler Sedimentfarbe	Sirocko et al. (in prep)		ca 4000			4,43	4,39			
4050 BC	Ulmenfall, Warvenzählung HM1, 14C UM2	Sirocko et al. (in prep)		4050	6050						
Atlantikum (Eichenmischwaldzeit)	Ausbreitung Linden und Eschen	Sirocko et al. (in prep)			8600		5,50	5,50			
Boreal (Haselzeit)	Haselmaximum	Sirocko et al. (in prep)			10000		5,70	5,70			
	Ausbreitung der Hasel auf den frisch gebildeten Böden	Sirocko et al. (in prep)			10800		6,00				
Präboreal (Birken-Kiefern-Zeit)	Ulmener Maar Tephra (UMT)	Zolitschka et al., 1995			11000			5,88	5,98		
11700 BP	Ende YD	Walker et al., 2008			11700		6,10	6,00			
Jüngere Dryas	Ausbreitung der Graspollen, Intensivierung der Staubsturmaktivität				12800		6,30	6,30			
	LST Top						6,40	6,24	6,20	3,18	3,40
Alleröd	LST Basis	van den Bogaard, 1995			12900		6,50	6,33	6,26	3,20	3,49
Beginn Alleröd		Litt et al., 2007			13350		6,80				
Beginn Bölling	Ausbreitung Kiefern-Birken Wald	Litt et al., 2007			13670		7,00	7,00			
13800 BP	kurzer Kälterückschlag der älteren Dryas	Litt et al., 2007			13800						
Meiendorf	Grassteppe mit einzelnen Zwergbirken und Kiefern,	Rasmussen et al., 2006			14700		7,80				8,50
Ende GI2 Eiszeitmaximum	Ende dunkle Sedimentfarbe				21000						19,70
Anfang GI2 Eiszeitmaximum	Beginn dunkle Sedimentfarbe, Org.-Werte	Andersen et al., 2006			23340						21,00
Ende GI3	letzte Diatomeen, letzte Graspollen				27500						27,00
Beginn GI3		Andersen et al., 2006			27780						
GS4											
Ende GI4					28628						
Beginn GI4		Andersen et al., 2006			28900					28,52	29,12

Zeitmarken	Typische Umweltänderungen	Referenz (für Alter)	AD	Alter BC	b2k	SMf m	SM2 m	SM3 m	SM4	DE2 m	DE3 m
GS5											
Ende GI5					32140						
Beginn GI5		Andersen et al., 2006			32500					29,65	30,38
GS6											
Ende GI6					33440					32,89	34,03
Beginn GI6		Andersen et al., 2006			33740					33,90	34,51
GS7											
Ende GI7					34760					34,32	35,06
Beginn GI7		Andersen et al., 2006			35480					35,65	36,00
Ende GS8											
	Tephra dunkel, Top helle Lage				36400					37,30	37,82
	Basis Tephra: dünne helle Lage; Pulvermaar-, Meerfelder Maar - od. Wartgesbergtephra	Sirocko et al. (in prep)			36400					37,37	37,94
	Top Schutt mit groben kantigen Komponenten									37,40	37,98
	Basis Schutt mit groben kantigen Komponenten									38,10	38,75
Beginn GS8											
Ende GI8					36660						
Beginn GI8	letzte Birken	Andersen et al., 2006			38220					39,88	40,27
Ende GS9											
	Laschamp Event (Ar/Ar Alter nach Guillou et al.,2004): 40.000 +/- 2.000 BP				39000						
	Top Tephra				39400					42,09	42,78
	Basis Tephra; Pulvermaar-, Meerfelder Maar - od. Wartgesbergtephra	Sirocko et al. (in prep)			39400					42,20	42,93
Beginn GS9											
Ende GI9					39980						44,09
Beginn GI9		Andersen et al., 2006			40160						44,77
GS10											
Ende GI10					40980						46,15
	Ende Ruschung										fehlt
	Beginn Rutschung										fehlt
Beginn GI10		Andersen et al., 2006			41460						46,44
GS11											
Ende GI11					42300						46,67
Beginn GI11		Andersen et al., 2006			43340						47,71
GS12											
Ende GI12					44400						49,60
	Top Tephra: dunkel; nach Veres: im OW ist es die MMT				46400						*50,87*
	Basis Pulvermaar-, Meerfelder Maar - od. Wartgesbergtephra: hell, aber kein Phonolith	Sirocko et al. (in prep)			46400						*50,90*
Beginn GI12	Fichten verbreitet	Svensson et al., 2008			46860						51,09

Zeitmarken	Typische Umweltänderungen	Referenz (für Alter)	Alter AD	Alter BC	Alter b2k	SMfm	SM2m	SM3m	SM4	DE2m	DE3m
	Ende Ruschung										53,60
	Beginn Rutschung										57,00
GS13											
Ende GI13					48520						58,36
Beginn GI13		Svensson et al., 2008			49280						59,59
GS14											
Ende GI14					49620						60,70
Beginn GI14	Beginn wärmeliebende Pollen	Svensson et al., 2008			54220						64,76
	Top Tephra										
	Basis Tephra										
GS15											
Ende GI15					55440						
Beginn GI15		Svensson et al., 2008			55800						
GS16											
Ende GI16					56620						69,31
Beginn GI16		Svensson et al., 2008			58280						71,05
GS17											
Ende GI17					58640						72,05
Beginn GI17	erste Baumpollen	Svensson et al., 2008			59440						etwa 73,60

D Detailed XRF results

Table D.1: WD-XRF results from the core De3 from the Dehner dry maar (main elements).

Tiefe [m]	LOI (wt%)	SiO_2 (wt%)	TiO_2 (wt%)	Al_2O_3 (wt%)	Fe_2O_3 (wt%)	MnO (wt%)	MgO (wt%)	CaO (wt%)	Na_2O (wt%)	K_2O (wt%)	P_2O_5 (wt%)	SO_3 (wt%)	Sum (%)
4.50	7.05	74.28	0.95	10.59	4.41	0.09	1.54	4.26	0.68	2.39	0.12	*0.404*	99.7
6.49	7.68	73.93	0.96	10.87	4.45	0.07	1.56	4.96	0.66	2.43	0.11	*0.472*	100.5
8.70	7.45	73.58	1.02	11.39	4.81	0.07	1.64	4.52	0.67	2.49	0.13	*0.452*	100.8
10.60	6.14	78.70	1.08	8.05	3.40	0.06	1.33	4.72	0.74	1.98	0.11	*0.422*	100.6
14.50	6.56	75.87	0.98	10.60	4.32	0.07	1.54	3.67	0.73	2.37	0.12	*0.322*	100.6
20.10	6.68	75.68	1.05	10.80	4.21	0.06	1.49	3.58	0.73	2.31	0.11	*0.225*	100.3
21.78	6.33	79.17	0.91	8.05	2.93	0.06	1.33	4.73	0.85	1.93	0.09	*0.225*	100.3
23.45	6.73	77.60	0.96	8.85	3.39	0.06	1.48	4.97	0.8	2.03	0.11	*0.207*	100.5
29.50	7.84	71.78	0.99	12.55	4.71	0.09	2.01	4.70	0.78	2.64	0.16	*0.175*	100.6
33.50	6.30	69.05	1.15	16.16	6.23	0.11	2.11	1.51	0.72	3.19	0.18	*0.062*	100.5
39.55	6.41	67.84	1.25	17.00	6.8	0.09	2.00	1.25	0.68	3.27	0.20	*0.022*	100.4
41.31	9.61	55.75	1.01	26.20	8.53	0.09	2.2	1.04	0.36	4.96	0.20	*0.035*	100.4
41.45	6.73	69.14	1.16	15.18	5.99	0.11	2.05	2.41	0.75	3.00	0.19	*0.117*	100.1
43.81	7.07	69.16	1.17	15.33	6.14	0.09	2.09	2.55	0.76	2.98	0.20	*0.119*	100.6
49.50	7.31	66.31	1.39	17.90	7.44	0.09	2.09	1.16	0.64	3.20	0.27	*0.022*	100.5
52.50	7.20	66.00	1.55	16.31	8.08	0.15	2.73	1.93	0.51	2.70	0.30	*0.023*	100.3
57.51	8.09	63.86	1.77	18.05	9.30	0.16	2.16	1.39	0.46	2.86	0.35	*0.011*	100.4
59.57	16.98	59.15	1.22	12.72	19.42	0.93	1.52	1.52	0.23	1.96	2.04	*0.025*	100.7
63.26	16.50	66.05	1.47	14.57	10.33	0.45	1.91	1.69	0.27	2.26	1.46	*0.086*	100.6
68.47	9.05	60.60	1.48	20.83	9.11	0.18	2.53	1.08	0.47	3.70	0.30	*0.03*	100.3
68.63	10.05	56.71	1.37	19.81	12.35	0.21	2.42	0.97	0.43	3.58	2.38	*0.018*	100.3
71.70	8.69	61.19	1.44	20.59	8.66	0.11	2.43	1.04	0.48	3.74	0.36	*0.03*	100.1
77.88	6.75	62.61	1.35	19.59	8.12	0.08	2.82	1.40	0.47	3.70	0.22	*0.023*	100.4
80.70	7.04	61.02	1.19	19.84	8.12	0.15	2.54	2.03	0.48	3.79	0.92	*0.01*	100.1
83.31	10.19	61.64	1.44	20.10	8.07	0.08	2.84	1.83	0.45	3.57	0.26	*0.043*	100.3

Table D.2: WD-XRF results from the core De3 from the Dehner dry maar (trace elements).

Tiefe [m]	V (ppm)	Cr (ppm)	*Co (ppm)*	Ni (ppm)	Cu (ppm)	Zn (ppm)	Rb (ppm)	Sr (ppm)	Y (ppm)	Zr (ppm)	Nb (ppm)	Ba (ppm)	Pb (ppm)	La (ppm)	Ce (ppm)
4.50	79	97	13	33	18	54	90	132	36	545	19	379	21	42	85
6.49	80	98	13	31	22	62	94	142	37	541	20	391	21	46	79
8.70	80	103	15	37	34	61	96	137	39	551	19	401	19	41	84
10.60	60	110	8	24	13	46	69	134	45	956	22	344	20	48	84
14.50	78	105	13	34	15	57	91	128	38	615	20	367	18	47	90
20.10	77	104	11	30	16	58	90	131	41	649	20	387	19	50	87
21.78	48	91	4	20	10	41	70	141	38	721	19	347	16	51	79
23.45	59	99	8	29	14	48	73	143	39	681	19	337	16	42	82
29.50	88	105	14	40	23	64	105	154	37	469	20	407	21	43	83
33.50	122	120	20	53	34	81	135	160	38	368	23	535	23	60	99
39.55	137	121	24	60	39	85	140	142	37	341	28	505	25	46	107
41.31	195	149	17	71	58	99	224	153	29	183	31	497	33	59	119
41.45	117	113	21	52	40	76	126	150	37	380	26	486	21	49	102
43.81	121	109	17	54	39	78	125	164	38	379	28	532	21	50	104
49.50	160	133	23	62	54	91	149	184	36	313	37	623	24	62	115
52.50	179	161	26	87	105	91	127	189	35	303	42	667	24	57	117
57.51	201	156	26	80	71	92	136	180	38	345	51	705	25	63	118
59.57	220	106	22	76	74	91	99	134	24	166	42	568	22	49	99
63.26	260	109	30	82	93	107	115	158	26	187	53	735	23	66	114
68.47	215	146	36	88	87	120	170	151	34	222	40	625	35	65	140
68.63	199	132	33	79	67	112	158	148	34	205	39	612	30	56	118
71.70	205	151	32	82	75	113	168	149	34	228	37	567	33	70	131
77.88	176	142	30	79	74	104	156	233	35	238	33	669	30	69	123
80.70	164	139	27	76	62	96	164	225	34	226	29	573	33	56	117
83.31	284	135	29	75	102	110	154	174	33	216	45	573	32	76	134

E GridMAT scripts

The MATLAB toolbox for AGCM analysis.

Table E.1: The main functions of the GridMAT toolbox.

Script Name	Function
Basic Functions	
gridmat.m	starts script
grd_start.m	input script
grd_load.m	loads netCDF files
grd_save.m	saves netCDF files
CDO-like Functions	
grd_fldmean.m	calculates a field mean
grd_seasmean.m	calculates seasonal means
grd_sellonlatbox.m	selects a field
grd_seltimestep.m	selects a time step or a period
grd_selvar.m	selects a variable
grd_timmean.m	calculates the temporal mean
Converting Functions	
grd_360dcalendar.m	converts calendar year to a 360-day long model year
grd_cart2pol.m	converts Carthesian in polar coordinates
grd_daydecomp.m	decomposes n-th day into year, model, day of a 360d model calendar
grd_freqchart.m	sorting + counting function: Number of events per month per year
grd_monchart.m	sorting function: Number of events per month per year
Analyzing Functions	
grd_mapplot.m	plotting function for maps

continued on next page

grd_tclusteranalyzer.m	analysing of temporal cluster; frequency and size of a temporal cluster per month, saison, year
grd_tclusterfinder.m	finds temporal cluster in a vector and write them in a cell array
grd_tclustermonth.m	analysing monthly distribution of temporal cluster
grd_tclusterplot.m	plots statistics and figures of temporal clusters
grd_tclusterseason.m	analysing season's distribution of temporal clusters
grd_winddiranalyst.m	monthly distribution and wind roses of wind directions and intensities

Opening and saving netCDF files

Opening netCDF files in GridMAT consists of two steps: 1. Opening the netCDF file and converting to MATLAB structure using `grd_load.m`. This function extracts the lons and lats, too. 2. Selection of Variables, time steps, lonlatbox. The selection of the variable needs a permution of the Variables.

```
% GRD_LOAD  Loading netCDF file, output of the data as MATLAB structure and
% Lon/Lat as a grid.
%
%   SYNTAX: [ds lon0 lat0] = grd_load(file)
%       file - netCDF input file
%       ds - output data
%       lon0 - longitude (grid matrix)
%       lat0 - latitude (grid matrix)
%
%   SEE ALSO netcdf meshgrid

function [ds lon0 lat0] = grd_load(file)

%% open files

% using MATLAB native netCDF-Support
ds = netcdf.open(file,'NC_NOWRITE'); %varargin{0}

% define grid
lon1 = single(netcdf.getVar(ds,netcdf.inqVarID(ds, 'lon')));
lat1 = single(netcdf.getVar(ds,netcdf.inqVarID(ds, 'lat')));
[lon0, lat0] = meshgrid(lon1, lat1); % long lat sind prdefiniert mapping tb

```

```
end
```

```
function grd_save( in_file, lons, lats, time_steps, var1, var2)

% create file
ncid = netcdf.create(in_file,'NC_CLOBBER');

%set dimensions and varibales
lat_name = 'lat';
lat_dimid = netcdf.defDim ( ncid, lat_name, size(lats,2) );
lon_name = 'lon';
lon_dimid = netcdf.defDim ( ncid, lon_name, size(lons,2) );
time_name = 'time';
time_dimid = netcdf.defDim ( ncid,time_name,netcdf.getConstant ('
    NC_UNLIMITED') );

%  Define the coordinate variables.
lat_varid = netcdf.defVar ( ncid, lat_name, 'double', lat_dimid );
lon_varid = netcdf.defVar ( ncid, lon_name, 'double', lon_dimid );
time_varid = netcdf.defVar ( ncid, time_name, 'double', time_dimid );


%  Assign units attributes to coordinate variables.
units = 'units';
lat_units = 'degrees_north';
netcdf.putAtt ( ncid, lat_varid, units, lat_units );
lon_units = 'degrees_east';
netcdf.putAtt ( ncid, lon_varid, units, lon_units );

long_name = 'long_name';
lat_long_units = 'latitude';
netcdf.putAtt ( ncid, lat_varid, long_name, lat_long_units );
lon_long_units = 'longitude';
netcdf.putAtt ( ncid, lon_varid, long_name, lon_long_units );

std_name = 'standard_name';
lat_std_name = 'latitude';
netcdf.putAtt ( ncid, lat_varid, std_name, lat_std_name );
lon_std_name = 'longitude';
netcdf.putAtt ( ncid, lon_varid, std_name, lon_std_name );

```

```
39 %  Define the NETCDF variables. The dimids array is used to pass the
40 %  dimids of the dimensions of the NETCDF variables.
41 dimids = [ lon_dimid, lat_dimid, time_dimid ];
42
43 u10_name = 'var165';
44 u10_varid = netcdf.defVar ( ncid, u10_name, 'float', dimids );
45 v10_name = 'var166';
46 v10_varid = netcdf.defVar ( ncid, v10_name, 'float', dimids );
47
48 %  Assign units attributes to the variables.
49 velocity_units = 'm/s';
50 netcdf.putAtt ( ncid, u10_varid, units, velocity_units );
51 netcdf.putAtt ( ncid, v10_varid, units, velocity_units );
52
53 % Grid definition
54 grid_type = 'grid_type';
55 var_grid_type = 'gaussian';
56 netcdf.putAtt ( ncid, u10_varid, grid_type, var_grid_type );
57 netcdf.putAtt ( ncid, v10_varid, grid_type, var_grid_type );
58
59
60 % Leave define mode and enter data mode to write data.
61 netcdf.endDef(ncid);
62
63 %%
64 %  Write the coordinate variable data.
65 netcdf.putVar ( ncid, lat_varid, lats );
66 netcdf.putVar ( ncid, lon_varid, lons );
67 % netcdf.putVar ( ncid, time_varid, time );
68
69 %  Write the data. This will write our surface pressure and
70 %  surface temperature data. The arrays only hold one timestep worth
71 %  of data. We will just rewrite the same data for each timestep. In
72 %  a real application, the data would change between timesteps.
73
74   for rec = 1 : time_steps
75
76     start(4) = rec - 1;
77     netcdf.putVar ( ncid, u10_varid, start, count, u );
78     netcdf.putVar ( ncid, v10_varid, start, count, v );
```

```
79
80    end
81
82  %%
83  % Verify that one variable was created.
84  % [varname xtype dimid natts ] = netcdf.inqVar(ncid,0)
85
86  %  Close the file.
87  %
88  netcdf.close ( ncid );
89
90  end
```

Saving of netCDF files using `grd_save.m`. The function saves a dataset as a netCDF file. Example of a generated file:

```
1  >> nc_dump('uva_test.nc')
2  netcdf uva_test.nc {
3
4  dimensions:
5    lat = 2 ;
6    lon = 2 ;
7    time = UNLIMITED ; (1 currently)
8
9  variables:
10   double lat(lat), shape = [2]
11     lat:units = "degrees_north"
12     lat:long_name = "latitude"
13     lat:standard_name = "latitude"
14   double lon(lon), shape = [2]
15     lon:units = "degrees_east"
16     lon:long_name = "longitude"
17     lon:standard_name = "longitude"
18   double time(time), shape = [1]
19   float var165(time,lat,lon), shape = [1 2 2]
20     var165:units = "m/s"
21     var165:grid_type = "gaussian"
22   float var166(time,lat,lon), shape = [1 2 2]
23     var166:units = "m/s"
24     var166:grid_type = "gaussian"
25 }
```

E.1 cdo-like functions

Selection of variables (`grd_selvar.m`), time steps (`grd_seltimestep.m`), field of interest `grd_sellonlatbox.m`.

```
% GRD_SELVAR  Select variable from netCDF file, output of the data as
% MATLAB structure.
%
%   SYNTAX: dsVar = grd_selvar(ds, varname)
%       ds      - netCDF input file
%       varname - nae of variable, not the code
%       dsVar   - output file

    function dsVar = grd_selvar(ds, varname)
        dsVar = single(netcdf.getVar(ds,netcdf.inqVarID(ds, varname)));
        % needs to transpose of MxNxP to NxMxP to fit to the original size of
        % Lon/Lat
        dsVar = permute(dsVar,[2 1 3]);
        disp(['The following variable is selected: ', varname]);
    end
```

```
% GRD_SELTIMESTEP Select timestep from expanded netCDF file.
% Part of GridMAT - Grid Modell Analysis Toolbox (Dietrich 2010).
%
%   SYNTAX: Xt = grd_seltimestep(X, timestep)
%       input X, of the size X(Lon,Lat,Time), eg. u (128x64x5400)
%       timestep, to be selected
%       output Xt, of the size X(Lon,Lat)
%
    function Xt = grd_seltimestep(X, timestep)
        Xt = double(X(:,:,timestep));
        disp(sprintf('Time step %i was selected.', timestep))
    end
```

```
% GRD_SELLONLATBOX Selection of gridbox, which incorporates at least the
% given longitude/latitude borders.
%


    function [Xll, lonll, latll] = grd_sellonlatbox(X, lon, lat, lona, lonb,
        lata, latb)
        % input X, of the size X(Lon,Lat,Time) or X(Lon,Lat)
```

```
7         % input lon/lat-arrays which depends on X
8         % selection of box by lona to lonb and lata to latb, with a < b
9         % output Xll, lonll, latll of the new size which covers the selected
              grid points
10
11    lonll = lon(1,find(lon(1,:)>=lona & lon(1,:)<=lonb));
12          lonll = repmat(lonll,size(lonll,2),1);
13          latll = lat(find(lat(:,1)>=lata & lat(:,1)<=latb),1);
14          latll = repmat(latll,1,size(latll,1));
15          Xll   = X (find(lat(:,1)>=lata & lat(:,1)<=latb), ...
16              find(lon(1,:)>=lona & lon(1,:)<=lonb), : );
17
18          disp(sprintf('A %ix%i box was selected over %i timesteps.', size(Xll
                ,1), size(Xll,2), size(Xll,3)))
19      end
```

```
1       function dsVar = grd_selvar(ds, varname)
2           dsVar = double(netcdf.getVar(ds,netcdf.inqVarID(ds, varname)));
3           % needs to transpose of MxNxP to NxMxP to fit to the original size
4           % of Lon/Lat
5           dsVar = permute(dsVar,[2 1 3]);
6           disp(['The following variable is selected: ', varname]);
7       end
```

Calculation of mean values for a field and the time.

```
1   % GRD_FLDMEAN   calculates the fieldmean of variables in a grid.
2   %
3   %   SYNTAX: Xmean = grd_fldmean(X)
4   %       input X, of the size X(Lon,Lat,Time), where time is optional , eg. u
        (128x64x5400)
5   %       output Xmean, of the size X(Lon,Lat,Time)
6
7       function Xmean = grd_fldmean(X)
8           for i = 1 : size(X,3)
9               Xmean(:,i) = mean(mean(X(:,:,i)));
10          end
11          fprintf('The fieldmean of %i timesteps was calculated.\n', ...
12              size(X,3))
13      end
```

```
1   % GRD_TIMMEAN   calculates the time mean of variables in a grid.
```

```
%
%   SYNTAX: Xtmean = grd_timmean(X, sts, ets)
%       X       - input of the size X(Lon,Lat,Time), where time is optional
%                   , eg. u (128x64x5400)
%       sts     - start time step
%       ets     - end time step
%       Xtmean  - outputof the size X(Lon,Lat,Time)

    function Xtmean = grd_timmean(X, sts, ets)
        Xtmean(:,:) = mean(X(:,:,sts:ets),3);
    end
```

E.2 Analysis of Wind Vectors

The two-dimensional Cartesian coordinates of u10 and v10 are transformed into polar coordinates.

```
  [winddir, windspeed] = cart2pol(u,v);
  winddir = winddir.*(180/pi);     % transforms angle from radian to degree
  winddir = mod(-90-winddir,360); % rotates 0° towards N (compass) and shows
                                   % the direction where wind is coming from
```

The monthly distribution of days with easterly wind direction (wind directions between 0° and 180°) is calculated using the function `grd_daydecomp.m`.

```
% GRD_DAYDECOMP Decomposes n-th day into year, mo, day of a 360d model
    calendar
%   SYNTAX: MonthCum = grt_daydecomp(day)
%       with MonthCum = [myr mmon mday day]

   function MonthCum = grd_daydecomp(day)
      i = 1 : length(day);
      myr   = ceil(day(i)/360);
      mmon  = ceil(day(i)/30) - (myr(i)-1)*12;
      mday = ceil(day(i) - ((mmon(i)-1)*30) - ((myr(i)-1)*360) );
      MonthCum = horzcat(myr,mmon,mday,day);
   end
```

E.3 Analysis of LEWIC

Temporal clusters of east wind, the long-persisting east wind conditions (LEWIC), are defined as time-related events with a length of at least three days and are separated from the rest of the data matrix (`grd_tclusterfinder.m`).

```
% GRD_TCLUSTERFINDER finds temporal cluster in a vector and write them
% in a cell array.
%
% ATTENTION: The output will contain the chosen vector with new index, only.
%
%   SYNTAX: C = grd_tclusterfinder(A, dim)
%       A - input array
%       C - output cell array (sorted)
%       dim - if input data is a array dim defines the column with data of
%       interest
%
%   % v.0.1 does not use angel of wind direction
%
%   Start/End of a temporal cluster is defined by change of algebraic sign
%   in the u-vector. Clusters are defined as a group of continous days,
%   with a minimum of 3 days.
%
%   Example: If A(:,2) = [2 -2 -2 2 -2 -2 -2] and A(:,1) = [1:length(A)].
%   In A are to clusters (A(2:3) and A(4:7), since A(i+1,1)-A(i,1) == 1.
%
%   SEE ALSO cellfun

function C = grd_tclusterfinder(A, dim)

% DEFINE cluster minimum size
mincellsize = 3;

% select dependence for clustering: using u
depvar = 0;

% If last element of input array is negetave, the vector is expanded with
% one element artifically for correct funtion of the following loop
if A(end,2) < 0
    A = cat(1,A,[A(end,1)+1; A(end,2)*-1]');
end
```

```
36
37  % Building the output cell
38  C={}; len_count = 0; cell_count = 0; switch_count = 0;
39  for i = 1 : length(A)
40
41      if A(i,2) <= depvar % Decision for forming a new cell
42          len_count = len_count + 1;
43          switch_count = switch_count +1;
44      elseif A(i,2) > depvar
45    cell_count = cell_count + 1;
46    switch_count = 0;
47      else
48          error('should be 0 or 1')
49      end
50
51      if switch_count == 0 && i > 1 % Creating cell array
52    C(cell_count) = { A(i-len_count : i-1 , :) };
53          len_count = 0;
54      end
55
56  end
57
58  % Empty cells in cell arrray will be deleted.
59  C = C(cellfun(@(C) ~isempty(C),C));
60
61  % 'small' cells in cell arrray will be deleted.
62  C = C(cellfun(@(c) size(c,1) >= mincellsize, C));
63
64  % Sorting (descending) cell elements reagarding its elements sizes
65  C = sortcellsize(C);
66
67  end
68
69      function Y = sortcellsize(X)
70      % Sorting (descending) cell elements reagarding its elements sizes
71          x = cellfun('size',X,1);
72          [~, is] = sort(x,'descend');
73          Y = X(is');
74      end
```

These clusters are investigated after their length as well as after their time of occurrence (`grd_tclusteranalyzer.m`).

```
% GRD_TCLUSTERANALYZER - Analysing of temporal cluster
% eg. frequency ans size of a temporal cluster per month, saison, year.
%
%   SYNTAX: [FreqChart, MonChart2L, c_sizeL, c_occL] = grd_tclusteranalyzer(C
    )
%
%       C         - input cell array (usually, output of grd_tclusterfinder.m)
%       FreqChart - output array [cluster frequency x month x year]
%       MonChart - output array [monthly distribution of temp. clusters]
%       c_sizeL   - output size of clusters (L: Large >3dayx)
%       c_occL    - output starting day of cluster occurence
%
%   SEE ALSO grd_daydecomp grd_monchart grd_freqchart

function [FreqChartL, MonChart2L, c_sizeL, c_occL] = ...
    grd_tclusteranalyzer(C)

%% DEFINE variables
    global in_mincellsize % minimum cell size to be analyzed
    global TextClusterSize

%%  analysis of cells
%   cell size, monthly cell frequency

    for i = 1 : size(C,2)
        % measuring all cell sizes
        c_size(i) = size(C{1,i},1);

        % selects starting day when cluster occurs
        c = C{1,i};
        c_occ(i) = min(c(:,1));
    end

    % Number of large clusters
    numlargeclust = ...
        size(C(cellfun(@(c) size(c,1) >= in_mincellsize, C)...
        ),2);
    c_sizeL = c_size(1:numlargeclust);
```

```
    c_occL = c_occ(1:numlargeclust);

    % Compute for day: modelyear, mmonth, mday
    MonthCum2 = (grd_daydecomp(c_occ'));
    MonthCum2L = MonthCum2(1:numlargeclust,:);

    % Transforming into month x year table
    MonChart2 = grd_monchart(MonthCum2);
    MonChart2L = grd_monchart(MonthCum2L);

    % Transforming into frequency x month x year form
    FreqChart = grd_freqchart(MonthCum2, c_size);
    FreqChartL = grd_freqchart(MonthCum2L, c_sizeL);

end
```

The occurrence of LEWIC are finally analyzed by their relative frequencies in the annual cycle (`grd_tclustermonth.m`).

```
% GRD_TCLUSTERMONTH - Analysing monthly distribution of temporal cluster.
%
%   SYNTAX: [TClusterSizeChart var165timemeanM var166timemeanM] ...
%             = grd_tclustermonth(c_occ,c_size)
%
%      c_occ      - input ocurrance day of temporal cluster
%      c_size     - lenght (in days) of temporal cluster
%      var1       - input var1 (eg var165)
%      var2       - input var1 (eg var166)
%      TClusterSizeChart - output array [cluster length x month]
%      var1timemeanM - monthly average of var1
%      var2timemeanM - monthly average of var1
%
%   SEE ALSO grd_daydecomp grd_timmean eval

function [TClusterSizeChart var165timemeanM var166timemeanM] = ...
    grd_tclustermonth(c_occ,c_size,var165,var166)

%% DEFINE
global in_mincellsize

%% calculation
```

```
23 CMonChart = grd_daydecomp(c_occ');
24 CMonChartX = cat(2,CMonChart,c_size'); % including temp. cluster size
25
26 % allocation of variables MonCahrt01..MonChart12
27 for m = 1:12 % '%02.0f' makes the leadin 0 at Jan..Sep
28     eval(sprintf('CMonChart%02.0f = zeros(1,size(CMonChartX,2));',m));
29 end
30
31 % Computes single month charts from Jan .. Dec
32 for i = 1 : size (CMonChart)
33     for m = 1:12
34         if CMonChart(i,2) == m  % search month
35             eval(sprintf(...
36                 'CMonChart%02.0f = cat(1,CMonChart%02.0f,CMonChartX(%02.0f,:))
                        ;',...
37                 m,m,i));
38         end
39     end
40 end
41
42 % delete alloc row in var
43 for m = 1:12
44     eval(sprintf('CMonChart%02.0f(1,:) = [];',m));
45 end
46
47 % and pastes its cluster sizes together to TClusterSizeChart
48 TClusterSizeChart = nan(max(c_size)+1,12);
49 for m = 1:12
50     eval(sprintf(...
51         'TClusterSizeChart(1:size(CMonChart%02.0f,1),%02.0f) = CMonChart%02.0
               f(1:size(CMonChart%02.0f,1),5);'...
52         ,m,m ,m,m));
53 end
54
55
56 %% time mean of each CMonChart01..12
57 % disp(TClusterSizeChart)
58
59 cellexist = 0;
60 for m = 1:12
```

```
61
62      for i = 1 : eval(sprintf('size(CMonChart%02.0f,1)',m))
63      % calculates time mean of each cluster per month for large temporal
64      % clusters
65
66      if TClusterSizeChart(i,m) >= in_mincellsize
67
68              cellexist = 1; % check if cell size >= mincellsize to get out of
                    the loop
69
70              var165timemeanA(:,:,i) = grd_timmean(var165, ...
71                  eval(sprintf('CMonChart%02.0f(i,4)',m)), ...
72                  eval(sprintf('CMonChart%02.0f(i,4)+CMonChart%02.0f(i,5)-1;',m,
                        m)));
73
74              var166timemeanA(:,:,i) = grd_timmean(var166, ...
75                  eval(sprintf('CMonChart%02.0f(i,4)',m)), ...
76                  eval(sprintf('CMonChart%02.0f(i,4)+CMonChart%02.0f(i,5)-1;',m,
                        m)));
77
78          else
79              cellexist = 0;
80          end
81
82      end
83
84      % calculates time mean per month from its single clusters
85      if cellexist == 1
86
87          var165timemeanM(:,:,m) = grd_timmean(var165timemeanA, ...
88              1, size(var165timemeanA,3));
89
90          var166timemeanM(:,:,m) = grd_timmean(var166timemeanA, ...
91              1, size(var166timemeanA,3));
92
93      else
94          continue
95      end
96
97  end
```

```
disp(' ')

end
```

E.4 Visualization of Wind Speed and Wind Direction in a Map

The Visualization of the data in a map uses the function `grd_mapplot.m` which applies the external function `ncquiverref.m` by Roberts (2010).

```
% GRD_MAPPLOT  Plotting Maps of input data
%
%   SYNTAX: handle = grd_mapplot(lat0, lon0, u, v, projection, maplimits)
%       lon0       longitude (grid matrix)
%       lat0       latitude (grid matrix)
%       u          input u vektor
%       v          input v vektor
%       projection map projection (eg. 'lambert')
%       maplimits  maplimits [lona lonb lata latb]
%       title      map title
%
%   Using MATLAB mapping toolbox with external ncquiverref package by
%   Andrew Roberts;
%
%   SEE ALSO ncquiverref

function grd_mapplot(lat0, lon0, u, v, projection, maplimits, mtitle)
%% using mapping toolbox
    landareas = shaperead('landareas', 'UseGeoCoords', true);
    rivers = shaperead('worldrivers', 'UseGeoCoords', true);

    figure
    axesm(projection,'MapLatLimit',[maplimits(1:2)],'MapLonLimit',[maplimits
        (3:4)])
    framem('on'); gridm('on'); mlabel('on'); plabel('on');
    geoshow(landareas, 'FaceColor', [.9 .9 .9], 'EdgeColor', [.6 .6 .6]);
    geoshow(rivers, 'Color', [.3 .3 .3])
    % plots a rectangular over AOI
    % clim dyn
    linem([54; 48; 48; 54; 54],[4; 4; 12; 12; 4],'r-')
    plotm([50.295 6.505],'r*') % Dehner dry maar
```

```
31      % plots quivers
32      zmin = ceil ( min ( sqrt( u(:).*u(:) + v(:).*v(:) ) ) ); zmin(zmin == 0)
            = 1e-15;
33      zmax = ceil ( max ( sqrt( u(:).*u(:) + v(:).*v(:) ) ) );
34      ncquiverref(lat0,lon0,u,v,'m/s',10,'true','col',[zmin : 2.5 : zmax]);
35      t = title(mtitle);
36      set(t,'Interpreter','none');
37  end
```

Acknowledgment

I am deeply thankful to all that friends and people helping, inspiring or encouraging me directly or indirectly to progress and finish the thesis.

Eidesstattliche Erklärung

Ich versichere hiermit, die Arbeit selbständig und nur unter Verwendung der angegebenen Hilfsmittel verfasst zu haben.
Ich habe oder hatte die hier als Dissertation vorgelegte Arbeit nicht als Prüngsarbeit für eine staatliche oder andere wissenschaftliche Prüfung eingereicht.
Ich hatte weder die jetzt als Dissertation vorgelegte Arbeit noch Teile davon bei einer anderen Fakultät bzw. einem anderen Fachbereich als Dissertation eingereicht.

Mainz, März 2011